A Numerical Study of Internal Flow Effects on Skin Friction Gages

by

Matthew MacLean

A dissertation submitted to the Aerospace and Ocean Engineering Department of Virginia Polytechnic Institute & State University in partial fulfillment of the requirements for the degree of

Doctor of Philosophy

in

Aerospace Engineering

APPROVAL:

Joseph A. Schetz, Chairman

William Devenport

Bernard Grossman

Rakesh K. Kapania

Dominique Pelletier

Karen Thole

KEYWORDS: skin friction measurement, computational fluid dynamics (CFD), finite element method, boundary layer

April 15, 2002
Blacksburg, Virginia

Matthew MacLean

A Numerical Study of Internal Flow Effects on Skin Friction Gages

Abstract

This work examines the detailed flow characteristics of direct measuring skin friction gages with computational methods. This type of device uses a small movable head mounted flush to a wall such that the head is assumed to be exposed to the same shear stress from the flow as the surrounding wall. The force caused by the action of the shear stress on the head deflects a flexure system monitored by instruments such as strain gages mounted at the base of a beam.

The goal of the study was to develop an understanding of the effects that the geometric design and installation parameters of the sensor have on the surrounding flow and the ability of the sensor to reflect the undisturbed shear stress value. Disruption of the external flow due to poor design and/or improper installation of the sensor can take the form of intrusion into the flow, recession into the wall, and/or tilted alignment of the sensor such that the head is not flat in the plane of the wall, as well as flow into or out of the small gap surrounding the sensing head. Further, the performance of a direct measuring skin friction sensor in the presence of a pressure gradient has always been a concern. These effects are studied here with a three-dimensional, Navier-Stokes code based on a finite element method technique.

Numerical solutions for cases in which one or more design parameters were varied are shown for a variety of flow situations. These situations include: (a) a laminar fully-developed channel flow at a low Reynolds number, (b) a turbulent flat plate boundary layer flow at a high Reynolds number, and (c) strong favorable and adverse pressure gradient turbulent boundary layer flows created by converging and diverging channels at high Reynolds number. Reported results for all cases include detailed flow visualization and stress field imagery, and total surface forces on the sensing head and gage flexure. Under ideal circumstances, these total forces should reflect as accurately as possible the average value of undisturbed shear stress times the exposed sensing head area (the friction force). Any deviation from this value was considered an "error" in the simulated measurement.

The laminar channel flow case with a strong favorable pressure gradient showed the importance of proper alignment of the sensor. Protrusion or recession of the sensing head proved to be the dominant effect on resulting forces seen by the gage, changing the output by up to 15% for head protrusion and 10% for head recession for misalignments up to +/-1% of the head diameter. The thickness of the lip on the edge of the head also proved to have a significant effect on the output, with a smaller lip thickness generally showing better performance than a large

one. Zero lip thickness indicated accuracy to within 1% of the desired wall shear result, since the pressure differences had little influence on the sensing head. Finally, the assumption of a linear pressure variation from the surface to the cavity along the lip as has been suggested in the past was investigated. The results indicate that the linear assumption works well only for large ratios of lip thickness to gap size, a fact which is correlated with previous experimental results.

For the turbulent external flat plate case, misalignment remained the dominant effect on the sensor response. Results indicated that, in general, protrusion is more costly than the same level of recession, and a protrusion of +1% of the head diameter was shown to cause in excess of 100% error in indicated wall shear output. Both protrusion and recession produced large variations in both force and moment on the sensing flexure, but the outcome was that for protrusion the errors caused by these two effects tended to sum together, while for recession they tended to partially cancel out.

The gap size played an increased role in the high Reynolds number boundary layer cases. Gap sizes of 1.67% up to 6.67% of the head diameter were studied and were shown to produce output errors between 4% and 22% (with larger errors corresponding to larger gap sizes), thus showing the importance of minimizing the gap for high Reynolds number flows. The lip was shown to have no significant effect for a flow without a pressure gradient.

Finally, the favorable and adverse pressure gradient flows showed reasonable performance of the skin friction gage. Errors in output were shown to be -6% for the favorable pressure gradient case and 17% for the adverse pressure gradient case. Only the baseline gage design was studied for these situations, but the results from the two cases indicate that further reducing the lip thickness may not improve the performance of the gage. The error in output was caused almost entirely by applied moment for the adverse pressure gradient, while the applied force and applied moment had a cancellation effect in the favorable pressure gradient case.

As a general result, the use of computational fluid dynamics has been shown to be an effective tool in the design and analysis of skin friction gages. Using a computational approach has the advantage of being able to resolve the small, confined gap regions of the gage, providing information that has been shown to be unavailable from previous experimental studies. This work has contributed to a much better understanding of the detailed flow over, in, and around skin friction gages. This will lead to improved gage design and reduced uncertainty in these important measurements.

Acknowledgements

This work was funded in part by a grant from *Luna Innovations, Inc.* (Blacksburg, VA). I would therefore like to thank them for their generous support throughout the bulk of this project.

I wish to thank Dr. Schetz for his financial and technical support in this research project. He has provided guidance and direction throughout this research and dissertation as well as patience while I worked to understand the methodology and characteristics of a commercial CFD code. He also provided technical insight with much of the physics and general results of the viscous problems studied in this document.

I wish to particularly thank Dominique Pelletier from the *Ecole Polytechnique de Montreal* in Montreal, Canada for his extended help with the analysis contained in this document. He has been a primary source of information about the finite element method and workings of the Ansys/FLOTRAN code as well as information and guidance on the topic of grid convergence and dependency.

I would also like to acknowledge the additional members of my committee for their help in completing this dissertation: Dr. William Devenport, Dr. Bernard Grossman, Dr. Rakesh K. Kapania, and Dr. Karen Thole. These individuals contributed time during various points of this project and provided insightful ideas to polish this document to its finished form.

Finally, I must acknowledge Marlene and my parents for their presence since I started on this project.

Contents

List of Figures

List of Tables

List of Symbols

Arabic Symbols

A	area
a	friction force moment center [Allen, 1976]
A_1	actual fractional error estimator
b	normal force moment center [Allen, 1976]
b_i	geometric constants [Frei and Thomann, 1980]
c	lip length
C_f, C_F	skin friction coefficient
c_i	concentration of species i, geometric constants [Frei and Thomann, 1980]
C_D	drag coefficient
C_L	lip force coefficient [Allen, 1976]
C_M	total moment coefficient [Allen, 1976]
C_N	normal force coefficient [Allen, 1976]
c_P	specific heat
D	gage head diameter
D_{BEAM}	beam diameter
D_{ij}	diffusion coefficient
dP/dx	pressure gradient
E_1	Richardson extrapolation error estimator
E^K	kinetic energy term
ENDS	turbulent dissipation [Ansys]
ENKE	turbulent kinetic energy [Ansys]
F	force
f	grid dependent solution quantity
F_F	friction force [Allen, 1976]
F_L	lip force [Allen, 1976]
F_N	normal force [Allen, 1976]
F_P	drag due to pressure [Everett, 1958]
F_s	factor of safety

f_T	measured shear stress [Everett 1958]
G	gap length, linear (matrix) operator
GCI	grid convergence index
g_i	gravity (body force) component, continuum function for grid based Taylor's series
h	channel height, grid element size
K	force [Frei and Thomann, 1980]
K_i	constants
L	length
$\mathscr{L}$	far-field boundary position, linear (matrix) operator
L_{BEAM}	beam length
M	moment, Mach number
m	plate slope
M_Φ	convergence monitor for degree of freedom Φ
n_i	direction cosine
P	pressure
p	order of convergence (spatial), finite element shape function order
PRES	pressure [Ansys]
q	dynamic pressure
R	residual matrix
r	grid refinement ratio
Re	Reynolds number
Re_δ	Reynolds number based on boundary layer thickness
Re_{fr}	friction Reynolds number
Re_θ	Reynolds number based on momentum thickness
R_i	momentum source term
S	lip surface coordinate direction, slot width [Dhawan, 1953]
s_i	geometric constants [Frei and Thomann, 1980]
T	temperature
TEMP	temperature [Ansys]
u	finite element solution variable

u, v, w	Cartesian components of velocity
u_τ	friction velocity
U_∞	free-stream velocity
VX, VY, VZ	Cartesian components of velocity [Ansys]
w	channel width, finite element method weighting function
w_1	distance from channel symmetry plane to outer boundary placement
W^V	viscous work term
x, y, z	Cartesian coordinate directions
Z	misalignment distance

Greek Symbols

δ	boundary layer thickness
ε	turbulent dissipation
θ	momentum thickness
κ	turbulent kinetic energy
Λ	taper angle
μ	dynamic viscosity
μ_T	turbulent viscosity
ν	kinematic viscosity
ρ	density
σ	surface tension coefficient
τ	shear stress
τ_W	wall shear stress
Φ	degree of freedom, viscous dissipation
$\not{\psi}_i$	finite element method shape function
Ω	integration domain

Superscripts

*	non-dimensional or normalized value
~	finite element method approximate solution

Subscripts

dnstr	downstream condition

E	edge value
EXACT	exact (infinite grid) solution
INLET	condition at problem inlet
i, j, k	indices
o	true, or nominal value
OUTLET	condition at problem outlet
ref, REF	reference condition
upstr	upstream condition
w	wall value
x, y, z	Cartesian components
0	stagnation quantity
1	fine grid index
2	coarse grid index
∞	infinite or free-stream value, dimensionless scaling quantity

CHAPTER 1: Introduction

1.1 Introductory Comments

Since the beginning of recorded history, mankind has sought to understand and utilize fluids in every aspect of human life. A *fluid* is defined as any matter which continuously deforms under the presence of a tangential stress [Anderson, 1991], and is commonly thought of as a liquid or a gas. Even in ancient times, humans created irrigation systems, wells, and even boats and ships – all to utilize a fluid to improve their lives in some way. Within each human body, life is sustained by the presence and action of fluids, including the living fluid pump known as the heart driving the circulation of needed nutrients to various parts of the body, saliva and digestive fluids which isolate and bring those nutrients into the body, and the fluid cushion that helps to protect and support the brain itself. Indeed, from beginning to end, life is immersed in the presence and actions of fluids.

To mankind, however, it is typically not these fluids themselves that are so important. Whether it is the motion of air flow over an aircraft wing or the movement of a fluid through a pipe or channel, an essential piece of information about the process is how the fluid interacts with the solid objects that it come in contact with. A fluid and a solid affect each other by the exertion of forces on the other -- forces which can always be broken up into two components: a *pressure and viscous normal force* which is defined to be normal to the solid surface at a point, and a *viscous shear force* which is defined to be tangent to the solid surface at a point [Anderson, 1991]. These two forces are stress fields which act over finite areas of contact between a fluid and a solid. A diagram of such a component resolution is shown in Fig. 1-1.

The tangential shear stress term is often termed as “skin friction,” for its orientation of action is similar to what is experienced when two solids are rubbed together – a resistive force opposing the direction of motion for each of the two solids, acting at their interface. In modern aerodynamic profiles, where the pressure field is approximately symmetric, this skin friction force can account for over one-half of the total drag force on the body of interest.

As one of the defining parameters in such a calculation, skin friction is often given in coefficient form, a dimensionless or normalized version of shear stress as in eqn. (1-1).

$$C_f \equiv \frac{\tau_W}{\frac{1}{2}\rho_E U_E^2} \tag{1-1}$$

The shear stress is normalized by the dynamic pressure of the flow. This is the term given on the bottom of the fraction in eqn. (1-1), and it is sometimes abbreviated with the designation q.

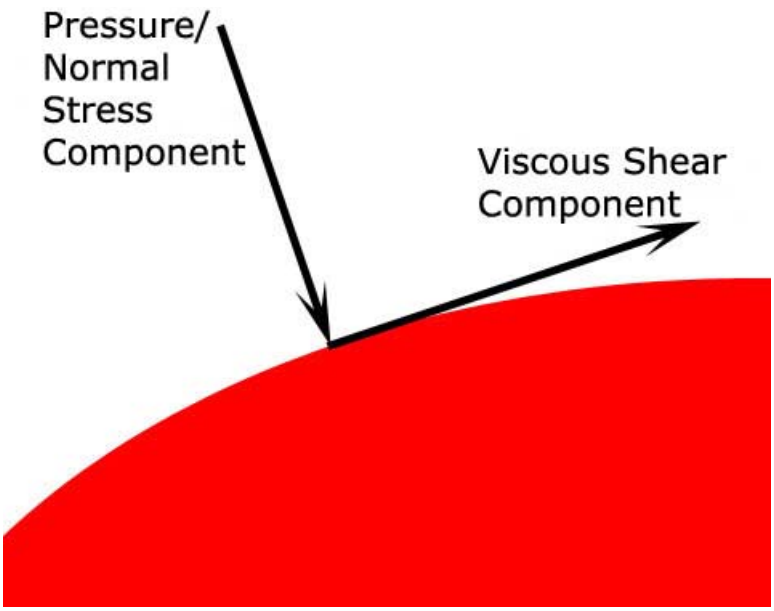

Figure 1-1. Component Illustration of Fluid Forces upon any Solid Object

These forces act on a solid object to resist its motion relative to the surrounding fluid. Drag in general opposes the direction of motion of an object, and is always caused by a combination of these two stress fields. The skin friction drag already discussed is a major contributor to most bodies, provided they are relatively streamlined. Another source of drag on an object is the force caused by a pressure field that is not horizontally symmetric about the body – one in which there is separation. This is also called form drag [Anderson, 1991], and is increasingly significant for bluff bodies (bodies with large frontal areas in general). Wave drag is caused by compressibility of the fluid at higher speeds. Shockwaves resulting from compressibility can create large pressure differences over the body, creating drag [Bertin and Smith, 1998]. Also, induced drag is a result of any finite length wing or aerodynamic shape.

The uneven lift distribution caused by the wing ends leads to an additional drag resulting from the change in effective angle of attack on the finite wing [Shevell, 1989]. These contributions can be analyzed individually or in summation, and are often given in coefficient form similar to the C_f definition. The drag coefficient is defined in eqn. (1-2). Again, the dynamic pressure appears specifically, multiplied by a given reference area.

$$C_D \equiv \frac{\text{Drag}}{\frac{1}{2}\rho U_\infty^2 A_{REF}} \tag{1-2}$$

Fluid-dynamic drag is, of course, probably the most fundamental parameter in evaluating the effectiveness or efficiency of any such solid object. The already referenced author John Anderson provides some of his vast historical knowledge about the interest here. In 1588, one of the largest naval battles in history was fought in the English Channel between Spain and England – a battle which was to forever change the course of history in both Europe and the world. The result of this battle is that the lighter, faster, and more maneuverable ships of the English fleet decimated the heavy, slow-moving Spanish armada despite their superior firepower. The outcome of this battle solidified the link between a ship's naval success and its speed and maneuverability on the water. Reducing resistance in the ocean became a central issue in engineering and design.

Many theories developed over the next few centuries, attempting to quantify the resistive drag caused by these forces. This progress eventually led to a stagnating point – caused by a seemingly complete description of fluid dynamics now termed the Euler equations of fluid motion. This set of equations for a fluid with no friction can be solved to illustrate the very famous d'Alembert's paradox. This concept stated that for a rigid, non-accelerating body moving in such an ideal fluid, the drag on that object was identically zero [Karamcheti, 1966]. The paradox is that this conclusion is obviously not true for real objects like ships moving through the water. Methods were sought to measure this drag, and one systematic study of this phenomenon hinted at aspects of things to come and formed one of the first relatively modern measurements of friction for streamlined shapes [Froude, 1872].

Froude dragged planks of approximately uniform cross-section, but varying length through the water at various speeds. Resistance in the water was measured by the extension of a spring holding the planks and recorded onto paper by a pen attached to the spring. Froude had

exceptional foresight however, making the following statement about the variation of drag with plank length:

> "It has always seemed [impossible that surface-friction varies directly with wetted surface area], because the portion of surface that goes first in the line of motion, in experiencing resistance from the water, must in turn communicate to the water motion in the direction in which it is itself traveling; …the portion of surface which succeeds the first will be rubbing, not against stationary water, but against water partially moving in its own direction, and cannot therefore experience as much resistance from it. …doubling, for instance, the length of a surface, though it doubles the area, would not double the resistance, for the resistance of the second half would not be as great as the first" [Froude, 1872].

He found, among other things, that the above statement was true, and that the drag scaled approximately with velocity to the 1.8 power (closely indicative of a constant drag coefficient as defined by eqn. 1-2).

His thought predated, but conceptually paralleled, the pivotal conclusions drawn by Prandtl, published to the world only a few years later – the concept of the boundary layer. In 1904, Prandtl showed that a thin layer of influence between a fluid and a solid is dominated by the viscosity of the fluid in an otherwise ideal, inviscid motion [Schetz, 1993]. The only qualification of this statement is based on the Reynolds number of the flow. Higher Reynolds number in general means that the viscous layer is increasingly thinner and more confined, while a very low Reynolds number (below about 600 or so for external flows) suggests that the entire flow-field must account for the effects of viscosity. The bulk of engineering subjects, however, have a sufficiently high Reynolds number to make use of the boundary layer.

So, since the origin of mankind's curiosity about the world around him, the problem of the resistance to fluid motion has been a central one in countless advancements and developments of better ways to do things. The age of flight has accelerated an already blooming field of analysis, and the need to understand shearing friction has been magnified. In the modern world, with the marvels of jet fighters, automobiles, hydraulics, power stations, aircraft carriers, and rockets, skin friction becomes one of the uniquely defining parameters of the development and improvement of such devices. Measuring and knowing skin friction quantitatively is essential for some of the following reasons:

(1.) Most often, resistance to fluid motion is a governing criterion in assessing the performance of the design of any fluid-mechanical device.

(2.) In both experimental and computational investigations of a fluid system, skin friction remains one of the most difficult quantities to quantitatively understand with accuracy.

(3.) In studying fluid flow turbulence, the shear stress is a central parameter in describing turbulent boundary layer characteristics through its presence in the friction velocity, given by:

$$u_\tau \equiv \sqrt{\tau_w / \rho} \tag{1-3}$$

1.2 Methods of Measuring Skin Friction

After addressing the question of *why* in relation to measuring skin friction, the next logical step is to ask *how*. Froude's work, Prandtl's theory, and the resulting work of many others have enhanced man's understanding of the physics through which this shearing stress is applied. The field of skin friction measurement has grown both in response and in need of continuing to take the next step.

Generally, skin friction measurement techniques can be divided into two broad categories: (1) direct measurement, and (2) indirect measurement. Significant variation exists in these categories (particularly the second), and techniques are often divided up in other ways, but this division suffices for the purposes here. Indeed, after a brief discussion, the indirect methods will be dropped and not mentioned again, as they are not studied further here.

Indirect methods, in general, operate on the principle of analogy; these methods measure some quantity and then get a measure of skin friction through a known relationship to that quantity [Nitsche *et al*., 1984]. Since there are many possibilities for relationships involving skin friction, there are many types of indirect methods. One obvious choice involves velocity profile measurement, using hot-wire techniques, laser-doppler-velocimetry, and similar methods. It is then possible to use an analogy like the famous *law of the wall* [Schetz, 1993] to obtain an estimate of skin friction. Similarly, Pitot devices like the Preston tube, Stanton tube, and boundary layer rake make measurements which can be correlated to skin friction through the same law [Winter, 1977]. Additionally, analogies for heat transfer and mass transfer exist with

the skin friction coefficient in their forms – a simple example of which is the Reynolds analogy [Schetz, 1993].

Readers interested in details about indirect methods are referred to authors like Haridonidis [1989], Winter [1977], and Brown and Joubert [1969]. Here, it is sufficient to recognize the nature of such methods. These methods certainly have validity and have been proven to work well in some applications. Indirect methods, however, have the common restriction that they require advance knowledge of some characteristics or relationships in the flow conditions. In other words, these methods tend to work well when the exact analogy is known. In complex flow situations, however, it becomes difficult to know the analogy. Coincidently, these very situations are often the ones where skin friction measurements are the most needed. Under these situations, tools like Reynolds analogy or the law of the wall become suspect or cease to be valid entirely, leaving a researcher with little alternative. Areas of difficulty for indirect methods in general include heavily 3D flows, unsteady flows, flows with chemical reaction or mixing, flows with shockwaves in the region of interest, uncertain laminar/turbulent transition zones, etc.

Direct methods, by contrast, operate on a very different principle. These sensors seek to measure shear stress directly by measuring the force distributed over a known area. These methods are the subject of this document, and are preferred here based on their universality and simplicity of operation. This method requires no prior knowledge of flow conditions, as (hypothetically) the shear force on the wall is the same as the shear force on the direct measuring sensor head. A two-dimensional schematic of a typical sensor of this type is shown in Fig. 1-2. In this figure, a small break is made in the wall surrounding the sensing head. This head is attached to a support structure, a cantilevered beam in this case, which feels the effects of a force applied on the head by the outer flow.

It is necessary to note at this point that there are two distinct types of direct measuring gages. What is pictured in Fig. 1-2 is called a non-nulling gage. In contrast, the second type – nulling – is similar in principle, but varies in mechanism and operation. The device in Fig. 1-2 is a cantilever-type structure that reacts to the flow force by deflecting somewhat. It is important to insure that the actual deflections are small enough that the head does not move significantly in relation to the gap, disrupting the flow field and altering the measurement. This small deflection can be measured by a displacement (proximity) system of some sort, or most commonly by the

application of high sensitivity strain gages near the base in a region of high strain. For a beam designed with sufficient stiffness to keep the shear force loading in the range of elastic, linear deflections, this static reaction is linearly scaling and highly repeatable.

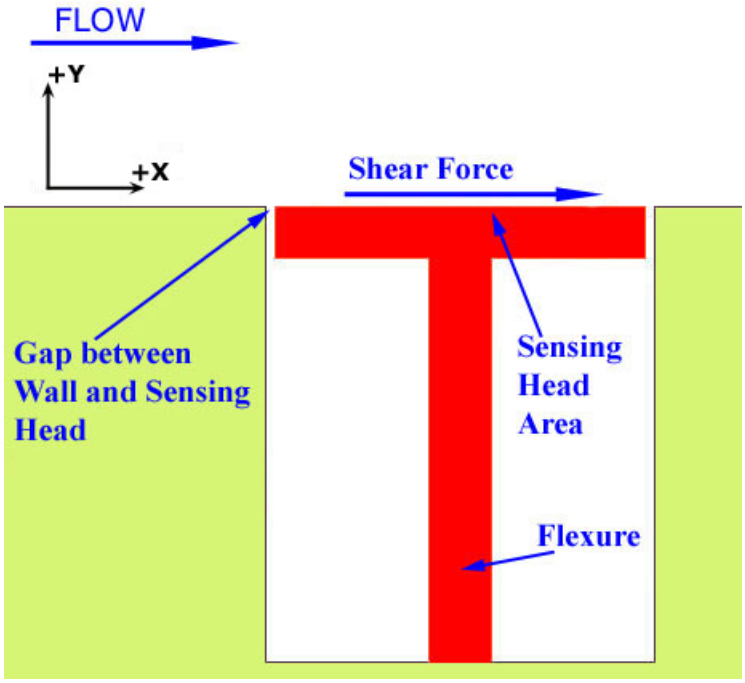

Figure 1-2. Typical Non-nulling Type Direct Measurement Skin Friction Sensor Schematic

Of course, one can utilize structural forms other than a cantilever beam. Parallel linkages are sometimes used [Haridonidis, 1989], which consists of a pair of cantilever beams on each side of the floating head, bending in parallel. More complex truss structures can be used as well to accommodate spatial or measurement constraints. Also, although Fig. 1-2 shows only a two-dimensional schematic, the more realistic beam shape can be pictured in Fig. 1-3. The floating head can be either rectangular or round (although circular is most common), as can the beam. For the beam, a circular cross-section avoids the issue of torsional warping during bending. As shown in Fig. 1-3, a circular beam usually has milled flats at the base on four sides, and a strain gage bridge is placed on opposing faces in two directions. Thus, two components of shear stress in the plane of the surface can be independently measured, and the vector direction of the shear force can be determined. This is important in flows where the direction of motion is either

unknown or changing with time. No special requirements are necessary to account for this with a gage built as shown in Fig. 1-3.

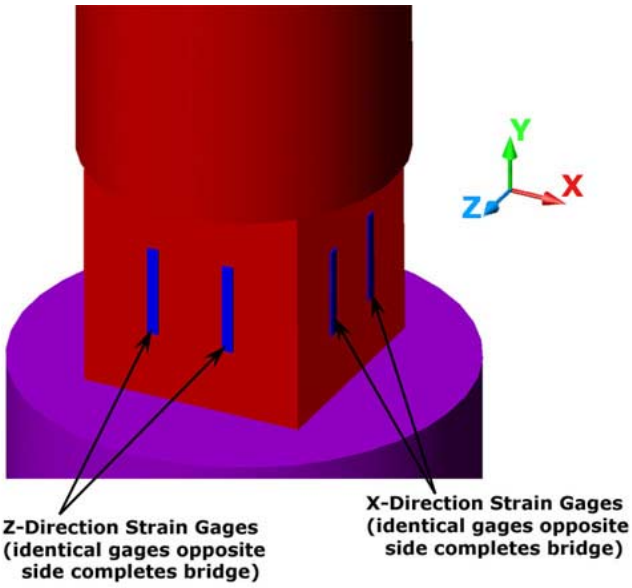

Figure 1-3. Three Dimensional View of Typical Non-nulling Skin Friction Gage Showing Strain Gage Placement

Nulling gages, by contrast, work to keep the structural member in its nominal or "null" position as a change in shear stress is encountered by providing a restoring force to the flexure. The measurement is taken with the head in the null position, which is done to avoid disturbing the flow any more than is necessary. Shear force is then read by the amount of countering force required to keep the device in its null position. Traditionally, most of these devices operate by replacing the cantilever boundary with a pivot point, the other side of which is connected to a level with a magnet or linear positioning motor. The current into the motor therefore represents the shear force on the beam. Unfortunately, these types of devices tend to be very large, heavy, and complex in order to accommodate the motors or magnets and deflection sensing instruments used. In addition, response time can be an issue as the device must detect a change in shear and then react by applying a countering force. An example of this type of device will be pictured in Chapter 2. It should be noted that most early devices were nulling gages, while more recent devices have tended to move toward the non-nulling type. Sensitive semi-conductor strain gages, better material choices, improved machining techniques, and experience have allowed the

non-nulling gages to become increasingly smaller, thus removing the fear that they will disrupt the flow. The increased complexity of nulling gages has begun to offer little reward. Alternate terminology that is sometimes used refers to nulling gages as feedback gages, while non-nulling gages are also known as displacement gages [Haridonidis, 1989]. The standard terms "nulling" and "non-nulling" are much more popular, but the choice of the alternate terminology for each type is obvious.

In general, it is possible now to create a non-nulling cantilever type gage shown in Fig. 1-2 for a particular range centered on a design shear load. The design shear load dictates many design variables like head area, beam length, and other overall dimensions. Things like material choice, temperature stabilization (cooling), vibrational characteristics, and physical handling and installation are all factors which must be considered in an application design. The interest here, however, is in analyzing induced variance from the desired measurement, and not to design for one particular application. Effort will be made in this document to keep the analysis as generic as possible. Winter [1977], Nitsche *et al*. [1984], Haridonidis [1989], and Schetz [1997] give some useful, broad overviews of the capabilities of direct skin friction design, and a variety of examples and tests done with these sensors in recent years. These papers provide many references for different interests. Interested readers seeking design information can view recent documents like Magill [1999], Sang [2001], or Smith [2001] for case studies and discussions of design choices for specific given applications.

One additional item of note involves a common technique used to enhance the performance of direct measuring gages. Often, the internal cavity of the sensor is filled with viscous liquid, like silicone oil or glycerin. Fig. 1-4 shows the use of such a substance, and a comparison with the schematic of Fig. 1-2 shows its implementation in the cavity. The presence of this oil serves a wide variety of purposes. First, with the use of strain gages, the oil provides a great deal of thermal stability to the gages. Second, it provides additional viscous damping for the beam, alleviating some vibrational distress. Third, the high viscosity of the liquid compared to most gases serves to lessen the flow rate through the cavity, providing a more continuous surface for the external flow being measured. Finally, an incompressible liquid with a high surface tension is typically used to alleviate the application of pressure differences from the main fluid flow upon the sides of the sensing head [Hirt *et al*., 1986].

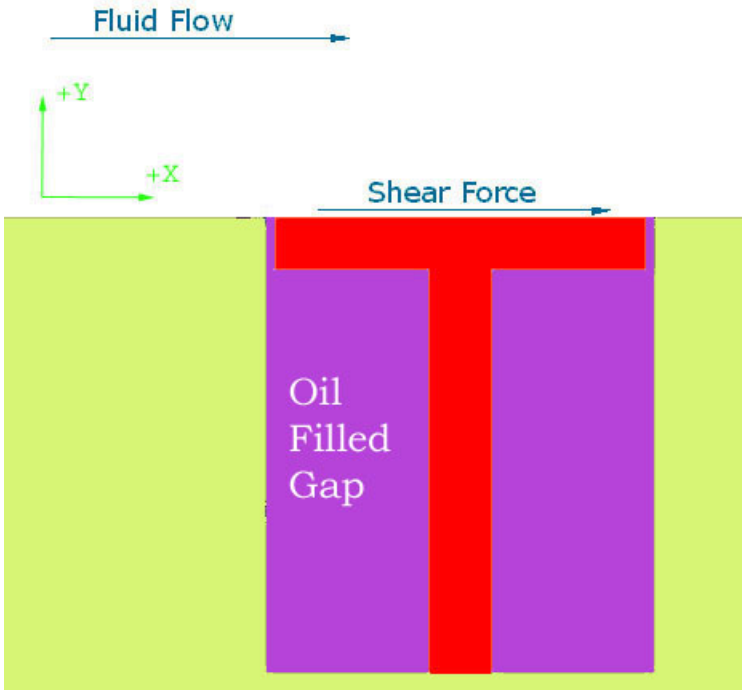

Figure 1-4. Typical Non-nulling Type Direct Sensor Schematic Showing Oil Fill Technique

This liquid, however, extracts a high price with its benefits. Both from pressure differences and from the bulk convective motion of the external fluid, the liquid is typically extracted from the cavity and pulled downstream with the flow. This means that the gage requires almost constant refilling. A vacuum usually needs to be applied to the surface during filling to insure that air does not get trapped in the cavity and compromise a measurement. This inadequacy precludes long duration tests with the oil, and the constant maintenance hinders commercialization of products of this type. Further, in a moving flight vehicle, or in any application where the gage is not upright, it is almost impossible to use the oil at all.

Basic notation must now be introduced, to provide a foundation for analysis and discussion that follows. Fig. 1-5 shows a typical skin friction gage of the type discussed here already. The dimensions listed are some of the major design parameters that have some bearing on the fluid mechanics of a gage and over which a designer has some control. Using the convention employed here, D_{HEAD} represents head diameter, G represents gap width, c represents a dimension termed lip thickness, and L_{BEAM} will be used for the total beam length (including beam and head height). Additionally, Z represents a misalignment variable, defined normal to the head surface. One other important thing to define on the subject of notation is that,

frequently in this document, variables such as these (and others) will be annotated with an asterisk, *, superscript. This asterisk denotes that that variable is non-dimensional, being equal to that variable normalized by some scale. The scaling value will be apparent in each individual discussion as the case arises.

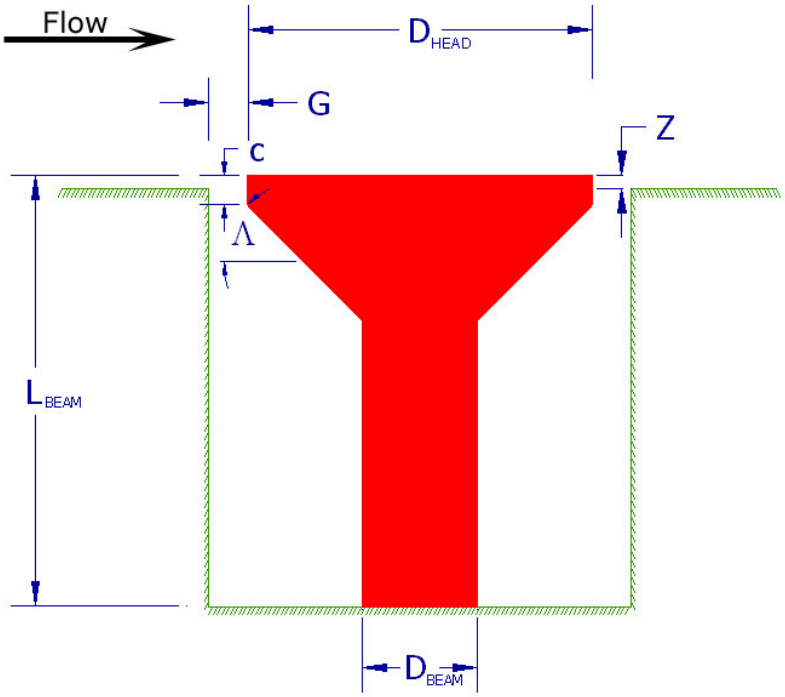

Figure 1-5. Non-nulling Direct Skin Friction Sensor Design Variable Notation

1.3 Research Focus

Despite any problems with it, the direct measurement method of skin friction has been used successfully both with and without oil fill many times. It offers a universality that is missing with any of the indirect methods, allowing a researcher to get a measure of skin friction without knowing anything about the fluid flow. The previous discussion though, stands on one particular assumption: the assumption that the shear force as shown in Fig. 1-2 is the only force on the beam. Sheltered though they are, it should be apparent to a fluid dynamicist that, in reality, the floating head and flexure structure below the surface are exposed to a surrounding pressure field and shear stress field. It certainly seems reasonable to expect that there are

circumstances in which these force fields cause significant deviations from the desired measurement of the surface shear force acting on the floating head.

The general purpose of this document, then, is to look at some of the effects associated with this deviation from the desired outcome for some generic circumstances, without specific reference to a particular gage or application. It is important to point out up front that this departure from the desired output shall be termed here as *error* in skin friction analysis. This error is distinct and different from experimental error in which the reading of a measurement is uncertain and thus allows for some value other than the true value to be recorded. This document looks at the force fields actually present on the head and support flexure, and considers these to be the true conditions for the problem in question. One should not look here for things like uncertainty in strain gage readings. This document will assume that the true reading is recorded without bias or precision uncertainties; it simply is not the reading that the researcher wants, as it is comprised of forces other than the one sought. The issues of measurement uncertainties are not a concern in this work since all work is computational in nature, and the skin friction gage errors discussed here are determined by comparison with a computationally or analytically determined target value. No experimental measurements are involved.

For this analysis, some objectives are presented, to be addressed and answered in a fashion in the following chapters:

(1.) to understand the details of the flow in and around a typical direct measuring skin friction gage and also causes and contributions to error in measurement resulting from the complex and subtle flow and stress fields involved

(2.) to develop general guidelines for minimizing inherent errors in direct measuring, non-nulling skin friction sensor design

(3.) to quantify and provide typical performance benchmark data and also develop a procedure for estimating error in an actual experiment using a skin friction gage

The first goal is one of understanding. With the small physical sizes of many of the features such as the gap size and lip thickness of the gage, it is difficult to judge the effectiveness of the gage operation for a given stress load and flow condition without first understanding what causes the gage to behave in the way that it will.

The second goal will address the issue that some configurations must certainly perform better than others in a given circumstance. It is always desirable to design with the thought of minimizing imperfection as much as possible from the outset. To facilitate this, variations of several of the major design parameters (shown in Fig. 1-5) will be presented, showing clearly what values of those parameters may be the best.

The third goal addresses the issue that no design, even from the second point, can be perfect. This document will provide estimations for some generic designs under relatively basic circumstances. Where applicable, this will provide quantitative data for estimating error in an experiment. For applications that do not match those analyzed here, it is hoped that this document will serve as a template for performing an analysis specific to those relevant circumstances. This will allow a researcher to answer these important questions for the specific case of interest if they are not sufficiently similar to what is covered here.

CHAPTER 2: Errors in Direct Skin Friction Measurement

2.1 A Description of Common Sources of Error in Direct Skin Friction Measurements

In principle, direct skin friction measurement offers the simplest and most straight forward methodology in attaining the goal of successful shear stress quantification that any technique could offer. Despite this simple approach, the direct technique is, of course, not without problems and issues regarding accuracy and usability. In a 1977 overview paper on the subject of skin friction measurement, Winter [1977] summarizes the main concerns with this method. These items are listed in Table 2-1.

The ten items listed in Table 2-1 will first be discussed briefly in order to gain an appreciation for advancements in direct skin friction measurement that have brought about changes since the writing of the information by Winter. In light of recent trends of this technique, several of these points will be highlighted here as having priority in terms of lack of understanding and, hence, their possibility of causing inaccuracies in experiment. Some of these points will be the focus of subsequent sections of this document.

Point (1) is an important design criterion in that the size of the floating element must be designed to be sufficiently large to provide measurable deflection for a given nominal shear stress load. Further, Winter's comment was actually made at a time when nulling-type sensors were the standard. In moving to a non-nulling gage, keeping the deflections small while still maintaining accuracy becomes more important, since large deflections will intrude on the flow field, thus altering the conditions of the measurement. The application of semi-conductor strain gages provides a gage factor (output for a given strain) of approximately 100 times that of conventional metal foil gages, thus allowing for the measurement of very small movements of the floating element. Many successful measurements have been made at Virginia Tech employing these semi-conductor strain gages, as outlined by Schetz [1997].

Table 2-1. Summary of Itemized Problems with Accuracy of Direct Measuring Skin Friction Method [Winter, 1977] Showing the Particular Issues Studied Here in this Dissertation		
(1)	Provision of a transducer for measuring small forces or deflections, and the compromise between the requirement to measure local properties and the necessity of having an element of sufficient size that the force on it can be measured accurately.	
(2)	The effect of the necessary gaps around the floating element.	✓
(3)	The effects of misalignment of the floating element.	✓
(4)	Forces arising from pressure gradients.	✓
(5)	The effects of gravity or of acceleration if the balance is to be used in a moving vehicle.	
(6)	Effects of temperature change.	
(7)	Effects of heat transfer.	
(8)	Use with boundary-layer injection or suction.	
(9)	Effects of leaks.	✓
(10)	Protection of the measuring system against transient normal forces during starting and stopping if the balance is to be used in a supersonic tunnel.	

Points (2), (3) and (4) are the central foci of this document. These three points are still little understood, and their investigation is paramount to assessing the error bounds of skin friction measurement. These items offer uncertainty of two forms. First, the presence of gaps, or breaks, in the wall and protrusion or recession can disrupt the flow of thin, high Reynolds number boundary layers. Second, these items all change the total amount of force on the floating head, thus altering the total reading of the strain gages. With no way to differentiate the desired force from the undesired forces, these phenomena must be well understood in order to separate their effects.

Some of the possible manifestations of these items are pictured schematically in Fig. 2-1. Point (3), misalignment, can take various forms. Fig. 2-1 (a) shows the issue of tilting such that the head is no longer oriented with the plane of the wall. With a non-nulling gage design, the

flexure actually deflects, producing a small amount of tilt during operation. This was initially thought to possibly be a central problem, but some simple calculations of the structural properties of a typical sensing flexure studied here (the data of which is given in Chapter 4) revealed that typical deflections are on the order of one one-hundredth of the gap size for this design for most common metallic material choices (e.g. aluminum, stainless steel, and copper). The associated tilt rotations at the end of the beam caused by this deflection are on the order of 0.01 degrees at maximum. These values are simply too small to make a significant effect of the gage performance, so tilt was not studied in later chapters. This simple analysis assumed the sensitivity requirements of the semi-conductor strain gages discussed already for point (1), giving a practical example of their utility in this design process.

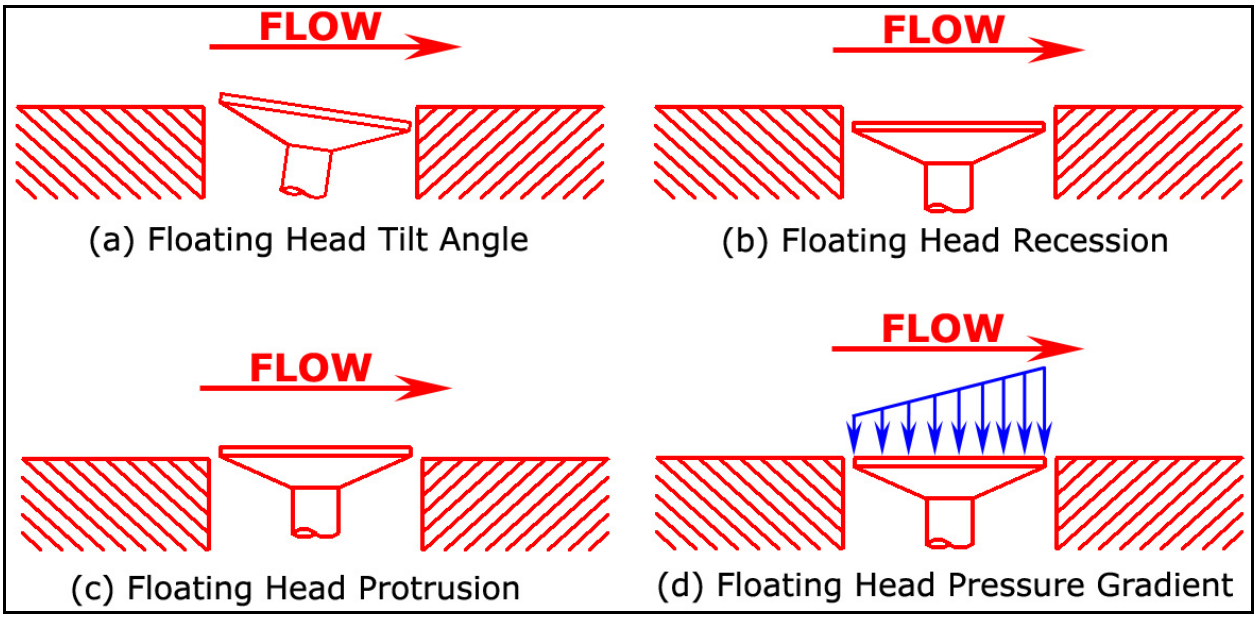

Figure 2-1. General Types of Misalignment Errors Possible with a Direct Measuring Skin Friction Gage

Tilt can also occur as a result of machining and fabrication. A beam with uneven concentricity, poorly machined edges, etc., or even poor assembly of the gage pieces can result in a flexure that is not straight in the housing. For a beam that is tilted in the null position by poor construction, these effects could be large depending on the amount of tilt. Unfortunately, only some of the most significant effects could be studied here, and tilt could not be included. The types of misalignment seen in Fig. 2-1 (b) and Fig. 2-1 (c) were assumed to occur more

often than tilting in sufficiently compromising magnitudes. This conclusion was based both on previous experimental literature and observation from practical design experience. Tilt is, however, an excellent starting point for future work to continue the study of skin friction gage effects.

As seen in Fig. 2-1 (b) and Fig. 2-1 (c), misalignment can be either protrusion out into the flow or recession back in the wall, respectively. These effects pictured have the potential to significantly change both the pressure field and the shear stress field of the sensing head. These two effects are given a high priority in this study.

Finally, Fig. 2-1 (d) pictures a pressure gradient, placing an uneven pressure force on the head and into the side gap areas. This gradient has the general effect of placing both extra forces and extra moment on the sensing head, doubling its capability for damaging the measurement. Of course, what is implied in all parts of Fig. 2-1 is that, from point (2), the simple presence of the gaps alone can cause changes in a measurement by disrupting the boundary layer development and by allowing the flow an opportunity to access the sensing head and flexure in the cavity and place extraneous forces upon the gage. These three points are central to this document, and Section 2.2 focuses on previous publications discussing these issues.

Point (5) is not an issue discussed here as it is not a result of the fluid motion it is exposed to; rather, it is a result of the solid body motion of the test conditions. Although important, this, like number (1), has been shown to be addressable via recent research techniques. In particular, Sang [2001] and Smith [2001] have demonstrated successful gages for actual flight vehicle tests at transonic and higher speeds. By innovative and careful design as well as information collection, this problem has been circumvented by these researchers.

Points (6) and (7) also represent issues in which particularly little information is available. Although they are not addressed in detail in this document, there is certainly a need to do so in the future. What relevant information exists about temperature and heat transfer effects is reviewed briefly at the end of Section 2.2.

Point (8) is probably the least understood of the ten listed, and represents the final boundary in skin friction sensor design and use. Although there is some literature involving applications of skin friction gages in the presence of injection (porous plates and similar devices used by Schetz and Nerney [1977] and some others), no literature has been discovered concerning a detailed assessment of skin friction gage performance under these conditions.

Influence of mass transfer is, however, the ideal argument for the techniques of computational fluid mechanics employed here to study some of these phenomena.

Point (9) is a particularly bothersome item which is addressed in later chapters. As discussed already in Chapter 1, skin friction gages are often filled with viscous oil, and this oil "leaks" out over time. In fact, at supersonic speeds, where surface tension and capillary forces become negligible, it can typically take only a matter of seconds to significantly decrease the oil reservoir in the cavity of the gage. This makes it necessary to constantly refill and maintain the gage. This is one reason why skin friction gages have not undergone extensive commercial development. Other limitations of the oil can be seen in Chapter 1. There is little discussion of this issue from a quantitative perspective in relevant literature. Even without oil fill, there is still a "leaking" effect from simple flow rate of the external fluid through the exposed gap.

Finally, point (10) is again an issue that needs to be addressed in a design, but one that is well understood and that can be circumvented with intelligent design. Almost all design projects at Virginia Tech are tested in the Virginia Tech Aerospace and Ocean Engineering supersonic wind tunnel. This tunnel ranges in speed from Mach 2.4 to 4, and is described in detail in Chapter 4. Many researchers in recent years have demonstrated survivability in this tunnel and in other supersonic facilities [Schetz, 1997].

From this Table 2-1, points (1) and (10) can be considered to be a non-issue with proper design thanks to advancements since the time of Winter. Points (2), (3), and (4) concerning the effects of the gap presence on the boundary layer, the changes caused by pressure gradients, and the effect of misalignment in the form of protrusion and recession are the central subjects of this document. Although not comprehensively addressed, point (9) concerning leakage through the gap is studied from the point of view of mass flow rate and flow patterns in and out of the cavity. The effect of an oil filled gap leaking out is not studied, but an oil free (air only) gage can be considered to be the worst possible condition in terms of flow rate. The other points – temperature effects, heat transfer, mass transfer, oil fill performance and leaking, and acceleration effects – are not studied here, although these issues certainly need to be addressed. Unfortunately, it is not possible to study everything, so a few of the most fundamental concerns were selected here as a starting place.

2.2 A Review of Literature Addressing Error in Direct Skin Friction Measurements

Skin friction has been studied and measured by a large number of researchers spanning more than 100 years. All of this work has employed an equally wide variety of methods in its path to fruition. Interestingly, despite a wealth of studies on measuring skin friction, there is significantly less research on looking at the *errors* of those measurements. Historical investigation reveals that, with the exception of Schultz-Grunow, who performed low speed wind tunnel tests [Dhawan, 1952], there is a period of many years during the early to mid part of the twentieth century in which little effort was made in direct skin friction measurement. There was, consequently, even less effort in skin friction error analysis for some time. Winter [1977], in providing the information given in Table 2-1, also gives a comprehensive overview of the attempts to deal with errors caused by those points discussed in the table. Some of this is recounted here, with additional information from the original sources and subsequent sources as appropriate to this discussion.

2.2.1 Gap Effects

Dhawan [1952] gives some early discussion of the effect of the presence of gaps in the wall. He provides assessment of the size of a "small" gap, under the postulation that a small enough gap around the floating head will not affect the flow noticeably. For this purpose, he tested the effects of small slots in a flat plate under laminar and turbulent boundary layers at Mach 1.4. Schlieren photographs of the flows indicated small disturbance waves for the turbulent plate near the slots. Investigation with a sensitive static-pressure probe, however, could find no indication of pressure variations. Additional experiments involved matching the Reynolds number based on slot width of the previous case in a low speed wind tunnel – where the boundary layer thickness was sufficiently thick to be easily measurable. Hot wire data was taken for a 2 mm slot at various positions normal to the wall to form a velocity profile. The data in Fig. 2-2 shows a small amount of velocity into the gap, on the order of 1% of the free-stream

speed. However, Dhawan's analysis indicated no noticeable change in velocity gradient near the surface due to the disruption.

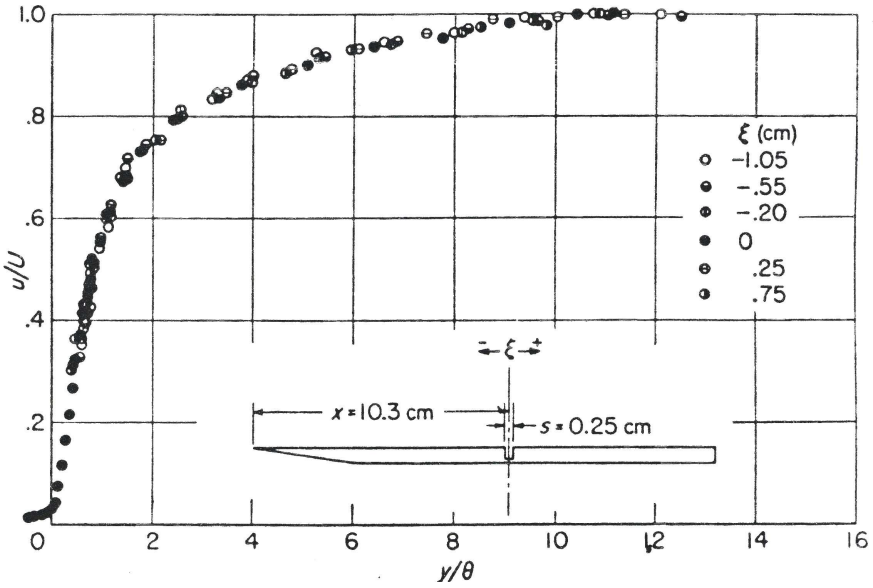

Figure 2-2. Velocity Profile on a Turbulent Flat Plate with Slot, Re_X = 40,000 and Re_S = 1000 [Dhawan, 1952]

In the same time frame, Hakkinen [1955] suggests that the problem of the presence of the gap around the sensing head be looked at as changing the effective area of the sensor. After recognizing that there is indeed some correction required for this, Hakkinen argues qualitatively that the "total effective area" is equal to the actual head surface area plus at least ½ the area of the surrounding gap. Citing a lack of concrete data, this reference uses an extra 8.25% for the value of the effective area over the actual head surface area (being equal to ¾ of the gap area).

Much later, Acharya *et al.* [1984] provided a brief discussion of these phenomena in their investigations for the development of a 20 mm head diameter floating element sensor. A variety of tests by these authors includes some attempts to acquire evidence of flow through the gaps of their gage. They tried to visualize the flow with smoke, followed by measurements with a hot wire probe at stations over the center of the head and over the gap (similar in theme to the measurements made by Dhawan decades earlier). According to them, the visualization attempt failed to show anything, thus suggesting to them that the flow rate must be of a very low magnitude. Additionally, the velocity measurements could detect no changes in the velocity

profile, leading them to believe that the flow through the gap of the gage is negligible (at least in their case).

2.2.2 Misalignment Effects

A group from the University of Texas (Austin) is particularly noted for early work on this problem of misalignment errors. Their citing of earlier data indicated that depressions (negative Z) of as much as 13 μm caused no disruption, while any protrusion produced more noticeable deviations [O'Donnell, 1964]. They found no existing coherent study of this effect and that some earlier references [Coles, 1953 and Dhawan, 1953] saw the need for extreme care in aligning the balance, while others [Smith and Walker, 1959 and Shutts *et al*., 1952] seemed to feel that less stringent requirements were needed [O'Donnell and Westkaemper, 1964]. In their work, a gage of head diameter approximately 25 mm (1 inch) was tested for a range of supersonic Mach numbers. By adjusting conditions, they took care to remove any pressure gradients in the tunnel during the test runs. In the absence of any pressure gradient (ideally) and at a flush position, there is no contribution to the reading other than the friction component. O'Donnell found in his work that any amount of misalignment in either direction produced a change in output from the flush reading. He noted that a protrusion (positive Z) tends to produce more error than an equal recession (negative Z). He also noted that any effect of Mach number is minor. He also made some significant practical observations. He claimed that, on a smooth surface, a misalignment error of 5 μm could possibly be felt, while 13 μm could be visually seen for his sensor.

Fig. 2-3 shows some results for a range of Reynolds numbers at Mach 2.67 and for a range of Mach numbers at a Reynolds number based on momentum thickness of 10,000. As O'Donnell states, there is no clear dependency on either Mach number or boundary layer Reynolds Number in any of his data. It seems more likely that a Reynolds number based on gap size or some other dimension directly related to the sensor would provide more clear information. The large range of Mach numbers tested – 1.73 through 3.62 – seems to indicate that this phenomenon is not a particularly strong function of external conditions – at least in the supersonic flow range.

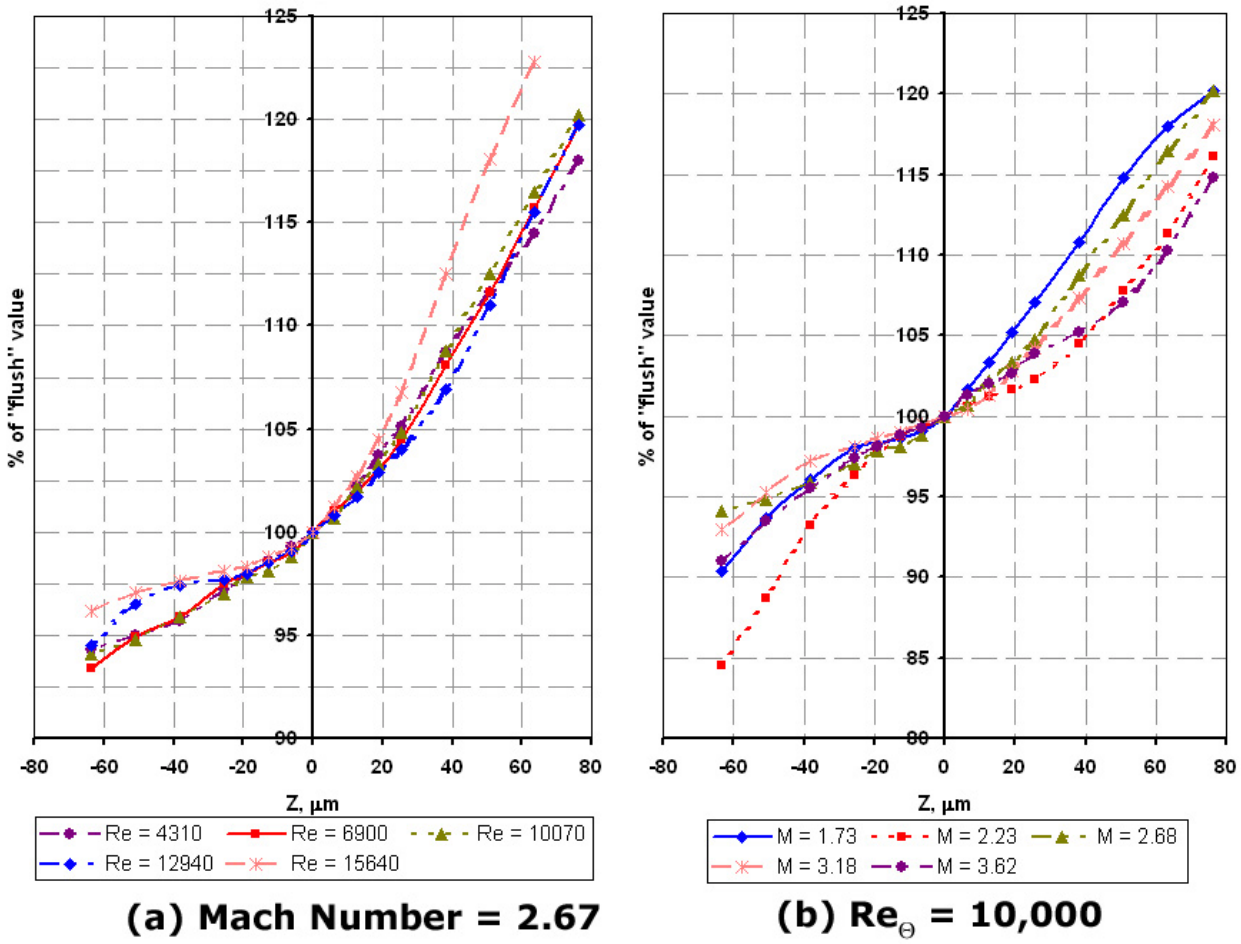

Figure 2-3. Percent Change from Nominal Value for Various Reynolds Numbers (Re_θ) and Mach Numbers as a Function of Misalignment (Z), [O'Donnell, 1964]

Probably the most comprehensive study of error effects of direct skin friction measurement can be attributed to Allen from NASA Langley in the late 1970's, who released some pivotal documents on the subject. Fig. 2-4 shows a typical floating element, with component forces on it. Allen's supposition was that the effects on a direct measuring skin friction gage head could be divided up into these components.

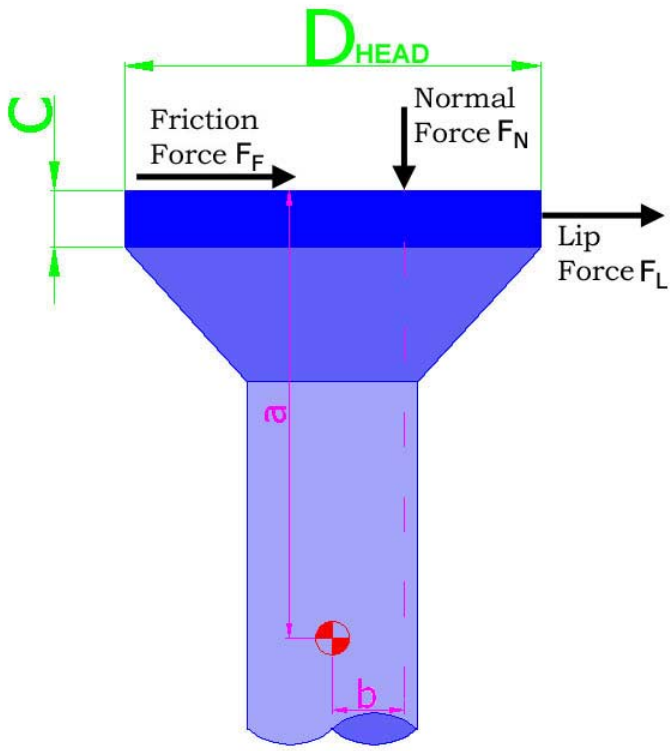

Figure 2-4. Schematic of Aerodynamic Forces Present on Floating Head, [Allen, 1976]

By summing the aerodynamic moments about the moment center, remembering the internal moment of the beam itself, the following equation can be found [Allen, 1976]:

$$M = F_F a + F_N b + F_L\left(1 - c/2\right) \tag{2-1}$$

Dividing by the dynamic pressure, q, times the length, a, times the head area, A, gives the same equation in a useful non-dimensional form with the skin friction coefficient, C_F, explicitly appearing:

$$C_M = C_F + \frac{b}{a}C_N + \left(1 - \frac{c}{2a}\right)C_L \tag{2-2}$$

At the time of Allen's writing, he was concerned primarily with nulling skin friction gages. In his original work, the beam moment, M, was referred to as a "restoring" moment, as that was the moment necessary to restore the gage to its nominal position. Also, the moment center was typically a physical pivot point to which the beam was pinned. The movement of the beam would be a rotation about this point in the nulling case. Since 1976, non-nulling gages have gained significant popularity, but eqn. (2-2) still holds for both cases. The former pinned pivot

point about which the moments were taken becomes the point about which the beam moment is read.

Allen tested extensively an apparatus designed by Fowke a few years earlier. This device was a nulling floating head sensor of 127 mm (5 inch) head diameter and rated for skin friction values from 17.5 Pa to 175 Pa [Fowke, 1969]. The total weight of this apparatus was around 630 N (140 lb_f). A picture of this device is given in Fig. 2-5 for perspective against the types of devices analyzed here. Besides the 127 mm (5 inch) head diameter, this nulling gage possessed variable heads such that the gap distance could be varied between 127 μm and 1,270 μm. The lip size was approximately 5 mm. A mechanism allowed the sensor to be purposely misaligned by values of up to plus or minus 1.27 mm.

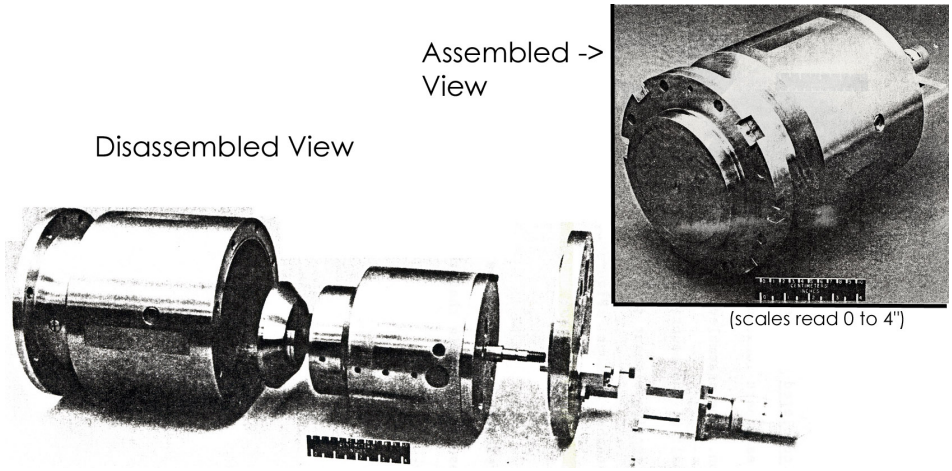

Figure 2-5. Images of Fowke's Gage [Fowke, 1969]

Allen studied the performance of the gage in Fig. 2-5 in a supersonic environment. His work covers mainly the effects of misalignment in a nominally zero pressure gradient flow situation. Figures 2-6 and 2-7 show a summary of some essential data from Allen [1976] giving his results of the contributions of the terms in eqn. (2-2) as a function of misalignment. The heaviest, solid line in each of the two figures shows the sum of the three component terms, which are graphed as well on the same scale for reference. The data in these figures was obtained by Allen via a Preston tube for the friction coefficient, and pressure taps normal to the gage head and in the wall opposite the gage lip region for the normal and lip components, respectively.

Both graphs show similar numbers and identical trends at Re_θ values of 16,200 and 38,400, further backing O'Donnell's assertion that the Reynolds Number of the external flow has only a small effect on the readings. It is easy to see, as might be expected, that both the lip component and the normal component have little effect at or near perfect alignment, while both quickly climb in magnitude to overpower the contribution from the desired source as the gage was misaligned. Both effects are due to extra forces from pressure, a phenomenon often referred to in the existing literature, albeit confusingly, as wave drag for the purposes of misalignment.

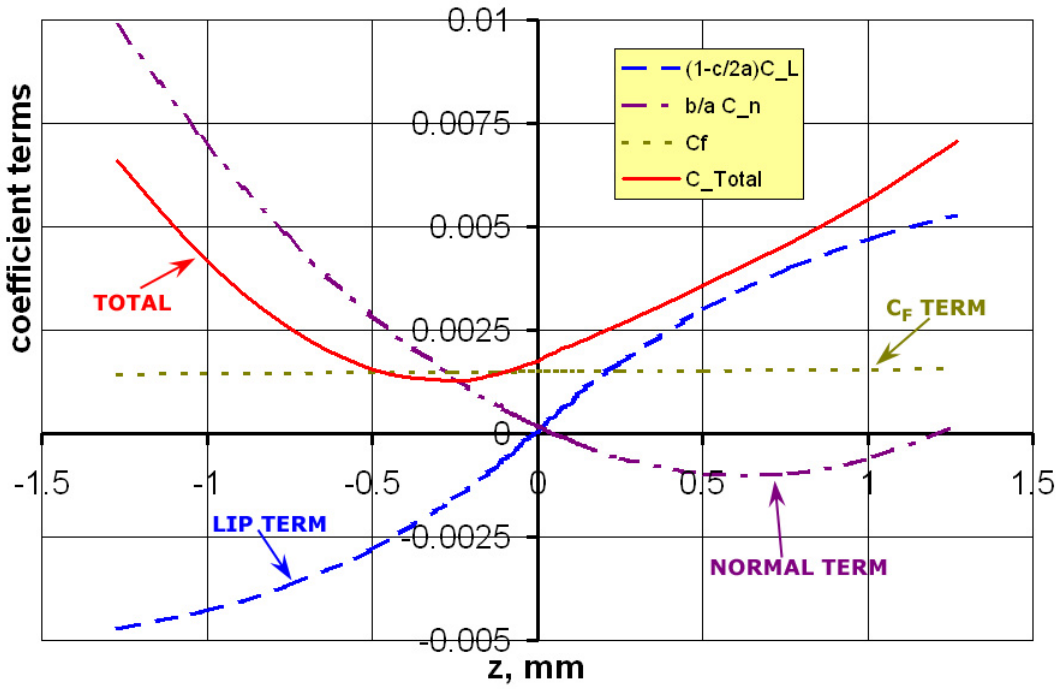

Figure 2-6. Coefficient Contributions of Eqn. (2-2) for Allen's gage at Re_θ = 16200 [Allen, 1976]

Wave drag was discussed in Chapter 1 and is defined as a compressibility effect [Bertin and Smith, 1998]. Although compressibility is certainly a factor in Allen's supersonic work, this phenomenon given here is simply a part of form drag instead. The presence of the body exposed in the flow indeed can cause excessive extra drag even in incompressible regimes. Thus, the term "wave drag" as it is used in the referenced works is a point of continuing confusion on this matter of misalignment in skin friction.

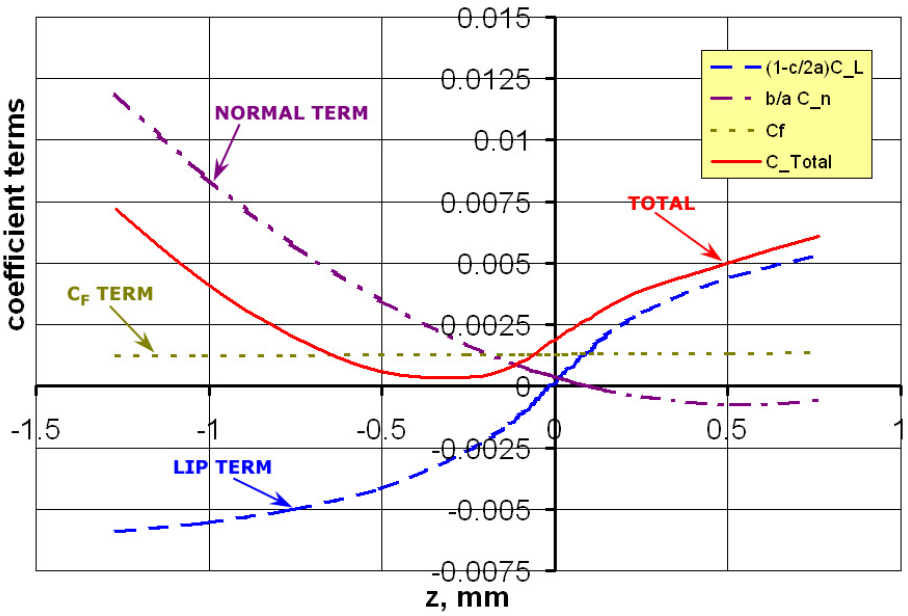

Figure 2-7. Coefficient Contributions of Eqn. (2-2) for Allen's gage at Re_θ = 38400 [Allen, 1976]

Some of Allen's overall observations about his work are of great interest.

1. His first, and most famous, postulation is that a *larger* gap makes the balance less sensitive to misalignment errors. Further, for a well-aligned (zero misalignment) head, the effect of gap size on the reading becomes negligible [Allen, 1980]. Thus, there is no advantage to a small gap at all.
2. From Figs. 2-6 and 2-7 and Allen's other data, he could find no particular preference for protrusion or recession from the perspective of measurement accuracy [Allen, 1976].
3. Reducing the size of the lip, *c*, reduced the area over which the pressure could act, thus improving measurement accuracy dramatically. It also served to reduce the effect of gap size [Allen, 1980].

It seems that eqn. (2-3) adequately captures at least some of the basic physics of the error issues. Correct functionality of the coefficients of that equation should adequately capture these effects. Allen's research shows that this functionality can work by his comparison of his force summation estimates (Figs. 2-6 and 2-7) to those read from the actual gage in some of his tests. Although not shown here, it is sufficient to note that those values match reasonably well for most of his cases. Interested readers are referred to his work for actual graphs [Allen, 1976].

2.2.3 Pressure Gradient Effects

Discussion of the effects of pressure gradients on direct measurement of skin friction opens with a relatively recent reference by Seto and Hornung [1991]. These authors explored the possibility of measuring shear stress by calculating the distortion rate of a thin film of oil on the surface. As this technique is not the central focus of this work, the specifics of their method will not be discussed. Interested readers should seek their paper directly for more information. What is relevant here is that they compared their technique to a floating element gage for reference in favorable, zero, and adverse pressure gradient situations. One of their postulations about their method is that, under the correct conditions, it becomes indifferent to the effects of pressure gradient. A look at their results in Fig. 2-8 illustrates the core of the problem with the direct method, as it is easy to see how the pressure gradient affects the direct method severely. The oil film methods of Seto and Hornung are not discussed or analyzed here, but if one were to assume for the moment that their hypothesis of pressure gradient independence for their methods is correct, the direct method sees a change by +/- 70% of the nominal value from the pressure gradient.

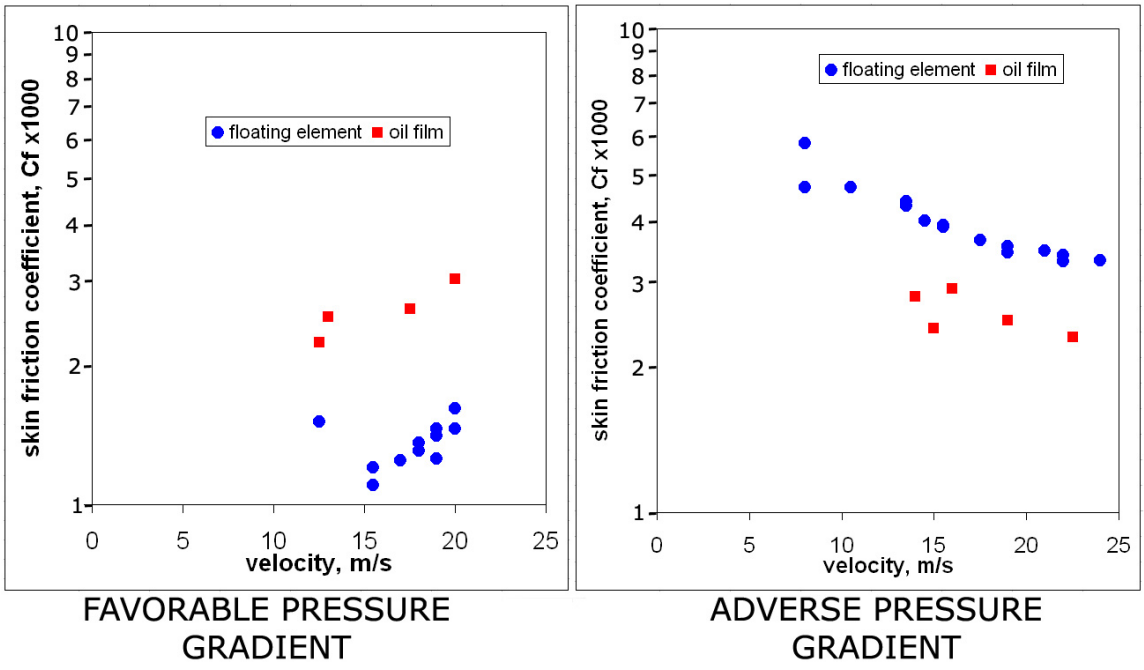

Figure 2-8. Plots of Skin Friction Coefficient of Technique of Seto and Hornung vs. Direct Method for Favorable and Adverse Pressure Gradient Conditions [Seto and Hornung, 1991]

An important note needs to be made here concerning terminology. Discussion here refers to this effect in terms of the pressure gradient or pressure variation, and is a consequence of different pressures being present on the upstream side of the gage than the downstream side. This pressure imbalance becomes a force imbalance on the output measuring system. Classically, however, many references, including Brown and Joubert [1969] and Acharya *et al*. [1984], refer to this phenomenon as *buoyancy force*. These terms are one and the same in the world of skin friction measurement, and it was deemed important to address this issue here to avoid confusion.

It was apparent from early results that this effect of pressure variations around the floating element can be quite severe. For instance, Eimer [1953] measured skin friction via a direct method to be 6% to 11% higher than theoretical predictions. One of the major reasons cited for this discrepancy was that the measurements occurred under a severe pressure gradient. One of the first systematic investigations of this pressure phenomenon again comes from the University of Texas [Everett, 1958]. Everett suggested from an earlier source [Coles, 1953] that the pressure variation could be described by a linear variation from the free-stream down the sides of the floating head to the gage cavity pressure. He postulated the following corrections to shear stress for a rectangular (not cylindrical) gage,

$$F_P = -\tfrac{1}{2} Ac \frac{dP}{dx} \tag{2-3}$$

$$f_T = \tau_0 (1 + \frac{c}{h}) \tag{2-4}$$

where eqn. (2-3) estimates the total pressure drag by integrating the assumed linear pressure variation over the lip surface, and eqn. (2-4) gives a correction to the shear stress due to this extra term in (2-3). A similar form can easily be derived for the cylindrical gage body that has been commonly used in more recent experiments. The symbol A is the exposed head surface area of the gage. The variable τ_0 represents the true shear value, and f_T represents the measured value. He tested this hypothesis in a channel of variable height, h. He found from these experiments that the term in eqn. (2-3) did not adequately capture the effects of the pressure gradient error, though he noted that the correction performed the best for small gap size, G, and greater lip height, c. This analysis indicates that there is indeed something much more complex occurring than a simple linear correction.

A somewhat more complex model of the buoyancy effect, or pressure variation effect, comes from Brown and Joubert [1969]. These authors utilize the same formulation from eqn. (2-3) above for the force, but do not restrict themselves to a constant of ½. Further, they allow for momentum exchange between the external flow and the flow through the cavity. Their form is given in eqn. (2-5):

$$\frac{F}{\tau_W A} = 1 - K_1 c \frac{dP/dx}{\rho u_\tau^2} + K_2 \frac{G\left(dP/dx\right)^{1/2}}{A^{1/4} u_\tau \rho^{1/2}} \tag{2-5}$$

What is important to note from eqn. (2-5) is the explicit presence of the friction velocity u_τ. This value, of course, contains the shear stress, and it is an important parameter for turbulent boundary layers. Once again, note that the second term on the right hand side is identical in form to eqn. (2-3), except that the arbitrary constant, K_1, can be taken to reflect situations other than the simple linearly varying pressure through the gap. The last term again serves to quantify a momentum exchange contribution between the external flow and that in the gap, as it contains a proportionality to flow rate through the gap.

It is also interesting to note the basic similarity of eqns. (2-3) and (2-5) in appearance to the form of Allen in eqn. (2-2), noting that a more robust estimate of the effects of pressure gradients can be wrapped up in the coefficients. It seems apparent that Everett [1958], Brown and Joubert [1969], and Allen [1976] have developed functionally similar corrections to shear stress readings, and that transformations are possible to move between one formulation and another.

Brown and Joubert also note the importance of "minor" effects, which include the presence of the gaps and the effective area of the head due to shear stress transmission that has already been mentioned [Hakkinen, 1955]. What is interesting about these effects is their assumption of the form that the effects take, being a function of parameters like a friction Reynolds number, given as:

$$\mathrm{Re}_{fr} = \frac{A^{1/2} u_\tau}{\nu} \tag{2-6}$$

Looking through all of this literature, it is easy to see that a variety of different Reynolds number scales are used by different authors. One of the main conclusions drawn by many people is that there seems to be little dependence of the shear stress errors on flow Reynolds numbers (such as Re_δ and Re_θ). It certainly seems -- to this writer at least -- that a scale like that given in eqn. (2-

6) makes much more physical sense than one based on free-stream flow conditions or boundary layer parameters. Brown and Joubert found errors caused by the pressure gradient of up to 15%, which seems consistent in magnitude with what has been seen so far.

One additional recent reference deserves some consideration as well. In parallel to their attempts to see effects of the gaps, Acharya, *et al.* [1984] proposed an equation very similar to the forms seen in eqns. (2-2), (2-3) and (2-5). They too tried to capture the effect of the buoyancy contribution in the gap by assuming a linear pressure variation form identical to Brown and Joubert (see eqn. 2-5). Likewise, they allowed for the constant to be other than ½, and further did experiments to try to find this constant for different situations. Interested readers can consult their paper, and study their equation (1) [Acharya, *et al.*, 1984]. They found, at least for their particular sensor design, that the pressure gradient was approximately linear in the gap. The particular sensor that they gave data on had a lip thickness to gap size ratio (c/G) of 27, which was much higher than those studied by Everett – showing consistency with his main conclusion. These researchers found, as well, that their experiments revealed different values of the constant for positive and negative pressure gradients. They give a value of 1/2 for favorable pressure gradient, and 1/5 for adverse pressure gradients for their particular sensor (remember again their large lip thickness).

Thus, from these studies by these researchers, it is apparent that pressure causes important effects on a direct measuring skin friction gage. The effects of a pressure gradient can be seen by Fig. 2-4, showing that a pressure gradient can affect the read measurement, C_M, both through application of a lip force, C_L, and by creating an asymmetric normal force by shifting the moment arm location, b.

2.2.4 Oil Fill Effects

One of the only attempts to treat the issue of filling the cavity with the oil is given by Frei and Thomann [1980], who provide an analytical model of surface tension of a viscous liquid in the gap of a sensor. Their equations are strongly based on geometry, which is shown in Fig. 2-9. They found from this analysis that the largest pressure difference that could be statically supported is given in eqn. (2-7). In eqn. (2-7), σ is the liquid surface tension coefficient, and all other parameters are given in Fig. 2-9.

$$(p_1 - p_{F1})_{MAX} = \frac{2\,\sigma\, b_1}{b_1^2 + s_1^2} \tag{2-7}$$

Their corresponding equation for the net force, *K*, induced by the surface tension effect is reproduced in eqn. (2-8).

$$\frac{K}{\sigma L} = \frac{b_2}{c_2}\left(1 - \left(\frac{p_2 - p_{F2}}{2\sigma} c_2\right)^2\right)^{1/2} - \frac{b_1}{c_1}\left(1 - \left(\frac{p_1 - p_{F1}}{2\sigma} c_1\right)^2\right)^{1/2} + \frac{s_2(p_2 - p_{F2}) + s_1(p_1 - p_{F1})}{2\sigma} \tag{2-8}$$

The important thing that eqn. (2-8) shows is that (for no misalignment), the force, *K*, becomes small as gap size becomes small (b_1 and b_2). Frei and Thomann determined that the maximum supported pressure difference, given in eqn. (2-7), was more than sufficient for their needs, and made attempts to minimize the extra force seen from eqn. (2-8). This analysis is an interesting one in looking at the effect of the oil, but it does not seem to capture all that happens in a skin friction experiment. Experience has shown that even a nominally zero pressure gradient flow causes all the oil to be pulled from the cavity if the external fluid is moving fast enough. For supersonic tests, this process happens quite rapidly. The surface tension effects in Fig. 2-9 are purely static and do not account for the effect of bulk fluid convection. Convection becomes dominant in higher speed flows. The interplay between surface tension and convective transport is beyond the effects studied here.

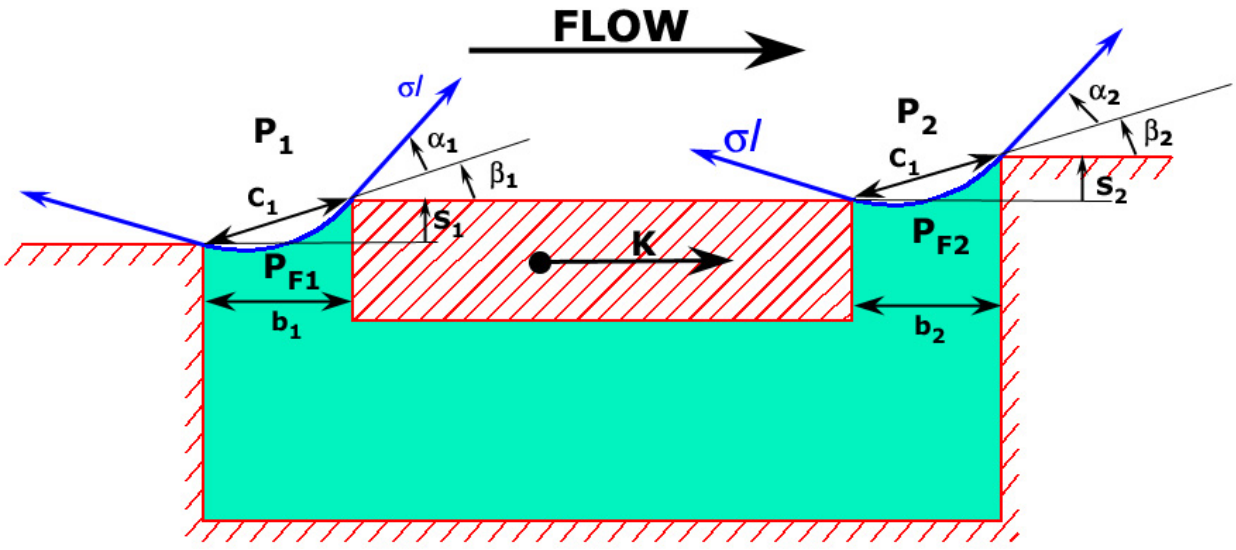

Figure 2-9. Geometry Considerations for Surface Tension Effect [Frei and Thomann, 1980]

2.2.5 Other Effects

Additional issues that are not addressed in this document, but which certainly contribute to understanding of error effects in direct skin friction measurement, are the concerns of temperature mismatches between the floating head and the surrounding wall surface, heat transfer, and mass transfer at the gage locations. As mentioned earlier, there is even less information on these topics than there is on the issues of pressure gradients and misalignments. The group at the University of Texas (Austin) once again appears in the literature. One of them developed an experiment in which a plate was kept at a constant temperature by means of water cooling and a copper bodied-gage was allowed to heat up by aerodynamic heating during the flow runs at Mach 5.0 [Westkaemper, 1963]. The copper gage was used with the intention that there would be little chance of thermal gradients existing within the sensor itself. The outcome of this experiment was that no clear correlation could be shown between temperature mismatch and variation in the shear stress reading. If any correlation existed for his test conditions, Westkaemper concluded that it could account for no more than a 2% deviation in measurement [Westkaemper, 1963].

A later and more in depth analysis by Voisinet [1978], reveals a more pronounced effect of temperature mismatch. His analysis at Mach numbers of 2.9 and 4.9 consisted of long duration data of up to 90 minutes. Several different Reynolds numbers were tested resulting in the following curve fit by Voisinet for his data:

$$\frac{\tau_{FE} - \tau_0}{T_{FE} - T_W} = 0.0310988 Log_{10}(\mathrm{Re}/m) + 0.1795555 \tag{2-9}$$

The shear stress values are measured in Pascals, the temperatures in degrees Kelvin, and Re/m represents the local Reynolds number per meter. The "FE" subscript indicates the values of the measured floating element, and τ_0 is the extrapolated value of shear stress for no temperature mismatch. Voisinet goes one important step further by referencing the earlier work of Westkaemper [1963], and uses the above formula (2-9) to calculate the shear stress variation for Westkaemper's maximum temperature mismatch of 34 ^{o}K. This value comes out to be 1.96%, which matches well with Westkaemper's estimate of 2%.

Paik and Schetz [1995] found much higher estimates of temperature effects on skin friction. Their work was in an unheated supersonic facility at Mach 2.4 at a nominal 300^{o}K total

temperature. Their work consisted of a heated element within the skin friction sensor, increasing the head temperature by as much as 18.7^{o}K over the nominal wall temperature. This temperature difference produced a 24% increase in skin friction values as a result.

Finally, the subject of skin friction measurement with injection or suction has seen very limited review. Dershin and Gallaher [1967] provide one of the first dedicated studies that could be found on the subject. They discuss measurements of skin friction with injection or suction dating back as early as 1954. Their particular experiment consisted of a porous flat plate at supersonic Mach number in which the skin friction gage itself was made porous and placed in the wall. Their experiments correlate well with their analytical predictions of the skin friction coefficient. However, there is no discussion of any particular errors associated with the measurement, related or unrelated to the presence of injection or suction.

A few more recent studies of skin friction measurements involving wall injection can be found in Schetz and Nerney [1977], Schetz and Kong [1981], and Kong and Schetz [1982]. All three of these papers made measurements on a cylindrical body for varying surface roughness and porosity values. Although these works included measurements of a direct measuring skin friction gage, there is no mention of error analysis present in these works. Although these papers may provide a starting place for future work on gage error estimation, it is clear that this scenario bestows a difficult problem in separating the effects occurring simultaneously.

2.3 Motivations and Approach to Present Study of Errors in Direct Skin Friction Measurement

In looking at the wealth of research reviewed in the previous section, two things become obvious. First, all of the studies addressing the issues of error management in direct measuring skin friction gages are purely experimental. Second, the majority (although not all) of the research utilized nulling-type gages.

The current work provides the first known analysis of these phenomena using a different technique – computational fluid dynamics (CFD). CFD offers capabilities unique from experiments. In a CFD model, certain effects can be isolated and studied, as a model is defined *a priori*. Conditions and geometries are defined, and as such, are exact within the computational

framework. This is in contrast with an experiment, where experimental apparatus contains inherent uncertainty in things like geometry, positions, distances, etc.

One common result of many researchers is that the tiny gaps and cavities of the gage, as well as the thin boundary layer profiles, are far too small to effectively make measurements over. Indeed, several independent researchers already mentioned tried to measure flow rate through the cavity of the sensor and failed to achieve noticeable results. CFD removes these scaling and sensitivity issues and provides a different perspective on the problem. Among other things, this document will use this capability to provide the first look at the flow vectors through a typical sensor. Although so small as to be impossible to measure, it is known that these flows exist; providing the first look at the flow through a sensor will provide valuable understanding to the induced errors of skin friction measurement.

Secondly, recent trends have shown that nulling is typically not necessary since semi-conductor strain gages and fiber optic displacement sensors can detect very tiny deflections far below the threshold of affecting the flow conditions. Although much of the research should be applicable to both nulling and non-nulling types, many of the gages tested have been rather large and heavy (as demonstrated in Fig. 2-5) because of the necessary internal motors and electronics used to null the gage head. It is desired to provide some data that is more directly applicable to the small, non-nulling gages built today.

The approach taken here does not seek to refute experimental work done so far, but to complement and complete it in new ways. In fact, the previous section of this document has been included for more than historical perspective. As CFD results are developed here, they will be compared to some of the experimental graphs and formulas already discussed in Section 2.2 in order to provide some “real world” perspective to the computational analyses. CFD can look at things that experiment never could, and experiment can verify the applicability of computational solutions. Each of these techniques brings with it some uncertainties in the final measured product. These uncertainties are different, however, and they can provide perspective for the other.

CHAPTER 3: Aspects of Computational Fluid Dynamics

3.1. Formulation of Numerical Methods

As the central analysis technique utilized, computational fluid dynamics (CFD) is an integral part of the research performed in this document. The purpose here is not to make a detailed study of the techniques of CFD directly or to develop or study new algorithms. However, it is essential to have a good understanding of the fundamental concepts and issues involved in solving a computational problem.

Any computational mechanics code solves a particular partial differential equation (or set of equations). In fluid mechanics, there are a variety of mathematical governing equation sets for various conditions. These include formulations like (1) Navier-Stokes, (2) thin layer Navier-Stokes, (3) parabolized Navier-Stokes, or (4) Euler equations [Walters, 2000]. Each of these formulations can contain equations for mass conservation, momentum conservation, energy conservation, chemical reactions, and other effects depending on circumstances. Technically, the term Navier-Stokes refers specifically to the instantaneous momentum equations only (there are 3, for 3 coordinate directions in space), but this term is often used to refer to the whole composite set of time-averaged equations, as the momentum equations require support from continuity and other equations in order to obtain a solution. Such a meaning is used here.

Ascertaining the validity of a differential, mathematical model is a complex issue in itself. The issue is one of cost, and the answer depends on the nature of the problem, and what the desired output is. For instance, the Euler equations typically offer a huge calculation savings versus the Navier-Stokes equations. For many problems, the Euler equations are sufficient, depending on what the desired results are. For a generic aerodynamic shape in a high Reynolds number flow, the Euler equations tend to do a reasonable job calculating aerodynamic lift, but

not drag. But, of course, this depends on the exact problem, accuracy requirements, and a variety of other concerns. For the purpose here, the full Navier-Stokes formulation is used to solve problem, and thus, will be the only one considered further. This model is typically considered to be the "standard" in fluid mechanics, containing only a few very basic assumptions about fluid motion. The details of the development of the Navier-Stokes equations and its related forms can be found in a variety of references, including Bertin and Smith [1998], Schetz [1993], and Tannehill, Anderson, and Pletcher [1997]. The major assumption of the Navier-Stokes formulation is that the fluid must be a Newtonian one; a Newtonian fluid is one in which the shear stress for a fluid element varies linearly with the rate of strain. This proportionality constant is, of course, the dynamic viscosity, which can vary with temperature and other conditions, but which is a constant at any fixed state for a Newtonian fluid. The standard Navier-Stokes formulation seems to be clearly valid for all problems solved here. All problems treated here are incompressible with common Newtonian fluids.

With a selected mathematical model, the numerical discretization scheme can then be applied, giving birth to a computational algorithm. There are three common broad categories of schemes of computational codes – finite element, finite volume, and finite difference. All schemes have the same basic goal – turn the continuous partial differential mathematical problem into a set of algebraic equations that can be solved by a computer. This is done by cutting the continuous domain of the problem up into manageable pieces and making a limited number of assumptions to turn a differential equation into an algebraic one which is valid for that piece [Tannehill, Anderson, and Pletcher, 1997].

The differences in these schemes come through the way in which this goal is realized. There are many differences in the details of these methods, in the assumptions of the forms of the governing equations in the "cells," in the connectivity between adjacent cells, and other things. As a general rule, however, finite differencing tends to be concerned with the values at distinct points, or nodes. Connectivity is built by developing relationships from point to point. The finite element method by contrast is more concerned with a discrete volume, or element, over which the solution is obtained. This formulation is built by assuming a particular profile over this element, then solving for the values of this profile. Finite volume discretization combines features of both of these methods, and it builds a formulation where both the points and the space between the points are important in solving the problem. An excellent source of information on

finite volume and difference methods is Tannehill, Anderson, and Pletcher [1997], while excellent sources of information on the finite element method are Reddy [1994] or Bathe [2000]. These discretization methods are simply mathematical tools for solving a difficult equation and have nothing to do with the physics or the problem to solve, so any relationship with the physical domain is simply one of convenience. All three formulations have been demonstrated successfully many times in solving the Navier-Stokes and similar equations. Here, the finite element method is used exclusively, selected as part of a commercial code called FLOTRAN by Ansys, Inc.

The finite element method operates by making use of a weak form or Galerkin-type procedure. Interested persons are again referred to the references by Reddy or Bathe for details on the finite element method. The first step is to decide on a differential equation model, as discussed above. This differential operator will be of the form in eqn. (3-1), with the variable *u* as the dependent variable.

$$\mathscr{L}(\mathrm{u}) = \mathrm{f} \tag{3-1}$$

This equation can be of arbitrary order, contain any number of independent variables, and even non-linearities, at this conceptual stage. Obviously, an exact solution (sometimes there can be more than one) for *u* satisfies this equation. An inexact solution does not. However, the finite element method implementation allows for a minimized approximate solution, $\tilde{u}$, such that the equation can be satisfied in a *weighted* sense. This is called the weighted-integral form, and the Galerkin method gives the form of eqn. (3-1) as:

$$0 = \int_{\Omega} \mathrm{w}\left[\mathscr{L}(\tilde{\mathrm{u}}) - \mathrm{f}\right] \mathrm{d}\Omega \tag{3-2}$$

In eqn. (3-2), the function *w* is called a *weighting* function, and many integrable functions can be used, although there are some standard choices. Now, an approximation to *u* can be made such that *u* is of the form:

$$\tilde{\mathrm{u}} = \sum_{i=1}^{N} \mathrm{u}_i \psi_i \tag{3-3}$$

The approximate solution is the summation of values at known points, or nodes, given by the u_i's, coupled with the ψ_i functions. These are called shape functions, for they determine the shape of the solution over the element surface.

One of the advantages of the finite element method is that it allows eqn. (3-2) to be reduced to a more advantageous form. As written, using eqn. (3-3) in eqn. (3-2) requires that the approximation for u is differentiable at least as many times as the order of the differential equation. So, for a second order equation, like those found in the Navier-Stokes formulation, $\tilde{u}$ must be at least parabolic (if it is a polynomial) or twice differentiable (in general) to correctly satisfy all the terms of the equation. However, the technique of integration by parts allows the differentiation to be equally distributed between the differential operator $\mathcal{L}(\tilde{u})$ and the weighting function w. This means that one can use shape functions of a lower order to approximate u. This is called the weak form, since u no longer has to satisfy such stringent requirements in the function. The weak form of eqn. (3-2) is given in eqn. (3-4).

$$\int_{\Omega} \nabla w \bullet \nabla G(\tilde{u})\, d\Omega - \oint_{\Gamma} (\hat{n} \bullet \nabla G) w\, dS = -\int_{\Omega} wf\, d\Omega \tag{3-4}$$

In this case, $G(\tilde{u})$is simply a more specific form of the general operator $\mathcal{L}(\tilde{u})$. For the weak form development, $\mathcal{L}(\tilde{u})$ must be at least twice differentiable to distribute one differentiation onto the weighting function (it can be more than twice differentiable if appropriate). The notation switch is a convenience to allow $\mathcal{L}(\tilde{u})$ to be expressed equivalently as $\nabla^2 G(\tilde{u})$.

There is, however, an important thing to note about eqn. (3-4), as integration by parts causes the highest order boundary conditions to appear explicitly in the equation. These boundaries are called *natural* boundary conditions, and now become part of the weak form directly. This has the additional advantage that the natural boundary conditions are satisfied approximately through the weak form solution, and the choice of $\tilde{u}$ need not satisfy these equations. Boundaries below one-half the equation order are *essential* boundary conditions, and are still handled by the approximate u function of eqn. (3-3). Thus, the choice for the shape functions has less strict requirements on the selection than in the original weighted-integral form. Reduction to the weak form of the equation causes the additional requirements that the natural boundary conditions are implicitly prescribed to be zero on a boundary where essential boundary conditions are not specified [Shames and Dym, 1985].

With the approximate $\tilde{u}$, and an assumed set of weighting functions (the shape functions themselves are used in the Galerkin method), the weak form of the integral can be solved to form a system of equations, for the only remaining unknown values become the u_i's, which have no

spatial dependence. The finite element method works by assembling this algebraic system of equations from the integrated results and accounting for interconnected elements. A linear or non-linear system of equations can be solved by any number of matrix algebra solver routines on a computer.

For problems in this document, a pre-developed and pre-tested commercial code was selected that solves the full Navier-Stokes equations using the finite element method. Ansys/FLOTRAN is part of much larger package capable of solving fluid, static structural, dynamic structural, buckling, heat transfer, electromagnetic, acoustic, and a variety of other types of problems. Contact information for Ansys, Inc. can be found in Appendix A.

Ansys/FLOTRAN seemed the logical choice for the problems studied here for many reasons. It was selected partially because it is part of such a large suite of products. For an application like the design of skin friction gages, such a product is ideal. Designing and building a floating head flexure requires structural, vibrational, CFD, and other analyses to be successful. Much of this analysis is beyond the scope of this study, but the flexibility and power of such capabilities is an asset in remaining competitive in such a field as direct skin friction measurement.

Although Ansys/FLOTRAN does not have some of the advanced capabilities of some other CFD codes, it is well-suited to solve the problems studied in this work. As will be shown, Ansys/FLOTRAN is built with incompressible problems in mind. As well, it offers some common choices for turbulence models and allows for structured, unstructured, or hybrid gridding – useful for complex geometries.

As shown in Fig. 3-1, Ansys/FLOTRAN provides both 2D and 3D fluid elements, both with linear shape functions; these elements have 4 and 8 nodes respectively. The *ANSYS Theory Reference* [Kohnke, 2001] gives details related to the Ansys/FLOTRAN code. Ansys/FLOTRAN manipulates each of the equations in the Navier-Stokes governing system to solve for a particular variable associated with it. These variables are the u_i variables in eqn. (3-3), and are called *degrees of freedom* for the finite element solution; the nodal degree of freedom list for these elements and the associated Navier-Stokes equation for each is given in Table 3-1.

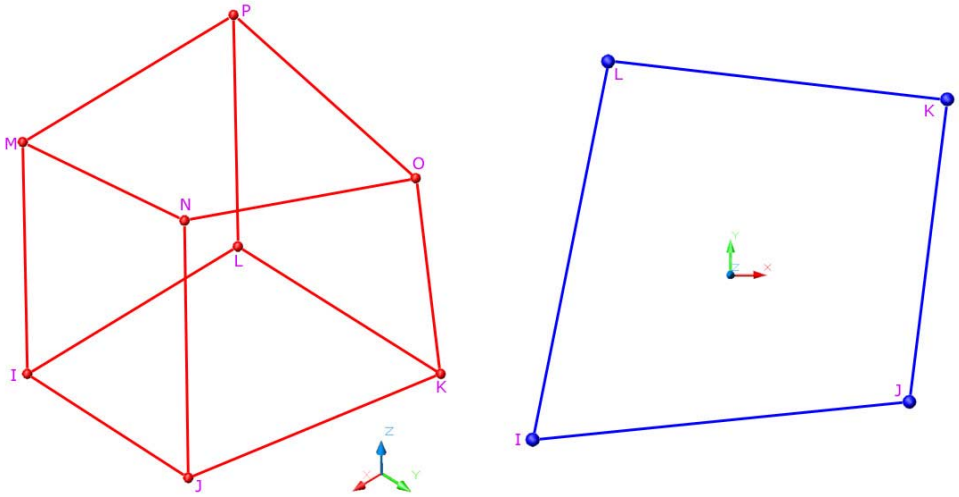

Figure 3-1. Nodal Patterns of CFD Elements Featured in Ansys/FLOTRAN

Table 3-1. List of Nodal Degrees of Freedom for Ansys/FLOTRAN

symbol	DOF	equation associated
u	x-velocity	X-momentum
v	y-velocity	Y-momentum
w	z-velocity	Z-momentum
P	pressure	continuity
T	temperature	energy
κ	turbulent kinetic energy	turbulent kinetic energy
ε	turbulent dissipation	turbulent dissipation
c_1 - c_6	species concentration	species transport

One of the major issues in a set of transport equations like the Navier-Stokes equations is the ratio of convection to diffusion in the equation, also called the Peclet number. According to Tannehill, Anderson, and Pletcher [1997], this can also be referred to as the mesh Reynolds number and it plays an important role in the characteristics of the equation. Since the convection terms contain the non-linearities, careful consideration must be made of the way in which these terms are discretized (Peclet number tends to play an important role in this). The convective

terms have a considerable effect on the stability and convergence properties of the numerical scheme.

FLOTRAN offers two schemes for integrating the weak form of the Navier-Stokes equations, both of which offer variations on the simplified, general version of the integral given in eqn. (3-2). The first, the monotone streamline upwind scheme (MSU), is described by Rice and Schnipke [1985]. In a few words, this method basically takes the two-dimensional or three-dimensional convective terms and integrates them in a single path along a streamline passing through a particular element. The process of Rice and Schnipke first calculates the downwind node of an element, and interpolates the upwind place where that streamline enters the element. Integration proceeds in an upwind manner, and the MSU method is known to be monotonically converging and to provide first order spatial accuracy [Kohnke, 2001].

The second scheme is the streamline upwind/Petrov-Galerkin (SUPG) method discussed by Brooks and Hughes [1982]. This method is somewhat more complex than MSU. From their discussion, the motivation for Brooks and Hughes was that the Galerkin method by default produces central-type differencing. This differencing tends to produce spurious oscillations in the solution. To combat this, upwind differencing can be employed as in the MSU method. Brooks and Hughes discuss that the upwind differencing schemes can be interpreted as a summation of a central difference plus an artificial diffusion term, which lowers the accuracy of the method and artificially corrupts the problem. The SUPG method basically uses the upwind approach in series with an additional term of negative diffusion in the stream-wise direction to balance that which is artificially added by the upwinding. This extra term is introduced by modifying the weight function w to reflect the reduced stream-wise diffusion. As the mesh is refined, the extra term goes to zero, and the method becomes second order spatially accurate. The SUPG formulation, however, tends to produce oscillatory spatial convergence behavior [Kohnke, 2001]. This is consistent with Godunov[1959] who discussed the fact that any convective scheme greater than 1^{ST} order cannot, in general, guarantee monotonic convergence. Note that this statement means something entirely different than the spurious nodal oscillations, discussed above, that the SUPG method seeks to remove – this is a stability issue, not a spatial convergence issue. Kohnke's reference is to the behavior of the converged solution as the mesh is refined, which contrasts with the MSU scheme which monotonically converges to the

continuous solution with increasing mesh refinement. More about discretization errors and convergence will be given in Section 3.6.

From a usability standpoint, the help guide of Ansys/FLOTRAN states that the SUPG formulation offers more accuracy, but less diagonal dominance and, therefore, less ideal convergence properties. This manual offers some tips for getting the SUPG method to converge correctly, but explains that it is sometimes much more difficult to get an SUPG solution started than with MSU (in fact, one recommendation is to start with MSU, then switch to SUPG after some iterations) [*ANSYS Online Help,* 2001].

Although most interesting problems here are completely steady-state problems, it will be noted for completeness now that Ansys/FLOTRAN uses a 2^{ND} order accurate implicit time formulation. As such, there is no Courant-Friedrichs-Lewy (CFL) number restrictions associated with doing a transient problem using Ansys/FLOTRAN. The code allows an arbitrary time step to be entered, or can calculate one automatically by analyzing all elements and determining the maximum time step for which any fluid particle entering any element still remains in that element.

Once the governing equations are properly discretized and the global matrices are built, solution of the finite element matrices in Ansys/FLOTRAN proceeds via a segregated solution. There are two basic types of solution algorithms, coupled and segregated. Coupled solvers try to solve the entire non-linear equation set at once by common methods like Picard iteration, variations of Newton's method, etc. Segregated solvers solve the equations one at a time, addressing the nonlinearities by using the current, approximate solutions for the other degrees of freedom in each equation. The segregated solver routine has the advantage of not needing to actually assemble one large global matrix all at once. Instead, smaller matrices can be assembled and removed as needed [FIDAP, 2001]. Remember again that a derived form of the continuity equation serves as the pressure equation (see Table 3-1).

In keeping with the segregated algorithm, Ansys/FLOTRAN uses a general class of segregated methods known as SIMPLE [Patankar and Spalding, 1972]. Specifically, Ansys/FLOTRAN uses a method of this class specially adapted for the finite element method called SIMPLEF [Schnipke and Rice, 1985]. SIMPLEF does not require the staggered grid used in some of the original formulation, as it appears in Patankar and Spalding. In this method, the velocities are solved for twice – once approximately near the beginning of the global iteration

and once near the end to update the velocities with the pressure solution from that iteration. For each individual equation matrix, a variety of iterative solvers and a direct solver can be used. These include common techniques like Gauss-Seidel iteration, conjugate gradient solution, etc. Once again, the theory reference manual [Kohnke, 2001] gives all the details of the solution algorithm. The program performs a specified number of global iterations, or marches until some convergence parameters are met.

3.2. Non-dimensionalization

One important matter that requires attention is that of non-dimensional form. Often, numerical codes based on any of these complex schemes solve a "normalized" set of equations, where all variables in the equation are divided by a reference value to scale the equations. This is typically done for a couple of reasons. First, in dimensionless form, characteristic parameters like Reynolds number, Prandtl number, Mach number, etc. appear explicitly in the equations [Tannehill, Anderson, and Pletcher, 1997].

Second, since all the values are normalized, they fall within prescribed limits. This can be advantageous by making the solution more understandable and sometimes by providing an easy check of solution quality. For example, if the maximum velocity is picked as the reference value, and the solution predicts a value greater than one, the solution should be questioned. Further, normalizing values seems to often provide some numerical benefits (at least in Ansys/FLOTRAN) by making the solution more stable and convergent [Pelletier, 1984]. Normalization tends to keep the code from making badly scaled calculations as the solution proceeds (like multiplying a very large number by a very small one), but the quantitative benefit here is difficult to ascertain in a general sense.

Third, and finally, normalizing also makes any generated solution more universal, as it applies to any of a class of geometrically similar problems; the scale simply changes. Any problem of the same geometry sharing the same Reynolds number and all other dimensionless quantities automatically shares the same scaled solution. This will become clearer later on after the detailed dimensionless scheme is revealed. This fact is particularly useful here as the goal of this work is to provide a general treatment of direct measuring skin friction gages.

Dimensionless scaling allows each solution to be applicable to a whole class of skin friction sensors.

FLOTRAN in particular makes no internal dimensionless scaling at all. However, there is also no tabulation of units or dimensions of any sort. Therefore, it is possible to put all values into the code in non-dimensional form and receive the corresponding non-dimensional output since the equation form is the same. This requires that a consistent scheme of non-dimensionalization to be used. The following pages will show that the correct form does indeed produce the correct equations, looking identical except for the asterisks, *, which indicate dimensionless quantities.

The non-dimensional scheme presented here starts with the particular forms of the equations in Kohnke [2001], since the focus here is particularly on the Ansys/FLOTRAN code. Other sources may tabulate the equations of interest slightly differently, but the derivation presented should work universally for the standard Navier-Stokes formulation. Readers are cautioned to note, however, that the equations used are actually the same as shown here. This is particularly true in the turbulence equation, as there are many variations in the κ–ε turbulence model [Schetz, 1993].

Continuity:

$$\frac{\partial \rho}{\partial t}+\frac{\partial(\rho u)}{\partial x}+\frac{\partial(\rho v)}{\partial y}+\frac{\partial(\rho w)}{\partial z}=0 \tag{3-5a}$$

X-momentum:

$$\frac{\partial(\rho u)}{\partial t}+\frac{\partial\left(\rho u^{2}\right)}{\partial x}+\frac{\partial(\rho u v)}{\partial y}+\frac{\partial(\rho u w)}{\partial z}=\rho g_{X}-\frac{\partial P}{\partial x}+R_{X}$$
$$+\frac{\partial}{\partial x}\left(\mu \frac{\partial u}{\partial x}\right)+\frac{\partial}{\partial y}\left(\mu \frac{\partial u}{\partial y}\right)+\frac{\partial}{\partial z}\left(\mu \frac{\partial u}{\partial z}\right)+\frac{\partial}{\partial x}\left(\mu \frac{\partial u}{\partial x}\right)+\frac{\partial}{\partial y}\left(\mu \frac{\partial v}{\partial x}\right)+\frac{\partial}{\partial z}\left(\mu \frac{\partial w}{\partial x}\right) \tag{3-6a}$$

Y-momentum:

$$\frac{\partial(\rho v)}{\partial t}+\frac{\partial(\rho u v)}{\partial x}+\frac{\partial\left(\rho v^{2}\right)}{\partial y}+\frac{\partial(\rho v w)}{\partial z}=\rho g_{Y}-\frac{\partial P}{\partial y}+R_{Y}$$
$$+\frac{\partial}{\partial x}\left(\mu \frac{\partial v}{\partial x}\right)+\frac{\partial}{\partial y}\left(\mu \frac{\partial v}{\partial y}\right)+\frac{\partial}{\partial z}\left(\mu \frac{\partial v}{\partial z}\right)+\frac{\partial}{\partial x}\left(\mu \frac{\partial u}{\partial y}\right)+\frac{\partial}{\partial y}\left(\mu \frac{\partial v}{\partial y}\right)+\frac{\partial}{\partial z}\left(\mu \frac{\partial w}{\partial y}\right) \tag{3-7a}$$

Z-momentum:

$$\frac{\partial(\rho w)}{\partial t}+\frac{\partial(\rho u w)}{\partial x}+\frac{\partial(\rho v w)}{\partial y}+\frac{\partial\left(\rho w^{2}\right)}{\partial z}=\rho g_{Z}-\frac{\partial P}{\partial z}+R_{Z}$$
$$+\frac{\partial}{\partial x}\left(\mu\frac{\partial w}{\partial x}\right)+\frac{\partial}{\partial y}\left(\mu\frac{\partial w}{\partial y}\right)+\frac{\partial}{\partial z}\left(\mu\frac{\partial w}{\partial z}\right)+\frac{\partial}{\partial x}\left(\mu\frac{\partial u}{\partial z}\right)+\frac{\partial}{\partial y}\left(\mu\frac{\partial v}{\partial z}\right)+\frac{\partial}{\partial z}\left(\mu\frac{\partial w}{\partial z}\right) \quad (3\text{-}8a)$$

Energy (in terms of T_0):

$$\frac{\partial(\rho c_{P}T_{0})}{\partial t}+\frac{\partial(\rho u c_{P}T_{0})}{\partial x}+\frac{\partial(\rho v c_{P}T_{0})}{\partial y}+\frac{\partial(\rho w c_{P}T_{0})}{\partial z}=\frac{\partial}{\partial x}\left(k\frac{\partial T_{0}}{\partial x}\right) \quad (3\text{-}9a)$$
$$+\frac{\partial}{\partial y}\left(k\frac{\partial T_{0}}{\partial y}\right)+\frac{\partial}{\partial z}\left(k\frac{\partial T_{0}}{\partial z}\right)+W^{V}+E^{K}+Q_{V}+\mu\Phi+\frac{\partial P}{\partial t}$$

Species Transport:

$$\frac{\partial(\rho C_{i})}{\partial t}+\frac{\partial(\rho u C_{i})}{\partial x}+\frac{\partial(\rho v C_{i})}{\partial y}+\frac{\partial(\rho w C_{i})}{\partial z}=\frac{\partial}{\partial x}\left(\rho D_{mi}\frac{\partial C_{i}}{\partial x}\right)$$
$$+\frac{\partial}{\partial y}\left(\rho D_{mi}\frac{\partial C_{i}}{\partial y}\right)+\frac{\partial}{\partial z}\left(\rho D_{mi}\frac{\partial C_{i}}{\partial z}\right) \quad (3\text{-}10a)$$

Turbulent Kinetic Energy Transport:

$$\frac{\partial(\rho\kappa)}{\partial t}+\frac{\partial(\rho u\kappa)}{\partial x}+\frac{\partial(\rho v\kappa)}{\partial y}+\frac{\partial(\rho w\kappa)}{\partial z}=\frac{\partial}{\partial x}\left(\frac{\mu_{T}}{\sigma_{K}}\frac{\partial\kappa}{\partial x}\right)+\frac{\partial}{\partial y}\left(\frac{\mu_{T}}{\sigma_{K}}\frac{\partial\kappa}{\partial y}\right)$$
$$+\frac{\partial}{\partial z}\left(\frac{\mu_{T}}{\sigma_{K}}\frac{\partial\kappa}{\partial z}\right)+\mu_{T}\Phi-\rho\varepsilon \quad (3\text{-}11a)$$

Turbulence Dissipation Transport:

$$\frac{\partial(\rho\varepsilon)}{\partial t}+\frac{\partial(\rho u\varepsilon)}{\partial x}+\frac{\partial(\rho v\varepsilon)}{\partial y}+\frac{\partial(\rho w\varepsilon)}{\partial z}=\frac{\partial}{\partial x}\left(\frac{\mu_{T}}{\sigma_{\varepsilon}}\frac{\partial\varepsilon}{\partial x}\right)+\frac{\partial}{\partial y}\left(\frac{\mu_{T}}{\sigma_{\varepsilon}}\frac{\partial\varepsilon}{\partial y}\right)$$
$$+\frac{\partial}{\partial z}\left(\frac{\mu_{T}}{\sigma_{\varepsilon}}\frac{\partial\varepsilon}{\partial z}\right)+C_{1\varepsilon}\mu_{T}\frac{\varepsilon}{\kappa}\Phi-C_{2}\rho\frac{\varepsilon^{2}}{\kappa} \quad (3\text{-}12a)$$

This is the complete Reynolds Averaged Navier-Stokes (RANS) formulation presented in Cartesian coordinates as it is given in Kohnke and solved by Ansys/FLOTRAN. The second

viscosity coefficient is neglected for Ansys/FLOTRAN since it is zero by definition for incompressible flow and negligible in many compressible situations.

First, it is necessary to expand on some of the terms in eqn. (3-8a), which were abbreviated in Kohnke for space reasons. This includes the viscous work (W^V), momentum dissipation (Φ), and kinetic energy (E^K) terms as used in this form of the governing equations.

$$W^V = u\mu\left(\frac{\partial^2 u}{\partial x^2}+\frac{\partial^2 u}{\partial y^2}+\frac{\partial^2 u}{\partial z^2}+\frac{\partial^2 v}{\partial x^2}+\frac{\partial^2 v}{\partial x\partial y}+\frac{\partial^2 w}{\partial x\partial z}\right)$$
$$+ v\mu\left(\frac{\partial^2 v}{\partial x^2}+\frac{\partial^2 v}{\partial y^2}+\frac{\partial^2 v}{\partial z^2}+\frac{\partial^2 u}{\partial x\partial y}+\frac{\partial^2 v}{\partial y^2}+\frac{\partial^2 w}{\partial y\partial z}\right) \quad (3\text{-}13a)$$
$$+ w\mu\left(\frac{\partial^2 w}{\partial x^2}+\frac{\partial^2 w}{\partial y^2}+\frac{\partial^2 w}{\partial z^2}+\frac{\partial^2 u}{\partial x\partial z}+\frac{\partial^2 v}{\partial y\partial z}+\frac{\partial^2 w}{\partial z^2}\right)$$

$$W^V = u_j\mu\left(\frac{\partial}{\partial x_i}\frac{\partial u_j}{\partial x_i}+\frac{\partial}{\partial x_k}\frac{\partial u_k}{\partial x_j}\right) \quad (3\text{-}13b)$$

$$\Phi = 2\left(\frac{\partial u}{\partial x}\right)^2+\left(\frac{\partial u}{\partial y}\right)^2+\left(\frac{\partial u}{\partial z}\right)^2+2\left(\frac{\partial u}{\partial y}\frac{\partial v}{\partial x}\right)+2\left(\frac{\partial u}{\partial z}\frac{\partial w}{\partial x}\right) \quad (3\text{-}14a)$$
$$+\left(\frac{\partial v}{\partial x}\right)^2+2\left(\frac{\partial v}{\partial y}\right)^2+\left(\frac{\partial v}{\partial z}\right)^2+2\left(\frac{\partial v}{\partial z}\frac{\partial w}{\partial y}\right)+\left(\frac{\partial w}{\partial x}\right)^2+\left(\frac{\partial w}{\partial y}\right)^2+2\left(\frac{\partial w}{\partial z}\right)^2$$

$$\Phi = \left(\frac{\partial u_i}{\partial x_k}+\frac{\partial u_k}{\partial x_i}\right)\frac{\partial u_i}{\partial x_k} \quad (3\text{-}14b)$$

$$E^K = -\frac{\partial}{\partial x}\left[\frac{k}{C_P}\frac{\partial}{\partial x}\left(\frac{1}{2}\left|V^2\right|\right)\right]-\frac{\partial}{\partial y}\left[\frac{k}{C_P}\frac{\partial}{\partial y}\left(\frac{1}{2}\left|V^2\right|\right)\right]-\frac{\partial}{\partial y}\left[\frac{k}{C_P}\frac{\partial}{\partial y}\left(\frac{1}{2}\left|V^2\right|\right)\right] \quad (3\text{-}15a)$$

$$E^K = -\frac{\partial}{\partial x_i}\left(\frac{k}{c_P}\frac{\partial}{\partial x_i}\left(\tfrac{1}{2}\left|u_k u_k\right|\right)\right) \quad (3\text{-}15b)$$

Next, it is beneficial to write the complete forms of eqns. (3-5a) – (3-12a) in tensor notation, as the length and complexity of some of these makes them difficult to manipulate. Eqns. (3-13b), (3-14b), and (3-15b) are used and inserted as appropriate. Further, since all components of any

vector will have the same dimensionality anyway, it is redundant to write all three components out (details of tensor notation can be found in Shames and Dym [1985]). Re-writing in tensor notation yields the following:

$$\rho_{,t}+(\rho u_i)_{,i}=0 \tag{3-5b}$$

$$(\rho u_j)_{,t}+(\rho u_i u_j)_{,i}=\rho g_j - P_{,j}+R_j+\left[\mu\left(u_{i,j}+u_{j,i}\right)\right]_{,i} \tag{3-6b) - (3-8b}$$

$$\begin{aligned}&(\rho c_P T_0)_{,t}+(\rho u_j c_P T_0)_{,j}=(k(T_0),j)_{,j}+u_j\mu\left((u_{j,i})_{,j}+(u_{k,k})_{,j}\right)\\&-\left[\frac{k}{c_P}\left(\tfrac{1}{2}\left|u_k u_k\right|\right)_{,i}\right]_{,i}+Q_V+\mu(u_{i,k}+u_{k,i})u_{i,k}+P_{,t}\end{aligned} \tag{3-9b}$$

$$(\rho C_i)_{,t}+(\rho u_j C_i)_{,j}=(\rho D_{mi} C_{i,j})_{,j} \tag{3-10b}$$

$$(\rho\kappa)_{,t}+(\rho u_i\kappa)_{,i}=\left(\frac{\mu_T}{\sigma_K}\kappa_{,i}\right)_{,i}+\mu_T(u_{i,k}+u_{k,i})u_{i,k}-\rho\varepsilon \tag{3-11b}$$

$$(\rho\varepsilon)_{,t}+(\rho u_i\varepsilon)_{,i}=\left(\frac{\mu_T}{\sigma_\varepsilon}\varepsilon_{,i}\right)_{,i}+C_{1\varepsilon}\mu_T\frac{\varepsilon}{\kappa}(u_{i,k}+u_{k,i})u_{i,k}-C_2\rho\frac{\varepsilon^2}{\kappa} \tag{3-12b}$$

In each equation, a non-dimensionalizing scheme can be inserted into the original eqns. (3-5b) – (3-12b), and after canceling terms, an identical form is produced with the non-dimensional quantities. This process is shown for all equations in Appendix B. The compatible non-dimensionalizing scheme for all variables appearing in eqns. (3-5b) – (3-12b) is given in Table 3-2. Note that the turbulent viscosity, μ_T, is defined as a derived quantity through either a zero-equation turbulence model or the two-equation κ–ε model. In either case, its definition is consistent with that of the laminar fluid viscosity in the equations. The forms given by the dimensional equations and dimensionless equations are identical, proving the validity of Table 3-2.

Table 3-2. Dimensionless Scheme for the Navier-Stokes Equation Set

length components	$x_i^* = \frac{x_i}{L_\infty}$	turbulent dissipation	$\varepsilon^* = \frac{\varepsilon}{\left(V_\infty^3 / L_\infty\right)}$
time	$t^* = \frac{t}{\left(L_\infty / V_\infty\right)}$	fluid viscosity	$\mu^* = \frac{\mu}{\rho_\infty L_\infty V_\infty}$
gravity components	$g_j^* = \frac{g_j}{\left(V_\infty^2 / L_\infty\right)}$	fluid density	$\rho^* = \frac{\rho}{\rho_\infty}$
velocity components	$u_i^* = \frac{u_i}{V_\infty}$	fluid specific heat	$c_P^* = \frac{c_P}{\left(V_\infty^2 / T_\infty\right)}$
pressure	$P^* = \frac{P}{\rho_\infty V_\infty^2}$	fluid thermal conductivity	$k^* = \frac{k}{\left(L_\infty \rho_\infty V_\infty^3 / T_\infty\right)}$
temperature	$T^* = \frac{T}{T_\infty}$	species diffusion coefficient	$D_{mi}^* = \frac{D_{mi}}{V_\infty L_\infty}$
species concentration	$C_i^* = C_i$	momentum source components	$R_j^* = \frac{R_j}{\left(\rho_\infty V_\infty^2 / L_\infty\right)}$
turbulent kinetic energy	$\kappa^* = \frac{\kappa}{V_\infty^2}$	volumetric heat source	$Q_V^* = \frac{Q_V}{\left(\rho_\infty V_\infty^3 / L_\infty\right)}$

3.3. Initial Conditions

Another matter which deserves some discussion is that of initial conditions. Here, analysis was, to a large extent, directed by the capabilities and design of the particular code. Ansys/FLOTRAN uses a default initial value of zero for all degrees of freedom unless otherwise specified. Of course, any specified Dirichlet boundary conditions override any specified initial

conditions. It seems advantageous to specify more accurate initial conditions whenever possible to speed up solution convergence.

One technique commonly used in CFD to accelerate convergence is the idea of *multigrid*. This relatively recent idea is based on two principles. Brandt [1977] is a classic reference for more details on the multigrid algorithm. The first, the smoothing principle, is that iterative solvers tend to smooth out the solution error over many iterations. High frequency errors tend to be damped out quickly, while low frequency (long) error waves tend to survive. The second principle, the coarse grid principle, is that these smooth or low frequency errors can be well approximated on a coarser grid [Trottenberg, Oosterlee, and Schuller, 2001]. Multigrid operates by solving for this smoothed error on a coarse grid to provide a better guess on the fine grid. Because the coarse grid iteration uses a small amount of calculations in comparison to the fine grid, this technique is successful.

Unfortunately, Ansys/FLOTRAN does not implement such a technique in its formulation. To gain any benefit from multiple grid interaction, it is necessary to look at a primitive precursor of multigrid. Trottenberg, Oosterlee, and Schuller refer to this as *nested iteration*. Nested iteration is a simple concept; one uses course grid solutions to obtain a better initial guess for a finer grid, which is a one-way process from coarse to fine rather than the interactive formulation of multigrid. In general, nested iteration uses Richardson extrapolation, which is a technique utilizing Taylor series expansion for several points at once to get a better estimate of an "exact" value [Matthews and Fink, 1999]. Kronsjö and Dahlquist [1972] used two coarse grid solutions (of element size h and $2h$) to obtain a 4^{th} order accurate approximation to a fine grid of mesh size $h/2$ for the two-dimensional, elliptic Laplace equation. This approximation was then used to start iteration on the fine grid such that it reached the designated level of accuracy in only a few iterations. Although not a necessary requirement, the steady state Navier-Stokes equations happen to be an elliptic problem as well for subsonic, incompressible flow. Complex geometries and non-linearities certainly complicate the process somewhat, but the method can be assumed to be useful. It is interesting to note that, although figuring much more prominently in the later Section 3.6 on computational errors, Roy, McWherter-Payne, and Oberkampf [2000] mention the use of this technique for their finest models to accelerate convergence of hypersonic flow problems.

This basic technique has been used quite successfully in Ansys/FLOTRAN here to accelerate convergence. Implementing this technique using Ansys/FLOTRAN is somewhat difficult however, so the steps involved are listed in Appendix C for future use. Because of the complexity, only a 1^{ST} order accurate approximation has been used to transfer conditions from a single coarse grid onto a fine grid. This amounts to simply using linear interpolation (via the shape functions) to transfer the coarse grid solution values directly as a starting guess on the fine nodes. Although not as robust and accurate as that used by Kronsjö and Dahlquist, this simple procedure is still significantly better than using zero as a uniform initial guess. Since the transferring of conditions in Ansys/FLOTRAN is time consuming in itself, using more than a 1^{ST} order approximation would probably be prohibitive except on extremely large problems where the savings could be large.

As a brief example, a sample pipe problem was run in Ansys/FLOTRAN with and without the 1^{ST} order coarse grid acceleration. This problem consisted of an incompressible, laminar, axisymmetric pipe with fully developed flow. A coarse grid with 600 two-dimensional elements was solved, as well as a fine grid with double the mesh density, or 2400 two-dimensional elements. The fine grid was solved twice, once with the nested iteration as an initial guess, and once with the Ansys/FLOTRAN default of 0. All three problems were solved to approximately the same level of convergence; a value of $1x10^{-8}$ on the PRES variable convergence monitor (discussed in the final section of this chapter) was used as a stopping criterion. Results of the total number of seconds that the CPU spent in solving each case are shown in Table 3-3.

Table 3-3. Nested Iteration Test Problem CPU Times

Case	CPU Time (seconds)
coarse grid	11.17
fine grid, nested iteration	59.70
fine grid, default initial conditions	90.96

It is easy to see that even for such a simple example, the nested iteration provided savings. Even with the additional calculation time of the coarse grid, nested iteration required

only 78% of the CPU time that the default problem did, saving about 20 seconds out of 90. Although no similar tests were performed on any of the primary problems of interest here, it is assumed that similar or better reductions were seen there, especially in the 3D problems where grid doubling multiplies by a factor of 8 rather than just 4.

3.4. Boundary Conditions

A brief discussion also must be made at this time on the subject of boundary conditions for general types of problems, specifically related to the finite element method. The exact boundary conditions used for specific problems will be given as they are discussed later, but a general understanding of boundary condition types will be given now.

As already discussed, there are two types of boundary conditions in performing a finite element analysis of this type: essential and natural. The relationship of these conditions within the finite element method has already been briefly discussed in Section 3.1. The implementation of the boundaries are equally important in solving a real problem, as making the correct boundary condition choices is probably the most important step to obtain a correct solution. In the typical form of any transport equation, the Navier-Stokes equations are second order in the velocity components u, v, *and* w. The turbulence equations are second order in the turbulent kinetic energy and dissipation, κ and ε. The energy equation is second order in temperature, T. And, of course, the momentum equations are first order in pressure, P.

One standard boundary type is the inlet condition. Flow is specified in the form of the three velocity components. Here, u, v, and w are given specifically as essential boundary conditions, even if that value is zero. Of course, this value need not be constant over the inlet, as a velocity profile can be utilized. Turbulence values κ and ε also must be specified at an inlet, although this is something that is often not known. Ansys/FLOTRAN has a feature which automatically places 1% inlet intensity (the ratio of turbulent velocity fluctuation to average velocity) and length scaling on any inlet where κ and ε are not specified. Specifying essential condition values for these variables on an inlet overrides this feature. One common choice is to make κ equal to zero and ε equal to 1, indicating that there is no incoming turbulence at all. The

Ansys/FLOTRAN manual specifically states that ε should never be set to zero [*ANSYS Online Help,* 2001].

Walls are traditionally defined by setting all velocity components to zero. Ansys/FLOTRAN allows a moving wall to be specified (as in a Couette flow, for example) by setting the tangential components to a value other than zero. Again, however, all velocities are specified as essential conditions. The difference between a wall and an inlet is that the normal velocity component is identically zero for a wall and non-zero for an inlet. The two-equation turbulence model is uniquely problematic at walls, as the standard κ-ε model is not defined at such a point. Because of this, no boundary conditions are specified by the user for κ and ε on a wall. The typical approach for this issue is to create a point above the wall in the log region of the boundary layer where the κ-ε model stops, and to use the *law of the wall* to solve the remaining distance to the wall. This is called a *wall function* [Schetz, 1993].

Many finite element codes have specialized wall elements to handle this situation along a wall surface [FIDAP, 2001]. The two region wall model of Ansys/FLOTRAN designates elements that border a wall with a special status. This is similar to the recommended procedure from Turgeon, *et al*., [2002], as they employ a two region model as well. The code internally makes a decision about whether the node adjacent to the wall lies in the laminar sublayer region or the log region based on the value of y^+ that is calculated. This quantity is a dimensionless scale of distance from the wall near the surface, and is given by:

$$y^+ \equiv \frac{yu_*}{\nu} \tag{3-16}$$

Most of the default wall parameters are consistent with the recommended values in Schetz [1993], with an additional transition y^+ value of 11.5. Although this numerical formulation of the turbulent wall model makes no allowance for an overlap region between the log and laminar sublayer regions, studying the plot of turbulent velocity profiles in these regions shows that little error is induced by neglecting the overlaping region. The details of the wall formulation can be found in the *Ansys Theory Manual* [Kohnke, 2001] and the *Ansys Online Help* guide [2001]. This formulation is critical here, since the wall shear stress calculation for turbulent flows comes as a direct result of the turbulence wall model.

From the information obtained by a calculation of the value of y^+ based on the distance between each wall node and near wall node for each designated wall element, it is determined

whether the specialized wall element resides in the log region or the laminar sublayer. With this determination, the effective viscosity for that particular element is set to either the laminar value only in the case of the laminar sublayer (turbulent viscosity of zero), or an effective viscosity calculated from the law of the wall in the case of the log region. In generating the nodal solution of the Ansys/FLOTRAN Navier-Stokes equations, the wall element would contribute to the coefficients of the operator matrix using an effective viscosity determined from the above wall function analysis, and all other elements would contribute to the coefficients based on an effective viscosity calculated using the values of κ and ε as in the bulk of the flow. Given the nature of the equations, non-wall nodes governed by the κ–ε model that are close in proximity to the near wall nodes (such as a corner where two walls meet at right angles) will be strongly affected by the boundary conditions from the wall treatment. Nodes farther out in the flow domain will be less strongly affected.

The result of this wall treatment is that the code allows for the near wall node (and hence the wall element) to fall either in the laminar sublayer or the log region. The code uses the special wall formulation to correctly utilize experimental turbulence information to calculate boundary conditions for κ and ε based on a calculation of y^+. Above this element, however, the calculation of effective viscosity requires that the κ–ε model be valid. Thus, any nodes above the first must lie within the log region. Values of y^+ above 30 or so are ideal for log region behavior. This issue will be discussed further later, but the correct use of the high Reynolds number, two option wall treatment κ–ε model requires that the nodes above the near wall node be far enough from the wall to correctly calculate κ and ε and thus effective viscosity. Clustering too many nodes too close to the laminar sublayer can have detrimental consequences on the solutions near the wall surfaces. The shear stress is also a product of the specialized wall element treatment, which calculates shear stress according to an appropriate formula based on the zone in which the element resides. Correct calculation of the shear stress along the wall surface requires that the mesh be correctly designed near the wall in order to make correct use of the wall function.

A most interesting boundary condition is that of the “free” condition. A free boundary is generally known as a type of far-field condition, or a boundary where disturbances have been damped out. The boundary is termed so because it allows unrestricted inflow or outflow, but it prevents this flow rate from changing at the boundary (i.e. no disturbances or fluctuations in

space), as described by Oberkampf and Blottner [1998]. The free condition is the easiest type of boundary to implement, as no effort is required. However, its effect is quite profound. This is the natural condition that has been discussed in Section 3.1. By not specifying a degree of freedom on a boundary in the finite element method, one is automatically inferring that a combination of velocity derivatives is zero. Ansys/FLOTRAN even explicitly states this in its boundary condition dialog box with the message "warning: Blank values not interpreted as zero!!." Developing from eqn. (3-5a), the natural boundary condition corresponding to the essential degree of freedom velocity component, u_j, is given by eqn. (3-17).

$$\left(\frac{\partial u_i}{\partial x_j} + \frac{\partial u_j}{\partial x_i}\right) n_i = 0 \tag{3-17}$$

The n_i variables are the direction cosine components of the respective surface. One or all degrees of freedom can be left as free. Leaving them all as free says that the values are no longer changing at that boundary. The actual values need not be zero, but their normal derivatives are zero. This boundary condition is useful far above a boundary layer in an external problem, sufficiently far away that the disturbance is no longer felt.

Symmetry boundaries are marked by setting the normal velocity component to zero. The other two components are left as free. If the *w* component is set to zero, for instance, then this infers that $\partial w/\partial x + \partial u/\partial z = \partial w/\partial y + \partial v/\partial z = 0$ as well from eqn. (3-17). A symmetry plane is exactly that – no flow passes through the symmetry plane, and an identical flow pattern takes place mirrored through the plane. Using symmetry where appropriate allows a reduction in computational effort required.

Finally, the outflow boundary condition is discussed. The inlet condition required known values of the velocity components based on problem definition. Unfortunately, it is rare that the outlet conditions will be known, so it is impossible to accurately specify them. The outflow is in fact an artificial boundary, as the continuous domain does not really stop at that point. However, computational feasibility requires that the problem domain be reasonably limited. Although unintuitive, the best choice for outflow conditions is also the free condition. Renardy [1997] indicates that using the free outlet condition masks an effective boundary condition at a point near the outlet. A somewhat longer paper by Griffiths [1997] discusses the implications of this free condition for some specific cases including $p=1$, where p is the order of the element shape

functions. This paper examines the effects of free outflow on the advection-diffusion equation given in eqn. (3-18).

$$\frac{\partial T}{\partial t} + u\frac{\partial T}{\partial x} = \mu\frac{\partial^2 T}{\partial x^2} + R \tag{3-18}$$

This equation is simply a general version of the forms seen in the Navier-Stokes equations already discussed. For the natural boundary condition to vanish at the last element as is necessary, a reduced form of the governing variational equation must identically vanish (since $\partial^2 T/\partial x^2$ is zero), as outlined in detail in his paper. This form is given in eqn. (3-19).

$$\int_{X_{N-1}}^{X_N} \psi_N \left(\frac{\partial T}{\partial t} + u\frac{\partial T}{\partial x} - R \right) dx \tag{3-19}$$

Since linear shape functions are always positive, application of the Mean Value Theorem to the reduced equation variational integral means that the terms of the integral must equal zero at some point in the last element. For this case, if the advection coefficient (a velocity component in the fluid flow case) and the momentum source term are linear functions in space, this point must be at 2/3 of the element length (or 1/3 of the element length from the outflow boundary). Thus, the no outflow boundary condition is equivalent to satisfying the reduced equation (given in the parenthesis of eqn. 3-19) at this point in the element. This is the implied condition suggested by Renardy.

The important result from Griffiths is that for this free outflow condition, the errors induced are on the order of μ^2, which is the viscosity in the Navier-Stokes equations. This is the deviance from the exact condition, which is actually only true at "infinity." On a practical note, the free outflow tends to cause some local smearing of the solution right at the outlet edge, but it serves adequately to close the problem and provide correct solution on the interior [Pelletier, 2000]. As long as a desired feature is not right at the outlet, the free boundary condition is useful.

For incompressible flows, pressure is only relative, as the gradient of pressure appears in the momentum equations, but no reference is made to pressure directly. Thus, a single pressure needs to be prescribed somewhere for reference, but only the difference from that reference matters. This pressure is often prescribed on the outlet, but it can sometimes be placed elsewhere as well.

Note that this entire discussion of boundary conditions is dependent on the fact that Ansys/FLOTRAN uses first order (linear) shape functions, as well as their choices in weak form reduction. Regardless, it would be necessary to, in some manner, enforce the same amount of boundary conditions due to the order of the governing equations. However, the interpretation and application to the code would be slightly different if higher order shape functions or alternate integration schemes were used.

3.5. The Embedded Region

One technique employed in this work is termed an "embedded region." A discussion of the embedded region concept follows directly from the boundary condition discussion, since the use of the boundary conditions is an integral part of an embedded region problem. The idea of the embedded region problem is to avoid the unnecessary and impractical need to solve an entire problem three-dimensionally in which the solution over the majority of the domain exhibits nominally 2D characteristics and the 3D effects are confined to a small percentage of the domain only.

Some of the flow problems studied in later chapters incorporate turbulence effects in the models. For the general problem of a direct measuring skin friction gage placed in the wall over which a nominally 2D turbulent boundary layer is developing, the study of errors on that skin friction gage under turbulent flow conditions requires that the gage be placed sufficiently far down the wall surface that the boundary layer has grown enough to display dominantly turbulent traits. Since a turbulent boundary layer requires very fine grid spacing near the wall, this makes the grid requirements quite large for 3D cases and this also makes the issue more difficult to treat with limited computational resources. For uniform free-stream boundary conditions and a 2D geometry, the boundary layer growth is essentially a 2D problem only. Therefore, it is simply inefficient to treat a large region where flow is essentially 2D with a 3D grid.

The effects generated by the skin friction gage are indeed three-dimensional, but they are confined to a small region of the boundary layer after it has already grown over a long distance on the wall. In this light, the embedded region concept was implemented for some problems here to make efficient use of the computational resources available. The implementation of the embedded region involves several steps. First, the entire global boundary layer problem is

solved in 2D only. For the problems here, this consisted of solving the turbulent boundary layer problem on the wall without the skin friction gage present. Then, at a selected station along the wall of the global problem, the solution conditions are extracted. Next, a 3D embedded region problem is created, including all 3D geometry (the skin friction gage in this case). The model is made only sufficiently large to safely encompass all 3D effects that the problem might generate. This requires testing of the boundary placement of the 3D embedded problem to insure that all of the three-dimensional effects are enclosed in the domain. The results from the global 2D problem without the gage or other 3D effects are then applied as fixed (constant) boundary conditions on the inlet on the embedded region. Since the embedded region contains all 3D effects within its domain, the inlet conditions are applied uniformly across the inlet plane in the third dimension of the embedded region. The other boundary conditions on the embedded problem along the top and bottom surfaces must be applied as they were for the represented section of the global, 2D problem (i.e. a symmetry plane must remain a symmetry plane, etc.). The 3D embedded region problem is finally solved.

The embedded region technique has theoretical validity because of the nature of the problems studied here. Although the Ansys/FLOTRAN CFD code itself numerically solves the full, elliptical, Navier-Stokes equations for the problems solved here, the physical nature of the problem of a boundary layer is a parabolic one. Thus, despite the fact that the CFD code allows for upstream communication, a high Reynolds number boundary layer physically shows almost no influence of the downstream effects on an upstream station. For this reason, the 3D embedded region is not expected to affect the boundary layer development in the upstream portion of the wall, and the inlet conditions utilized from the solution of the global 2D problem could be taken as fixed boundary conditions. Caution is warranted in using this approach in a general sense for elliptic problems where there might be strong two-way coupling in the flow, but for boundary layers, it is valid.

3.6. Sources of Computational Error

One of the most important issues in making a computational calculation is assessing the uncertainty in that calculation. Results from an experiment will always contain inherent uncertainties. These arise due to limited precision and/or capability of any and all instruments

involved in the measurement. These uncertainties can compound to adversely affect the desired result. For instance, a thermocouple might be limited to measuring a temperature accurately to within, say, 1 degree. Further, the placement of the thermocouple in the apparatus can only be determined to the accuracy of the ruler or calipers used. Thus, not only is the temperature measured uncertain, but so is the place where it is made. Computational analyses are just as prone to uncertainty, but the types and sources of this uncertainty are different. Much of what is discussed in this section is generic to all types of computational analysis, but particular emphasis shall be placed on CFD.

The first, and most fundamental, matter to consider in a CFD analysis was alluded to in Section 3.1 and it is the issue of modeling error. This can be best described in a paper by Roache [1997], who gives the definitions "of verification as 'solving the equations right,' and of validation as 'solving the right equations.'" Validation is the issue of addressing modeling errors in a CFD calculation – determining whether the equations solved correctly describe the problem or not. Thus, one must first be sure that a *valid* set of equations is being solved, otherwise there is, of course, a great deal of modeling error built into the calculation. As discussed in Section 3.1, Ansys/FLOTRAN solves the full Navier-Stokes equations, which are the "right" equations for just about any fluid calculation. The Navier-Stokes formulation contains very few approximations, and these equations should clearly be applicable for the problems solved in the next few chapters. Using the Navier-Stokes equation set, the most common issue of validation or modeling error is in the choice of turbulence modeling formulation. There are a large number of turbulence model variations available, and one finds that there are really no models that are particularly universal. A specific argument that the turbulence models chosen here for the turbulent flow analyses are adequate will wait until those chapters.

Once one is convinced that the calculation is performed using a valid set of equations and/or addressed any modeling errors as a result of validation issues, one must move on to the issue of verification. Verification is the issue of numerical errors accumulated in solving a set of equations with a computational algorithm. Assessing the accuracy of (or verifying) a valid calculation requires some further attention than looking at just the modeling error sources. Numerical error in a CFD calculation is due to several sources, which can be divided up into the following general categories:

1. computational round-off error

2. iterative convergence error
3. (ordered) discretization error
4. far-field boundary condition errors

These categories will be addressed one at a time in the order listed.

First, it is obvious that all computers operate on numbers of finite precision and this leads to round-off errors. For most things, like the word processing program that this document is being typed in, the numerical precision of a machine is inconsequential, for it provides much more precision than the word processing program needs. Engineering calculations, however, can sometimes suffer from round-off error due to the machine precision limits. An excellent, simple example of round-off error is to pick a simple function and evaluate its derivative using finite differences. Whether using forward, backward, or central differencing, the calculation will take the function evaluated at some points, and divide by the spacing between those points in some fashion. One finds that, as the spacing is decreased over a number of successive calculations, the approximation to the derivative gets better. As the spacing continues to decrease, however, one will find that suddenly the approximation begins to get worse again. This odd phenomenon is because the calculations of the derivative begin to suffer from round-off error as the subtractions and division approach the machine limits [Matthews and Fink, 1999].

One finds that this phenomenon can manifest itself in a couple of ways. First, round-off error becomes a problem when numerical calculations are poorly scaled. For example, subtracting a very tiny number from a very large number can cause the large number to appear unchanged (take $1x10^{20}$ minus $1x10^{-20}$ for instance). Even worse things can happen when one starts multiplying and dividing badly scaled numbers. One way to combat this in a preventative way is the method outlined in Section 3.2 – non-dimensionalization. Although not a guarantee against poor scaling, solving the non-dimensional problem tends to normalize things as outlined in that section. Further, round-off error can appear deviously in a complex calculation. Even if it is not a particular issue in a given operation, tiny round-off errors can compound together, because complex CFD computational codes do literally millions, and probably billions, of operations in order to obtain a solution. A small round-off error multiplied one billion times over can become an issue.

One finds in CFD that, for the issue of the third source of error (discretization error) to be discussed in detail below, it is desirable to have small element size. This must be balanced,

however, with the issue of round-off error, and one finds that in practice, literally driving a mesh to infinite density is not as fruitful as it might appear to be.

The second error source is that of iterative convergence error. This is a major contributor to computational error, but also the source that is probably easiest to identify and work with. Iterative convergence error occurs because the resulting algebraic system of equations is non-linear. Because of its non-linearity, it is necessary to solve the system by iteration (as seen in Section 3.1). Although each guess hopefully gets ever closer to the true solution, there is always going to be some difference between the iterated, approximate solution and the true solution to the algebraic system. There are a couple of ways to address the issue of incomplete convergence error. The design of the individual features of the code obviously plays a role in accessing this issue.

First, it is possible to use the solution variables directly to measure convergence. This is accomplished by calculating the norm of the change between two successive iterations divided by the true value. Since the true value is not known, the current guess can be substituted [FIDAP, 2001]. This rate of change can be calculated for any degree of freedom that is available. Ansys/FLOTRAN implements a convergence monitor which utilizes this basic concept. The rate of change of each degree of freedom (VX, VY, PRES, etc.) is normalized and summed up globally over all nodes as shown in eqn. (3-20).

$$M_{\Phi} = \frac{\sum_{i=1}^{N} \left| \Phi_i^k - \Phi_i^{k-1} \right|}{\sum_{i=1}^{N} \left| \Phi_i^k \right|} \tag{3-20}$$

This value is called a convergence monitor in Ansys/FLOTRAN, and is updated real time for each individual degree of freedom on the screen while the solution proceeds. Ideally, the rate of change should decrease as the solution approaches the correct one. This indicates that the solution is changing less and less as it approaches the true solution. In fact, the standard option in Ansys/FLOTRAN is to set a convergence criterion, which iterates the model until the convergence monitors of all degrees of freedom are below a specified level.

Obviously, this calculation is advantageous since it provides constant, real-time feedback of the solution process. However, it is not always as useful as it may appear. It is true that most of the time the convergence monitor indicates that the solution is converging as it (M_{Φ}) goes to zero. Occasionally, however, the numerical iteration of the solver can stall. The convergence

monitor could possibly show little change, but the solver is stuck at some incorrect solution. In practice, the convergence monitor tends to be better at doing the opposite of its intended purpose – it is usually good at detecting a diverging or erratic solution. If the convergence monitor stays at a large value over many iterations or fluctuates erratically, this usually indicates a problem with the model construction. A well-behaved convergence monitor is an excellent sign, but not a guarantee of success.

In real problems, the convergence monitors tend to fluctuate somewhat due to complex non-linearities, although extremely erratic behavior is always bad. This seems to be particularly true when the turbulence equations are involved due to the coupling of the boundary conditions. Also, if the true solution for a certain degree of freedom is small or zero, then the convergence monitor tends to fail. For instance, one of the problems studied in this document involves an external flat plate with zero pressure gradient in which the true solution is exactly zero relative pressure everywhere in the domain. As the pressure degree of freedom converges, it changes less and less, but approaches zero as well. Thus, the denominator of eqn. (3-20) shrinks too, and the convergence monitor never decreases much. The other variables decrease as normal however. A final issue is that the monitor is global in nature. Thus, the convergence monitor may be excessively dominated by only a few nodes, while the majority of the problem is well-converged, and the monitor cannot distinguish this behavior well.

Another standard method of addressing iterative convergence error in CFD is through the use of a *residual*. A residual is basically what it sounds like – it represents a measure of what is left over between the guessed, or approximate, solution and the true solution. In fact, a residual is actually the difference between a given equation evaluated with the true solution and the guessed one. Again, it is desirous to drive the residual to zero for complete convergence. For any numerical system as shown in eqn. (3-1), the approximate solution does not correctly satisfy that relation as described in that section. The true (unknown) solution does, however, satisfy eqn. (3-1). The residual appears in eqn. (3-21) by evaluating the relation with the approximate solution.

$$f - \mathcal{L}(\tilde{u}) = R(\tilde{u}) \tag{3-21}$$

This is both a standard and necessary part of all common commercial codes. Exactly how the residual is used varies from code to code. Probably most common is for the code to sum the nodal residual value over each node and normalize by the starting residual. This is similar to

what was done with the individual degrees of freedom directly in eqn. (3-20). When the residual has dropped a certain number of orders of magnitude from its original starting value, the calculation ceases.

FLOTRAN offers a slightly different way of interpreting the residual. The stopping criteria are set by the degree of freedom convergence rates as given in eqn. (3-20). The residual values are calculated as a secondary item just before the solution stops. The residual values are stored along with the data on a nodal basis, and it is possible to post-process the residual values just like the solution data. Thus, it is possible to see the entire residual field. This technique has the advantage of seeing not only how large the actual residual magnitude is, but also where the maximum values are located. As with the convergence monitor calculations, it is common to see that the portions of the model is at differing states of convergence. Very often, the majority of the model shows small residual values while a few nodes have much larger values. Seeing this can help to identify and address problem areas, mesh inadequacies, problem construction issues, etc. If the model is correctly created and the region of high residuals is not in an area of interest, then no further iteration may be required.

The actual output variables in Ansys/FLOTRAN represent normalized residuals, where the actual residual values are divided by the main diagonal entries of that particular matrix line for that node. The idea behind this is that, for a diagonally dominant matrix, the normalized residual value can be compared directly with the corresponding value of the degree of freedom at that node. A percent error could then be calculated.

Although the residual method generally tends to be more reliable than a solution variable convergence index, it is possible for a type of stall to occur in this sense as well. Oscillation can occur such that the degrees of freedom are changing dramatically, but the residual changes only slightly. Thus, it seems best to use a combination of the degree of freedom convergence monitor and the residual convergence monitor to evaluate a solution's progress.

One final note on convergence is actually an extension of the degree of freedom convergence actually discussed. It is often possible to monitor the desired global output quantities to evaluate their asymptotic convergence to the correct value. This might be a parameter like a lift coefficient or drag coefficient. Since these types of parameters are just summations of the degrees of freedom, the same benefits and deficiencies already discussed

apply here as well. However, since this is the actual output that is desired from the model, observing these quantities over a number of iterations seems prudent as well.

The third error source is that of ordered discretization, and that is the source to which the most consideration shall be given here. In the previous paragraphs, the issue was how close one could get to the true solution for a particular algebraic representation. Now, the discussion will broaden by one step to ask how close that particular algebraic system is to approximating the true differential equation system. Even if it could be assumed that one has the exact, converged answer for the algebraic system of one mesh, generating a new mesh or grid will yield a different system of equations, and hence a different solution. This new solution may or may not be similar to the solution on the first grid, and both may or may not be close to the exact, differential solution.

This is the issue of discretization. In order to solve the problem, the continuous domain must be broken up into discrete approximate pieces. The continuous problem is best represented by a mesh of *infinite* density, or zero element size. Obviously, this is not practical, and from the round-off error discussion, it is also apparent that there are numerical issues associated with doing so. Computing power, time, and precision constraints limit the density of the mesh. Therefore it becomes necessary to develop an estimate of the error associated with solving the discrete problem rather than the ideal, continuous one.

The typical way of addressing ordered discretization error is by using the technique of Richardson extrapolation. This technique was mentioned briefly in Section 3.3, and it can be found in Matthews and Fink [1999]. Roache [1998, 1997, 1994] provides the most comprehensive discussion of this topic, and the remainder of this section will follow his notation and development, although a virtually identical technique has been documented by many others [Roy, 2001; Roy, McWherter-Payne and Oberkampf, 2000; Oberkampf and Blottner, 1998; Blottner, 1990; etc.]. As pointed out by Roache [1997], the following technique is advantageous over simply reporting a percent difference between two finite grids, as things like the order of convergence of the method and the relationship of the grids to the exact solution are not accounted for.

A desired output value from a CFD model is assumed to be a general function of grid size, h, and thus a Taylor's series representation can be written for the relationship between that

output value, f, on the discrete grid compared to the "exact" value on an infinite grid. Eqn. (3-21) shows the Taylor's series expansion.

$$f_{EXACT} = f + g_1 h + g_2 h^2 + g_3 h^3 + g_4 h^4 + \cdots \tag{3-21}$$

The g_i terms are functions of the continuum, and thus are completely independent of h. This relationship is valid for any degree of freedom output provided that the scheme is monotonically converging and the grid is within the asymptotic region of refinement. More will be said about these two points later.

The power of the technique becomes apparent when two similar grids of differing grid size are used to eliminate the leading terms of the Taylor series. Using two grids in the most general sense can eliminate g_1 from the result. However, if g_1 is zero, then g_2 can be eliminated, and so on. This is the case if the method is second order accurate in space. Recall from Section 3.1 that the two discretization schemes used in Ansys/FLOTRAN are MSU and SUPG, of which the MSU is analytically first order ($g_1 \neq 0$), and SUPG is approximately second order ($g_1 = 0$) under ideal circumstances.

With two grids, grid 1 is noted as the fine grid and grid 2 is the coarser grid. If g_1 is not zero, for instance, then the fine grid Taylor's series can be multiplied by r_{12}, the ratio of h_2/h_1, and the coarse grid Taylor's series can be subtracted from it to get eqn. (3-22).

$$r_{12} f_1 - f_2 = r_{12} f_{EXACT} - f_{EXACT} + O(h_2^2) + O(h_1 h_2) \tag{3-22}$$

Assume that h_1 and h_2 are on the same order of magnitude, or alternately that r_{12} is on the order of 1. Rearranging and canceling gives eqn. (3-23).

$$f_{EXACT} = f_1 + \frac{f_1 - f_2}{r_{12} - 1} + O(h^2) \tag{3-23}$$

If the method is second order and symmetric in space ($g_1 = 0$), the same procedure can be used to obtain eqn. (3-24).

$$f_{EXACT} = f_1 + \frac{f_1 - f_2}{r_{12}^2 - 1} + O(h^3) \tag{3-24}$$

Thus, in general, the form of eqn. (3-25) gives an expression for the relationship of the exact solution to the fine grid solution for any arbitrary order method.

$$f_{EXACT} = f_1 + \frac{f_1 - f_2}{r_{12}^p - 1} + O(h^{p+1}) \tag{3-25}$$

There are several important things to note about eqn. (3-25). First, r_{12} by definition must be greater than 1. Second, the approximation is good to at least an order of $(p+1)$. Depending on the numerical scheme involved, cancellation of terms may provide better results if the $(p+1)$ order terms drop out. Thus, eqn. (3-25) gives an estimate of the "error," or difference between a grid of a certain finite resolution and the exact answer by means of a third, coarser, grid and a numerical scheme of known order of convergence, p.

Eqn. (3-25) says that the exact solution, f_{EXACT}, is equal to the fine grid solution, f_1, plus some additional error term as shown. With this definition, a fractional or percent difference, A_1, between the exact solution and the fine grid solution can be approximated by E_1 as shown in eqn. (3-26),

$$A_1 = E_1 + O(h^{p+1}, E_1^2) \tag{3-26}$$

where E_1 is defined in eqn. (3-27).

$$E_1 = \frac{f_2 - f_1}{f_1\left(r_{12}^p - 1\right)} \tag{3-27}$$

Since it is not readily obvious why eqn. (3-26) has the truncation error that it does, the details of this equation are derived in the Appendix D and can be found by using binomial series expansion [Stewart, 1991]. The Richardson extrapolation error estimator, E_1, contains the fractional error between the coarse and fine grids, but it also includes a correction based on the order of convergence, making it a more realistic and robust measure of discretization error. The binomial series expansion requires that E_1 be less than 1 for the series to converge, and since the truncation of the series is of order E_1^2, the estimation works best for small values of E_1.

Defined as such, E_1 is accurate to order of h^{p+1} or greater. Since there is no measurement of these terms of order h^{p+1} and greater, the E_1 estimator has – all things being equal – a 50% chance of overestimating or underestimating the true error. In cases where these higher order terms are significant, the E_1 estimator can easily be optimistic. Further, eqn. (3-27) requires that the order of convergence, p, be known. While most common CFD codes aspire to 2^{ND} order accuracy, many factors in real problems limit the observed order to less than the theoretical order. Factors like boundary conditions, turbulence models, coordinate transformations, discontinuities (shockwaves), flux limiters, and many other issues affect the order of convergence. Of course, the definition of the error estimator assumes that there is no iterative

convergence error as discussed earlier. Care must be taken to remove as much of this as possible, as an unconverged solution impairs the error estimator as well.

Specific reference has been made to hybrid methods, which depend on cell Reynolds number and approach 2ND order accuracy as this Reynolds number goes to zero. This is exactly the formulation used in the SUPG algorithm by Ansys/FLOTRAN. These types of methods present a problem, as the order of convergence for a practical grid is some imprecise value between 1 and 2. Uncertainty in p further contributes to uncertainty in the error estimator.

Roache recommends a factor of safety in the Richardson extrapolation error estimator to insure that the estimate is conservative. The presence of a factor of safety, F_s, overshadows uncertainties such as these mentioned here. Thus, the grid convergence index (GCI) is defined by Roache as given in eqn. (3-28).

$$\mathrm{GCI}_{fine} = 3\left|\frac{f_2 - f_1}{f_1\left(r_{12}^{p} - 1\right)}\right| \tag{3-28}$$

Eqn. (3-28) is for the fine grid, although a similar formula can be developed for the coarse grid. Again, this factor of safety, 3 in this case, all but insures that the estimation is conservative. In fact, Roache allows for a factor of safety of less than 3 for well studied situations in which multiple grids are used. However, the factor of safety of 3 is standard practice and has the effect of relating the *GCI* to an order of convergence, p, of 2 and a refinement, r_{12}, of 2 (since the denominator term and the factor of safety will cancel if r^p is 4). Roache [1997] emphasizes "that the GCIs are not error estimators but are three [or F_s] times the error estimators, representing error bands in a loose statistical sense."

A few final notes of interest are needed in the *GCI* derivation. First, using two grids provides a *GCI* value, if the order of convergence is already known. If three grids are used, the observed order can be determined from the results. As mentioned earlier, the observed order will usually be lower than the hypothetical order, and it may be much lower depending on the code and circumstances of the problem. Thus, using three grids is a much more robust procedure.

Second, although this discussion strictly applies to a degree of freedom, the same discussion applies to a global quantity derived from combinations of the degrees of freedom. This includes things like lift and drag coefficients on a body; for the specific skin friction sensors studied here, it applies to the global surface force integrations presented which are similar to lift,

drag and pitching moment. Because different quantities converge at different rates, the *GCI* of one quantity does not necessarily reflect the *GCI* of another.

On a practical note, using the *GCI* is not as simple as the foregoing description may seem. Again, the other sources of computational error pollute the ordered discretization estimate, particularly for global quantities which sum up many degrees of freedom. Even small convergence and rounding errors get summed as well, magnifying those effects. Hybrid methods, like the SUPG formulation, may not show a constant order of convergence over a range of grids as the method approaches 2^{ND} order cell by cell

A major issue in using this technique is that it requires the grid solutions to be in the asymptotic range. This means that the solutions must approach the true solution in a clean, asymptotic manner as the grid is refined. Grids that are too coarse will not be in the asymptotic range. In addition, many real problems will converge, but display non-monotonic convergence. The true solution is approached, but not in a steady manner. Fig. 3-2 shows a generic example of monotonic versus non-monotonic convergence.

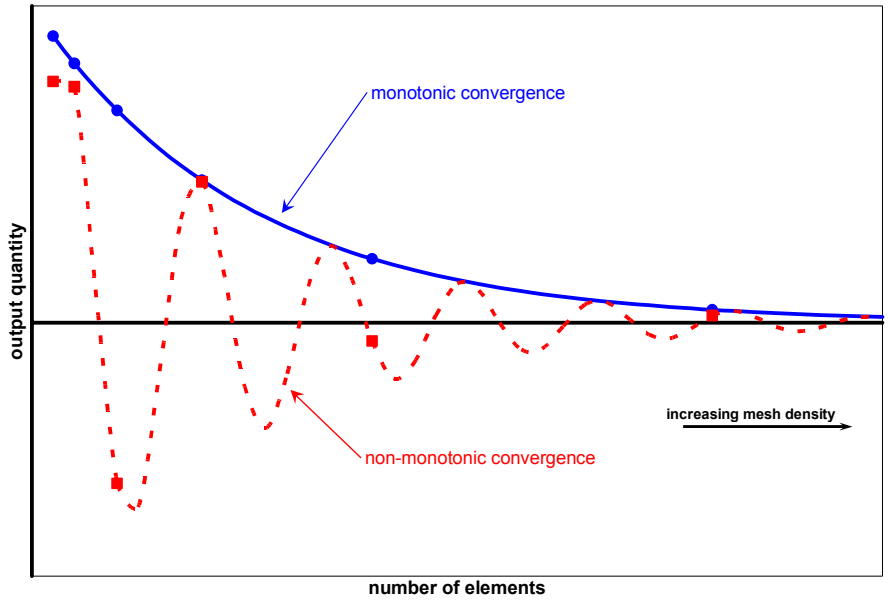

Figure 3-2. Example of Monotonic versus Non-monotonic Numerical Asymptotic Convergence Behavior for Successive Grid Doubling

Shown are several hypothetically obtained results by successively doubling the grid from each previous case. It is apparent that the numerical points represent the monotonic curve well, but

not the non-monotonic curve. This type of behavior results from interaction between error terms in the truncation error, causing canceling or additive effects at various grid levels [Hosder, 2002]. In fact, a general hybrid method will show both the first order and second order terms to be active and significant. Roy [2001] shows that this activity may produce non-monotonic convergence.

Strictly, the *GCI* is not valid unless the solution is monotonic and in the asymptotic range. Roy [2001] shows that using a third grid to determine the order of convergence fails if the convergence is strongly non-monotonic. Oberkampf and Blottner [1998] reveal that their cases required grids producing an error estimator E_1 on the order of 0.1% to demonstrate converging behavior. Thus, in their opinion, very tight error tolerances are required to even calculate the error (in part alluding to the fact presented earlier that the technique works best for small errors). The factor of safety of 3 provides a lot of room for uncertainty in the error estimation. Although the *GCI* with F_s incorporated provides excessively conservative results in many cases, it also serves to protect the researcher from some of these issues. It seems that some care must still be taken to address these practical concerns to insure the overall validity of the method, and that an F_s of 3 is sufficient.

The final issue of computational error deals with the problem of far-field constraints. This problem is, in a way, also a problem of discretization. However, it requires separate consideration, for it does not tend toward zero as the mesh is refined. This is simply the problem of placing the correct boundary conditions on the edges of the problem. For instance, a body (say, a car) is traveling at a speed of 30 m/s. Performing a CFD calculation of the aerodynamics of the external vehicle requires that a suitable grid be generated around the outline of the body, with some distance upstream of the body and some distance downstream of the body. An inlet condition of 30 m/s is then applied at the upstream surface. However, the upstream communication effect on the air flow by propagating pressure waves insures that the air stream is disturbed ahead of the body. Thus, at a given distance ahead of the car, the airflow is not actually moving at exactly an undisturbed 30 m/s in the physical problem. Thus, placing the boundary condition at that point produces some error from the desired physical result. Analytically, the air is only undisturbed at an infinite distance, thus being given the name of a "far-field" condition.

The discrete boundary condition will better approximate the far-field condition as it is moved farther from the object of interest. In fact, Roache [1994] has shown that the error associated with this boundary placement varies inversely with the distance from the region of interest to first order. This conclusion was drawn by Roache for airfoil flows in an infinite medium and may not hold for all cases. In other words, doubling the distance to a boundary in that case cuts the error it induces in half. This distance is referred to by a script "L," or $\mathscr{L}$.

In general, upstream conditions and downstream conditions may be subjected to this issue of boundary placement and dependence. Also of issue are free conditions, such as the upper surface of a boundary layer solution (i.e. placing the top of the domain too close to or into the boundary layer). As with the ordered discretization error, a simple percent difference can be calculated with two grids of differing boundary placement. As pointed out in the preceding pages, this is not technically reasonable, but since the far-field induced errors tend to be much smaller than the mesh dependent errors (at least in these cases), the issue is not so critical. Of course, the easiest thing to do in this regard is to double the boundary distance for the successive grids. This has been done for the cases studied here. The 1^{ST} order dependency on boundary placement is assumed to hold for these cases as well as in Roache's (citing a lack of more accurate empirical evidence). Since the method is assumed to be 1^{ST} order, from eqn. (3-27) the Richardson extrapolation error estimator resorts to the percent difference between the grids anyway.

In many cases, the ordered discretization error is the dominant error contributor. This is true in the cases studied here. As will be shown in the next chapters, the errors induced from the other sources are minor compared to the *GCI* calculations. However, in a strict sense, one caveat of the *GCI* derivation requires that these additional error sources are not there at all. In addition, changing the boundary placement means that a different mesh is generated. In short, these errors are not as decoupled as they might seem to be. Despite this, the computational errors will be presented for the various cases in this fashion. Most cases will reveal that only the mesh dependent error is particularly significant. Of course, the ever-present factor of safety in the *GCI* helps to envelope any uncertainty in the calculations.

CHAPTER 4: Studies of Skin Friction Gages in Laminar Two-Dimensional Channel Flow

4.1 The Physical Model

The first flow situation selected here for studies of error sources and their respective magnitudes in skin friction gages is that of a nominally two-dimensional, incompressible fluid channel. This problem was selected as a representative laminar, internal flow case, where the exact solution for the shear stress is available.

This flow also models an existing test facility in the Aerospace Engineering Department at Virginia Tech called the Skin Friction Gage Calibration Rig. The actual apparatus is pictured in Fig. 4-1 (a) with a supporting schematic representation in Fig. 4-1 (b). This device has been used as a calibration and testing apparatus, primarily for direct measuring skin friction gages. The working fluid is glycerin, which provides an incompressible, laminar flow that is steady for a reasonable length of test time. The customary method of calibrating a direct skin friction gage is to apply or hang a calibrated weight on the head. With the action of gravity, the force applied is known, and the output can be recorded. The resulting curve of output versus force should be linear with small flexural deflections. Dividing the force by the known gage head area gives the shear stress as a function of the signal output. However, since the static calibration method is not very representative of the actual conditions in which skin friction gages will be expected to perform, it is prudent to use a facility like the calibration rig to provide some verification of the gage's calibration and operation. In addition, some gage designs such as small MEMS type units make attaching a weight impractical due to constraints like the physical size of the head.

The advantages of using this type of channel in particular are many. First, the channel is easy to set-up and control. Second, as detailed below, the solution of a fully developed laminar

flow in a channel is one of the few exact solutions for the Navier-Stokes equations that are available. Third, the flow conditions of the channel are relatively mild in terms of the possibility of physically damaging or harming the gage. There are no shockwaves present, no significant vibration, etc. Finally, the shear stress levels that the facility can generate range up to about 100 Pa, which is indicative of much faster external flows in air.

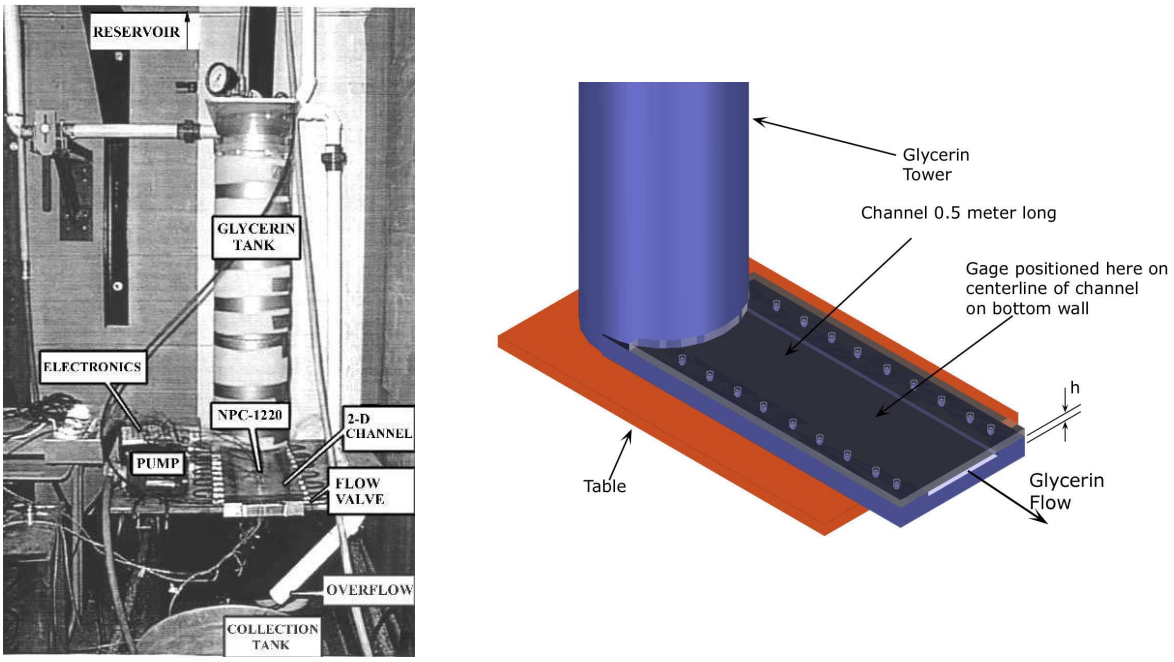

(a) **(b)**

Figure 4-1. Frontal Picture (a) and Schematic Rendering (b) of Virginia Tech Calibration Rig Facility

The physical apparatus is a long channel filled with glycerin, which is a thick, viscous fluid with a density of 1261 kg/m^3 and a viscosity of 1.41 Pa-s at room temperature (20^O C) [Dow, 1997]. The channel is 6.35 mm high by 127 mm wide, giving it an aspect ratio of 20:1. The channel is about 0.5 m long. As shown in Fig. 4-1, the flow is fed by a tank which is filled with glycerin from a large reservoir. This tank provides head pressure which sets up flow when the valve is opened. After a short entrance length, the flow becomes fully-developed in the channel. Also, because of the high aspect ratio, flow is two-dimensional in the center portion of the channel as well. A pump recirculates the glycerin back into the reservoir after it exits the channel. The tank can be filled to any desired height up to the maximum, but the full height

configuration has been used most, as this provides the highest shear stress level and longest run times. This is the condition studied in this chapter.

The solution of a two-dimensional (infinite) channel is a straight-forward manipulation of the laminar Navier-Stokes equations, consisting of a continuity equation, and two momentum component equations. The third component and the energy equation are not needed for this analysis. This solution is commonly called Poiseuille flow after the famous 19TH century French physician [Panton, 1984], and is one of the rare cases in fluid mechanics which offers an analytically exact solution. The velocity profile in the channel is given in eqn. (4-1).

$$u(y) = -\frac{h^2}{2\mu}\frac{dP}{dx}\left[\left(\frac{y}{h}\right)-\left(\frac{y}{h}\right)^2\right] \tag{4-1}$$

By either momentum balance or by taking the derivative of eqn. (4-1) in a Newtonian fluid, the shear stress can be shown to be:

$$\tau_W = -\frac{h}{2}\frac{dP}{dx} \tag{4-2}$$

Oddly, the shear stress in the fluid is constant in the channel, and completely independent of the fluid's viscosity. This formula depends only on the pressure gradient and channel height. Finally, the maximum centerline velocity can be found at a *y*-station of half the channel height (*h/2*), as given in eqn. (4-3).

$$u_{MAX} = -\frac{h^2}{8\mu}\frac{dP}{dx} \tag{4-3}$$

Fig. 4-2 shows a schematic of the gage placement in the channel and the region of the channel actually modeled in the physical model. The schematic is not to scale, as some dimensions (particularly the gap around the head and the channel width) have been exaggerated for clarity. Since the flow is fully-developed, only a section of the channel in the flow direction needs to be modeled. This piece needs only to be long enough upstream and downstream of the gage to account for any 3D effects and disturbances that the floating head might create.

Because of the high aspect ratio of the channel, it was not necessary to solve all the way to the outside wall for the computational models. Thus, the physical model was truncated with a free boundary (discussed in the previous chapter) at some distance from the symmetry plane, but less than the whole channel half-width. This distance is referred to as w_1 to distinguish it from the entire width, w. While w refers to the entire channel (both sides), w_1 is the distance from the

symmetry plane to the boundary of a single side. This boundary placement is justified in the final section of this chapter.

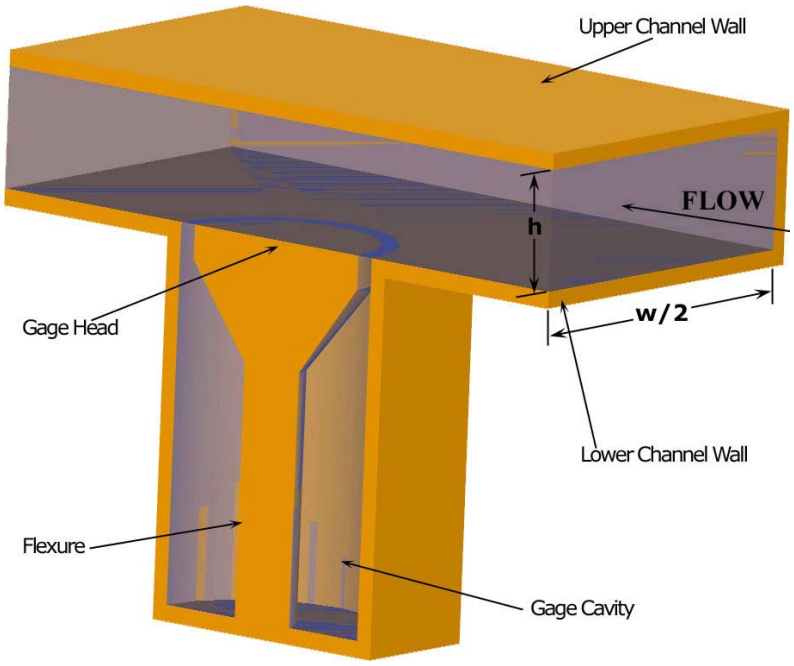

Figure 4-2. Schematic showing Relevant Components and Geometry of the Calibration Rig Physical Model (not scaled)

The pressure conditions come from experiment in the facility. Magill [1999] showed the pressure gradient to be -0.123 psi/in, which converts to -33,350 Pa/m, as measured from a series of pressure sensors mounted in a row along the centerline of the top of the channel. The pressure trace was shown to be linear over the bulk of the channel, and was certainly so around the mounting area of the skin friction gage that is represented in the physical model used here. This pressure gradient physically corresponds to an approximately full tank of glycerin.

As discussed in Chapter 3, all problems have been solved non-dimensionally. For this flow situation, the normalizing values for the non-dimensionalization were selected as follows: for the scaling length, L_∞, the channel height of 0.00635 m was picked, thus setting the dimensionless channel height in the model to 1.0. For the velocity, V_∞, the maximum analytically predicted value of velocity (found at the channel centerline) was used, as calculated from eqn. (4-3) and the known pressure gradient. This value equals 0.119 m/s. Thus, in the computational model, the solution should show a maximum dimensionless centerline velocity of

about 1.0, provided the gage effects do not greatly disturb the flow. Finally, the density, ρ_∞, was selected as the nominal density of glycerin of 1261 kg/m^3. Since the problem is incompressible, this results in a dimensionless fluid density, ρ^*, throughout the domain of 1.0.

Table 4.1 shows the dimensional values selected for all the gage parameters along with all relevant channel dimensions. Adjacent to these are the corresponding non-dimensional values actually used in the code.

Since this model is based on an actual facility, typical values were picked for all relevant parameters based on recent successful skin friction gage designs at Virginia Tech. In particular, the work of Smith [2001] provided general proportions for most of the gage dimensions. This gage design was developed for use in high speed flight vehicles and was tested successfully in multiple supersonic wind tunnel applications, flight vehicle qualifications tests, and, of course, the calibration rig. The known physical dimensions of the channel geometry complete the scaling. Since this gage design represents one of the latest in the field of skin friction measurement, these values were used so as to be practical by making the results of this work actually implementable in real experimental work. The gap size, G, and the lip size, c, in particular were chosen for the actual gages of Smith and for the hypothetical generic gage studied here to be representative of the smallest values that can be confidently manufactured without compromising quality of machining and fabrication.

Table 4-1. Relevant Geometry and Variable Definitions for Channel Flow Baseline Case, Shown Dimensionally and Non-dimensionally

dimensional values			dimensionless values	
h	6.35	mm	h*	1.00
w_1	8.76	mm	w_1*	2.00
L_{UPSTR}	8.76	mm	L^*_{UPSTR}	1.38
L_{DNSTR}	8.76	mm	L^*_{DNSTR}	1.38
D_{HEAD}	7.62	mm	D^*_{HEAD}	1.20
D_{BEAM}	3.175	mm	D^*_{BEAM}	0.50
G	0.127	mm	G*	0.02
c	0.254	mm	c*	0.04
L_{BEAM}	25.4	mm	L^*_{BEAM}	4.00
Z	0	m	Z*	0.00
Λ	30	deg.	Λ	0.53
P_{UPSTR} (gage)	847.1	Pa	P^*_{UPSTR}	47.43
P_{DNSTR} (gage)	0	Pa	P^*_{DNSTR}	0.00
P_{REF}	101,325	Pa	P^*_{REF}	5673.79
μ	1.41	Pa-s	μ*	1.48
ρ	1261	kg/m^3	ρ*	1.00

Fig. 4-3 shows a scaled representation of the geometry so one can appreciate the relative magnitudes of the numbers. This forms the "baseline" case to which all other variations are compared. Additional cases for this channel configuration simply vary one parameter at a time from this configuration to evaluate the effect of that parameter. All other variables remain the same. The geometric variables from Table 4-1 are defined again in Fig. 4-3. Dimensions that are difficult to see due to the scaling can be found in Fig. 1-5. The relative scaling applies to both the dimensional values and non-dimensional ones.

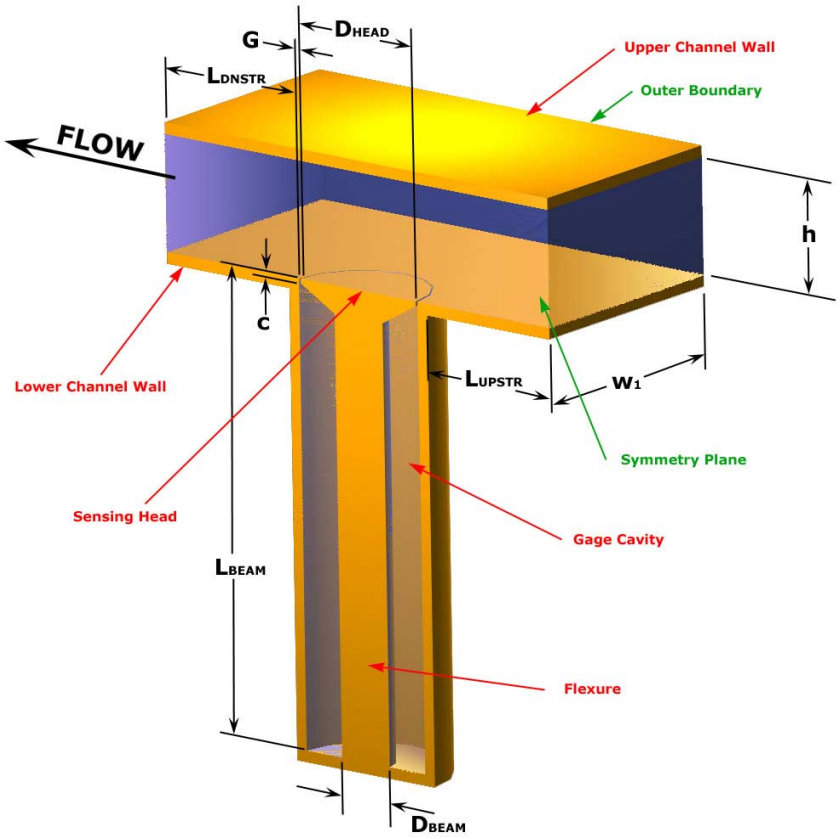

Figure 4-3. Scaled Three Dimensional View of Baseline Physical Model

4.2 The Computational Model

The computational model is an extension of the physical model. The Ansys/FLOTRAN program offers an integrated geometry and mesh generation pre-processor for all of its various modules. The mesh generator is capable of mesh generation in two or three dimensions. Grids can be structured (tetrahedral or hexahedral elements) or unstructured. Hybrid grids can be created by combining structured and unstructured elements in different regions of the same model.

It seemed from early testing in Ansys/FLOTRAN that structured grids tended to produce more accurate results and better convergence properties. Since shear stress calculations are a central result of the analysis, the structure near the walls seemed to provide better estimation of the sensitive shear stress quantity. This is not to infer that unstructured grids are inferior or could not have been used. Turgeon *et al*. [2002] have demonstrated the feasibility of unstructured

grids for applications generally similar to this one in their uncertainty analysis work, and their work is specifically mentioned here because their code formulation is similar to that of Ansys/FLOTRAN. Thus, the structured choice is really as much a choice of perception as a mathematical one.

Table 4-2 lists the cases that were solved along with a description of the variation involved in that case (the values not listed remained the same as in the baseline case). Cases #2 through #5 are gages with misalignment (*Z*) normal to the wall surface, Cases #6 and #7 vary the size of the lip (*c*), and Cases #8 and #9 change the gap size (*G*). For each case, multiple grids were used. Each grid is indexed for each case, starting at "A" for the finest, and increasing toward the coarsest mesh. Table 4-2 lists the total number of elements for each grid as an indication of the grid density. Uniform refinement was applied from the coarse grid to generate finer grids in each case. The various cases were compared to the baseline case #1 to evaluate any differences and assess the importance of that particular variable. Results of these cases are presented in the next two sections.

Table 4-2. Relevant Variations and Case Nomenclature for Three-Dimensional Channel Models

Case #	Modified Variable	Value	Grid A (finest)	Grid B	Grid C	Grid D (coarsest)
1	baseline	-	99,680	72,612	40,572	12,460
2	Z*	+0.012	73,710	21,800		
3	Z*	+0.006	68,040	15,700		
4	Z*	-0.006	71,820	21,240		
5	Z*	-0.012	72,660	21,100		
6	c*	0	68,580	20,280		
7	c*	0.08	76,680	22,680		
8	G*	0.01	54,480	15,580		
9	G*	0.04	59,130	17,360		

The choice of variation levels in all the cases was somewhat arbitrary, with the overall goal being to cover a conceivable range of practical implementation and possible usefulness to a

designer. The misalignment cases were chosen to represent a span of +/-1% of the head diameter, which was considered to represent a worst possible installation of the gage. This range mirrored the range covered by Allen [1976] (his was about +/-1% of his gage's head diameter as well) and exceeds by about three times the range studied by O'Donnell [1964]. The lip size was simply an extension of the baseline case value. A doubling of that lip size was a reasonable upper bound, and the Case #6 with 0.0 lip size was studied as a limiting case. Similarly, the gap size was halved for Case #8 and doubled for Case #9 in relation to the baseline case #1.

Fig. 4-4 shows the computational model of the finest grid density for the baseline case. The viewpoint is similar to that of Fig. 4-3. Again, the mesh is fully structured, utilizing entirely six-sided, eight-noded bricks like the one shown in Fig. 3-1 except at the center of the head, where five-sided wedges are used (which are just bricks with the surface area of one face set to zero). As Fig. 4-4 shows, elements are highly concentrated along the channel walls, along the head, and in the gaps. This is as it should be, since the quantities of interest are calculated in these regions and a high mesh density increases accuracy. The element fineness in the gaps extends upward through the channel over the head because the mesh is structured.

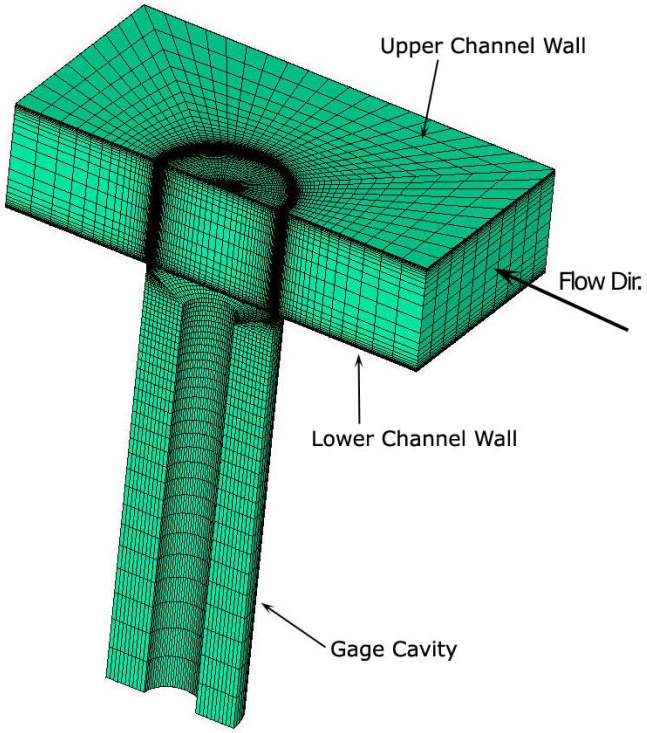

Figure 4-4. Structured Mesh of Computational Model of Baseline Case at Finest Grid Level

Fig. 4-5 shows a close-up view of the elements along the symmetry line in the area of the upstream gap (the downstream gap looks the same) for the finest mesh, Fig. 4-5 (a), as pictured by Fig. 4-4, as well as the coarsest mesh, Fig. 4-5(b). The refinement ratio between grids A and D is exactly 2 for this case. Thus, there are twice as many elements in each direction for grid A as for grid D. Since the refinement is uniform, relative scaling of the elements and element aspect ratios remains the same.

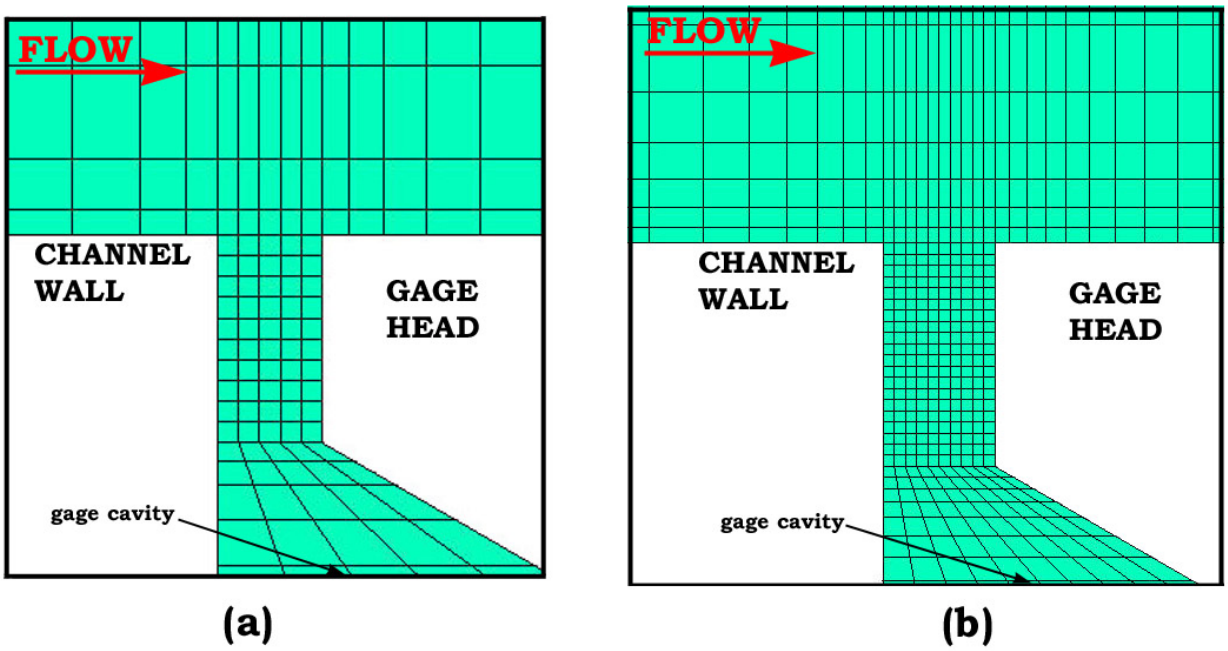

Figure 4-5. Mesh in Upstream Gap Vicinity for Baseline Case at (a) Coarsest and (b) Finest Grid Levels

Mesh structures for the remaining eight cases are virtually identical. In fact, care was taken to make the grids as consistent as possible from case to case to lend credibility to the comparisons made in the next sections. Of course, varying features required some small changes between cases. For example, Fig. 4-6 shows a view similar to that of Fig. 4-5 of the mesh in the sensitive gap area. Pictured in Fig. 4-6 (a) and (b) are the finest meshes for the misalignment Cases #2 and #5 respectively. The misalignment required that the mesh be modified slightly, but the basic style and size density is consistent.

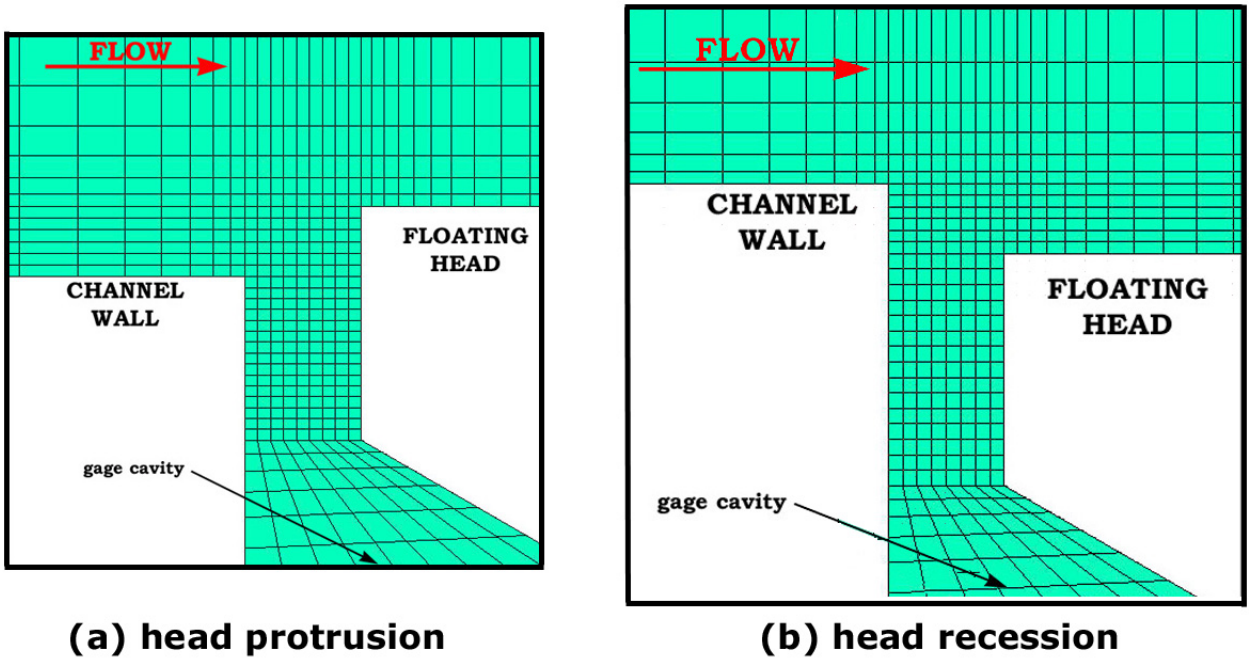

Figure 4-6. Mesh in Upstream Gap Vicinity of Finest Grid for (a) Case 2 and (b) Case 5

Boundary conditions were straightforward for this problem. The no-slip condition was applied to the entire upper channel wall, the lower channel wall, the floating gage head, the flexure body, and the internal cavity walls. This means that all three components of velocity (VX, VY, VZ) were set to zero at every node on these surfaces. The nodes at the inlet were given a dimensionless pressure condition (PRES) of 47.43 uniformly. The nodes on the outlet received a pressure condition of 0.0. Following the discussion of Chapter 3, this infers that the velocity derivative in the flow direction is zero, creating a fully-developed flow profile. The pressure gradient solution is linear throughout the domain, excepting in regions very close to the head where the flow may possibly be disrupted.

The symmetry plane was also discussed in Chapter 3, and the VZ component of velocity was set to zero on all nodes on the symmetry plane, which is consistent with the flow coordinate system. This leaves the VX and VY components set to free by default. Finally, the outer boundary was left as free in all velocity components, since the flow was not actually solved to the channel side wall. This numerically allows the three components themselves to be non-zero at this plane, but the actual solutions show the VZ component to be approximately zero for all cases. This physically means that the flow has not been disturbed by the effects of the gage at that distance.

4.3 Flowfield Results

4.3.1 Velocity Field Results

Analysis and results of this problem begins with a look at the nature of the overall flow for various model cases. Understanding the properties of the flow as a whole brings physical understanding to the numerical force results on the gage to be presented and discussed later. Thus, the results presented in this section will help to illustrate the sources of the force components on the various parts of the gage, i.e. the relative importance of shear stress, pressure, the flow through the gaps, etc. Since all cases studied have many similarities, the majority of the effort will be spent on the baseline case. Some interesting differences between it and the various other cases will be illustrated as necessary.

For the flow of glycerin in the basic channel configuration (making no special allowance for the gage effects), the Reynolds number based on hydraulic diameter and average velocity is 0.86. Since the Reynolds number is so low, one would expect the various cases to display properties typical of a low Reynolds number flow – i.e. flow remaining attached to surfaces and showing little separation, small steady flow rates, no turbulence, viscosity dominated flow field, etc. This is indeed the case as will be shown here.

Figure 4-7 shows the predicted flow pattern from a control case which is simply the two-dimensional channel problem only with no gage. This test case was an important benchmark of the performance of the code, and it helps to illustrate the correct formulation of the physical problem. Figure 4-7 (a) shows the contour plot of the non-dimensional x-direction velocity component, u^*, a quantity which is normalized by the maximum centerline velocity (see Table 3-1). Confidence in the code was built since the figure indicates that the velocity has a maximum of 1.001, indicating that the Ansys/FLOTRAN solution is virtually identical to the analytical solution that was used as a normalizing factor. Figure 4-7 (b) shows the velocity vector profile. The vector magnitudes (lengths) reflect the contours from Fig. 4-7 (a), since the y-direction component, v^*, is approximately zero. The vectors show the correct parabolic profile for this flow field. Also, Ansys/FLOTRAN predicted a constant value of 105.6 Pa for shear stress when the result was dimensionalized again. This value too agrees well with the 105.8 Pa predicted by eqn. (4-2) and the data of Table 4-1.

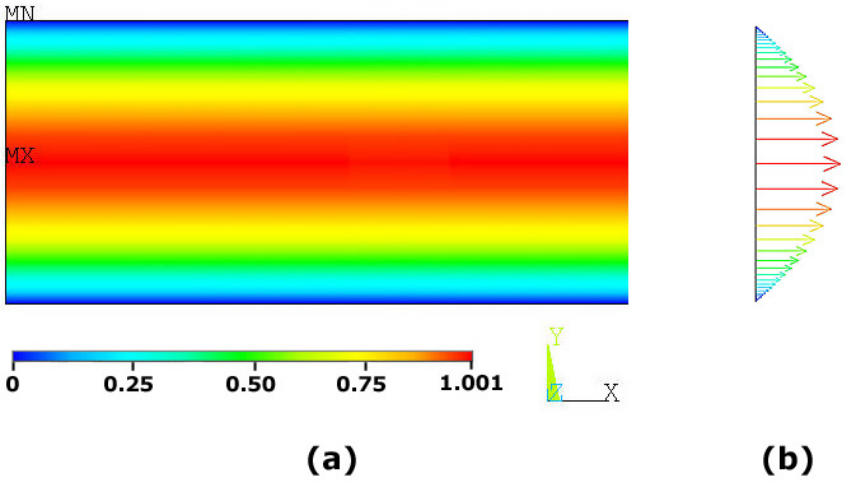

Figure 4-7. Non-dimensional X-direction Contours (a) and Velocity Vector Profile (b) of Channel Control Case

Since shear stress is the single most important quantity in the study, it is prudent to look at the important influences on that quantity. For a Newtonian fluid in laminar flow, the shear stress is directly calculated from the normal derivative of the tangential velocity at the wall. Thus, any disruption in the velocity, u^*, of the channel will result in a change in shear stress. In fact, even small changes in the values of u^* next to the wall can produce large changes in its derivative.

Figure 4-8 considers the results of the baseline Case #1 with the nominal skin friction gage mounted in the channel wall. This figure shows the velocity profile in the channel directly above the upstream gap of this case. The analytically predicted profile with no gage given by eqn. (4-1) is shown as well as the numerical result for the baseline case with the gage. It is clear that the two results match well over the whole channel height. From the formulation of the finite element method, the numerical solution at the nodes predicts the analytical solution from eqn. (4-1) almost exactly. The linear shape functions of the Ansys/FLOTRAN elements are apparent near the centerline where there is some discrepancy in between the nodes and the mesh is coarse. This small interpolation error does not affect any of the conclusions drawn here. Since the gap is present at the lower surface of the numerical solution, however, the no-slip condition is not enforced at the point, and the profile distorts accordingly. The close-up view of the 2% of the channel height against this lower surface shows the distortion in the x-component of the velocity.

This variation appears only very close to the surface, and is quickly damped out farther up into the channel. The derivative of tangential velocity over the gap is obviously altered in this region.

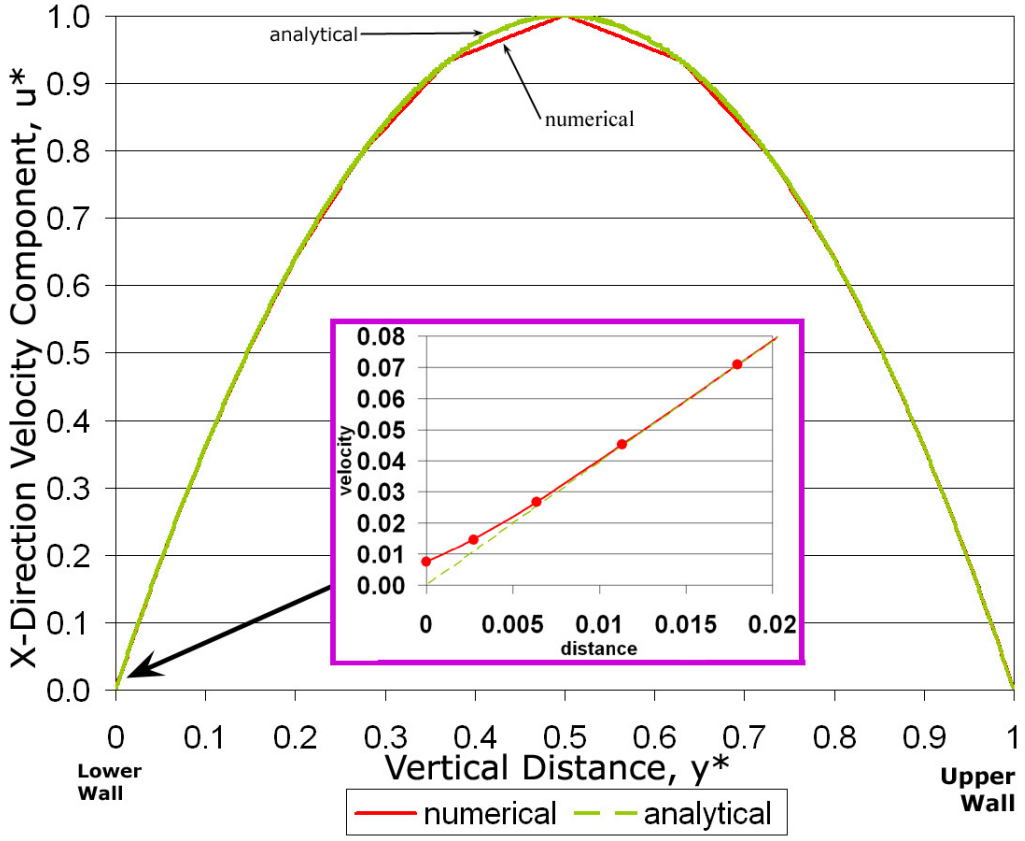

Figure 4-8. Channel Velocity Profile Stationed at Midpoint of Upstream Gap along Gage Symmetry Plane for Baseline Case #1

Figure 4-9 shows several of these close-up profiles at successive *x*-stations, starting with the one shown in Fig. 4-8. This is labeled as "x_1" in Fig. 4-9 and indicated in the position location drawing in the top corner of this figure. Three other near-wall profiles are shown as well, each successively downstream of x_1 as indicated in the top left corner. From the last profile (x_4), it is apparent that after only a relatively short distance – less than one gap width downstream of the gap – the profile has returned to almost normal. Thus, it should be expected that the presence of the gaps of this size has only a minimal effect on the total shear force on the head, at least in terms of the disruption to the *x*-direction velocity component, u^*.

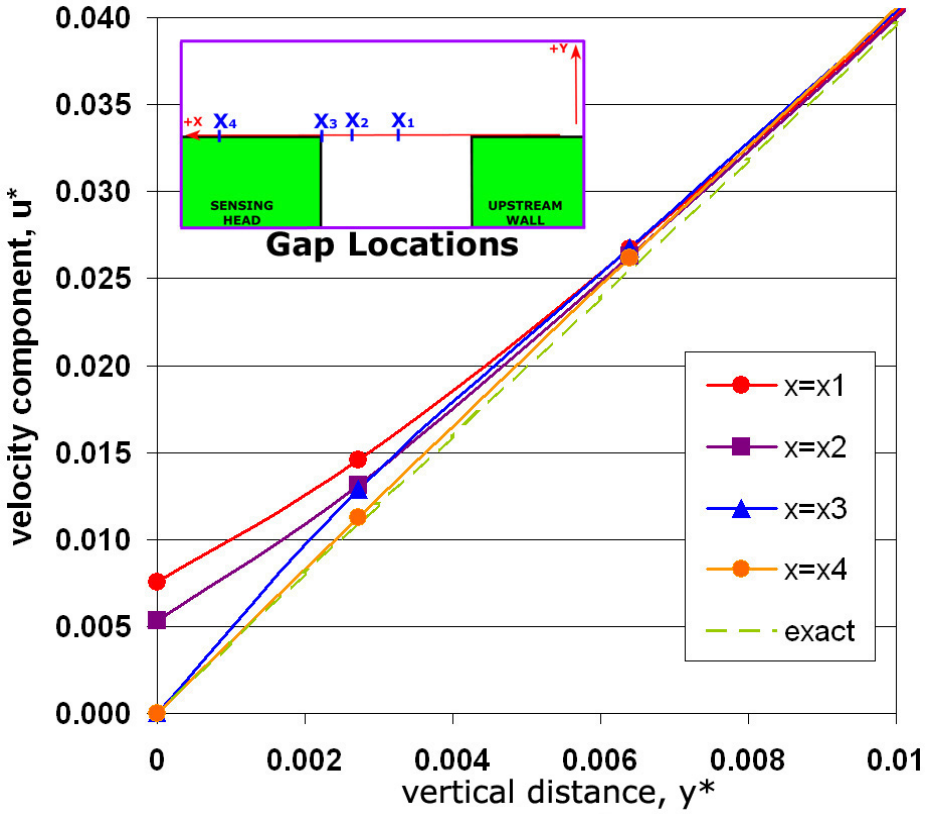

Figure 4-9. Channel Velocity Profiles at Given X-stations along Gage Symmetry Plane for Baseline Case #1

Figure 4-10 shows some views of velocity vectors at various stations along the channel symmetry plane for the baseline Case #1. Shown at the upper right for reference is a vector profile across the channel at the center of the head of the gage. This profile displays the classic parabolic velocity profile already seen in the previous several figures and predicted by eqn. (4-1). Even surrounded by a gap ring, this region is sufficiently far away from any disturbance in the flow, so that the profile mimics that found in the previous Fig. 4-7. The centerline velocity is labeled, and has a magnitude of approximately 1.0, just like in Fig. 4-7. The remaining four regions represent areas of interest around the upstream and downstream gaps.

Although the scale is different in each view in order to most clearly display the results in that view, a separate reference vector is provided for each individual view and is indicated in the wall region of each. In each view, this vector represents 1% of the maximum centerline velocity in the channel. As the various views indicate, the order of magnitude of the vectors moving into and out of the gage cavity by flowing through the gaps and around the head is much less than

1%. This is, of course, why the experimental efforts to measure this phenomenon resulted in such little success. Measuring a velocity that is less than 1 mm/s in a region which is only 100 μm wide is a difficult challenge experimentally, thus enforcing the argument made here about the advantages of using CFD for this application.

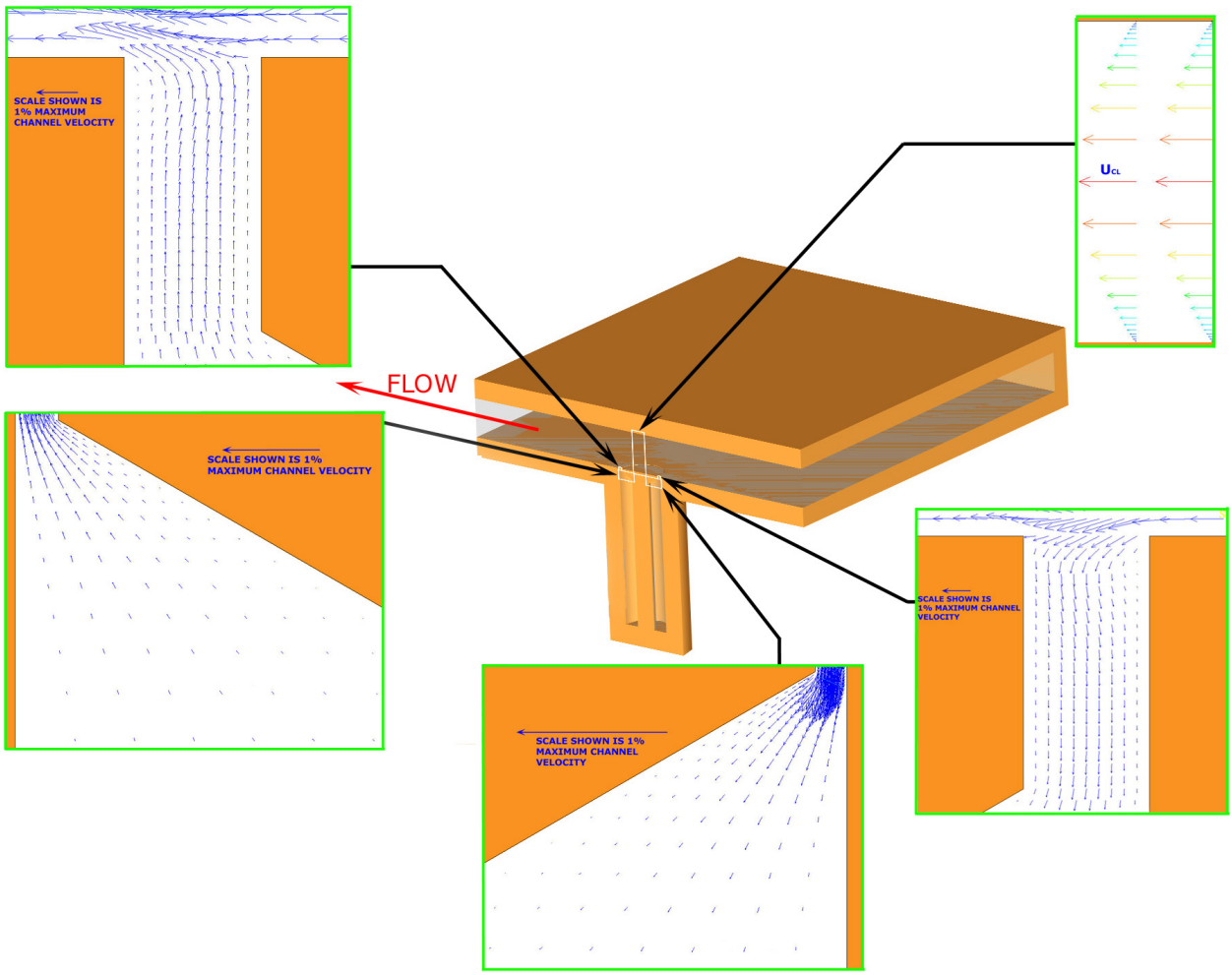

Figure 4-10. Velocity Vectors of Baseline Case #1 as Seen from Symmetry Plane, Flow Moving from Right to Left

In general, Fig. 4-10 shows what would be expected in a flow with a significant pressure gradient. The vectors indicate that the flow enters the upstream gap, moves through the cavity, and exits the downstream gap, always moving toward lower pressure region. The flow is smooth due to the low Reynolds number, allowing the fluid to make sharp turns without separation or re-circulation appearing in the flow-field.

Figure 4-11 shows contours of the *y*-direction velocity, v^*, for the baseline Case #1 along the gage symmetry plane. This plot is useful, because it gives an impression of the domain of influence over which the presence of the gaps extends. This region is obviously very small, and it exhibits a maximum normal velocity magnitude of less than 0.5% of the centerline velocity, corresponding to what was seen in Fig. 4-10. The encouraging result of this figure is that the flow over the surface of the head seems almost completely unaffected by the presence of the small gaps surrounding it. This should result in a minimal disturbance in the shear stress as well.

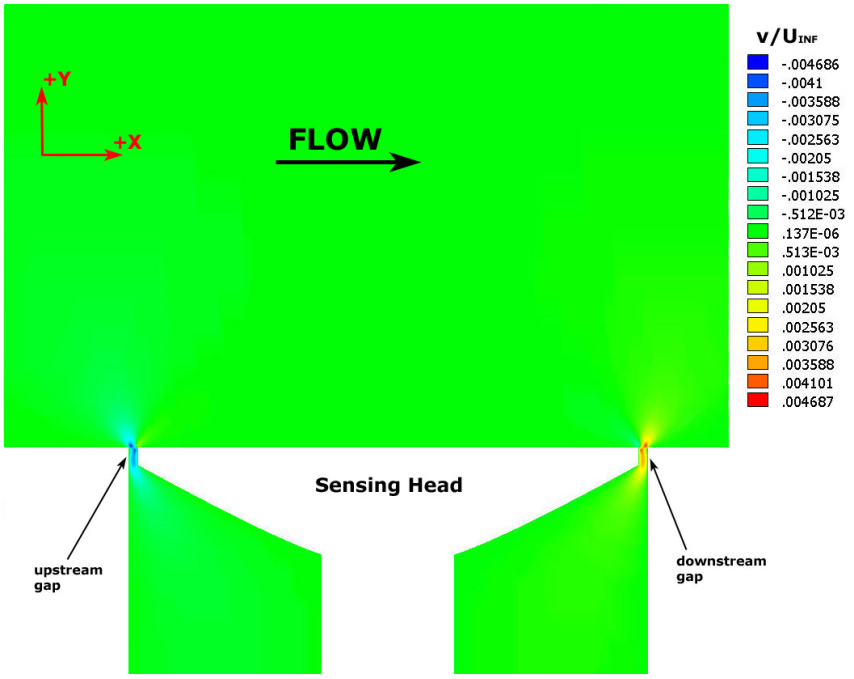

Figure 4-11. Non-dimensional Y-direction Velocity Contours Along Symmetry Plane for Baseline Case #1

Figures 4-12 and 4-13 show the same type of image for Cases #2 and #5, respectively. With either positive or negative misalignment of the floating head, the *y*-direction velocity disturbance becomes much more prominent. In contrast with the effect in Fig. 4-11, a disturbance reaches over the entire height of the channel, and it has a much wider upstream and downstream influence zone around each gap. For Fig. 4-12, the maximum magnitude is about 1.4%, and it is 1.5% for Fig. 4-13. Thus, not only is the influence zone of the disturbance much greater, but the magnitude of that disturbance is over three times greater than in the baseline case. This is certainly not a desirable feature of the flow.

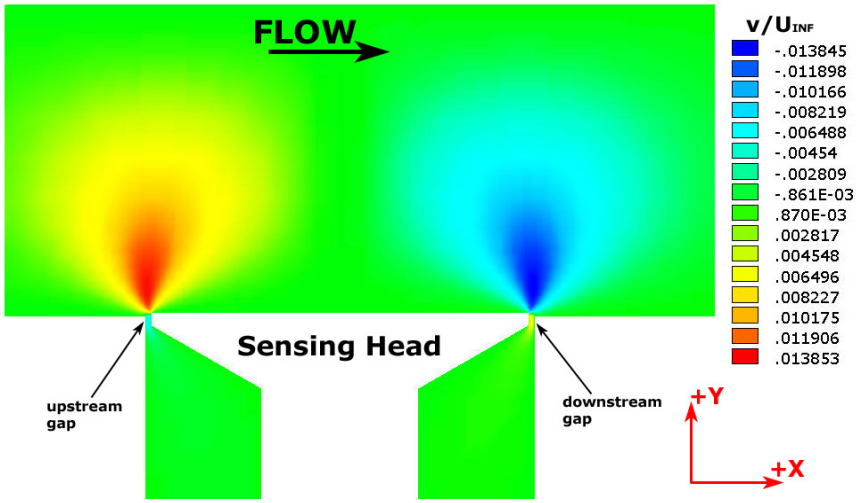

Figure 4-12. Non-dimensional Y-direction Velocity Contours along Channel Symmetry Plane for Protrusion Case #2 ($Z^* = +0.012$)

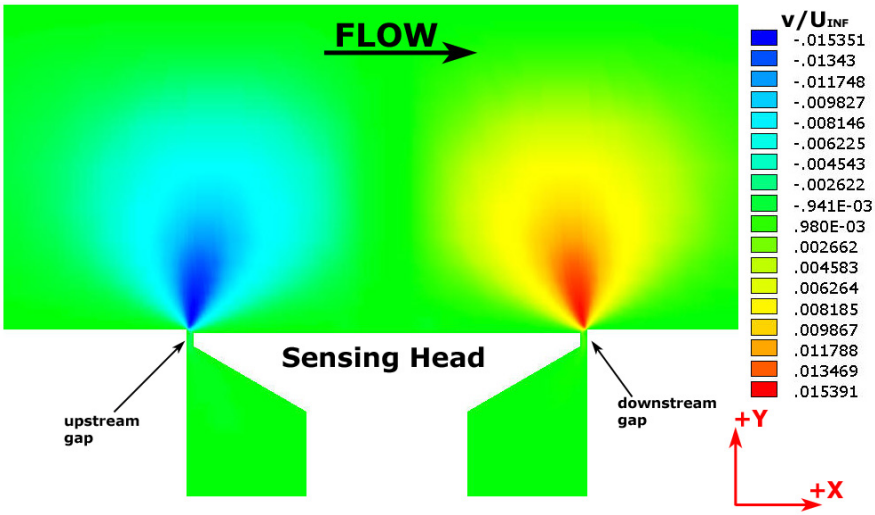

Figure 4-13. Non-dimensional Y-direction Velocity Contours along Channel Symmetry Plane for Recession Case #5 ($Z^* = -0.012$)

Since the models of Cases #2 and #5 contain both a gap and a misaligned sensing head, it is difficult to access whether the effects noted are caused by only one source or a combination of both. To address this question more completely, a set of two-dimensional models was created. These models illustrate the flow effects of an infinitely wide sensor with a gap at the Case #2 and Case #5 configurations compared to identical models without the gap (just a step in the wall).

Figure 4-14 (a) shows the 2D version of Case #2, and Fig. 4-14 (b) shows the corresponding identical step with no gap in the wall. Both images show the same behavior as that in Fig. 4-12. The small effects of the gaps themselves can be seen between the sensing head and the wall which is not present in Fig. 4-14 (b), while the effect of the misalignment accounts for the bulk of the disturbance and appears identically in both pictures. Looking closely, it is interesting to note in this case that the flow through the gap in the *y*-direction is opposite the bulk flow caused by misalignment. The flow above the surface at the gap upstream of the head in Fig. 4-14 shows positive v^* motion as it approaches the head and negative v^* values moving through the gap itself. The opposite occurs around the gap downstream. The same reasoning applies in Fig. 4-15 (a) for the 2D version of Case #5 and in Fig. 4-15 (b) for the corresponding step without a gap. The only exception is that the flow moves universally upward or downward in the gap regions for the recessed head cases.

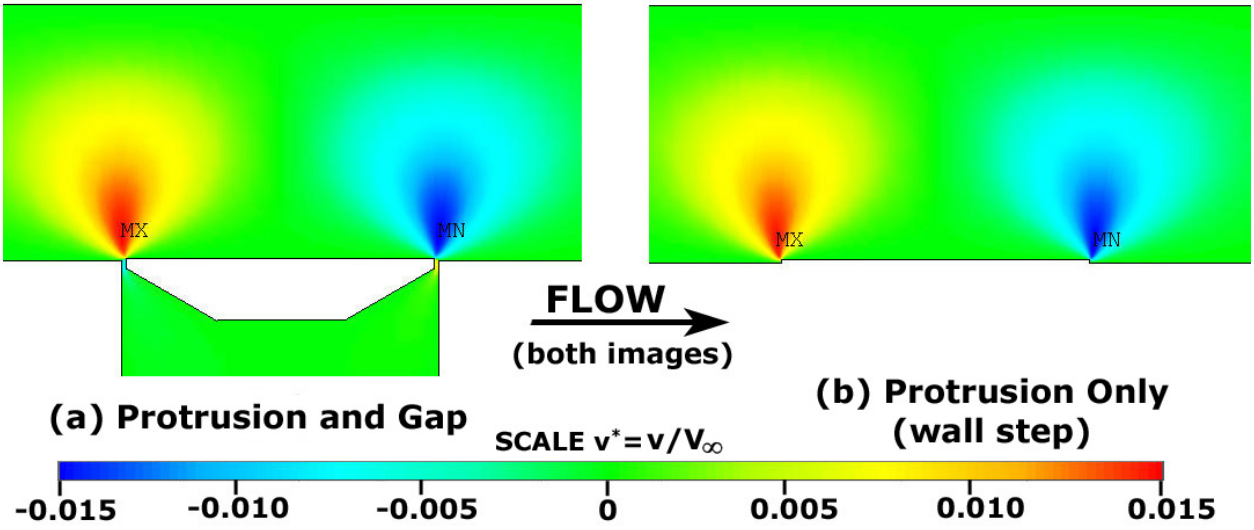

Figure 4-14. Y-direction Velocity Contours for 2D Representation of Z* = +0.012 Protrusion Case #2 with and Without Gap

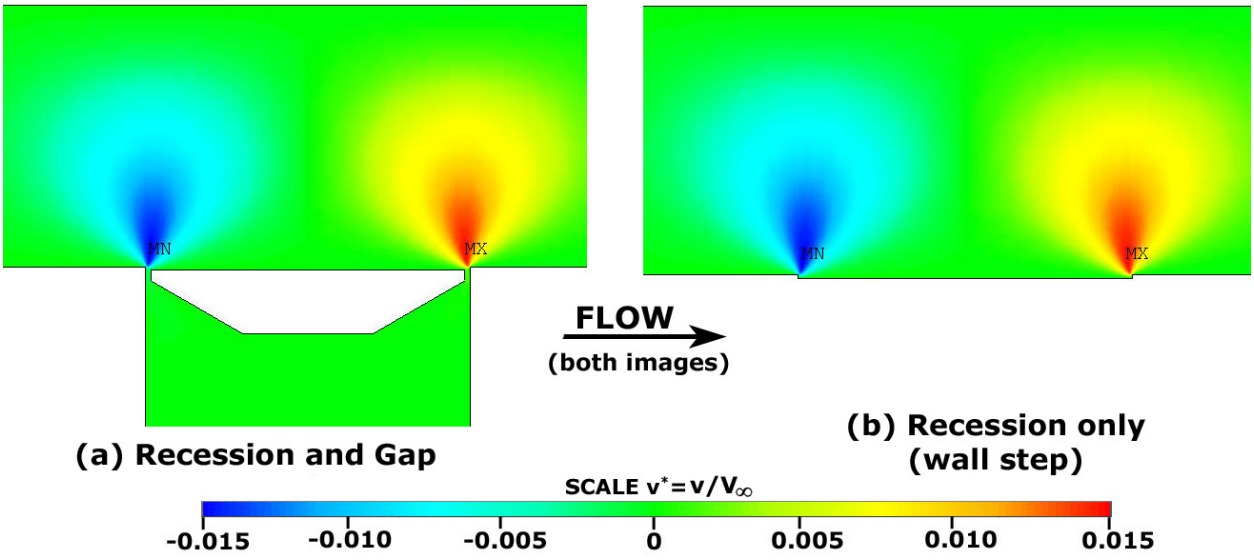

Figure 4-15. Y-direction Velocity Contours for 2D Representation of Z* = -0.012 Recession Case #5 with and Without Gap

4.3.2 Stress Field Results

The conclusion of the documentation of the velocity flow patterns is essential for understanding the results in the next section. All nine cases have a great deal of similarities, but with some subtle differences which result in the force variations shown in Section 4.4. The reasons for those variations will be illuminated by looking back at those results. Before presenting the global force parameter results, it is useful to look at a few features of the pressure and shear stress fields. As discussed in Chapter 2, Everett [1958] investigated the effects of a pressure gradient in a channel similar to that of these cases. His major finding was that the assumption that the pressure gradient varies linearly through the gap does not hold well, and gets progressively worse with small lip size, *c*. Acharya, *et al*. [1984] found good agreement with the linear pressure variation assumption for their sensor with a lip to gap ratio that was over one order of magnitude larger than Everett's.

In order to address this issue, Fig. 4-16 presents pressure traces along the lip surface of the head at various angles around the head with respect to the flow. The direction of the trace is also shown in the figure, and *S* also lies in the same direction as the negative *y*-direction. The various θ values are angles in the *x*-*z* plane as indicated. It is quickly apparent that the pressure

traces are not linear at all, supporting Everett's conclusions. After further examination, an interesting point to make is that the region near the center of the graph does show relatively linear characteristics. This is true between *S* values of about 0.15 to 0.3 or so, and can be seen to roughly be similar to fully developed pipe flow sufficiently far away from the entrance and exit of the pipe. It is likely that Acharya et al., with their very long (deep) gap, saw this effect over a much larger percentage of the surface, and thus saw much better agreement with the linear pressure variation assumption.

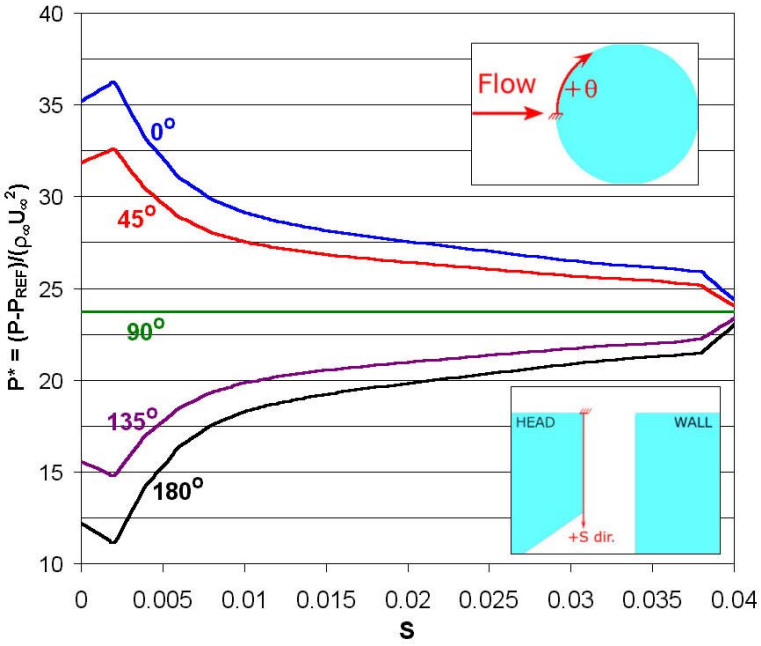

Figure 4-16. Pressure Traces along Head Surface for Baseline Case #1 at Various Angles with Respect to the Incoming Flow

This conclusion is supported by Fig. 4-17, which shows the same kind of pressure traces for Case #7, the case with double the baseline lip size. In this figure, a much higher percentage of the curves remain linear (about 75% or so). It could certainly be extrapolated that as the gap increases, so would this percentage, approaching 100% for a very deep gap, i.e. large lip size, *c*.

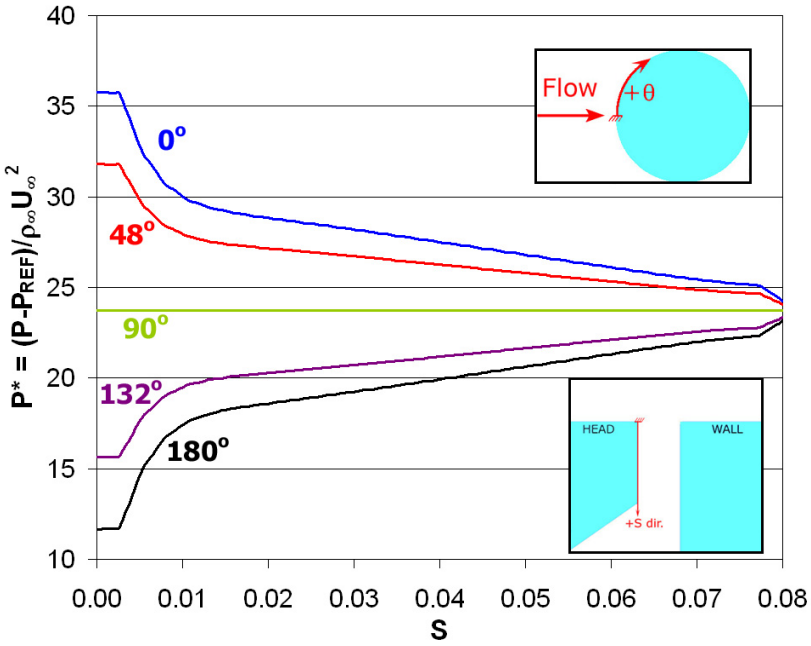

Figure 4-17. Pressure Traces along Head Surface for Case #7 with Double Lip Size (Deepest Gap) at Various Angles with Respect to the Incoming Flow

The discussion of Fig. 4-9 in the previous section indirectly discussed the issue of shear stress in looking at the disruption of the velocity profile in the vicinity of the gap for the baseline Case #1. The outcome was that the velocity profile is restored almost immediately after passing onto the head area again from the gap. Thus, one would expect almost no disruption in shear stress as a result. Fig. 4-18 shows the shear stress distribution over the head and surrounding channel wall. The target analytical value of shear stress is 5.93 as a dimensionless number. The dimensionless shear stress, incidentally, happens to be equal to ½ the skin friction coefficient, C_f, based on centerline velocity. Fig. 4-18 agrees well with this value, showing the same numeric result. Further, the shear stress distribution is constant over the whole head and surrounding wall area. The gaps make no visible impact except in a very narrow ribbon adjacent to the gaps. This region acts over an insignificant percentage of the surface area, and so it should not affect the total shear force appreciably. The shear stress distribution plot from Case #9 (the double gap model) is not shown here as it looks visually identical to Fig. 4-18. Although the gap is twice as large, it visually makes no more impact on the shear plot. Any numerical differences in the various gap variation models are not noticeable on the shear plots.

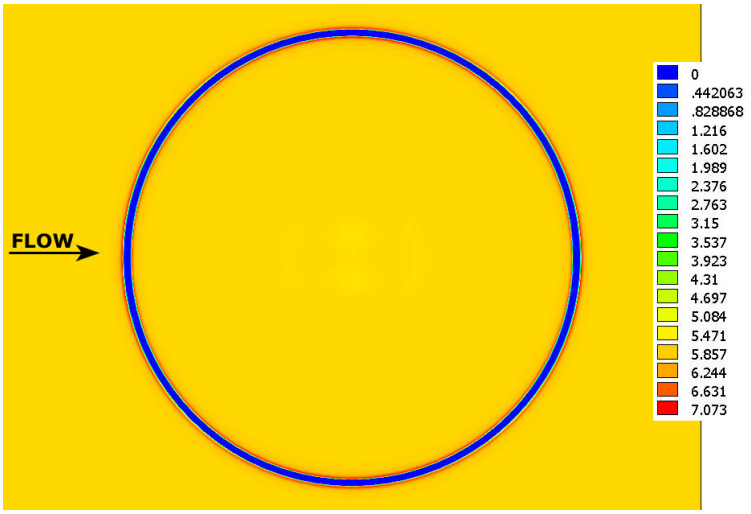

Figure 4-18. Dimensionless Shear Stress Distribution over the Exposed Head Surface and Surrounding Wall Area for Baseline Case #1

The shear stress changes caused by misaligning the gage do make a visual impact to some extent. Figure 4-19 shows the shear stress distribution over the head of the gage for Case #2 with misalignment Z^* of 0.012. The surrounding wall is not shown since it is not in the plane of the head surface for this case. The distribution is constant over the surface, which is an excellent sign, but the values are somewhat inflated, leading to an excessive contribution from shear stress. The Case #5 distribution (misalignment with Z^* of -0.012) is shown in Fig. 4-20, without the wall for the same reason. Here, the values are too low. Also, the values are varied significantly over the surface, as the leading and trailing sections of the head surface are sheltered by the presence of the wall. Of course, this will lead to a corresponding decrease in the total skin friction force compared to the expected value.

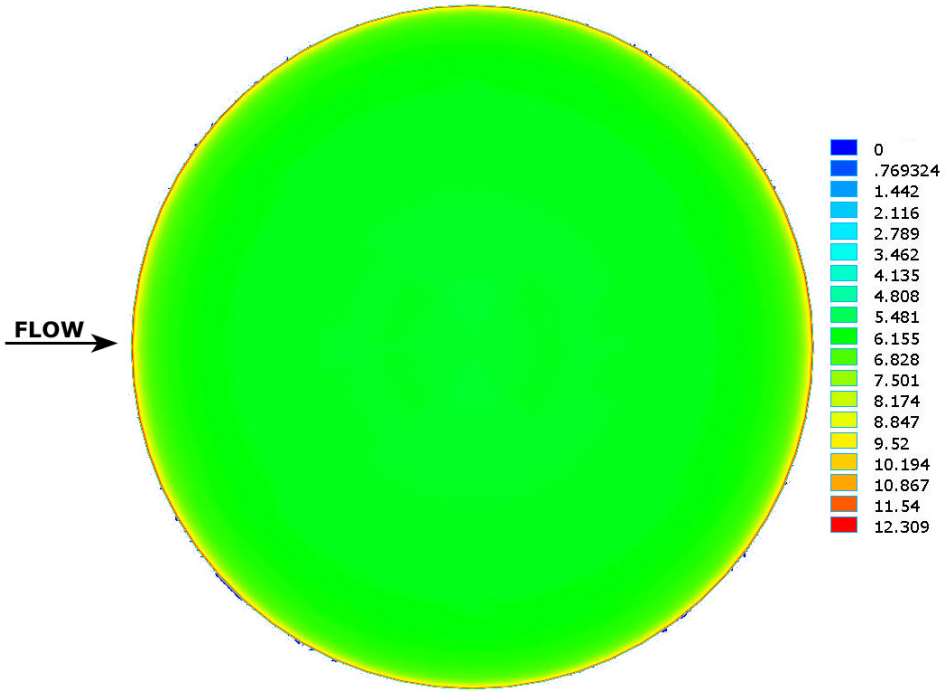

Figure 4-19. Dimensionless Shear Stress Distribution over the Exposed Head Surface for Protrusion Case #2 (Z^* = +0.012)

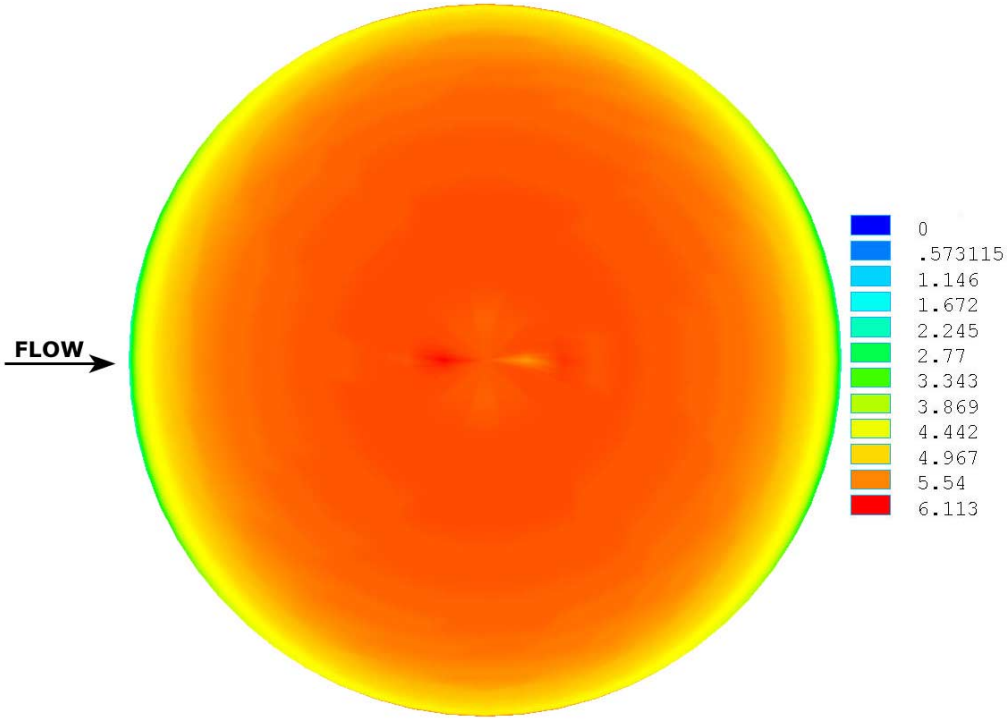

Figure 4-20. Dimensionless Shear Stress Distribution over the Exposed Head Surface for Recession Case #5 (Z^* = -0.012)

4.4 Force and Moment Results

Since the overall goal of this study is to see how much the total force on the sensing flexure deviates from the expected or desired value, the force results from each case are central. These forces are a result of a combination of a field of shear stress and a field of pressure acting over the exposed surface of the gage flexure. The nodal pressure and shear stress quantities are part of the finite element solution. Ansys/FLOTRAN offers a convenient function to integrate these stress fields over a specified surface, which calculates the total vector force and vector moment on that surface expressed in Cartesian components. Appendix E details the integration process, specifically applied to the non-dimensional form that was employed to solve the problems.

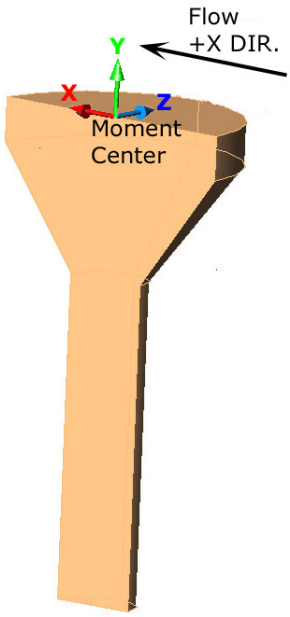

Figure 4-21. Floating Head Coordinate System with Moment Center Location

Since the entire computational model was developed in a dimensionless form to provide generality, the force component results are provided similarly. With the problem symmetry, the sideforce component in the *z*-direction cancels out, as do the corresponding *x*-direction and *y*-direction moment components. The remaining components on the gage are the *x*-direction force in the flow direction, the *y*-direction force pointing upward away from the head, and the *z*-direction moment. The coordinate system is consistent with that defined in previous sections and is shown in Fig. 4-21, which illustrates an image of the head alone with the coordinate origin applied at the head center. These components can be transformed from the form in the appendices to that presented in eqns. (4-4) through (4-6).

Each respective force is normalized by the desired (in this case analytical) value of shear stress times the head area. The moment is normalized by the same force multiplied by the head diameter, D_{HEAD}. Thus, a value of F^*_X of 1.0 is the desired value. Likewise, the values of F^*_Y and M^*_Z should ideally be zero, since the ideal shear force would pass through the coordinate origin. In the case of an F^*_X of 1.0 and an M^*_Z of 0.0, the gage would read exactly the correct value. In addition to the totals, it is also useful to look at the contribution to each of these components from shear

stress and pressure individually. This is useful to understand the causes of any inaccuracies in the reading.

$$F_X^* = \frac{F_{X,TOTAL}}{\tau_W^{EXACT} A_{HEAD}} \tag{4-4}$$

$$F_Y^* = \frac{F_{Y,TOTAL}}{\tau_W^{EXACT} A_{HEAD}} \tag{4-5}$$

$$M_Z^* = \frac{M_{Z,TOTAL}}{\tau_W^{EXACT} A_{HEAD} D_{HEAD}} \tag{4-6}$$

Although there are many possible arrangements for a flexure connected to the floating head, a cantilevered beam is a common choice. There are also numerous schemes for measuring the displacement or strain of the flexure resulting from the applied force, but the most common method is probably the use of strain gages like that shown in Fig. 1-3. It is straightforward to transform the dimensionless force parameters into an equivalent error in strain. From Budynas [1977], the summation of an end force and an end moment applied to a cantilever beam causes a total moment at the end of the beam as given in eqn. (4-7).

$$M = F_X L_{BEAM} - M_Z \tag{4-7}$$

Similarly, the desired moment is equal to the shear stress on the exposed head surface times the exposed head area times the beam length, so that a ratio of the actual total moment to the exact moment is given in eqn. (4-8).

$$\frac{M}{M_{EXACT}} = \frac{F_X L_{BEAM} - M_Z}{\tau_W A_{HEAD} L_{BEAM}} \tag{4-8}$$

Taking the ratio of the two provides an estimate of the ratio of strain as well, since the strain near the end of the beam is hypothesized to be proportional to the moment in that region. Taking advantage of the dimensionless forms in eqns. (4-4) to (4-6) produces the resulting strain ratio in (4-9). By turning this strain ratio into a percent error in strain, one obtains:

$$\frac{M}{M_{EXACT}} = \frac{\varepsilon}{\varepsilon_{EXACT}} = F_X^* - \frac{D_{HEAD}^*}{L_{BEAM}^*} M_Z^* \tag{4-9}$$

$$\%\varepsilon_{DIFF} = F_X^* - \frac{D_{HEAD}^*}{L_{BEAM}^*} M_Z^* - 1 \tag{4-10}$$

The strain expression does not contain any direct reference to the normal force, F^*_Y. This force comes almost entirely from pressure, and that is the normal force term accounted for by

Allen in eqn. (2-2). The only contribution of this force is through the moment if the normal force does not act through the center of the head because of a pressure gradient. Thus, M^*_Z is really inherently a function of the combination of the net F^*_Y and its line of action on the gage. The force itself applies compressive axial strain on the flexure, which should not be felt by a symmetric strain gage bridge; other measurement systems may need to account for the effect of this force depending on their particular functionality.

Although F^*_Y will be calculated and given for all cases in this document, it is necessary to understand at the front that this value only has limited meaning. The parameters F^*_X and M^*_Z are functions of the pressure gradient (or general pressure imbalances) only. For these terms, only the difference between two pressures matters. And for incompressible flow, the same is true – only the gradient of pressure appears in the equations, so pressure variations are always relative to some reference point. This is not true of the *y*-direction force. For these channel problems, dimensionless relative pressures of 47.43 and 0.0 were used as end conditions for the computational domain. Since Ansys/FLOTRAN uses relative pressures, this means that there is some reference value above absolute pressure. This value impacts the reading of F^*_Y as well. Using pressure conditions of 147.43 and 100.0 on the channel, for example, would produce the exact same flow pattern, the exact same values of F^*_X and M^*_Z, but would make a significant difference for F^*_Y. Defined as such and detailed in Appendix E, Ansys/FLOTRAN only gives the force results relative to the offset value. Thus, the actual value of dimensionless pressure on the head for the baseline case would be about 23.71 plus whatever reference pressure may exist. Since the reference pressure will cancel out over the head surface except directly above the flexure column, the actual value of F^*_Y can be shown to be of the form given by eqn. (4-11).

$$F^*_{Y,ABS} = \frac{\left(D^*_{BEAM}\right)^2}{\tau^*_W \left(D^*_{HEAD}\right)^2} P^*_{AVG}\left(1 + \frac{P^*_{REF}}{P^*_{AVG}}\right) \tag{4-11}$$

Thus, if reference pressure is zero, Ansys/FLOTRAN shows the correct value as it tabulates the term outside of the parenthesis in eqn. (4-11). But whatever P^*_{REF} may be, it has no impact on the physical flow characteristics, and thus is completely arbitrary in all respects except this one. Therefore, F^*_Y is of limited use except perhaps to compare cases in a restricted sense.

From the force terms of eqns. (4-4) through (4-6), in the terms of Fig. 2-4, the friction force term is the same as the contribution to F^*_X by the shear stress only. Again, the force due to shear stress on the head is the desired output. Shear stress acts on all parts of the head and the

flexure, but visual results from the models indicate that the shear contributions are negligible on parts other than the head surface. The normal force term comes from F^*_Y, and is due almost entirely to pressure only (shear contributes 1/100,000 of the pressure contribution as a typical estimate). The lip force is created by the contribution to F^*_X from pressure. The moment M^*_Z is due to the asymmetrical line of action of the normal force due to pressure and some small addition from the lip force. The two conventions can be seen to interrelate in this manner, and it is possible to calculate one from the other.

The presentation of the total force results for the sensing flexure begins with examination of the results of the misalignment variations. Fig. 4-22 shows the effects of varying misalignment values, Z, ranging from +1% to -1% of the head diameter or dimensionless Z^* from +0.012 to -0.012. Tables 4.1 and 4.2 give all the necessary geometry details. Fig. 4-22 (a) shows the x-direction force F^*_X, while Fig. 4-22 (b) shows the z-rotation moment, M^*_Z. Again, both of these components will contribute to equivalent displacement, stress, and strain in bending on the flexure. For the case of the cantilevered beam as used here, eqn. (4-10) gives this relationship for strain. Other structures may have slightly different relationships. The individual contributions from the shear stress field and the pressure field are shown for comparison, along with the total force and moment from both components together.

The effects of misalignment are apparent when considering that the ideal situation is for the F^*_X of the shear stress component to be identically 1.0, with no other contributions on the flexure. This component is not exactly zero at perfect alignment, but close, being too high by only a little under 2 percent. The difference is a small effect from the presence of the gap as discussed in the previous section, and also because the analytical solution that was used to normalize is not exactly identical to the numerical solution from the code. Additionally, the pressure term contributes several percent to the total force term since a higher upstream pressure acts on the lip surface than on the downstream. This is the lip force term from Fig. 2-4.

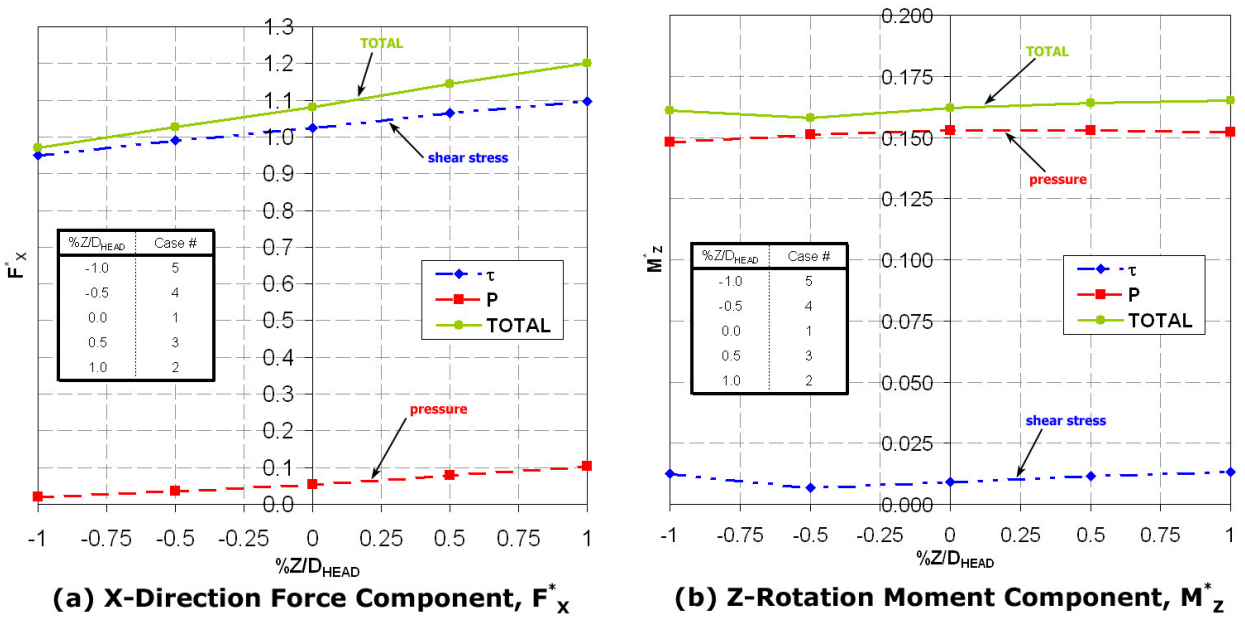

(a) X-Direction Force Component, F^*_X **(b) Z-Rotation Moment Component, M^*_Z**

Figure 4-22. Effects of Misalignment Variation on Pressure, Shear Stress, and Total Contributions to F^*_X and M^*_Z

Misalignment seems to be the most important factor in this particular flow scenario. Relatively small values of misalignment produce significant deviations from the desired result, on the order of 10 – 20 % in the presence of a small flow rates quantified by Fig. 4-10. Using eqn. (4-10), the results of Fig. 4-22 (a) and (b) can be combined to reflect the strain error. The total strain error is given in Fig. 4-23. Since the M^*_Z moment is positive for all values of misalignment, the moment tends to bring the strain error values closer to the desired value when compared to F^*_X alone. This can be explained by the normal force term of eqn. (2-2), which combines the normal force itself with its moment arm. In a negative pressure gradient, the upstream direction of the moment arm tends to provide a restorative moment to partially cancel out the effects of the additional lip force caused by the pressure difference.

For the misalignment cases, it appears that recession is somewhat preferential over protrusion, although neither is attractive. For a recessed (Z<0) gage, the reduction in shear force caused by the sheltering of the head somewhat offsets the additional force caused by the pressure gradient. In fact, Fig. 4-23 shows that there is a match point at a Z/D_{HEAD} of approximately -0.3% (Z^*=-0.004) where the two effects cancel out perfectly. It is *not* recommended, however, that the skin friction gage ever be purposely misaligned to try to take advantage of this fact. The match point will depend on geometry, pressure gradient, flow conditions, and a myriad of other

factors, making the prediction difficult in a general application. The protrusion cases experience increased shear force as well as increased pressure forces due to the intrusion into the flow. Although not studied here for this flow configuration, it is presumed that a gage in a positive pressure gradient will exhibit different characteristics where the lip force tends to reduce the total beam force rather that add to it.

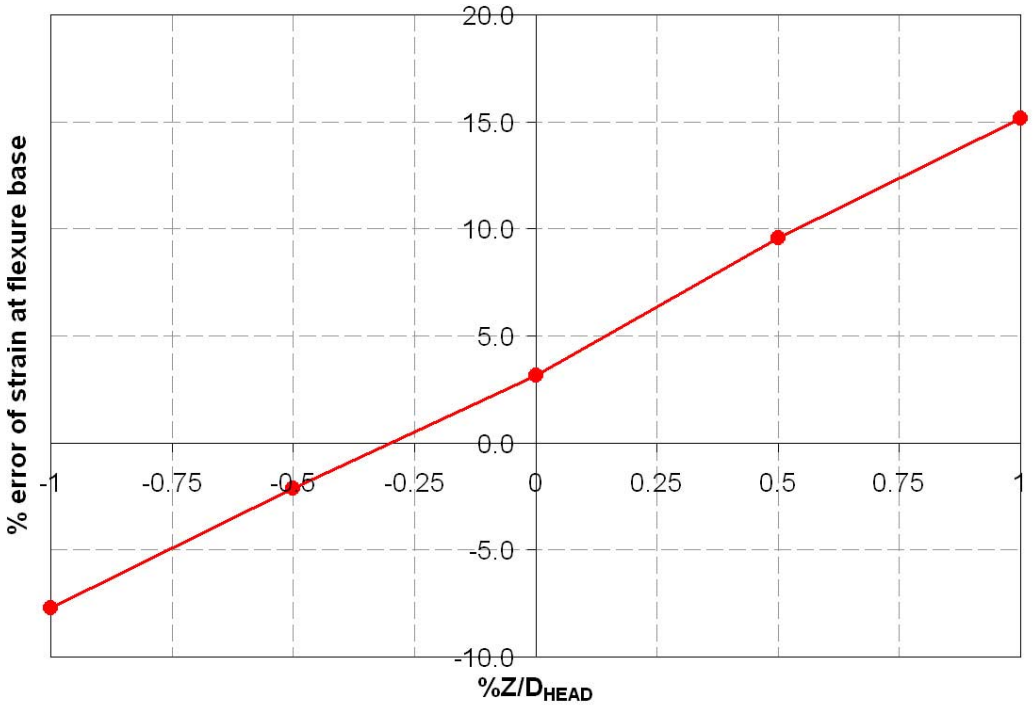

Figure 4-23. Percentage Error in Strain at Flexure Base for Misalignment Variation

The lip thickness bears scrutiny as the next parameter of influence in the channel flow results. Figure 4-24 shows the same data as for the misalignment cases – the F^*_X force for the shear stress, pressure, and total components in Fig. 4-24 (a), and the M^*_Z moments for the same in Fig. 4-24 (b). Generally, it seems preferable to minimize lip thickness, a conclusion which is consistent with the expectations from Fig. 2-4 and eqn. (2-6). By minimizing the area over which the lip force acts, it is presumed that this addition will also be minimized. The pressure force in Fig. 4-24 (a) does indeed go approximately to zero as lip thickness decreases to the same. The total force does not pass exactly through 1.0 because the gap is still present, even at zero lip size. In fact, the razor sharp edge of the head creates a relatively complex geometric situation for the flow. The contribution by the shear stress actually rises slightly at a lip

thickness of zero for Case #6, although this increase is within the numerical uncertainty, and thus cannot be interpreted too strictly.

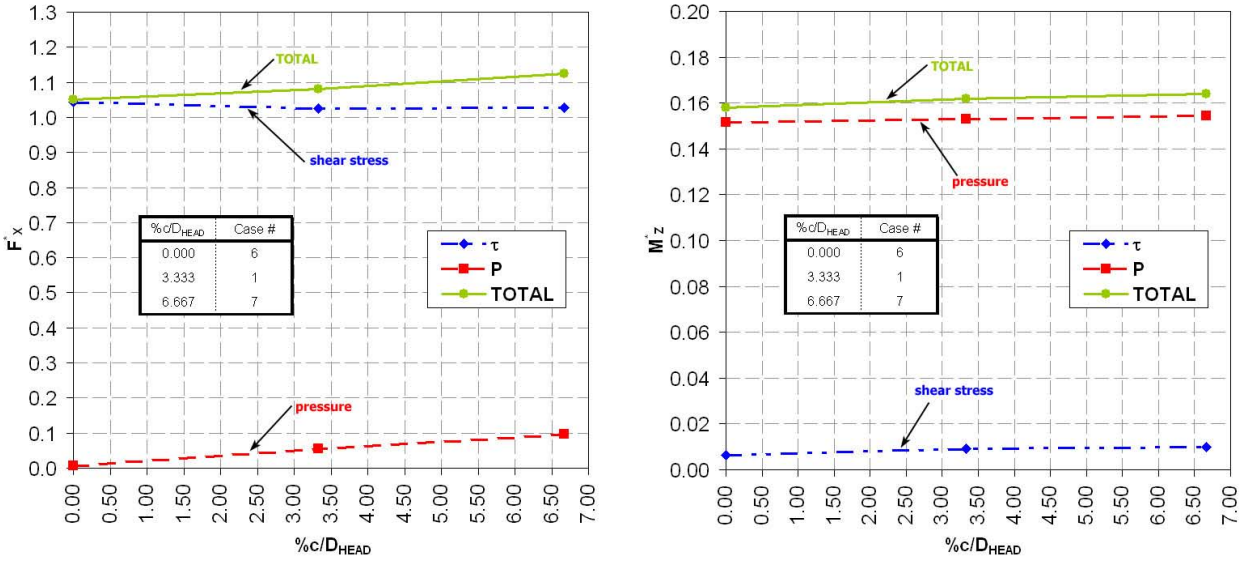

(a) X-Direction Force Component, F^*_X **(b) Z-Rotation Moment Component, M^*_Z**

Figure 4-24. Effects of Lip Thickness Variation on Pressure, Shear Stress, and Total Contributions to F^*_X and M^*_Z

Like with the misalignment variation cases, the lip thickness variation cases show very little change in the moment component contribution for different variations. Although the changing parameters shift the overall moment arm by small amounts, the generation of the moment comes almost exclusively from the presence of the pressure gradient. For a given constant pressure gradient, it seems that specific geometric variations have little influence. It is presumed here that only changing the pressure gradient imposed or possibly the head diameter will drastically impact the moment.

The strain error resulting from Fig. 4-24 for Cases #1, #6, and #7 are shown in Fig. 4-25. As with the misalignment cases, the moment effect here serves to lessen the severity of the *x*-direction force error also. Minimum lip area is preferable for the reasons already discussed. Although the pressure differential can have a component in the flow direction against the tapered surface with zero lip, the increasing area going down into the cavity quickly dissipates any pressure differences.

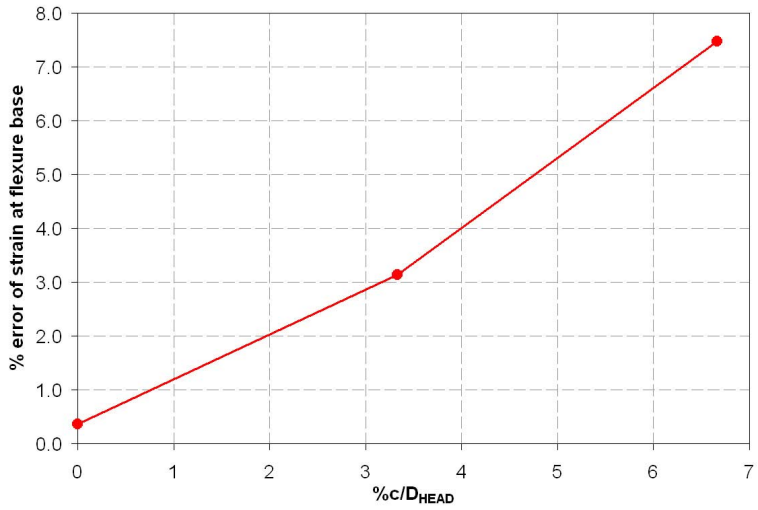

Figure 4-25. Percentage Error in Strain at Flexure Base For Misalignment Variation Cases

Finally, the results of the gap variation study are presented in Fig. 4-26. The F^*_X force contributed by the shear stress, pressure, and total is presented in Fig. 4-26 (a), while the M^*_Z moment is presented in Fig. 4-26 (b). The gap generally seems to have the smallest effect of the accuracy on a direct measuring skin friction gage in a negative pressure gradient of any of the parameters studied, but there is a distinct influence with changing gap size.

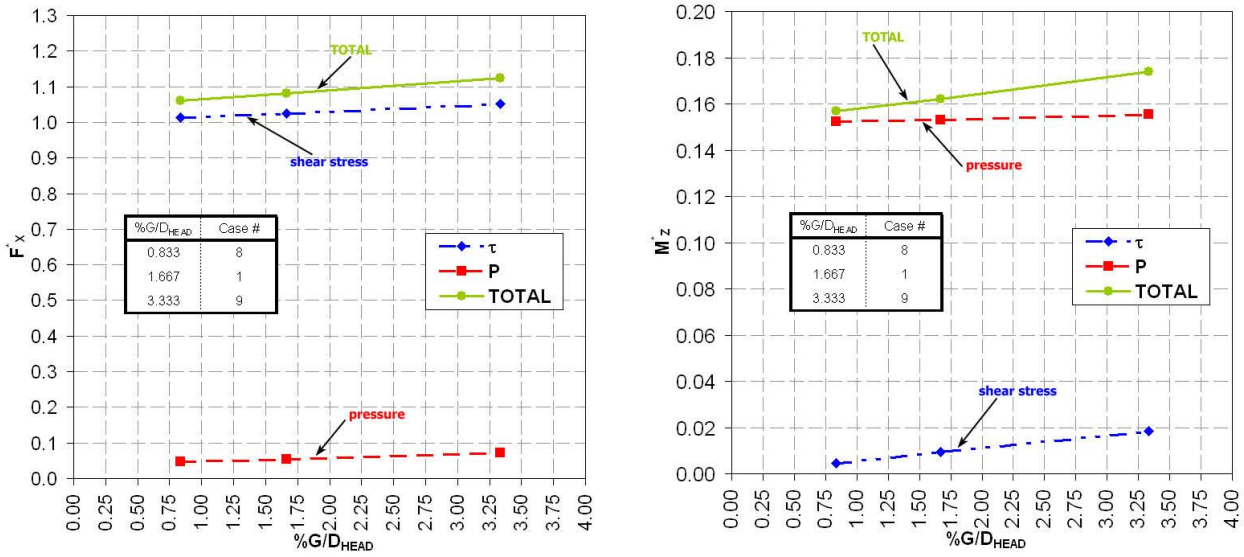

(a) X-Direction Force Component, F^*_X **(b) Z-Rotation Moment Component, M^*_Z**

Figure 4-26. Effects of Gap Size Variation on Pressure, Shear Stress, and Total Contributions to F^*_X and M^*_Z

The resulting strain error in Fig. 4-27 corroborates this conclusion as well. Although Allen stated that there is no benefit to a small gap, Fig. 4-26 indicates that there is some benefit. Allen's tests were under different flow conditions, but if it were assumed that the relative importance of the parameters remains consistent under different flow conditions, it may be that the importance of the gap was lost in Allen's misalignment analysis.

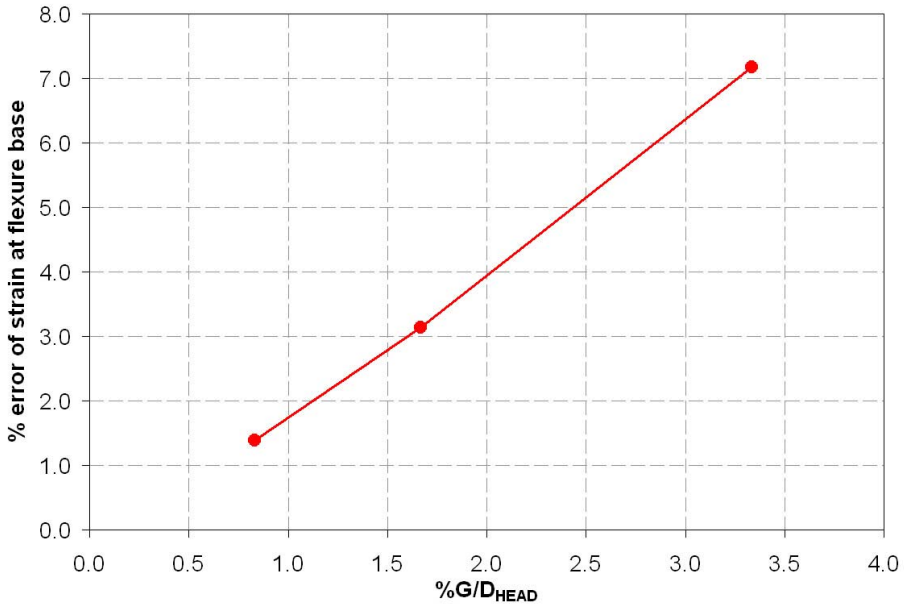

Figure 4-27. Percentage Error in Strain at Flexure Base For Misalignment Variation Cases

From Fig. 4-26 (a), it looks by extrapolation as if the shear stress term will indeed pass through approximately 1.0 if the gap size were reduced to zero. A gap size of zero is obviously absurd, as this would not correspond to an operating, functional gage (the sensing head could not move), but one would expect this to be a desirable limiting case. The pressure term from this figure, however, does not seem as if it would pass through exactly 0.0. This fact is not particularly surprising, since the pressure gradient would continue to act upon the head as long as there is any possibility of a flow rate through the gap. No doubt some complex effects would begin to dominate as the gap approached a small value where the molecular mean free path scale became important. This might occur in a MEMS type sensor, but the gap points selected for the cases presented here are typically of machining sizes on recent conventional gages.

One last note about parameter variation concerns the taper angle, Λ. Table 4-2 shows that this angle was set to thirty degrees for all cases. Taper angle variation was actually the first parameter that was studied, with angles of 15, 30, and 60 degrees. The results indicated that the change in angle only changed the total resulting force and moment coefficients by about 1%. Considering the uncertainty of the numerical aspects of the solutions, this is not a significant enough change to draw any strong conclusions. It seems that smaller angles offered a slight improvement, but that even the relatively large angle of 60 degrees had similar error levels. Obviously, from the results of the lip thickness variation study, it is necessary to have some significant tapering angle present below the head, but it seems the exact value of this angle is not particularly important. Thus, a reasonable value of 30 degrees was arbitrarily picked for the remainder of the study.

The *y*-direction component of force has not been mentioned in the foregoing analysis and results presentation. All nine cases that have been presented resulted in virtually identical values of F^*_Y. The dimensionless force ranged only from -0.698 to -0.700 for all cases. This component is the actual normal force from Fig. 2-4 (not its moment), and it comes entirely from pressure. It is important to note again that this force is dependent on the pressure directly and not the pressure gradient. This is unlike the *x*-direction force and the *z*-direction moment, where only the derivative of pressure was important. Thus, a channel that is pressurized such that it has the same pressure gradient characteristics will have a correspondingly higher value of F^*_Y. Again, using a symmetric strain gage bridge should nullify the effects of F^*_Y no matter what it happens to be if the flexure is perfectly machined, but it is still not desirous to have F^*_Y larger than F^*_X for sensitivity reasons. Unfortunately, conditions external to the gage determine what F^*_Y is, and this study shows that there is little that can be done to the gage itself to address this. Only one value of D^*_{BEAM} was used for this study, but it is presumed that decreasing the head diameter will decrease the effects of the normal pressure.

Finally, the numerical force results are presented in tabular format in Table 4-3. Although the previous several figures contain all the important results, these force computations are repeated in tabular format so that the exact values are available. Table 4-3 lists the values for F^*_X, F^*_Y, and M^*_Z for shear stress, pressure, and the combined total for each of the nine cases detailed in Table 4-2.

Table 4-3. Numerical Summary of Relevant Dimensionless Force and Moment Results for Various Channel Flow Cas

Case #	F^*_X			F^*_Y			M^*_Z		
	total	pressure	shear	total	pressure	shear	total	pressure	shear
1	1.0805	0.0553	1.0253	-0.6996	-0.6996	0.0000	0.1622	0.1529	0.0093
2	1.2009	0.1040	1.0969	-0.6979	-0.6979	0.0000	0.1654	0.1523	0.0131
3	1.1453	0.0797	1.0655	-0.6985	-0.6985	0.0000	0.1645	0.1530	0.0115
4	1.0261	0.0352	0.9909	-0.6993	-0.6994	0.0000	0.1578	0.1512	0.0066
5	0.9712	0.0211	0.9501	-0.6996	-0.6996	0.0000	0.1608	0.1481	0.0126
6	1.0507	0.0069	1.0438	-0.6990	-0.6990	0.0000	0.1580	0.1517	0.0062
7	1.1241	0.0959	1.0283	-0.6990	-0.6990	0.0000	0.1643	0.1542	0.0100
8	1.0607	0.0476	1.0131	-0.6990	-0.6990	0.0000	0.1568	0.1522	0.0046
9	1.0517	0.0000	1.0517	-0.6989	-0.6990	0.0000	0.1736	0.1553	0.0183

4.5 Validation and Verification

Validating the mathematical model of this flow scenario is relatively straight-forward in this instance. Since the Navier-Stokes equations are identified by a fully viscous description of the fluid, it would seem that a viscosity dominated problem would be the ideal match. The basic problem studied is one of the few *exact* solutions that are available from the Navier-Stokes equation set, so the choice of the mathematical model is in this respect validated *a priori*, particularly since this scenario is somewhat hypothetical anyway. The major objectives for this analysis were to illustrate direct measuring skin friction gage performance in a generic channel configuration in the presence of a strong pressure gradient and to learn and assess the performance of the code.

The geometry of the mathematical model was also initially motivated by the Skin Friction Gage Calibration Rig at Virginia Tech that is pictured in Fig. 4-1. This physical channel in particular is clearly modeled by the Navier-Stokes solution as well. Magill [1999] shows that the pressure gradient at the symmetry plane of the channel for most of the length of the channel is indeed linear. This is a central result of both the exact and numerical solutions from the Navier-Stokes set, thus illustrating that the physical channel facility is well-described by the mathematics. This closes the subject of validation of this chapter's flow conditions.

Convergence is a basic issue in all CFD solutions, and this case is no different despite its relative simplicity compared to many other fluid mechanics problems. Although the basic Poiseuille flow channel offers a linear, solvable solution that is mathematically exact, Ansys/FLOTRAN does not have the advantage of a symbolic solver, so it must still deal with the full non-linear system. Also, the presence of the gage in the wall introduces non-linearities, meaning that the full capabilities of the CFD code are required.

Fortunately, the low Reynolds number of the flow that reduces convective coupling and the absence of any complex boundary conditions (like turbulent wall functions) make the convergence behavior of the various cases almost ideal. Often, dominant convective coupling or other effects that strongly integrate the equations can slow the convergence rate down or even completely stall the solution in some cases.

For all nine cases, iterations were performed until all convergence monitors reached at least $1x10^{-10}$ or lower. The convergence monitors were defined in eqn. (3-20), and they indicated

the stopping criteria for the CFD code. A separate monitor for each of the three components of velocity and pressure all had to reach the stopping criterion individually. Because of the nature of the SIMPLE algorithm, the pressure monitor was in all cases the limiting factor as it was the last to reach the desired value.

Table 4-4 shows the corresponding residual values for the various cases by degree of freedom after converging to the aforementioned convergence level. As Ansys/FLOTRAN gives residuals on a per node basis, this table reflects the maximum value found at any node in the model. All other nodes have residuals smaller than the indicated number, many considerably so. As discussed in Chapter 3, these values are normalized residual values, an implementation that is intended by Ansys/FLOTRAN to be comparable to the actual value of that degree of freedom at that particular node. For reference in looking at Table 4-4, consider that the velocity in the channel varies between 0.0 and 1.0. Non-dimensional pressure varies between 0.0 and 47.43. Thus, the residuals are extremely small when compared to degrees of freedom, which are on the order of 1.0.

Table 4-4. Maximum Values of Normalized Nodal Residual for All Cases

case	Maximum Nodal Residual (absolute value)			
	VX	VY	VZ	PRES
1	$1.18\text{x}10^{-9}$	$5.20\text{x}10^{-11}$	$3.27\text{x}10^{-11}$	$3.07\text{x}10^{-8}$
2	$9.93\text{x}10^{-10}$	$7.13\text{x}10^{-11}$	$2.60\text{x}10^{-11}$	$5.09\text{x}10^{-9}$
3	$5.69\text{x}10^{-10}$	$3.45\text{x}10^{-11}$	$1.38\text{x}10^{-11}$	$1.92\text{x}10^{-9}$
4	$4.87\text{x}10^{-10}$	$2.60\text{x}10^{-11}$	$1.41\text{x}10^{-11}$	$1.43\text{x}10^{-9}$
5	$4.84\text{x}10^{-10}$	$2.71\text{x}10^{-11}$	$1.39\text{x}10^{-11}$	$2.01\text{x}10^{-9}$
6	$4.87\text{x}10^{-10}$	$2.32\text{x}10^{-11}$	$1.43\text{x}10^{-11}$	$2.93\text{x}10^{-9}$
7	$4.98\text{x}10^{-10}$	$2.32\text{x}10^{-11}$	$1.46\text{x}10^{-11}$	$1.07\text{x}10^{-9}$
8	$4.78\text{x}10^{-10}$	$2.68\text{x}10^{-11}$	$1.52\text{x}10^{-11}$	$8.02\text{x}10^{-10}$
9	$6.11\text{x}10^{-10}$	$3.32\text{x}10^{-11}$	$1.61\text{x}10^{-11}$	$1.86\text{x}10^{-9}$

Although Table 4-4 certainly indicates that adequate, perhaps even excessive, convergence was obtained for all cases, it is prudent to take a brief look at an iteration history for at least the baseline case as a further justification. Because of the relatively small changes in

total force from case to case given in the previous section, it was necessary to eliminate virtually all uncertainty from numerical errors in order to make those results meaningful in the numerical noise. Thus, iterative convergence was tightly controlled since it is a manageable source of error – i.e. it is easy to eliminate as much iterative convergence error as necessary, provided sufficient computer time is spent on the solution.

Figure 4-28 gives the iterative history for the changes in F^*_X, F^*_Y, and M^*_Z for the baseline Case #1. Since these three parameters are the major results required from the models, they are a more reasonable measure of the issue of convergence than nodal residual values. Seeing that these three numbers converge is what really counts here. For each of the three components, the values at any iteration are normalized by the final value obtained when the stopping criteria were satisfied. This makes it possible to view all three trends on one graph.

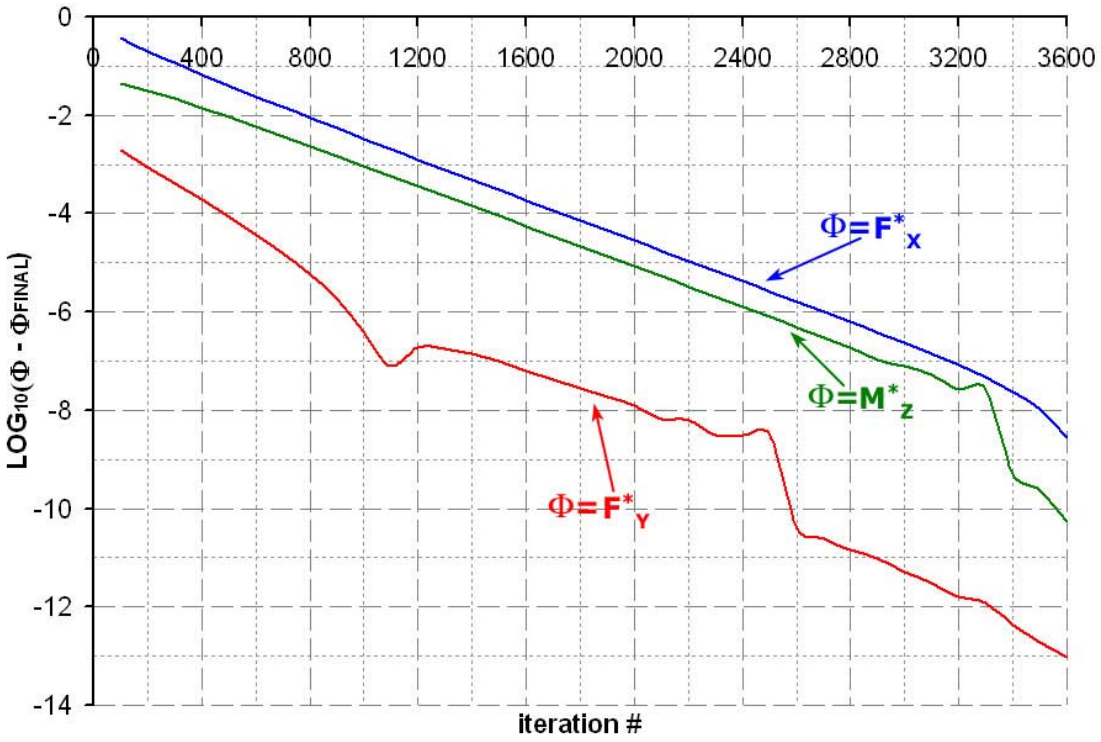

Figure 4-28. Iterative History of Normalized Change in Global Force Components for Change Case #1 Illustrating Convergence Properties

Ordered discretization error, or grid dependence, is a much more difficult issue to deal with than convergence. In order to address grid dependence error, multiple grids were used as

listed in Table 4-2. All solutions were run using the same stopping criteria just mentioned, but only results from the finest grids have been given in this and the previous two sections. The finest grids are considered to be "closest" to the exact solution, with error bounds to be given. The coarse grids served two purposes: to provide initial guesses via nested iteration described in Section 3.3 and to allow calculation of the Richardson extrapolation error estimators as described in Section 3.6.

The organization used was to solve the baseline case on at least three successive grids. This allows the computation of the observed order of convergence, p, via the discussion of Roache [1998]. This was done using grids A, B, and C. Then, grids A and B were used to calculate the error estimator and *GCI* for each global force and moment component via eqns. (3-22) and (3-24), respectively. For the remaining eight cases, the order of convergence for the baseline case was assumed to hold for all variations and the case was only solved on two different grids. This is a reasonable assumption since the models are all for the same basic type of problem and only relatively small variations exist between the cases. Additionally, from Roache [1998], it seems that actually calculating the order of convergence at all is an infrequent exercise among CFD users. In this light, the steps taken here to address grid dependence are quite robust in comparison to the norm. With p from the baseline analysis, the error estimators and *GCI*'s were found using grids A and B from each case, the only two used for all variation cases.

Calculating the order of convergence is quite difficult in practice despite its simplicity in principle. Since the discretization scheme in Ansys/FLOTRAN is a mixed-order scheme, there is no reason that the spatial convergence needs to be monotonic at all. This issue was already discussed with the work of Roy [2001] in mind. Despite this, an estimation was attempted. The results are given in Table 4-5 as they were found using the Richardson extrapolation method (requiring strictly monotonic convergence). Obviously, the order of convergence for the y-component force and the z-direction moment is not even sensible, with one value that is even negative. If the convergence was monotonic and well-behaved, one would expect values that fall somewhere between 1.0 and 2.0. Only the x-direction force results exhibit a sensible value, although it is almost certainly non-monotonic as well. This is an unfortunate drawback to using mixed-order schemes. The encouraging fact, however, is that the x-direction force is the primary quantity of interest. Also of issue is the fact that the values between grids are extremely close.

The narrowness of the differentiation between grids creates a significant digit issue, meaning that it is difficult to calculate the order of convergence with any accuracy and that other errors (like convergence error, rounding error, etc.) will be magnified in their influence on the calculation. The non-physical values for order of convergence, particularly with reference to the values from F^*_Y and M^*_Z, are likely to be functions dominated by this significance issue.

Table 4-5. Global Force and Moment Results (dimensionless) for Grids A, B, and C of Baseline Case #1 and Resulting Order of Convergence Calculation

	Grid C	Grid B	Grid A	p
F^*_X pressure	1.3134×10^{-04}	1.3186×10^{-04}	1.3228×10^{-04}	1.10
F^*_X shear stress	2.4462×10^{-03}	2.4507×10^{-03}	2.4545×10^{-03}	0.97
F^*_X total	2.5775×10^{-03}	2.5825×10^{-03}	2.5867×10^{-03}	0.98
F^*_Y pressure	-1.6729×10^{-03}	-1.6743×10^{-03}	-1.6747×10^{-03}	6.81
F^*_Y shear stress	-4.4532×10^{-08}	-2.8818×10^{-08}	-2.3900×10^{-08}	6.37
F^*_Y total	-1.6729×10^{-03}	-1.6743×10^{-03}	-1.6747×10^{-03}	6.81
M^*_Z pressure	2.7898×10^{-06}	2.7897×10^{-06}	2.7895×10^{-06}	-5.39
M^*_Z shear stress	1.6163×10^{-07}	1.6697×10^{-07}	1.6911×10^{-07}	5.00
M^*_Z total	2.9514×10^{-06}	2.9567×10^{-06}	2.9586×10^{-06}	5.46

Thus, after looking at the results, an order of convergence of 1.0 was used in all the error estimator calculations to follow. It is obvious that the actual observed order of convergence is actually non-monotonic, but this is to be expected given the discretization scheme. The value of 1.0 for p is considered to be very conservative for monotonic convergence, as the SUPG formulation approaches 2.0 as the mesh is refined. With a very conservative value for p, it is hoped that the error estimator A_1 will provide a conservative estimate despite the non-monotonic convergence behavior. The *GCI* with the factor of 3 again serves to protect against these types of problems with extreme error bounds.

The Richardson extrapolation error estimator value, A_1, and the corresponding *GCI* for each case are shown in Table 4-6. These values are given individually for each force and moment coefficient, since these values will converge at different rates in general. Again, the order of convergence is 1.0 for all calculations. Despite the issue of monotonic convergence, the

error estimator predicts relatively low values of uncertainty for all models, with the average *GCI* estimates from all nine cases being 1.6% for the *x*-direction force, 1.3% for the *y*-direction force, and 2.1% for the moment. The moment coefficient varies the most strongly, although all error estimates are still reasonably low. These values are low enough to make the results in the previous section significant and useful.

Table 4-6. Richardson Extrapolation Error Estimation and GCI of Global Force and Moment Components for All Cases Given as a Percentage

case	F^*_X		F^*_Y		M^*_Z	
	% A_1	% GCI_{fine}	% A_1	% GCI_{fine}	% A_1	% GCI_{fine}
1	-0.65	1.95	-0.10	0.29	-0.26	0.78
2	-0.80	2.41	-0.47	1.40	-1.10	3.30
3	-0.65	1.95	-0.47	1.42	-0.44	1.31
4	-0.36	1.08	-0.47	1.40	-0.60	1.81
5	-0.32	0.96	-0.46	1.38	-0.79	2.36
6	-0.10	0.30	-0.46	1.39	-1.08	3.23
7	-0.49	1.47	-0.47	1.41	-0.58	1.74
8	-0.64	1.93	-0.48	1.44	-0.73	2.20
9	-0.90	2.70	-0.49	1.47	-0.67	2.01

The final source of error to be discussed is the placement of the boundaries. The upstream, downstream, and side boundaries lie 69 gap sizes away from the gap for the baseline Case #1 (the gap variation cases will be proportionally different). It was shown in Section 4.3 that the disturbances caused by the gaps are damped out in a very short distance due to the highly viscous nature of the flow problem. Although the boundaries were not considered to be particularly an issue after looking at the flow patterns, the boundary placement was tested for the baseline case just to be sure of the accuracy of the model. It is assumed that the errors seen on the baseline case from the boundary sources will be consistent with other cases. This is justified because variations from case to case are relatively small, and the boundary placement is very far away from these variations.

The baseline Case #1 as given in Section 4.1 was compared to an expanded model which solved all the way to the side wall, using the no-slip condition at that surface. The full channel width, w^*, was 20, so the dimensionless half width was 10. This was compared to the Case #1 half width w_1^* of 2.0. In addition, the dimensionless upstream and downstream lengths of this boundary case were increased by a dimensionless length of 3.5 each. This is almost triple the values of Case #1.

The result of this comparison is that, of the three global parameters of eqns. (4-4), (4-5), and (4-6), none of them changed by more than 0.024%. Although the Richardson extrapolation error estimator could again be employed as with the grid refinement issue (even by varying the boundaries one at a time), it is clear from the simple percent difference that the change induced by the boundary placement is very small. It is over one order of magnitude smaller than the mesh dependent error described previously.

In fact, it is apparent that the mesh or ordered discretization error is the dominant source of error in the computational analysis. Although lack of convergence and boundary placement do add some small amounts to the total computational error, these contributions are relatively insignificant. This is to be expected, as grid dependence error is most often the main source of error in any computational analysis.

CHAPTER 5: Studies of Skin Friction Gages in a Turbulent Flat Plate Flow

5.1 The Physical Model

Although the treatment of the basic flow problem in the previous chapter offers a great deal of insight into the importance of relevant parameters in skin friction gage design and installation, engineers are most interested in situations that are much more complex than the one presented there. Since there is a direct correlation between the complexity of a flow and the interest in making a skin friction measurement, it is fruitful to look at a case that has at least some features that more directly resemble a situation which might be interesting to a fluid dynamicist. It is still necessary, however, to look at a situation that is well understood in order to evaluate the error effects on a skin friction gage. A typical complex application that requires accurate skin friction measurements might be a hypersonic engine inlet for example. However, since the "correct," or exact, answer is not well understood, it becomes impossible to address the accuracy of the skin friction gage in detail. A paradox results: one seeks a complex situation which is simple to understand.

The case of the turbulent flow over a flat plate is studied in this chapter as a reasonable compromise for this dilemma. The flat plate is undoubtedly the most well understood case involving external, turbulent flow. Turbulence is a key defining factor in virtually all practical applications requiring skin friction gage measurement. Unfortunately, turbulence invariably brings with it a lack of general understanding and an inability to make accurate predictions of the details of the flow (highlighting the need for an accurate skin friction measurement).

The flat plate is a unique case in turbulent flow. It is the simplest possible general case, and it is the best documented. Experimental data from flat plate models have been used in developing virtually every turbulence model available for computational analysis. This is the famous *law of the wall*, which is in some way a part of these turbulence models [Schetz, 1993].

Despite the fact that CFD is used for complex geometries involving pressure gradients, the turbulence models typically rely on this law and the assumption that the law of the wall holds for many general situations besides a flat plate. Thus, the flat plate was chosen partly out of a desire to avoid any excessive computational dependence on the turbulence modeling scheme. Although any CFD calculation is invariably dependent on the particular turbulence model used, it is assumed that a flat plate is the case for which the model will generally behave the most consistently and provide the best solution since it is what the models are based on.

Also, the flat plate case is well-documented. There have been a large number of measurements made for a flat plate by various researchers. Schetz [1993] documents two of the best known correlations for skin friction that have resulted from these experiments. The first is originally from Blasius, and is given in eqn. (5-1). The second, originally by Schoenherr, is given in eqn. (5-2). Both of these relations are valid for a smooth flat plate in turbulent flow.

$$C_f = 0.0456 Re_\delta^{-0.25} \tag{5-1}$$

$$\frac{1}{C_f} = 4.15 \log(Re_X C_f) + 1.7 \tag{5-2}$$

Kays and Crawford [1993] also document a similar formula from Schultz-Grunow, valid for Reynolds numbers above 500,000 in the same circumstances. It is given in eqn. (5-3).

$$C_f/2 = 0.185 (\log_{10} Re_X)^{-2.584} \tag{5-3}$$

The disadvantage of eqn. (5-1) is that it is based on the turbulent boundary layer thickness, so a correlation is then needed for boundary layer thickness as a function of plate distance. Unfortunately, boundary layer thickness is not well-defined, even for a flat plate. A typical crude approximation for $\delta(x)$ comes directly from the *1/7-power law*, the result of which is given in eqn. (5-4) [Schetz, 1993].

$$\delta(x) \approx \frac{0.375x}{Re_X^{1/5}} \tag{5-4}$$

The Schoenherr formula, in contrast, has the advantage of being directly in terms of the desired plate station, x. The fact that it is non-linear is trivial given standard numerical solution techniques such as the Bisection method [Matthews and Fink, 1999]. Eqn. (5-3) from Schultz-Grunow is ideal in that it is a function of Re_X and requires no iteration to solve.

The flat plate problem has, of course, zero pressure gradient. In this respect it is quite different from the channel problem of Chapter 4, so one would expect that the effects of the skin friction gage parameters will be somewhat different without a governing pressure force affecting the results.

The global flat plate problem shown in Fig. 5-1 is two-dimensional in nature. Turbulence effects in the third direction are not considered in this scenario, at least in the global sense. The plate is exposed to incoming air of uniform free-stream speed, incident in a direction parallel to the plate itself. Since the flow is subsonic for this case, there is some upstream communication in the free-stream. The velocity profile at the start of the plate, $x = 0$, is no longer uniform, as the flow has already started to adjust to the plate presence. Because of this, the physical model domain includes an upstream section of length L_{ENT} ahead of the plate to allow the flow field to adjust correctly to the plate edge without being unfairly influenced by the inlet boundary conditions. The boundary layer thickness drawn in Fig. 5-1 is not exactly to scale, but is given as an indication of what behavior the physical problem will exhibit. All the other geometric dimensions in this figure are to scale, however. The embedded region highlighted in this figure will be discussed below.

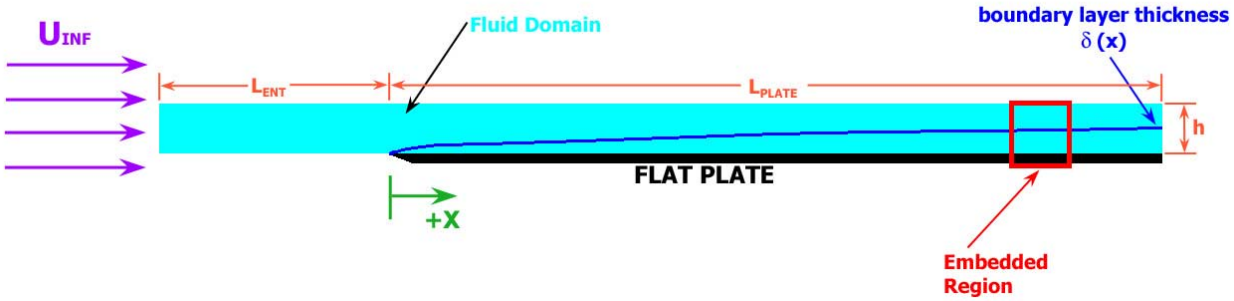

Figure 5-1. Scaled Drawing of Physical Model of Incompressible, Turbulent Flat Plate Problem

The fluid in this problem is air, which is typical of a realistic aerospace application. At room temperature and sea level conditions, air has a density of approximately 1.225 kg/m^3 and a dynamic viscosity of approximately 1.90x10^{-5} Pa-s in SI units. Table 5-1 lists these and all other relevant parameters for the flat plate model, given both dimensionally and non-dimensionally. For this plate, the reference length, L_∞, was selected to be 0.075 m. The reference velocity, V_∞,

was chosen to be 103.4 m/s, and the reference density, ρ_∞, to be the density of the fluid 1.225 kg/m^3. Since the incoming velocity was set to 1.0 in the code, the incoming velocity is identical to the reference velocity. This represents a very much higher value than that of the channel flow that was studied in Chapter 4. Assuming the standard value of the speed of sound in air at room temperature, this corresponds to a Mach number of 0.30. Although there is no clear line, this Mach number is typically considered to be about the upper limit for which incompressibility still holds, and this flat plate problem was designed so.

Table 5-1. Relevant Geometry and Variable Definitions for 2D Global Turbulent Flat Plate Problem, Shown Dimensionally and Non-dimensionally

dimensional values			**dimensionless values**	
h	18.75	mm	h*	0.25
L_{PLATE}	300	mm	L^*_{PLATE}	4.00
L_{ENT}	112.5	mm	L^*_{ENT}	1.50
P_{REF}	101,325	Pa	P^*_{REF}	7.64
μ	1.90×10^{-5}	Pa-s	μ^*	2.0×10^{-6}
ρ	1.225	kg/m^3	ρ^*	1.00

A critical parameter in designing the physical problem is the Reynolds number. With the values given in Table 5-1, the Reynolds number at the end of the plate, Re_L, works out to be 2,000,000. In a physical sense, the flow over a flat plate like this one transitions from laminar flow to turbulent flow somewhere around a Reynolds number of 500,000. With a value of 2×10^6 at the plate end, the flow will certainly be turbulent.

On a final geometric note, prescribing the Reynolds number automatically infers the plate length. The correct domain height for the problem was selected based on simple analyses. For correct boundary placement, the domain height, h^*, should be significantly higher than the maximum boundary layer thickness. First, and most simply, the boundary layer height can be estimated from eqn. (5-4). Using the Reynolds number at the end of the plate and Table 5-1, the boundary layer thickness, δ, is 0.00618 meters or 0.0824 in dimensionless units.

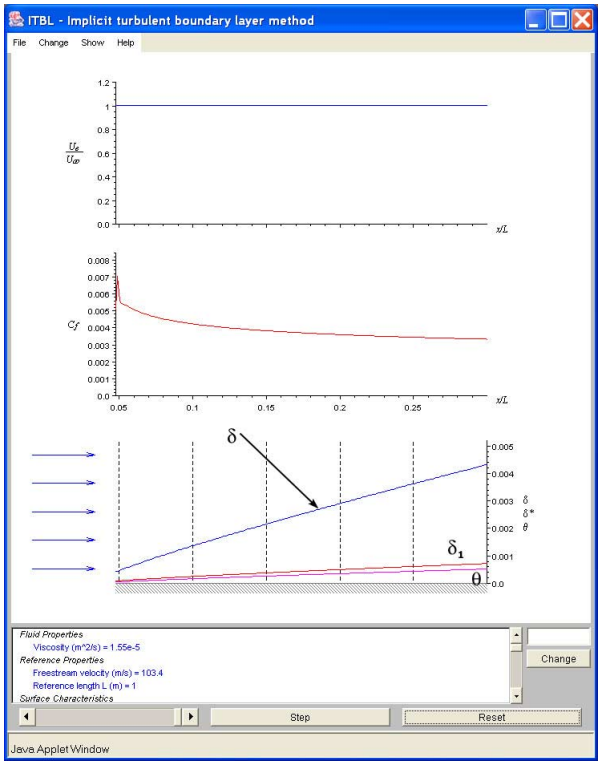

Figure 5-2. Screen Capture Image of Java ITBL Program Showing Boundary Layer Thickness Solution Estimate

This value was then verified using slightly more sophisticated means. The values from Table 5-1 were input into a pair of Java applets found on the Virginia Tech Java Engineering Applets Webpage [Devenport *et al*., 2001]. The first of these is titled "ILBLI," short for *incompressible laminar boundary layer implicit*, was started and run to a transition Reynolds number of 500,000. The information from this program was used to start the companion "ITBL" program, short for *incompressible turbulent boundary layer*, which was used to solve to the end of the plate. The resulting value for boundary layer thickness, δ, was given from this program as 0.00432 meters, which is 0.0576 in dimensionless terms. This value is somewhat lower than the estimation from eqn. (5-4), because the laminar portion of the boundary layer is accounted for at the leading edge of the plate using the Java applet. Laminar boundary layers tend to be much thinner than corresponding turbulent ones, thus creating a smaller final thickness. The applet window is pictured in Fig. 5-2, showing the applet layout and the boundary layer plot as indicated. The second curve labeled is labeled δ^* by the applet graph but is annotated as δ_1. This quantity is not the non-dimensional boundary layer value, but rather is the displacement

thickness, which is defined in Schetz [1993]. Displacement thickness is referred to as δ_1 here to avoid confusion.

From these two estimates, the domain height, h^*, was set to 0.25 as a rounded value of sufficient magnitude. This number is approximately three times the value predicted from eqn. (5-4), and over four times that predicted by the program as shown in Fig. 5-2.

The global flat plate problem discussed already is two-dimensional in nature, but the specific goal is to study the performance of a typical direct measuring skin friction gage under these conditions. This particular aspect of the problem is three-dimensional in nature. Therefore, the problem is approached here using the embedded region idea discussed in Section 3.5. First, the global 2D flat plate problem was solved as described by the physical model in Fig. 5-1. This global problem contained no gage or cavity. Next, the area circled in red on Fig. 5-1, termed an "embedded region," was separated out. This region is the region containing the gage itself. This region only was solved as a 3D problem, and it was created to be large enough to encompass all the 3D effects caused by the presence of the gage. The embedded region problem is shown in Fig. 5-3, scaled with appropriate dimensional labeling. The choice of the geometry and location of the embedded region is justified just below.

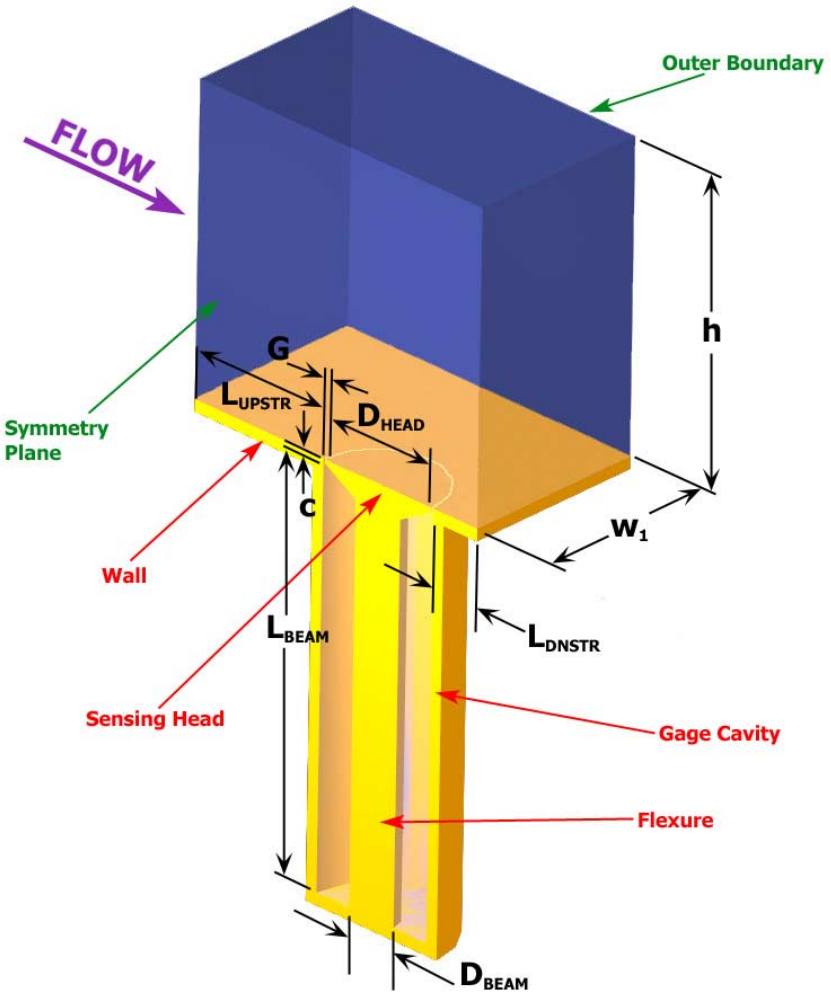

Figure 5-3. Scaled Drawing of 3D Embedded Region with Skin Friction Gage for Flat Plate Turbulent Boundary Layer Problem with Relevant Dimensions

The solution of the physical model of the embedded problem shown in Fig. 5-3 is similar to that of the global problem in Fig. 5-1 (in terms of boundary conditions, problem set-up, etc.), with one important aspect: the coupling of the global to the local solution through the placement of the inlet conditions. More details will be given in the next section, but the inlet conditions for the region in Fig. 5-3 come directly from the global problem at the indicated inlet x station as the process was described in Section 3.5. This includes velocity components, turbulent kinetic energy, and turbulent dissipation, which come from the solution at a dimensionless x^* station of 3.23 on the plate. This results in the center of the gage head being placed at a Reynolds number of approximately 1.7×10^6. This was chosen to be sufficiently high to see a dominantly turbulent flow, but short of the plate end where the global solution might be compromised by the

proximity of the outflow boundary. Table 5-2 covers all the relevant dimensional and dimensionless parameters for the embedded region. The parameters of the gage are the same as the gage model in Chapter 4. The dimensionless values are different because of the different scaling used, but the physical model represents the same gage body.

Table 5-2. Relevant Geometry and Variable Definitions for 3D Embedded Region of Baseline Case, Shown Dimensionally and Non-dimensionally

dimensional values			**dimensionless values**	
h	18.75	mm	h*	0.25
w_1	11.43	mm	w_1*	0.1524
L_{UPSTR}	9.218	mm	L^*_{UPSTR}	0.1229
L_{DNSTR}	3.142	mm	L^*_{DNSTR}	0.04189
D_{HEAD}	7.62	mm	D^*_{HEAD}	0.1016
G	0.127	mm	G*	0.001693
c	0.254	mm	c*	0.003387
L_{BEAM}	25.4	mm	L^*_{BEAM}	0.3387
D_{BEAM}	3.175	mm	D^*_{BEAM}	0.0423
Z	0	mm	Z*	0
Λ	30	deg.	Λ*	0.53
P_{REF}	101,325	Pa	P^*_{REF}	7.64
μ	1.90×10^{-5}	Pa-s	μ*	2.0×10^{-6}
ρ	1.225	kg/m^3	ρ*	1.00

5.2 The Computational Model

5.2.1 The Global Problem Model

The computational model for the global flat plate problem is straightforward, and is shown in Fig. 5-4. Since the problem domain is completely two-dimensional and rectangular, meshing proceeds simply. As any turbulent boundary layer should be treated, the elements are

highly staggered with the first few points extremely close to the wall. In fact, there are 75 divisions in the vertical (+*y*) direction, although the points near the wall are too close to see effectively.

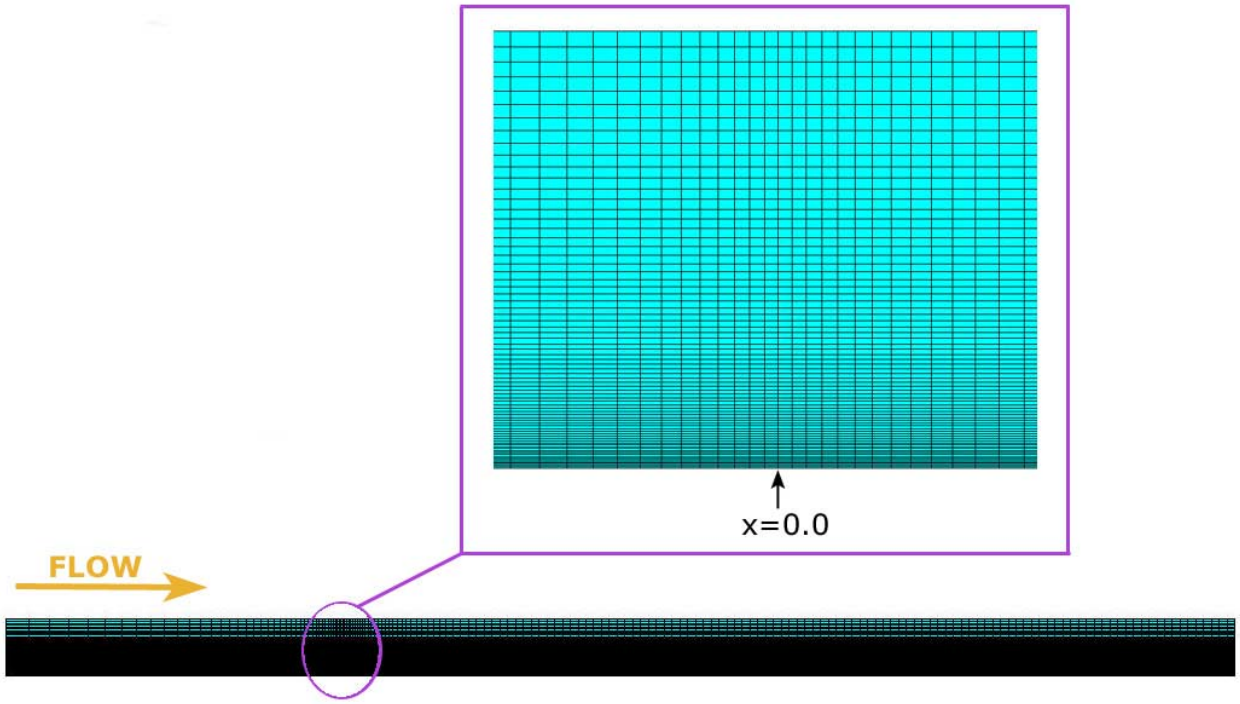

Figure 5-4. Mesh of Global 2D Turbulent Flat Plate Problem with Entry Length

The big issue in the global mesh is the proximity of the near wall nodes (the first points directly adjacent to the wall). The staggering of points was kept consistent between this problem and the embedded region, so the issue reflects on the following models as well. As discussed in Section 3.4, Ansys/FLOTRAN employs a two-option wall treatment for the κ–ε turbulence model which divides the wall region into two zones – the log region and the laminar sublayer – using special wall elements and makes a determination about the location of the wall element.

This formulation was investigated very systematically by varying the point spacing throughout the range of the two wall regions, and comparing the predictions for skin friction to the experimental correlations of eqns. (5-1), (5-2), and (5-4). After examination, it was found that the shear stress result got increasingly better as the near wall node moved closer to the wall itself, but still within the log region. However, the results got increasingly worse after the near wall point moved into the laminar sublayer. This conclusion is actually not a direct result of the

position of the near wall node. Instead, it is a result of too many points residing in the region defined by a y^+ of less than approximately 30.0, which is the approximate lower limit for which the κ–ε model is valid.

As a result of this systematic investigation, the following conclusions were drawn based on theoretical and practical observations. Ansys/FLOTRAN allows for the near wall node to be very close to the wall and deep within the laminar sublayer. However, logical grid spacing indicates that the distance from the second point to the wall will be slightly more than twice the distance to the first node to the wall. Since the second point must have a y^+ distance of approximately 30.0 or so for adequate validity of the κ–ε model, the first point cannot, in practice, be deep within the laminar sublayer. The other criterion for mesh design involves the nature of the problem being studied. Since the objective of this work is to study the flow and force results over a small intricate object in the wall with tiny gap regions surrounding it, it is also necessary to get as many points in the region of interest as possible. Particularly just above the gaps, it is desirable to have elements with as close to an aspect ratio of 1.0 as possible. Thus, the near wall node along the wall surface needs to be as close as possible.

Therefore, the logical conclusion was to design the near wall node to fall just above the laminar sublayer at a y^+ in the range of 13-14 or so. This design choice causes Ansys/FLOTRAN to use the log region wall function option in the wall modeling treatment. This choice satisfies as best as possible both criteria – the aspect ratios of the elements just above the gaps are made as small as possible while still allowing for proper turbulence model operation, and the choice of near wall node placement allows for valid operation of the turbulence model over all nodes beyond the first, near wall node (resulting in nodes above the first node residing in the log layer at y^+ in the range of 30.0 or so). Meshing the turbulent wall in this way insures that the κ and ε values are applicable in the elements above the wall element and a quality solution is obtained along the wall surface. This criterion really drove the design of the mesh, both for the global flat plate problem and the embedded region. The results of the global problem showing the agreement with the experimental values will be presented in Section 5.3.

The boundary conditions are relatively simple for the global problem. For the flow in Fig. 5-4, the inlet was given values for the velocity components *VX* and *VY* of 1.0 and 0.0 respectively. Conditions for the turbulence model are required for the inlet, and Ansys/FLOTRAN automatically assumes values if they are not given. The value of turbulent

kinetic energy, *ENKE*, was set to 0.0, and the turbulent dissipation, *ENDS*, to 1.0. This corresponds to zero free-stream turbulence or completely smooth air quality. Since this problem is not modeling a particular physical situation, this seems to be a reasonable choice. These values correspond to those indicated by the *Ansys Online Help* guide [2001] for a region where the turbulence model is totally inactive. Thus, any turbulence levels in the solution will be generated by the boundary layer forming on the plate.

The plate surface itself received the no slip condition, with both velocity components set to zero. As discussed earlier, the κ–ε conditions are governed by the special wall formulation. The bottom surface of the entry length before the plate start received a value for *VY* of 0.0 with *VX* left free, registering that line as a streamline. The entire top surface was left free for all degrees of freedom, indicating that this surface is well above the boundary layer. This is the correct condition for this surface, but it emphasizes the need to make sure that this surface is much farther away from the wall than the maximum boundary layer thickness. Finally, the outlet condition was discussed at some length in Chapter 3, and all conditions are left free except the pressure, which was set to 0.0 on this surface. Like the channel problems of Chapter 4, this problem is incompressible, so pressure is all relative. Thus, the pressure value really does not matter as long as a condition is specified somewhere in the problem. For the flat plate, the pressure gradient is zero, so the pressure works out to be approximately zero throughout the domain anyway.

5.2.2 The Embedded Region Model

Just as for the cases of Chapter 4, the computational models and solution proceeded by creating variations on the baseline case of the embedded region problem, changing one or two parameters at a time to evaluate the effects. Table 5-3 lists the cases along with the total number of elements for each case model.

Table 5-3. Relevant Variations and Case Nomenclature for Three-Dimensional Embedded Region Models

Case #	Modified Variable	Value	# of Elements, Grid A
1	baseline	-	84,636
2	Z*	+0.001016	82,980
3	Z*	+0.000508	84,348
4	Z*	-0.000508	85,320
5	Z*	-0.001016	86,004
6	c*	+0.001693	83,484
7	G*	+0.003386	93,836
8	G*	+0.006774	101,772
9	Z* / G*	+0.001016 / +0.006774	99,468
10	Z* / G*	-0.001016 / +0.006774	101,124

In the case of a turbulent boundary layer, it is useful given the nature of the operation of the device to provide some measure of the physical parameters of the device in terms of scaling appropriate to the inner region of the boundary layer. The variable y^+ defined earlier in Chapter 3 is a logical measure of inner boundary layer scaling. Looking at the dimensions of the device in this way is useful in extrapolating the results of the device to other flow conditions – flows where the actual physical dimensions might be different, but the turbulent scaling values may be similar. Table 5-4 provides the major gage dimensions and the parameter variation levels in terms of boundary layer units.

Table 5-4. Relevant Parameter Baseline Values and Parameter Variation Values in Wall Unit Terms

parameter	Case #	value	Parameter variation	Case #	value
D^+_{HEAD}	1	1991.0	Z^+	2	19.9
G^+	1	33.2	Z^+	3	10.0
c^+	1	66.3	Z^+	4	-10.0
D^+_{BEAM}	1	6635.0	Z^+	5	-19.9
L^+_{BEAM}	1	829.0	c^+	6	33.2
			G^+	7	66.3
			G^+	8	132.7

In these alternate wall units terms, the laminar sublayer of the boundary layer typically has a height of approximately 7 – 10 and the boundary layer itself can be very crudely considered to be of the order of 5,000 or so [Schetz, 1993]. These reference values give an indication of the scaling of the parameter variations within the framework of the boundary layer and provide points of comparison to other flows. The parameter variations will be discussed in terms of the dimensionless star quantities in giving the results, but Table 5-4 is useful in further understanding the results.

Fig. 5-5 shows the mesh for the baseline Case #1 for the embedded region. Shown to the right at the inlet in this figure is a scaled representation of the velocity profile that was applied from the global problem. This profile is indeed typical of a turbulent boundary layer profile, with a very steep gradient near the wall, and very little change in the upper part of the boundary layer.

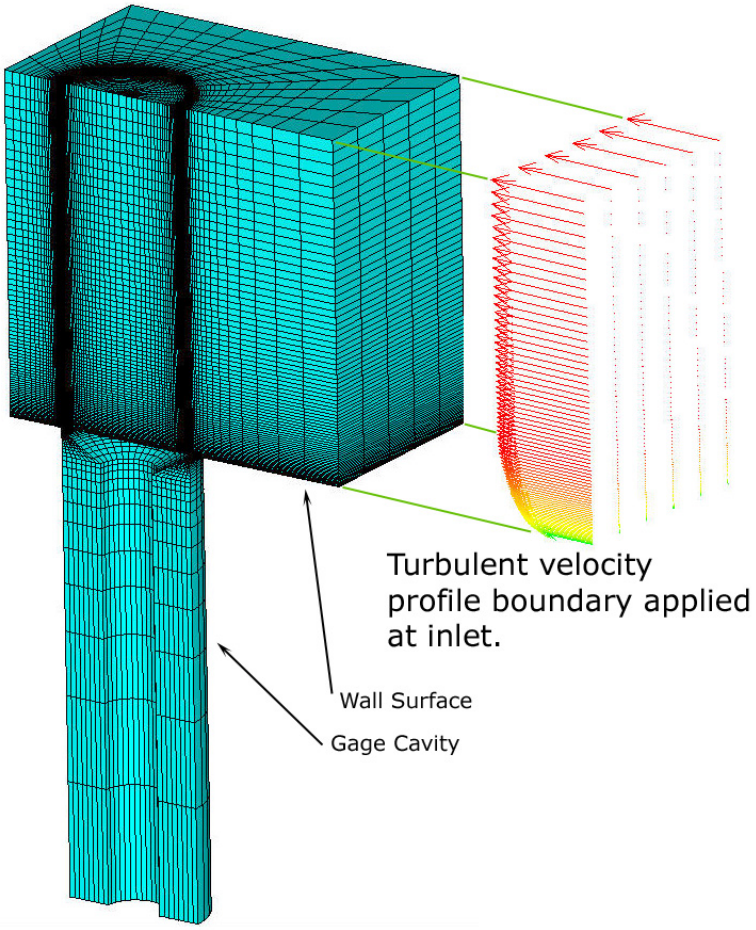

Figure 5-5. Mesh of 3D Embedded Region Baseline Case #1 with Velocity Profile Boundary Conditions

For all of the embedded region cases, conditions were taken from the well-converged global flat plate problem of Fig. 5-4 for all nodes at the $x^* = 3.23$ station. The two components of velocity (x and y), turbulent kinetic energy (κ), and turbulent dissipation (ε) were transferred. The conditions were applied uniformly in the z-direction, with the third component of velocity set to zero. The nodal spacing in the y-direction (the normal direction to the wall) for the embedded region exactly matched that of the global problem. This was done to insure that no interpolation was needed to transfer the conditions. Given the sensitivity of the degrees of freedom in the near wall region of a turbulent boundary layer, interpolation could have been a compromising problem.

Again here, all the wall surfaces of the gage body and surface wall received the no-slip condition. As before, the upper surface of the model was left to be free in all degrees of

freedom. Just like the global problem, the outflow boundary received the pressure condition of zero only, with all other degrees left free.

The new boundaries in the third dimension received standard treatment as well. The symmetry plane had a condition of VZ of 0.0 (normal to that surface), while all other conditions were left free. The outer boundary again was completely free just like the upper boundary, again indicating that the effects of the gage are not felt at that distance.

Fig. 5-6 shows a contained view of the gap region, upstream and downstream, for the symmetry plane of the baseline Case #1. As with the channel problems, the three-dimensional grid is just an extrusion of this mesh revolved around the gage centerline 180 degrees. As discussed briefly before, the placement of the elements adjacent to the wall was critical in these models, with a very tight range of accuracy in the wall treatment. Great effort was made to properly develop the mesh in this region, particularly at the gap interface, within the constraints for the design of the mesh. The resulting aspect ratio of the elements directly above the gap itself is not particularly desirable since large gradient levels are expected in this region of the model. It is, however, necessary to fulfill the more fundamental constraint of keeping the y^+ value just above 11.5. Fortunately, the mesh size is still of an order smaller than the gap size. Any issues of quality will be dealt with in Section 5.6 in analyzing the ordered discretization error.

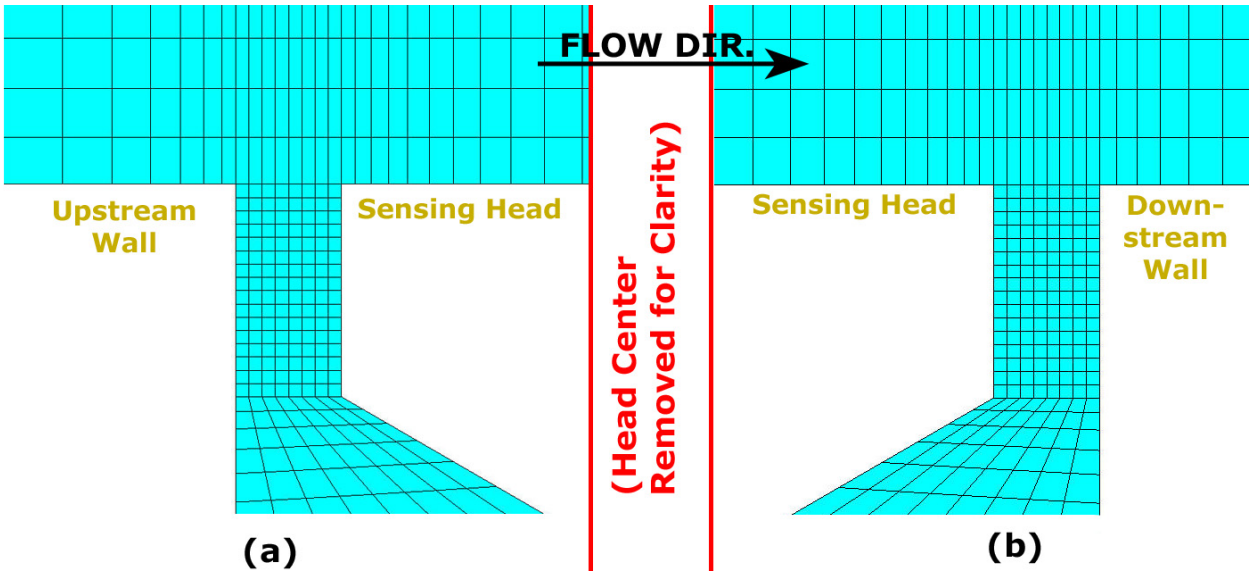

Figure 5-6. Mesh of 3D Embedded Region for Baseline Case #1 along Symmetry Plane in Gap Regions

Fig. 5-7 shows similar examples of the local symmetry plane mesh density around the gap region for some of the misalignment cases, where slight alterations were obviously necessary to account for the non-planar configuration. It was important to keep the wall element placement consistent, even though the elements on the head surface did not line up with their counterparts on the exterior walls. Fig. 5-7 shows the results of the necessary modifications to insure the correct and consistent calculation of shear stress. Given are the symmetry plane meshes for head protrusion Case #3 and head recession Case #5 in Fig. 5-7 (a) and (b), respectively as examples.

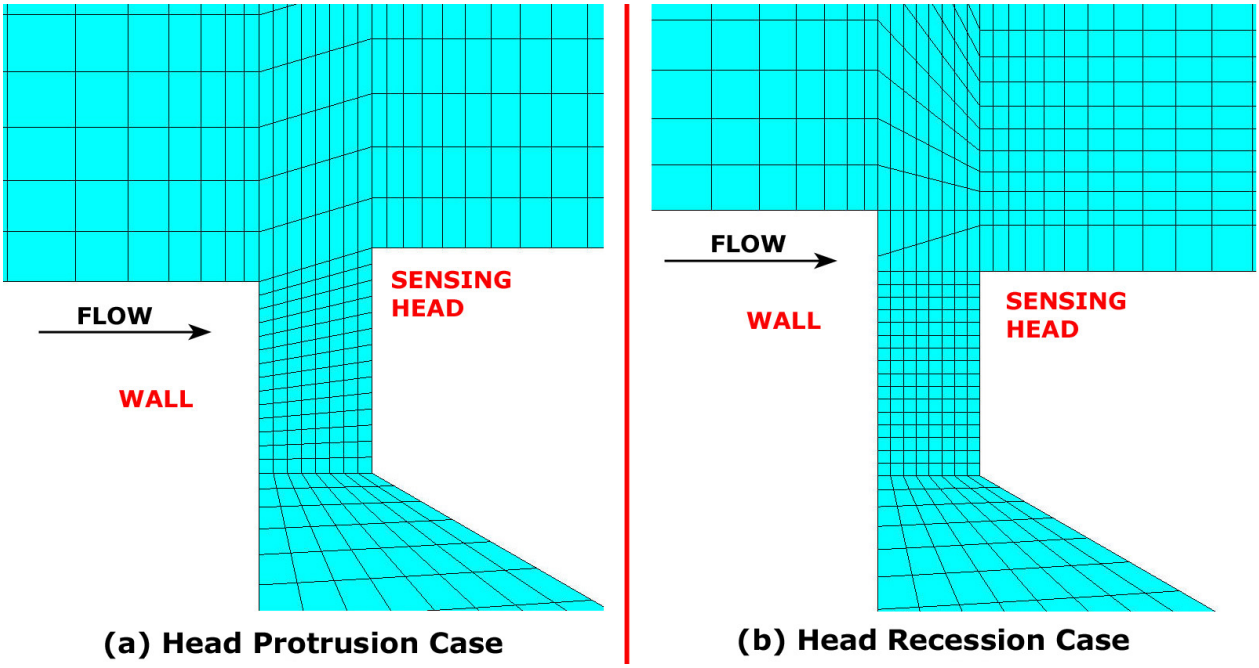

Figure 5-7. Mesh of 3D Embedded Region along Symmetry Plane around Upstream Gap for Head Misalignment Cases

5.3 Solution of the Global Flat Plate Problem without a Gage

The solution of the 2D, global flat plate problem is examined briefly first since it will impact the embedded region problem that is more centrally important. It was necessary to insure that the global solution is reasonable to avoid damaging the quality of the embedded region calculations. This is the reason for the discussion about near wall placement in the preceding section.

Fig. 5-8 shows the solution of skin friction coefficient, C_f, over the plate length for the mesh of Fig. 5-4, along with the matching experimental correlations of eqns. (5-1), (5-2), and (5-4). First, it is worth noting that the experimental curves do not really match very well with each other. The Schultz-Grunow formula matches quite well with the Blasius formula, but the Blasius formula required the crude $1/7^{TH}$ power law assumption from eqn. (5-3). Thus, its result is quite crude, and not as reliable as the other two. The Schoenherr formula predicts similar, but lower, levels of skin friction than the other two. The current numerical prediction falls right in the middle of the range covered by these experimental curves. This is encouraging, particularly considering the fact that one should not expect the numerical solution to exactly follow any one experimental correlation. Although the κ–ε turbulence model does make use of the empirical log law in its wall formulation, none of the experimental correlations are of the form required for compatibility with the log law results [Schetz, 1993]. All three correlations are simply curve fits of experimental data.

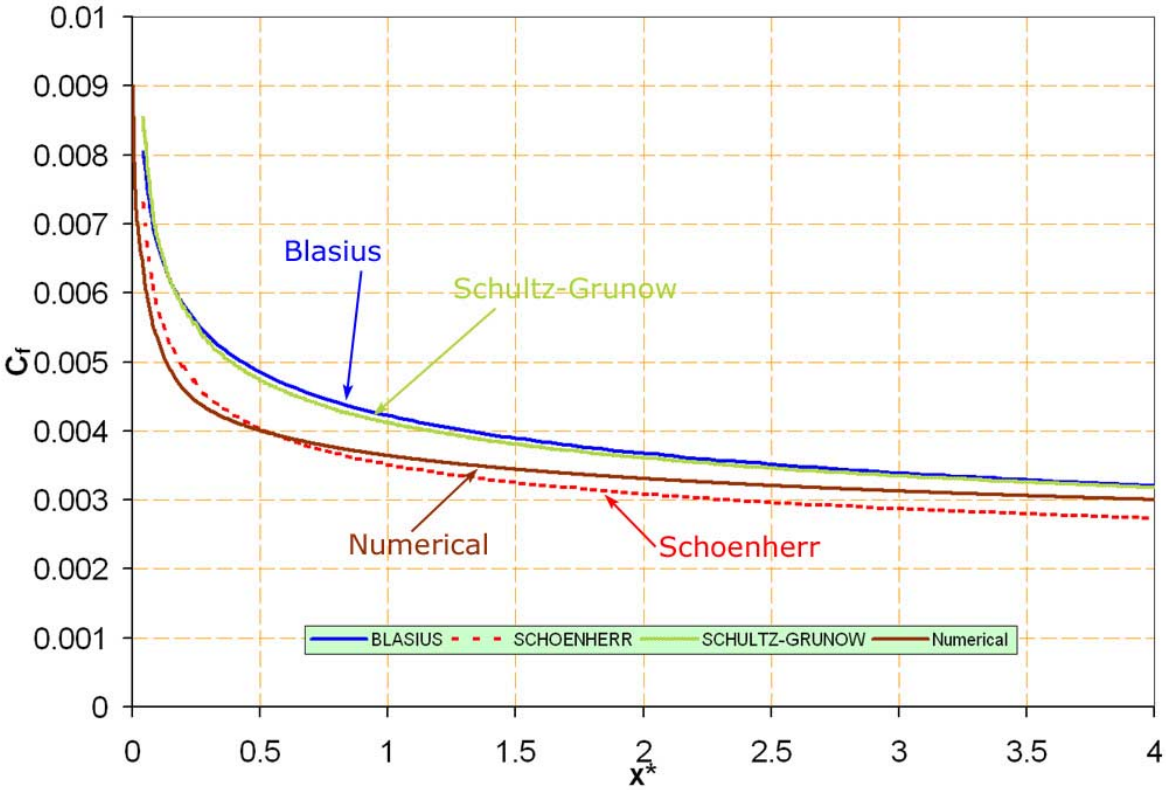

Figure 5-8. Computational and Experimental Results of Skin Friction Coefficient over Turbulent Flat Plate Length

The discrepancy occurs partially because of the laminar region which is known to physically exist near the leading edge of the plate. Fig. 5-9 shows a plot of the effective viscosity, which is just the sum of the laminar viscosity of the fluid and the additional turbulent viscosity from the turbulence model. Comparing with the dimensionless laminar viscosity of $2x10^{-6}$ from Table 5-1, the figure illustrates that the levels near the plate and near the upper boundary are very close to the laminar value, with a turbulent viscosity near zero. The turbulent viscosity grows with plate distance as the boundary layer becomes increasingly more turbulent, and the turbulent region never grows too large for the domain. Despite the fact that turbulence levels are low near the plate beginning, the algorithm itself is still turbulent, solving for values of κ and ε (even if they are small), and calculating shear stress based on these values rather than what one might use in a fully laminar problem. This changes the results, making laminar calculations difficult. Of course, the experimental correlations are not trustworthy near the plate leading edge either. Kays and Crawford [1993] explicitly state that eqn. (5-4) is really only valid above a Reynolds number based on plate length (Re_X) of 500,000. There are similar restrictions on the formulas in eqns. (5-1) and (5-2) as well.

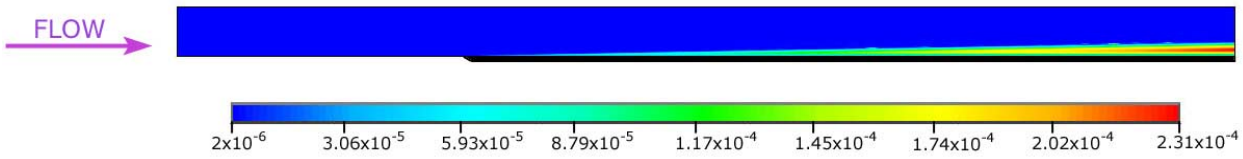

Figure 5-9. Turbulent Global Flat Plate Dimensionless Effective Viscosity Contours over Computational Domain

Even into the turbulent region there are other factors to consider. The computational model is a perfectly smooth flat plate. Also, the inlet boundary condition has exactly 0.0 incoming free-stream turbulence levels – perfect conditions in an ideal world. For all of the real experimental correlations, these conditions are not reasonable. Although the plates studied by all those researchers were smooth, the plates must have contained some small amount of surface roughness. As well, there is no discussion of free-stream turbulence attached to those formulas, but it is impossible for it to be exactly zero. Differing conditions like this, along with the usual experimental uncertainties help to explain why the correlations do not provide better agreement, and why the numerical result does not match exactly with any of the correlations.

Fig. 5-10 shows the y^+ values on the wall over the plate length, which are in the target range to stay just above the critical value of 11.5. Thus, from discussion in Section 3.4 and previously in this chapter, this is the optimal nodal wall placement for this particular CFD code. With this mesh, the nodes in the boundary layer that require solution based on the values of κ and ε reside the proper distance from the wall in the log region as they should for accurate boundary layer and shear stress calculation.

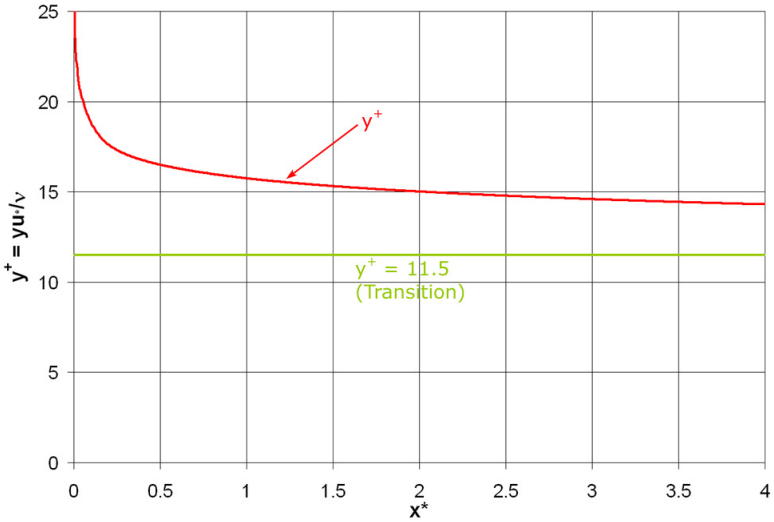

Figure 5-10. Plot of y^+ Values along Wall Surface over Turbulent Flat Plate Length

Finally, given the variations between the various results in Fig. 5-8, it will, unfortunately, not be possible to compare the results from the embedded region cases with an "exact" answer. Comparing these solutions to any one of the experimental correlations obviously seems to be unfair. Thus, the current global flat plate problem solution itself must be used as a comparison in order to be consistent. Since the position of the gage in the wall is known exactly, the length of the plate where the gage head will reside was numerically integrated to produce an average skin friction coefficient as a target value for the gage. Using the trapezoid rule over the 0.1016 length of the wall at the correct station resulted in an average C_f value of 0.00307. This is the number for the converged and undisturbed flat plate predicted with the numerical turbulence model. Thus, it is the target value for the sensing head, and the value used later to non-dimensionalize the force results for eqns. (4-4), (4-5), and (4-6).

5.4 Flowfield Results

As with the channel flow scenario considered in the previous chapter, presentation of the turbulent flat plate problem results begins with a look at the flows generated by the floating head of the gage to build understanding of the physical effects causing any changes in force and moment output. Flow analysis starts with a brief look at an initial test that was performed to evaluate the concept of the embedded region, as discussed in Section 3.5. This model consisted of a simple 2D representation of the floating head in the embedded region that was set up exactly as the later 3D embedded problems were with the transferred inlet conditions.

Fig. 5-11 shows the predicted skin friction results in the embedded region, compared with the global flat plate solution. The result verifies the hypothesis about the nature of the problem. The two places where the skin friction coefficient drops to zero represent the two gaps, upstream and downstream, where there is no "wall" and thus no wall shear stress. Even with the disruption of the gaps, the skin friction coefficient remains very consistent with that predicted for the 2D global problem with no gage. Upstream of the first gap, the two curves are identical, which is exactly what is expected. Thus, the embedded region concept and the choice of the upstream and downstream boundaries are validated for this case. Indeed, the region of influence of the gage for a 2D equivalent model will be much larger than in a 3D model of the actual gage geometry.

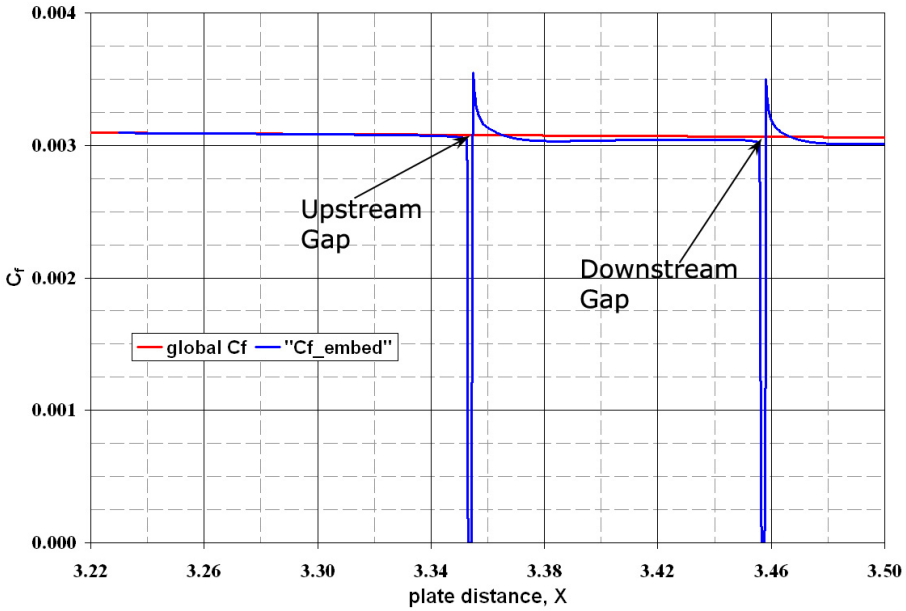

Figure 5-11. Plot of Skin Friction Coefficient in the 2D Embedded Region Test Case Compared with the Global Solution

5.4.1 Velocity Field Results

The flow patterns for the baseline Case #1 show some different characteristics than the results in Chapter 4 for the channel flow, since there is no longer a governing pressure gradient to drive the flow in the upstream gap region and out the downstream region of the gap. Instead, the result is the flow pattern in Fig. 5-12. This figure shows the upstream and downstream gap regions of the symmetry plane of Case #1. The large head area between the gaps is removed for clarity. Plotted in the background are contours of the *y*-direction dimensionless velocity component, overlaid with selected velocity vectors shown with scaling. Many points have been removed to make those remaining more visible. Fig. 5-12 (a) shows the flow in the upstream gap while Fig. 5-12 (b) shows the flow in the downstream gap, both at the symmetry plane of the gage body.

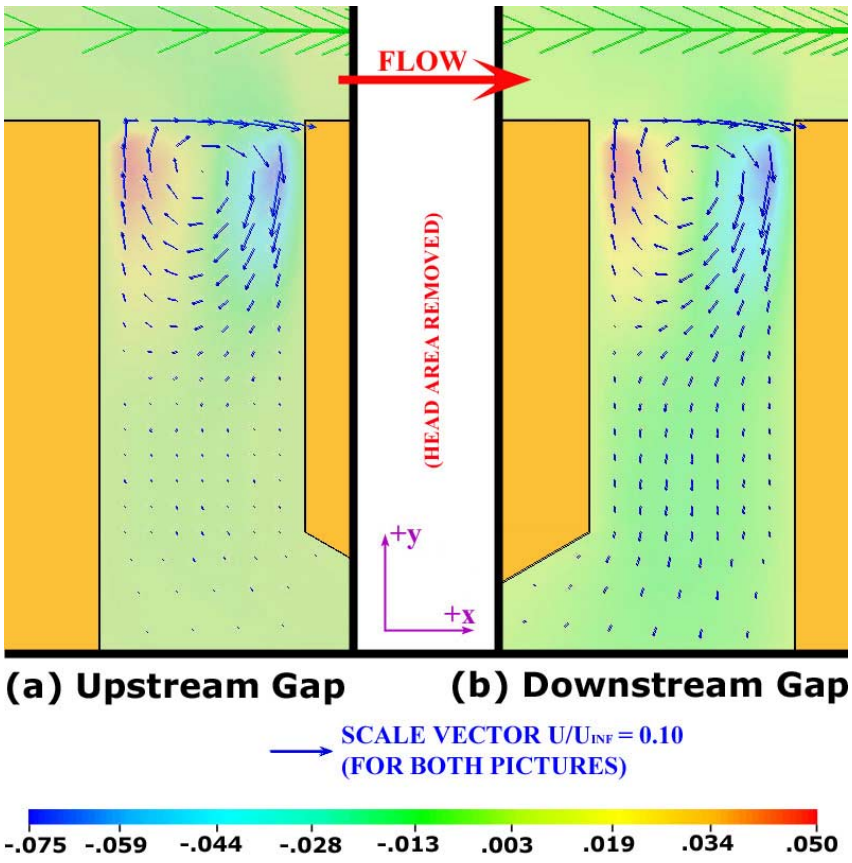

Figure 5-12. Velocity Vectors Over Y-component Velocity Contours along Symmetry Plane for Baseline Case #1 in Gap Regions (Vector Points Arbitrarily Selected for Clarity)

The flow patterns show the flow circulating in both gaps in almost the same manner, moving downward near the right edge of each gap where the *y*-component contours are blue and upward at the left edge of each gap where the contours are red. With most of the flow circulating in this region, only a small fraction of this flow actually escapes down through the gap. What is most interesting about this flow pattern is that at both the upstream and downstream gaps, the flow moves in the negative *y* direction, or into the cavity.

This seems counterintuitive, since mass must balance via the continuity equation for steady flow. Thus, any mass that enters the gage cavity must leave at the same rate. The solution to this issue can be found by looking at the flow from a different perspective – from the top down. Fig. 5-13 shows several contour plots of the *y*-direction velocity component at varying stations in the gap seen from above the gage looking down into the cavity. Positive values of the contours indicate flow moving out of the page and out of the gap, while negative

values indicate motion into the page and into the gap toward the cavity. The *y*-coordinate locations of the stations are indicated corresponding to the surface, Fig. 5-13 (a), the midpoint of the lip, Fig. 5-13 (b), and the bottom of the lip, Fig. 5-13 (c), or the top of the cavity. The result is that, as Fig. 5-12 indicates, the flow does indeed move down into the cavity at both the upstream and downstream locations of the gap (negative values). However, for the gap near the sides of the gage, the opposite occurs – flow moves out of the cavity back into the main flow (positive values) to balance the continuity equation. At the surface, Fig. 5-13 (a) at $y = 0$, the effect is strongest as the flow accelerates, and this effect has an important influence on the skin friction pattern that will be shown in the next section.

It should be noted that the flow shows some recirculation characteristics within the cavity itself, as the flow patterns do not seem to follow a direct path into and out of the cavity region. This determination is a purely qualitative observation, however, and it is difficult to make any quantitative conclusions in this region. The actual magnitudes of the dimensionless velocities in this region are on the order of 1×10^{-6} or lower. With this small scaling in the cavity region, the numerical uncertainty in the solution of this region is too high to make any definitive judgments. The fact that the velocity is close to zero, however, means that the shear stress along the walls of the cavity is also nearly zero, and the results also show that the pressure is approximately uniform in this region as well. These two results indicate that the flow pattern in the cavity is not an important feature in this analysis. The important internal effects occur only in the gap regions.

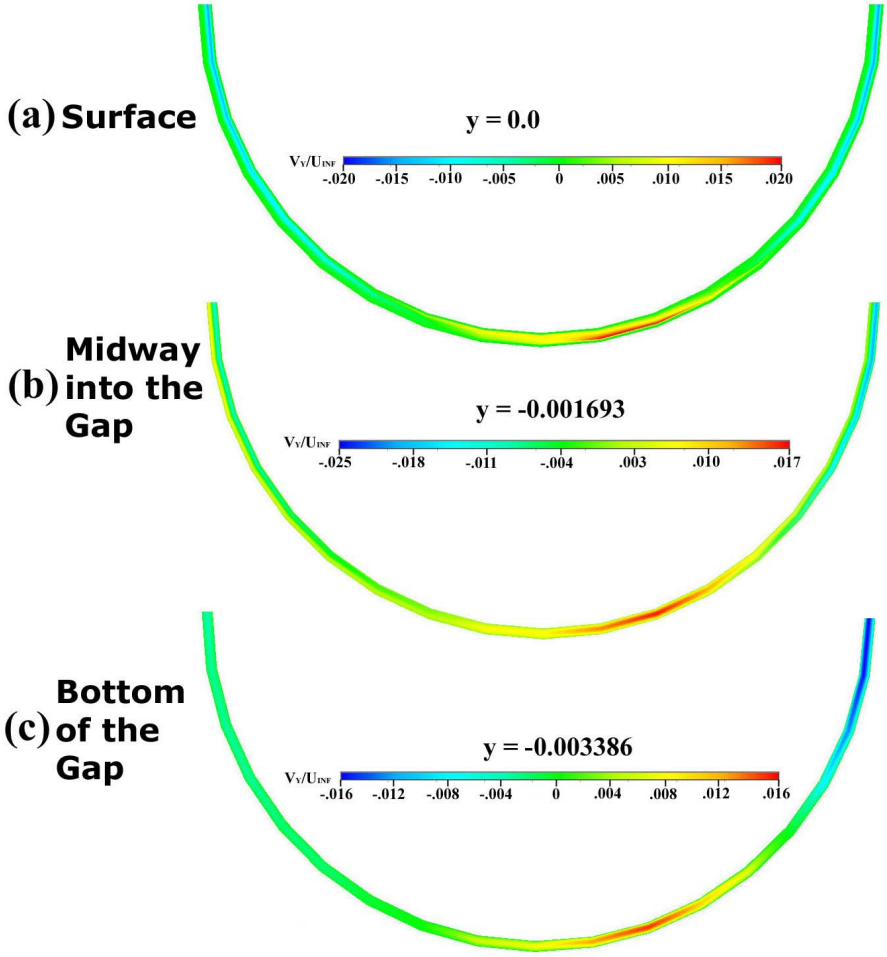

Figure 5-13. Y-component Velocity Contours in the Gap Region at Various Stations as seen from Above for Baseline Case #1

One issue that deserves some consideration is that of turbulence propagation, looking at effective viscosity values in some critical regions and assessing the physical realism of the turbulence modeling algorithm. More will be made of this in the final section of this chapter on the issue of validation, but a look at the visual aspects of the issue is prudent now. Fig. 5-14 shows contours of turbulent kinetic energy for the symmetry plane of the baseline Case #1. Turbulent kinetic energy (κ) is, of course, a measure of turbulence, and thus, this shows the regions of active turbulence in the model (along the symmetry plane at least).

Out in the free-stream flow above the boundary layer, the turbulence is expected to be small. Although Fig. 5-14 shows only the region around the sensing head along with about 25% of the exterior height of the domain, turbulent kinetic energy has already dropped to a very small

relative value. This corresponds approximately to the edge of the boundary layer region. Also, it was expected that turbulence levels would be minimal in the cavity of the gage, since the gap is quite small and the velocities are very low in the cavity region. Fig. 5-14 shows that indeed this expectation was justified by the physics of the flow.

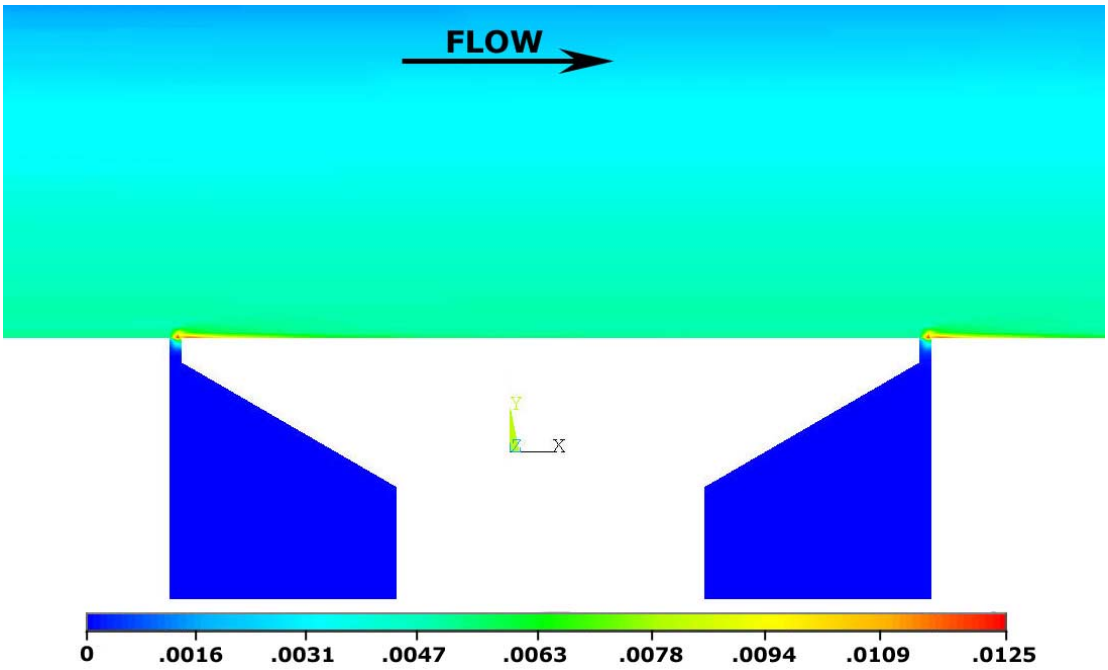

Figure 5-14. Contours of Dimensionless Turbulent Kinetic Energy from κ–ε Turbulence Model Solution of Baseline Case #1 as Seen in the Gage Symmetry Plane

In the gap and cavity regions, the value of the friction velocity u_τ decreases significantly, altering the characteristics of the turbulent wall model in the code. Since there are several nodes across the gap region, the code proceeds much as it does with the free-stream boundary layer flow. The near wall node is designated as being in the laminar sublayer in this case by the wall model, and the solution at the nodes out in the middle of the gap is calculated using an effective viscosity calculated from the κ–ε equation solution. The solution shows that values of turbulent kinetic energy are so small in the tiny gap regions of the gage that the turbulent viscosity is approximately zero regardless of the nodal wall placement. Equally, shear stress is small enough on the lip surface and wall cavity surface that its effects on the total forces are negligible. Thus, node placement in these areas is not governed by the same criteria of the node placement in the external boundary layer flow. Finally, it can be seen that streaks form near the wall after both

the upstream and downstream gaps, with high turbulence values in those regions. This feature will be discussed further in Section 5.6. It seems that the disruption of the gap with the sharp edge of the following walls generates the additional turbulence seen in these regions.

Fig. 5-15 confirms these observations, showing contours of effective viscosity over the same region as the previous figure for baseline Case #1. Effective viscosity is also a measure of the importance of turbulence, and it is a combination of turbulent kinetic energy (κ), and turbulent dissipation (ε). As with the turbulent kinetic energy, the solution shows that effective viscosity goes to approximately zero in the cavity region. Small disruptions directly above the gaps are to be expected, and they seem to disrupt the boundary layer only locally. Thus, the result is exactly what might be guessed, but concrete evidence validates what would only be hypothesis otherwise.

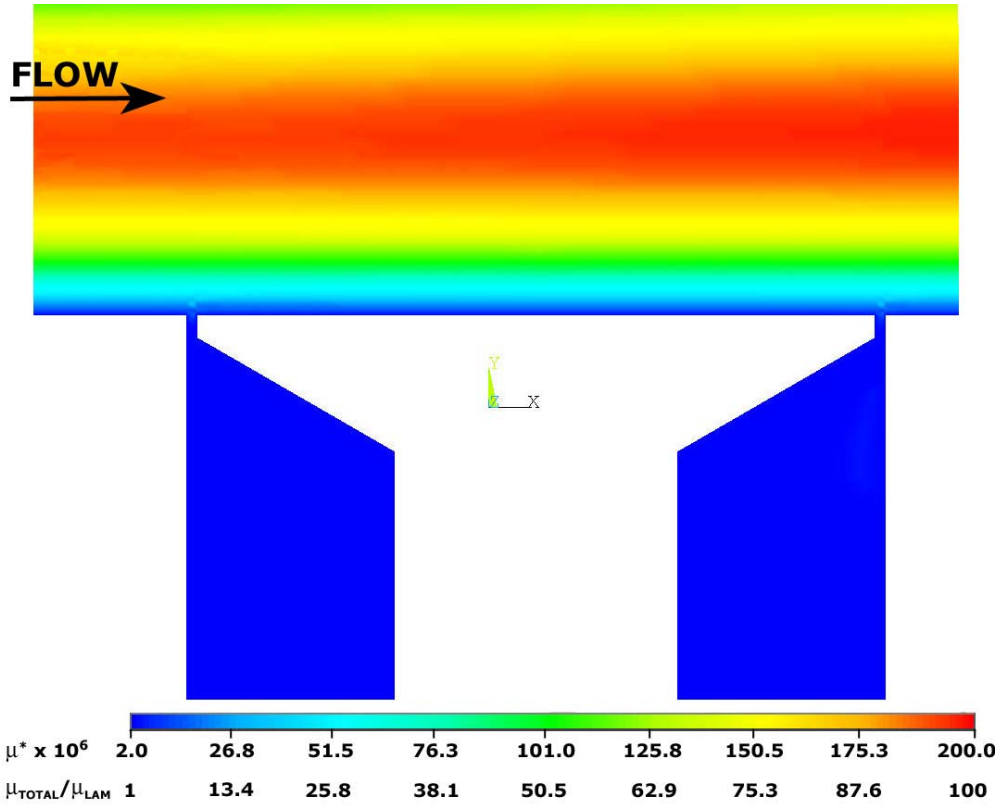

Figure 5-15. Contours of Dimensionless Effective Viscosity (Laminar plus Turbulent Contributions) of Baseline Case #1 in Gage Symmetry Plane

As might be expected, wider gaps cause increasingly stronger effects. Figure 5-16 shows selected vectors in the gaps, upstream and downstream of Case #8 with the largest gap in this study. Although the patterns are similar to that of the baseline Case #1, with flow swirling in both gaps, a comparison with Fig. 5-12 shows that the magnitudes of the vectors in this region are much larger than with the smaller gap. The visual patterns of flow are similar in both instances, but it is apparent that the differences in geometry in these two cases lead to a pronounced result. Because the gap is wider than the lip height in the case shown by Fig. 5-16, the velocity remains relatively high all the way down into the cavity, where in baseline Case #1 there was a significant decrease in flow strength caused by resistance into the cavity. This translates into a larger flow rate into the cavity area for Cases #7 and #8, the larger gap cases. This will certainly have an impact on the force characteristics presented in the next section, but even the simple presence of the flow is not desirable since the goal is to avoid disrupting the external flow at all.

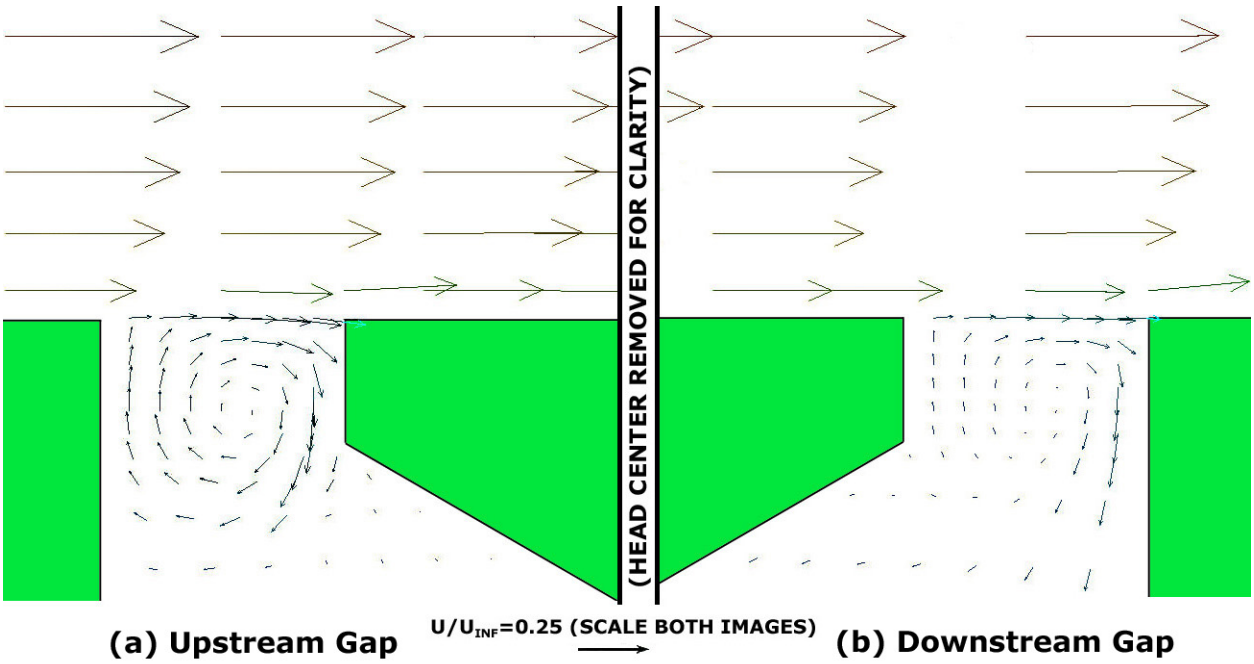

Figure 5-16. Velocity Vectors along Symmetry Plane for Largest Gap Case #8 in Gap Regions (Vector Points Arbitrarily Selected for Clarity in Flow Region)

As in the channel cases, misalignment plays a very important role in skin friction gage performance. This effect was studied by Allen along a flat plate similar to this one, although at

much higher speeds. As discussed in Chapter 2, his general conclusions included the fact that misalignment was extremely detrimental in making a good measurement. Flowfield imagery here solidifies this conclusion, as the flow contours for misalignment cases show a very different pattern than for the cases seen already.

Figure 5-17 shows the upstream and downstream gap regions for the maximum positive misalignment (protrusion) Case #2. The velocity vectors with appropriate scaling information is plotted over contours of the *y*-direction velocity component, giving an estimation of the flow rate through the gap into the cavity. The flow is quite different than for the zero misalignment cases. In this case, the flow proceeds along a definite course from upstream to downstream, moving into the cavity via the upstream gap and out via the downstream gap region. Magnitudes of the flow are somewhat larger than for baseline Case #1, but no more so than for the larger gap cases as shown by Fig. 5-16. However, the protrusion into the main flow produces large asymmetries in the flow which make the overall effects on the beam flexure much more dramatic than for a simple gap increase.

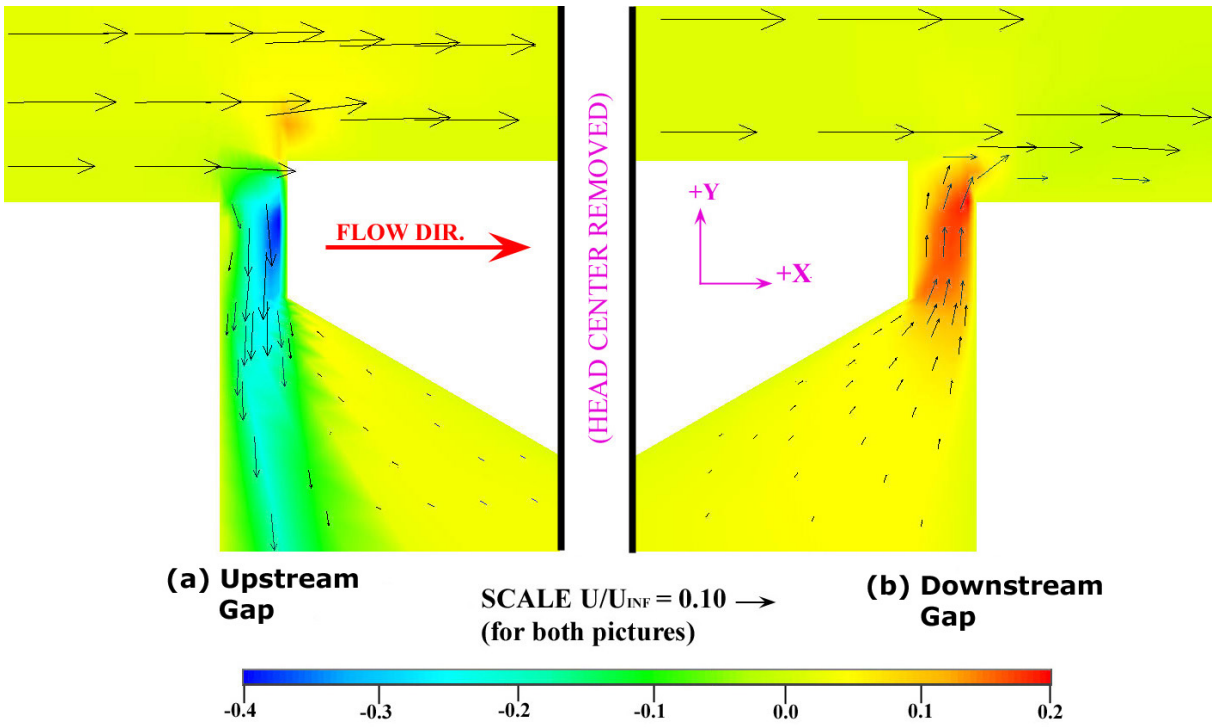

Figure 5-17. Velocity Vectors and Y-Direction Velocity Component Contours along Symmetry Plane for Upstream and Downstream Gap Regions for Head Protrusion Misalignment Case #2 (Vector Points Arbitrarily Selected for Clarity)

Figure 5-18 shows additional flow characteristics of this head protrusion Case #2. In this case, the flow field is viewed from above, with both the velocity vectors and magnitude contours (which are equivalent to the length of the vector) plotted. With a head protrusion, a very short, stubby cylinder sticks up into the main flow and away from the wall. A wake-like region is evident immediately behind the cylinder area as air is forced to flow around the sides of the cylinder and over the top. Although the wake directly is of no concern, it has the indirect effect of generating large pressure forces on the sensing head (a buoyancy force). In addition, the head surface is exposed farther out into the turbulent boundary layer, since it is no longer in line with the wall. This causes the total shear force to increase somewhat above the target value. Combined, these effects generate considerable deviation from the exact F^*_X of 1.0.

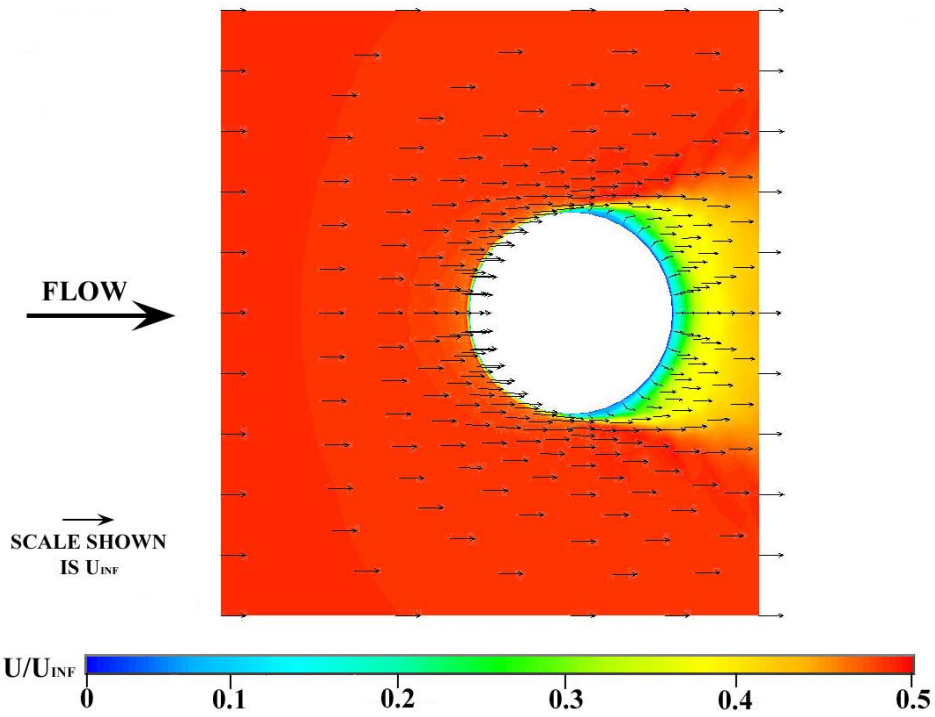

Figure 5-18. Scaled Velocity Vectors and Total Velocity Magnitudes at a Y* Station Approximately +0.0007 with Head Protrusion, Just Above Surrounding Wall and Below Head Level for Case #2

With the head protrusion cases in particular, turbulence model performance is a concern. The stagnation region just in front of the exposed cylinder where the flow is quickly decelerated to a stop and the region just behind the head with the wake characteristics generates some

concern, due generally to the complexity of the situation and the fact that the standard κ–ε model tends to have problems calculating in regions of high strain. Figure 5-19 shows the symmetry plane contour values of turbulent kinetic energy for the head protrusion Case #2 from the κ–ε solution. Regions of turbulence appear on the leading edge of the head surface, resulting from the sharp leading edge of the head sticking out into the flow. Additional turbulence generation occurs from the rear edge of the head, carrying downstream for a short distance before slowly damping out again to nominal levels. This seems as it should be in a general sense, leading to a general feeling of satisfaction over the qualitative performance of the turbulence model. Again, the details of the model will be looked at in Section 5.6 in a bit more detail.

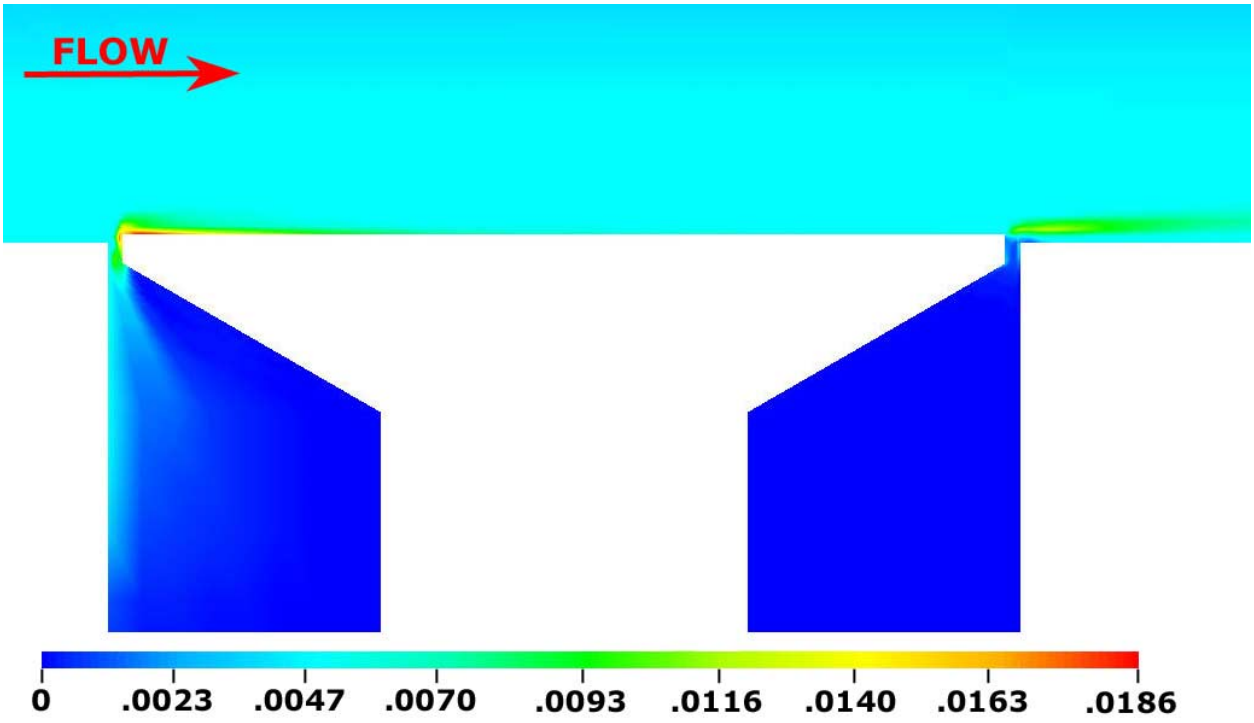

Figure 5-19. Dimensionless Contours of Turbulent Kinetic Energy (κ) in Head Region from Head Protrusion Case #2 along Gage Symmetry Plane

Results for the head recession Case #5 are pictured in Fig. 5-20, again along the gage symmetry plane. As with the other cases, this figure shows velocity vectors overlaying contours of the *y*-direction velocity component, illustrating flow into or out of the gap. The normal velocity magnitude is of a similar level to that of the head protrusion case shown earlier. The flow pattern, however, is exactly opposite what that case as revealed in Fig. 5-17. Here, the flow

moves into the gap at the downstream station, and back out at the upstream station in a reversed motion, showing little to none of the swirling flow that was seen in the non-misaligned cases.

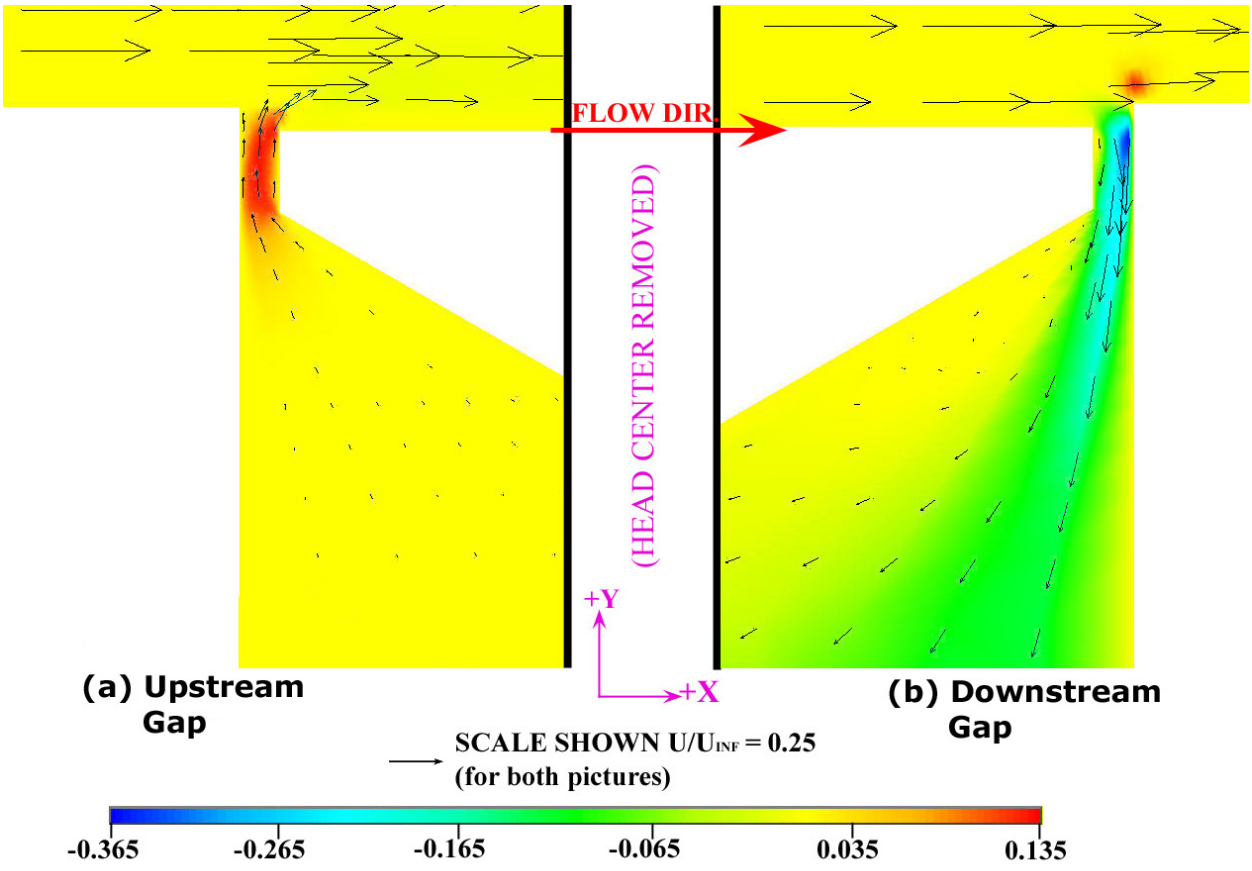

Figure 5-20. Velocity Vectors and Y-Direction Velocity Component Contours along Symmetry Plane for Upstream and Downstream Gap Regions of Negative Misalignment (Head Recession) Case #5 (Vector Points Arbitrarily Selected to Provide Clarity)

Finally, Fig. 5-21 presents the results of a comparison of the numerical results with the law of the wall at a point at the center of the gage head for the baseline Case #1, the protrusion Case #2, and the recession Case #5. This view of the velocity profile in the boundary layer illustrates the capability of the κ–ε turbulence model to model the experimentally obtained law of the wall in the boundary layer. The numerical data indicates that the turbulence model sufficiently replicates the law of the wall throughout its range of applicability. The law of the wall is typically quoted as being valid up to a y^+ of approximately 300, and one sees the expected departure from this standard for y^+ values higher than this range while the aligned and recession

cases show good correlation with the range of less than 300. Figure 5-21 also gives an indication of the changes to the flowfield caused by the misalignment parameter variation of each case. As shown by this figure, the aligned and the recessed cases show only minimal changes from the law of the wall within the log region. The protrusion case does show some significant changes in the boundary layer as a result of the misalignment of the gage. This change in the boundary layer will have strong effects on the total force on the floating head.

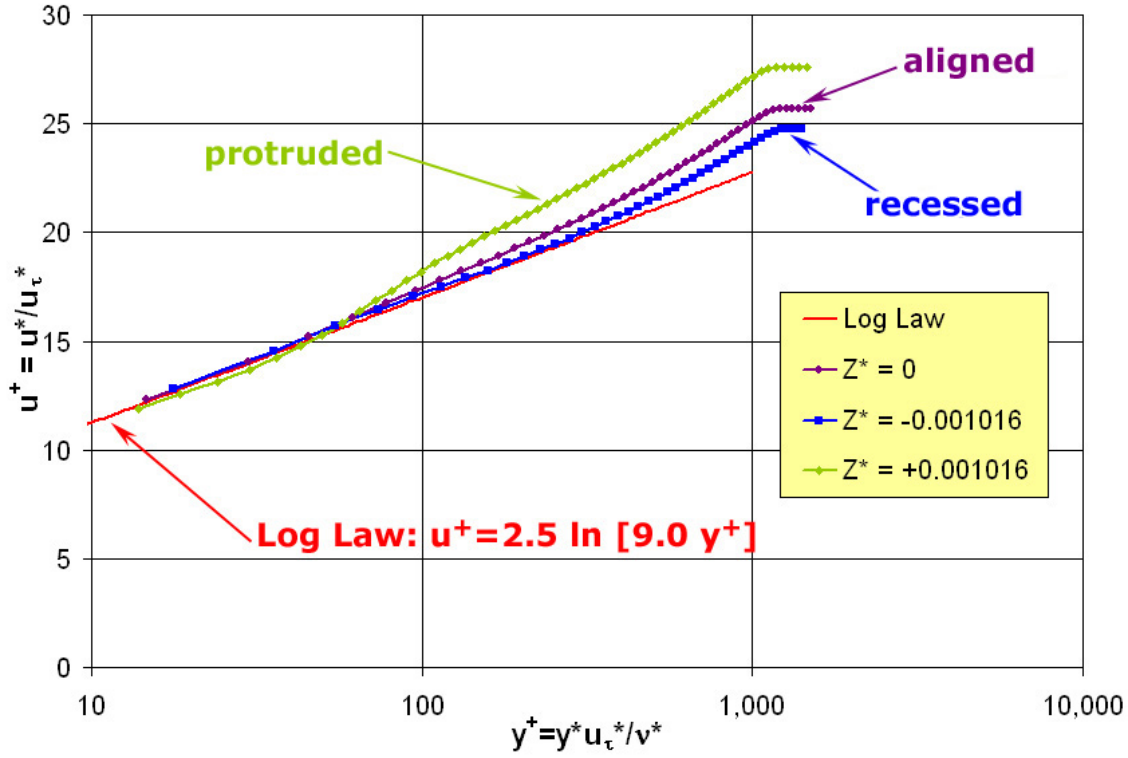

Figure 5-21. Comparison of Law of the Wall with Dimensionless Velocity Profile over 3D Boundary Layer of Baseline Case #1, Protrusion Case #2, and Recession Case #5 at Gage Center Station

5.4.2 Stress Field Results

For the baseline case, there is no bulk pressure gradient to affect the force measurement, and thus, one would expect the lip and normal forces defined by Allen in eqn. (2-2) to be small. The friction force should ideally be undisturbed by a small gap, but changes in the total friction force caused by the presence of the gap may affect the readings. This is generally the case, as

Fig. 5-22 shows a plot of skin friction over the head surface and surrounding wall region caused by the flow of the baseline Case #1. This plot shows the result of some features that were discussed in reference to Fig. 5-13 in Section 5.4.1. As Fig. 5-22 illustrates, the skin friction coefficient is relatively constant over the bulk of the head surface, and this constant value is close to the target value of 0.00307 calculated from the 2D global solution. Looking at the leading edges of the head and the rear wall behind the head, one can see a small localized increase in the skin friction value right at the rim of each. Also, on the wall directly behind the outside gap edges, there is a localized decrease in skin friction trailing downstream from the gap edges.

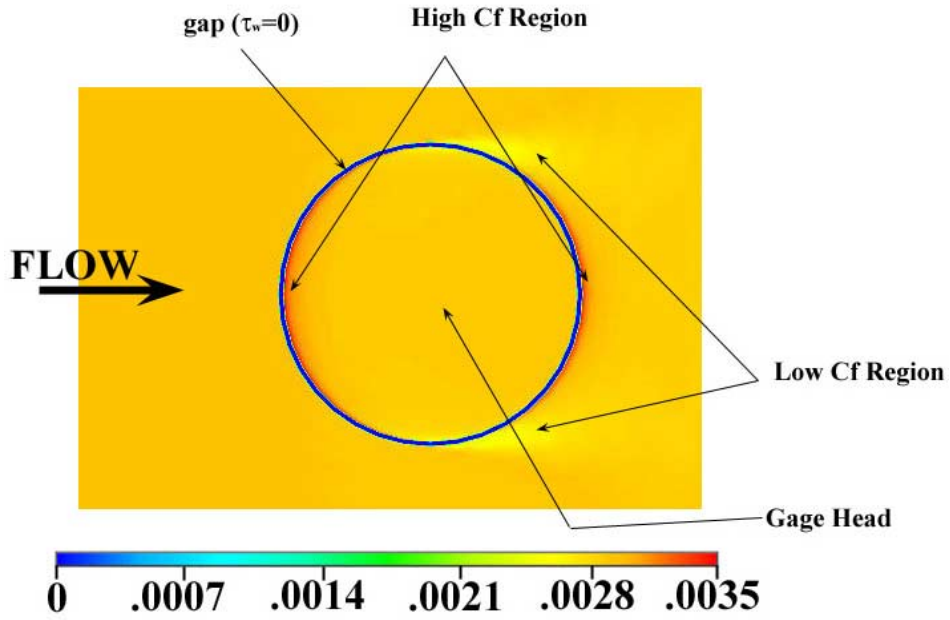

Figure 5-22. Variation in Skin Friction Coefficient, C_f, on Head and Surrounding Wall for Baseline Case #1

Schetz [1993] shows that, as a general rule, injection decreases skin friction, while suction increases it as does roughness (of which the gap might be considered a single element). It is no coincidence that these variations in skin friction on the surface correlate with the flow patterns seen in Fig. 5-13. One can see that the patterns of normal flow in and out of the gap correspond to the variations in Fig. 5-22. Earlier it was shown that much of the flow becomes trapped in the gap region for this case, circulating with only small amounts of flow actually

entering and exiting the cavity. Fortunately, these variations are small, and they act over a very small percentage of the head, with some of the effect on the surrounding wall rather than the head itself. Because of this, the total force due to shear stress is impacted only slightly for this case. Although small, these effects are nevertheless important.

For this case, the pressure force variation also deserves some brief consideration. Of course, the 2D global problem is one of a flat plate, which is a flow with zero pressure gradient. This is true in a numerical sense with the global problem, as the relative pressure solution is approximately zero within round-off and iterative convergence errors. Even with the gage body introduced, the pressure variations remain relatively low, but not zero as shown by Fig. 5-23. As a general statement, pressure is actually a little bit higher in the cavity than in the external flow, and it is quite uniform on all parts of the flexure inside this cavity.

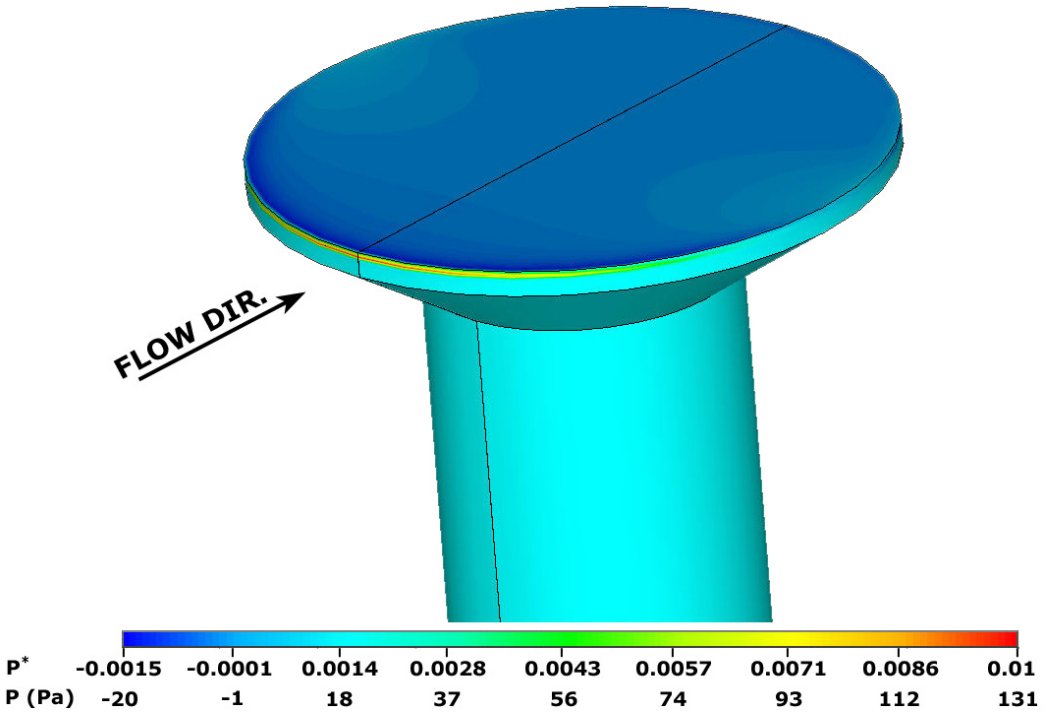

Figure 5-23. Variation in Pressure on Head for Baseline Case #1 as Seen from Upstream (Scaled Dimensionally and Non-dimensionally)

Although first intuition may be to assume that this is a purely numerical feature, a little reflection provides a different explanation. Since the velocity in the cavity goes virtually to zero, the dynamic energy of the flow must go somewhere. Much of the energy is dissipated within the

boundary layer, but some small part of it survives and is converted to pressure within the cavity. This effect is on the order of only a few Pascals, only a tiny fraction of the absolute pressure, but remember that small changes in pressure can be significant compared to the tiny shear forces sought. This pressure effect will contribute to the F^*_Y force, which will cancel out with symmetric strain gages, but which must be considered.

The same basic theory is true with the other interesting feature of Fig. 5-23. One can see a significant high pressure region just under the gage surface. This is also a stagnation issue, where the flow near the wall surface comes to a halt against the far wall of the upstream gap (against the head), as it begins to enter the cavity. Again, the boundary layer dissipates much of the flow energy, but some remains to affect the gage head. As Fig. 5-23 shows, this pressure force has a maximum of dimensionless pressure of 0.01, or 131 Pa in dimensional terms. In contrast the free-stream dynamic pressure is 0.5, or 6550 Pa. That dynamics pressure is 50 times the maximum pressure against the head. The pressure effect is small in this case, but it does make an impact on the total force. Misalignment cases obviously have much more complex pressure fields surrounding the head.

Figure 5-24 shows the contours of pressure for Case #8 with quadruple the baseline gap along the gage symmetry plane. The previous pressure graph, Fig. 5-23, showed the contours against the three-dimensional surface of the entire head, while Fig. 5-24 shows a cut through the entire symmetry plane of the flow. The pressure patterns on the surface are similar, and thus this view provides some contrast to the previous one. The same pattern can be seen in both cases, with a stagnation region forming against the upstream wall just under the surface. As this figure shows, the same thing happens on the downstream wall, although this fact is of no direct consequence in terms of the gage performance. However, the significant facet of comparison is the magnitude of the pressure variations. Comparing with Fig. 5-23, one sees that the pressure is almost 4 times higher in the stagnation region than in the corresponding location of baseline Case #1. The force results presented later in this section will show that the pressure contribution for baseline Case #1 is small compared to the shear force (which is good of course), and the pressure contribution for Case #8 with the large gap is still small, but much more significant, and an undesirable effect.

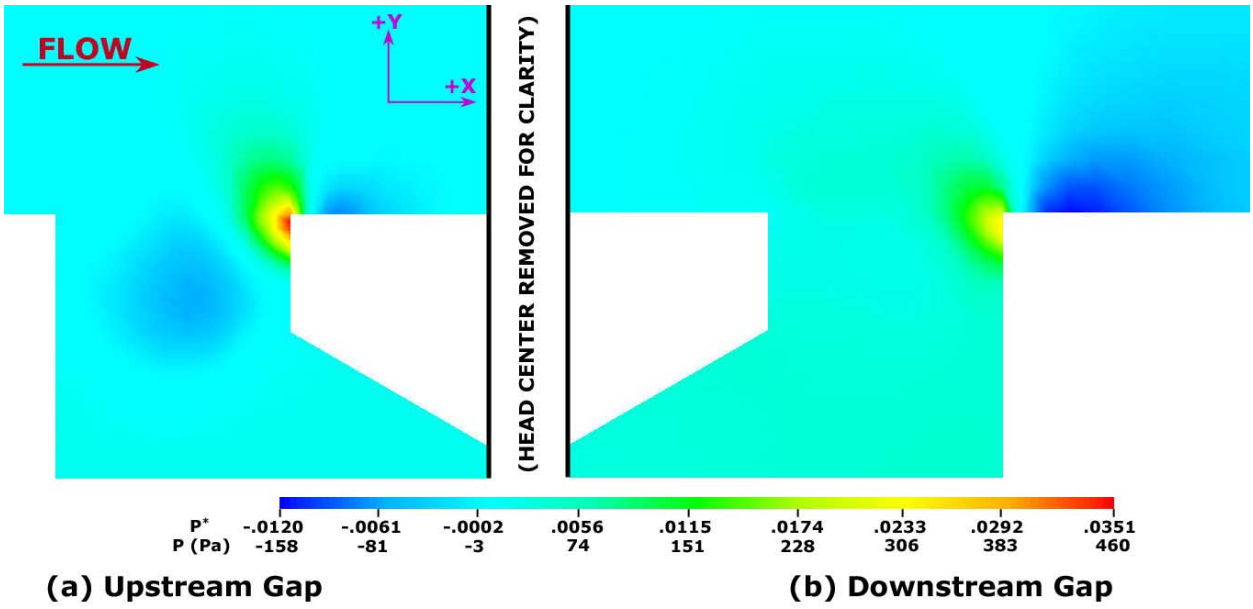

Figure 5-24. Variation in Pressure along Gage Symmetry Plane for Maximum Gap Size Case #8 (Scaled Dimensionally and Non-dimensionally)

Misalignment produces a much more complex situation, just as it did in the channel flow cases. Head recession Case #5 produces significantly different pressure variations than the non-misaligned cases do. Fig. 5-25 shows the pressure contours over the head surface for this head recession case. Here, remember that the front of the sensing head is sheltered down below the wall. In this case, the previously seen stagnation region in the upstream gap is not visible on the head. Instead, the pressure is high at the back half of the head surface, and it actually reduces considerably near the upstream edge. The magnitude of the pressure variations is moderately higher than in baseline Case #1. The placement of the pressure field, however, is such that a large negative moment will be created about the head center caused by the imbalance between the front and back edge pressure differences. This effect was not noticeable in the baseline case.

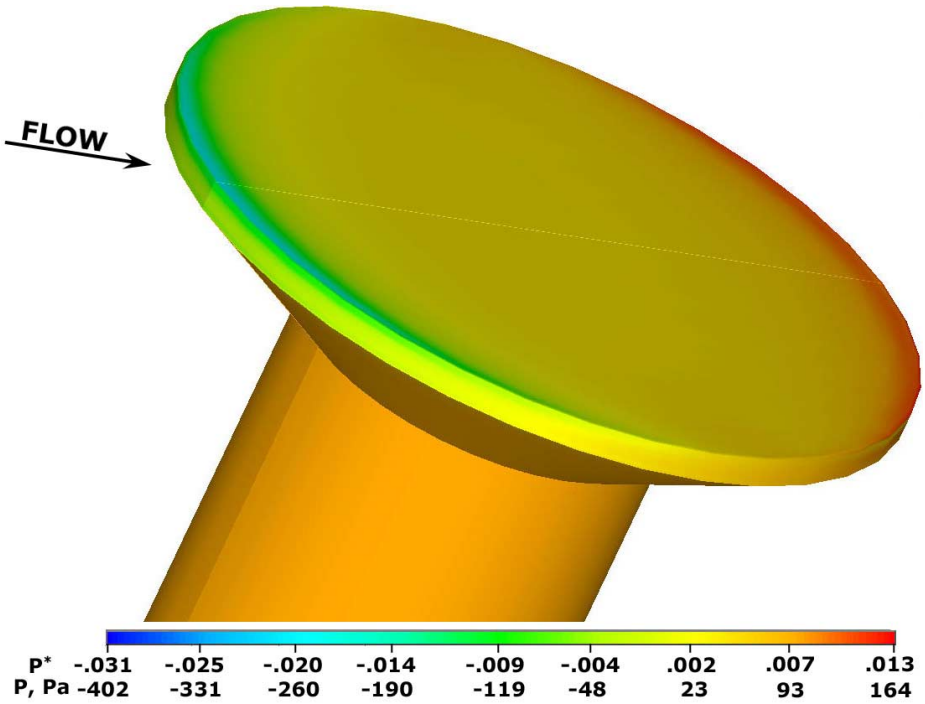

Figure 5-25. Variation in Pressure on Head for Z/D_{HEAD} = -1% Recession Case #5 as Seen from Upstream (Scaled Dimensionally and Non-dimensionally)

Fig. 5-26 shows the shear stress distribution over the sensing head surface, as seen from above. One may infer from the flow imagery and the pressure contours of Fig. 5-26 that the shear stress will be equally disrupted by the misalignment. This is true, although the disruption is perhaps not as dramatic as it might seem to be. It is easy to see immediately, however, that the skin friction coefficient reaches only a maximum value of 0.0028 for this case, meaning that the shear contribution will be at least 9% too small when compared to the nominal value of 0.00307. Also, since the distribution over the surface is not constant, the upstream part of the head experiences much lower stress values, further reducing the shear contribution below the desired value.

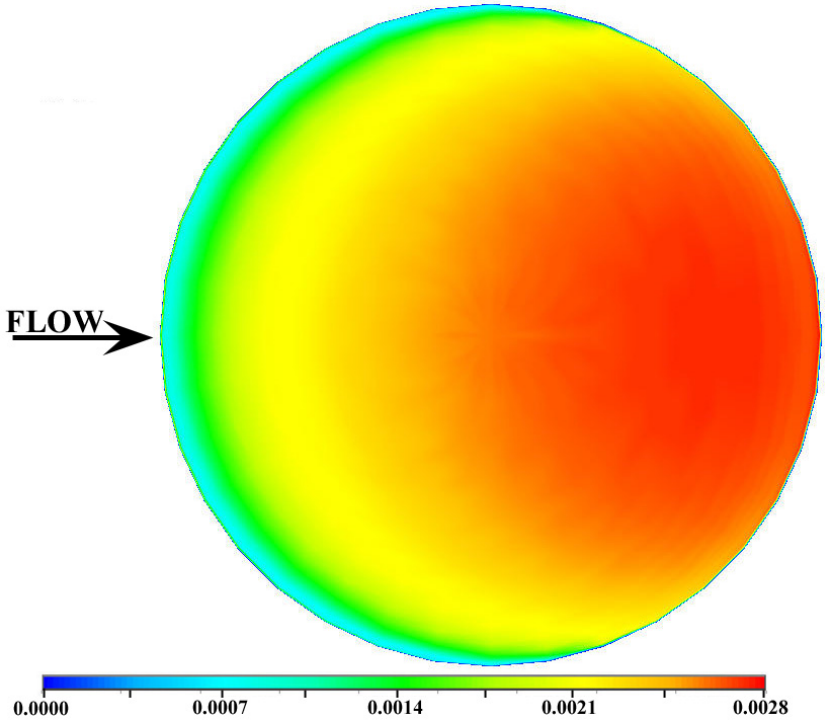

Figure 5-26. Variation in Skin Friction Coefficient on Sensing Head for Recession Case #5

Positive misalignment, or protrusion, is even worse in terms of force misbalance. Figure 5-27 shows the same pressure contours over the head surface for Case #2, the maximum protrusion case. Here, the sensing head is partially exposed out into the flow, and thus generates a much more significant stagnation region around the lip of the head. For this case, 30% of the lip area is actually exposed above the wall surface, and, with the gaps, the entire area is much more vulnerable to the flow effects. Obviously, as this figure shows, the pressure levels are much more significant, approaching quantities comparable to the dynamic pressure itself. The characteristics of the pressure variations are similar to that of the baseline Case #1, showing a seemingly uniform distribution with the exception of the front stagnation edge. This is somewhat of an optical illusion, however, because of the excessive magnitude of pressure for this region. Looking at the scales, the entire pressure variation scale from Fig. 5-23 can fit into one color division on Fig. 5-27. Thus, large variations exist on the surface of this head protrusion case which are masked by their scale in comparison with the maximum variation for the surface. Even though the pressure looks uniform on the head, large forces and moments are generated that contribute to the global totals. From the visual information in Fig. 5-27, one

would expect to see at the very least a large contribution to F^*_X from pressure. This is the case, as will be shown later.

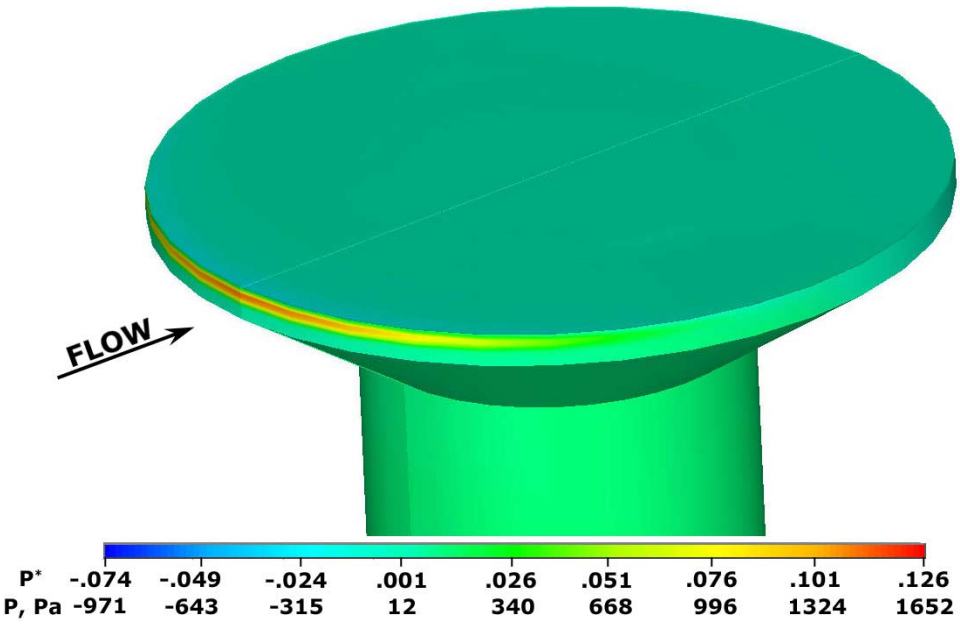

Figure 5-27. Variation in Pressure on Head and Flexure Surface for Z/D_{HEAD} = +1% Protrusion Case #5 as Seen from Upstream (Scaled Dimensionally and Non-dimensionally)

The shear stress pattern for the head protrusion case is equally interesting. Figure 5-28 shows this information as it is distributed over the head surface. Exposed out into the flow, the shear stress obviously increases significantly over the desired level. While the head recession case showed skin friction level deficits from the nominal value, the protruded sensing head sees skin friction coefficients substantially higher over large areas than the baseline Case #1, by about 10% to 15%. Much higher values occur locally near the leading edge of the gage, with skin friction coefficient values in that region exceeding the baseline by a factor of almost two. Thus, one sees that the shear stress contribution to *x*-direction force will be higher than desired. Coupled with the high contribution by the pressure term, deviations in output for protrusion cases can be expected to be excessively large.

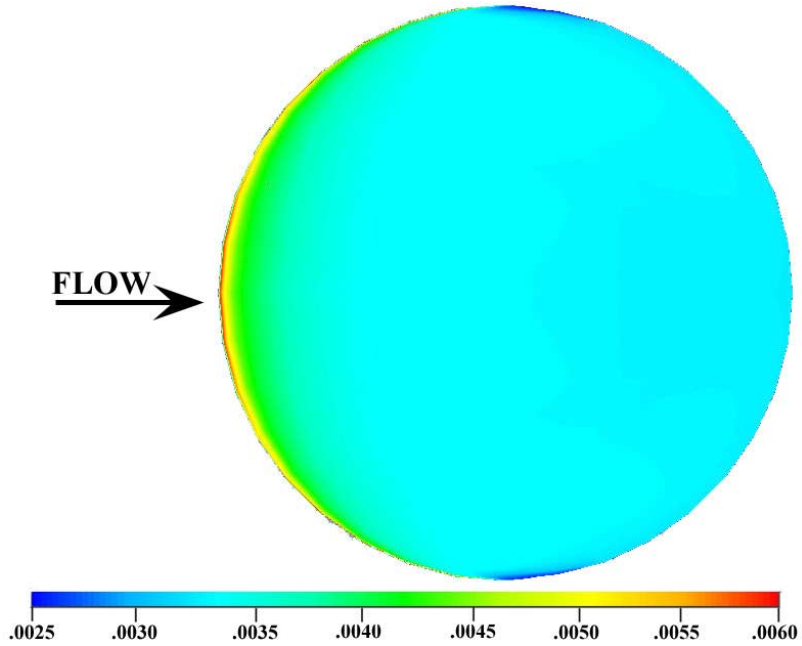

Figure 5-28. Variation in Skin Friction Coefficient on Sensing Head Protrusion Case #2

5.5 Force and Moment Results

As in Chapter 4, the force results are presented in a dimensionless form. Eqns. (4-4), (4-5), and (4-6) define the *x*-direction force, F^*_X, the *y*-direction force, F^*_Y, and the *z*-direction moment, M^*_Z. These values are exactly as defined in Fig. 4-21 with respect to directionality and location. Variation of the forces over the flexure becomes much more significant in this scenario because of the relatively high Reynolds number when compared to the low Reynolds number of the channel flow, in which the disruptions caused by the gage were small.

After looking at the stress fields above in Section 5.4.2, integration of the pressure and shear stress follows directly, as outlined by Appendix E. Misalignment is considered first, since it seems to be the most important parameter again for this external flow scenario. It also creates the most complicated effects of any of the parameters studied.

The effect of misalignment on F^*_X and M^*_Z are given in Fig. 5-29 (a) and (b) respectively. Figure 5-29 (a) shows that misalignment does affect the shear stress totals by the amounts indicated previously, which is on the order of +/- 20% for a given misalignment up to 1% of the head diameter. Figures 5-26 and 5-28 gave an indication of why this is so. The effect on the shear stress is small, however, when compared to the effect that misalignment has on the

pressure force. Figure 5-29 (a) shows that the pressure force changes dramatically, particularly for protrusion. The pressure effect remains small for modest recessions. Perfect head alignment results in some positive pressure force contribution, so that recessing the gage forces the pressure effect to cross zero before subtracting from the total at higher recession values. Thus, modest recessions offer some reprieve from the error levels that larger misalignments feel.

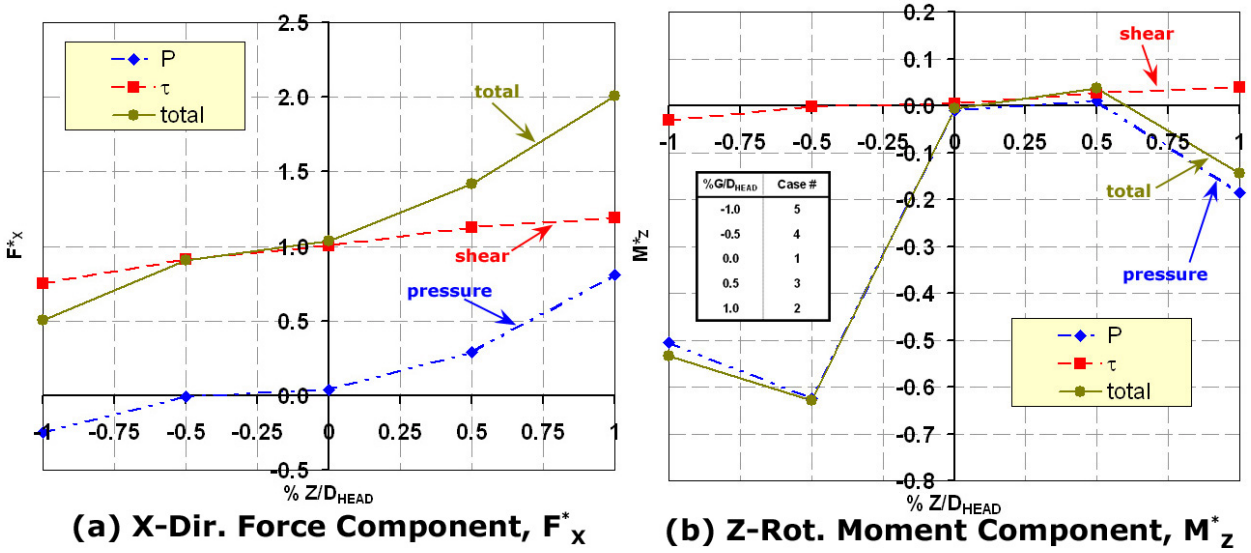

(a) X-Dir. Force Component, F^*_X (b) Z-Rot. Moment Component, M^*_Z

Figure 5-29. Effects of Misalignment Variation on Pressure, Shear, and Total Contributions of F^*_X and M^*_Z

Moment values are more erratic than the force values. The moment levels for the misalignment cases were among the most difficult values to calculate in this study due to their sensitivity to small uncertainties in pressure. Thus, Section 5.6 will show that these values are among those with the largest error estimations attached. The trend however, is that the gage produces virtually no moment effects at perfect alignment. This is excellent and to be expected since the shear stress passes through the moment center and the pressure force is both small in magnitude and acting quite close to the moment center via Fig. 5-23. As soon as misalignment occurs, however, the moment effect gets very large. Both protrusion and recession tends to produce negative moments, although recession interestingly seems to produce larger magnitudes because of the pressure imbalance seen in Fig. 5-25. The pressure acts such that the moment arm about the head center is long.

The ultimate result of the moment can be felt by the strain error, pictured in Fig. 5-30. For a given protrusion case, F^*_X is over-predicted, and a negative moment effect tends to increase the strain error beyond what the force contributes alone. For recession, however, the force F^*_X is under-predicted, but the moment still tends to add to the total strain error. Thus, there is a cancellation effect, with small recessions actually increasing strain error. This is a subtle point that is not intuitive without numerical evidence – a result of the fact that the moment increases with much smaller recession values than the force decreases. Ultimately, however, large recession values cause large negative strain errors, which is the logical conclusion.

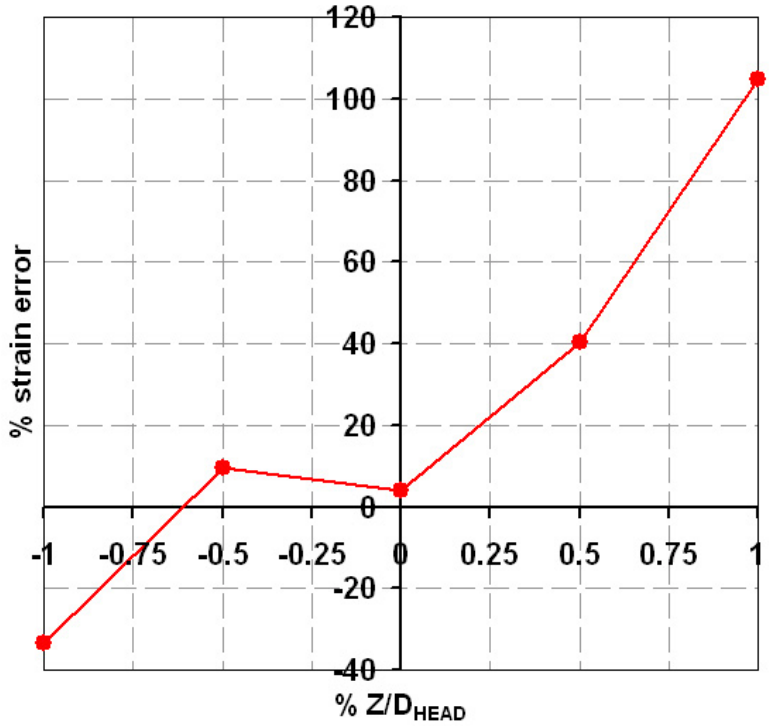

Figure 5-30. Variation of Strain Error with Misalignment Variation

The result of Fig. 5-30 is that recession really is somewhat to be preferred over protrusion, if a choice must be made between the two. This correlates to what was seen in the last chapter, and also with the conclusions of O'Donnell [1964]. Further, it tends to be the logical conclusion, since it seems intuitive that sticking the head out into the flow would be much more disruptive than removing it from the flow. This contradicts Allen's statement that there in no preference for misalignment.

It is useful to transform the results given from Fig. 5-29 to the form given by Allen in eqn. (2-2) for comparative purposes. Figure 5-31 shows the comparison of the lip force term and the normal force term from Allen's experimental data in Fig. 2-6 versus the numerical data from Fig. 5-29. The coefficient terms are given normalized by the target friction force component in each case, and this comparison is given as a function of misalignment as a percentage of the respective head diameters of the gages. First, it is difficult to make any exact quantitative comparisons of the data due to the large discrepancy in the flow conditions, gage dimensions, etc. A basic qualitative comparison, however, shows agreement with many of the general trends of the data.

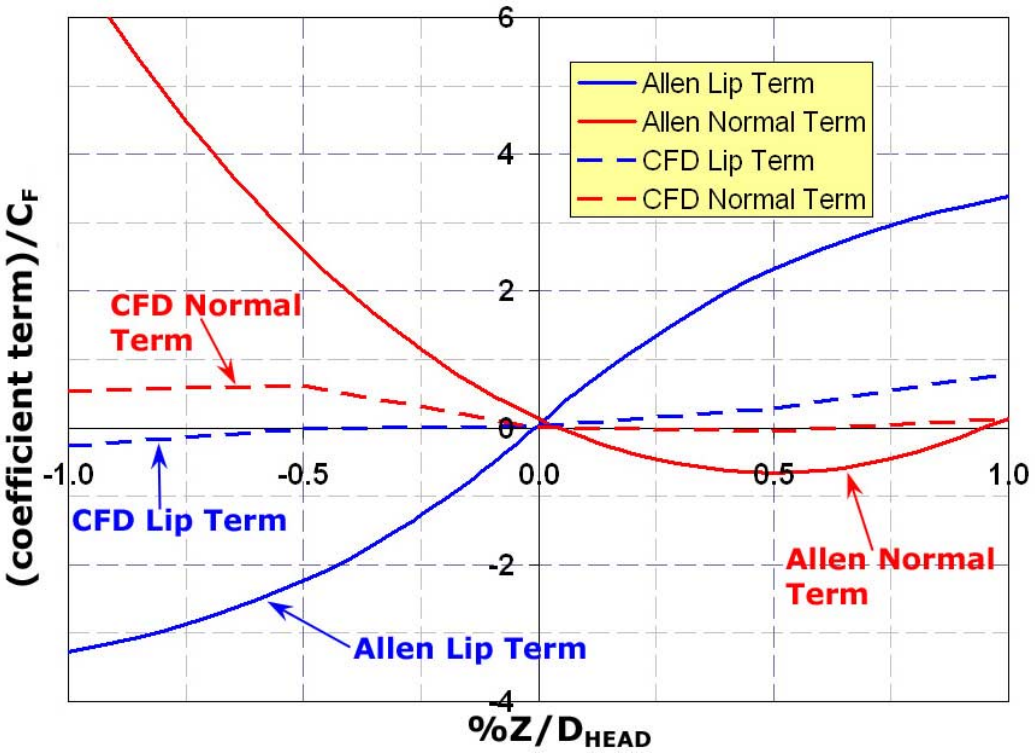

Figure 5-31. Comparison of Trends Given by Numerical Results from Fig. 5-29 with Experimental Results of Allen from Fig. 2-6

For the lip force term, both studies show a negative contribution to the total output for a recessed gage and a positive contribution for a protruded gage. Both Allen's experimental data the numerical data from Fig. 5-29 show increasing levels of lip force output for increasing misalignment in either direction. For the normal force term, a more complex relationship

follows. Recession shows large positive contributions to output for even small recession values. Protrusion shows that small positive Z values actually provide a small negative contribution to output, while this contribution becomes positive for larger protrusions. The numerical and Allen's experimental results show this trend for the normal force as well. Allen's supersonic test results show generally higher magnitudes than the incompressible flow numerical results given in Fig. 5-29, but a detailed quantitative comparison is impossible.

Finally, Fig. 5-32 presents the F^*_Y results for the misalignment variation cases. This is the only space devoted to the y-direction force in this chapter. The reasons for this were outlined in the last chapter, and continue to be valid here. Further, the F^*_Y values have a lot of uncertainty in them. The imbalance of pressure in the cavity and the external flow is what causes F^*_Y to exist. As with the moment presentation, this solution quantity is highly sensitive to even a small uncertainty in the pressure surrounding the head, and additionally the misalignment cases offer an extremely complex and delicate geometry to solve. Because an uncertainty in pressure gets integrated out over the entire surface area, F^*_Y is difficult to predict accurately for these cases. Of course, shear stress contributes nothing to the normal force. It does seem from the trends that misalignment, particularly protrusion, can generate increased levels of relative normal force when compared to the baseline Case #1. Again, shear stress levels tend to be so much smaller than the pressure forces that it does not take much change in pressure to overshadow the intended measurement. F^*_Y is normalized by the shear stress, so it is really a scale factor of the relative pressure to the skin friction coefficient. Of course, the importance of these values depends on the reference pressure level as already discussed and given by eqn. (4-11).

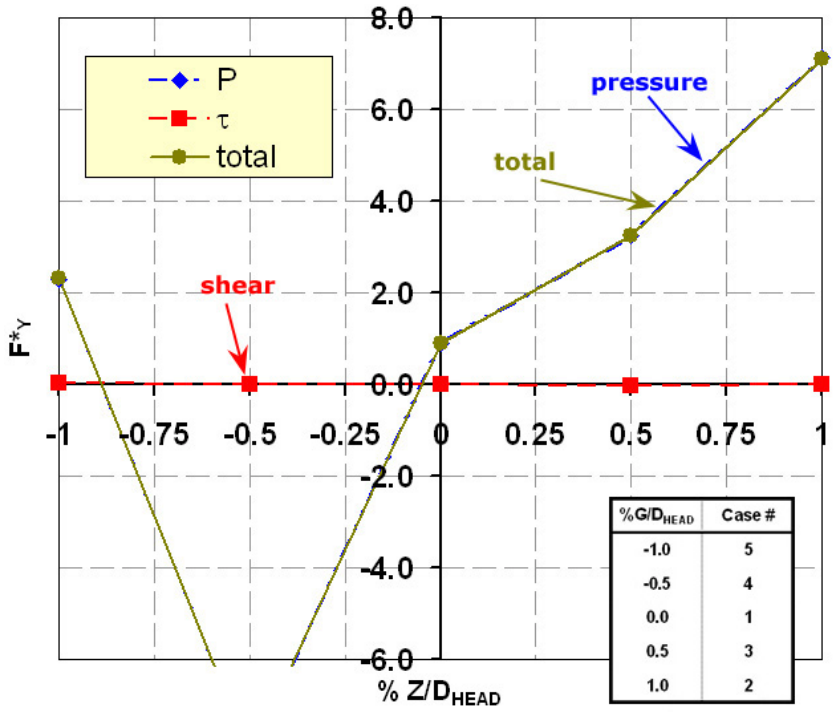

Figure 5-32. Variation in Y-Direction Force F^*_Y with Misalignment Variation Cases Showing Pressure, Shear, and Total Contributions

Next the effects of the gap are considered. In the channel flow problems, the effect of the gap was noticeable, but much smaller than the misalignment effects. The same is true here. Figure 5-33 shows the effects of gap size variation on the F^*_X force, which directly affects the error in shear stress interpretation. From Fig. 5-33, the shear contribution equals almost exactly 1.0 for all three cases, which is excellent. The fact that changing the gap size does not appreciably change the shear stress on the head is quite an encouraging result. With an increase in gap size, however, pressure begins to assert itself more. This is exactly what was expected from looking at Figs. 5-23 and 5-24. Increased gap size allows for more significant intrusion by the outer flow field, and thus higher pressure values against the upstream lip.

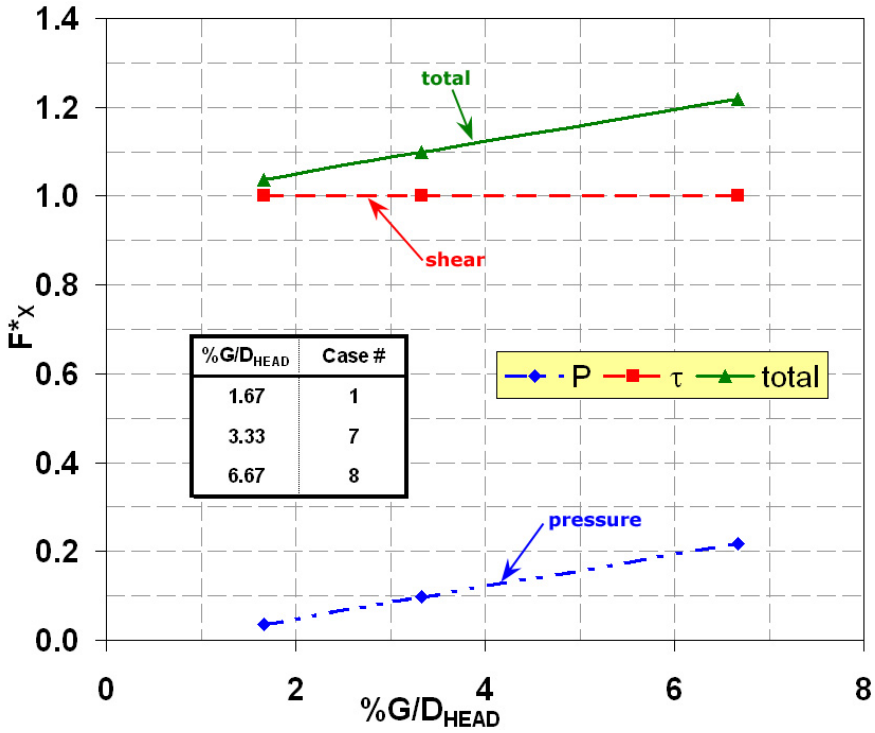

Figure 5-33. Change in X-Direction Force F^*_X with Gap Size Variation Showing Pressure, Shear, and Total Contributions

Figure 5-29 previously showed that the moment M^*_Z contribution from baseline Case #1 is almost zero, and this remains true for all three gap cases. There is some small moment increase with gap size, but this value is small enough to be inconsequential in terms of output error. Thus, there is no point in showing a graph for this component. With a trivial moment, strain error is a function of the total force only. This strain error is pictured in Fig. 5-34, which is approximately a straight line. The interesting issue in this figure is that the strain error will pass quite close to zero as gap size is reduced (within about 2%). Since the strain error is almost totally a function of pressure force alone, the same point can be made by Fig. 5-33. Any non-zero intercept in the graphs can easily be accounted for as being within the numerical uncertainty of the results. This fact, too, is an encouraging one. The result of the gap analysis is that the error caused by gap size can be considered to grow as a linear function of the gap spacing, with a perfect result occurring at zero gap size. This is in contrast to the channel flow problems where the pressure gradient seemed to impose some non-linear effects at small gap sizes. The slope of the strain curve can be estimated from the points, and, by forcing the intercept through zero, a

statement of error as a function of gap size can be postulated in eqn. (5-6) for these types of flow conditions – subsonic turbulent flow with no pressure gradient.

$$\%\varepsilon_{ERROR} = \left(41.5\text{mm}^{-1}\right)G \tag{5-6}$$

It is impossible given the current data to say whether eqn. (5-6) could possibly hold for supersonic conditions as well. The strain error estimation is given as well in Fig. 5-34 for comparison.

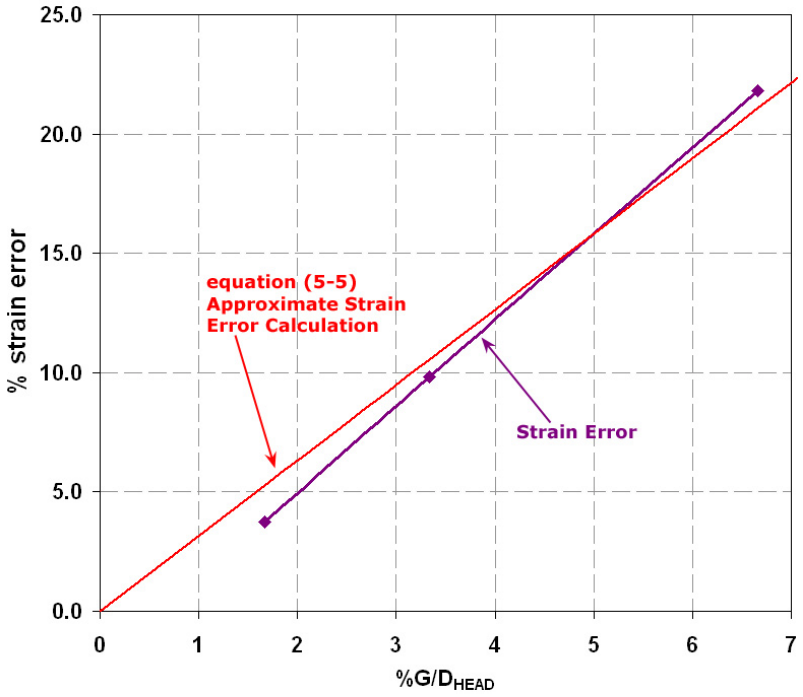

Figure 5-34. Change in Strain Error for the Gap Size Variation and Resulting Design Formula (5-6) Comparison

Eqn. (5-6) was developed based on a dimensional gap size in millimeters. Although the figures of this section are presented non-dimensionally as a percentage of the head diameter, this strain error is a result of the pressure force alone. The plots of Fig. 5-23 and 5-24 would seem to suggest that it is the gap size directly that has an impact on the strain error, as the spacing allows more or less pressure to infiltrate the gap region. Since the head is so much larger than the gaps, it is reasonable to assume that the gaps have no influence on each other, and thus G/D_{HEAD} is not a good choice for developing eqn. (5-6). This equation is contingent upon the caveat, however, that the gaps are actually much smaller than the head diameter so there is no communication

across the width of the head. The utility of eqn. (5-6) is twofold. First, it provides a tool for a designer of a skin friction gage to target a certain accuracy of measurement, assuming that the gage could be properly aligned. For crude applications, a larger gap may suffice, which would mean that the gage will be easier to machine and build (less strict tolerances). Second, it gives a reasonable estimate of the penalty paid for a given operational gage. This formula is an example of the fulfillment of the two primary goals outlined at the beginning of this document.

One of the major experimental results found from the literature search on the topic of skin friction error analysis is that a larger gap makes the head less sensitive to misalignment. Since it has already been shown that there is indeed some advantage to small gap size in these situations, this secondary issue was looked at as well to fully understand the premise. Cases #9 and #10 varied the sensor by the maximum misalignment extremes, but with the gap enlarged to the same value as in Case #8 (four times the baseline case). This represents four times the baseline gap size, allowing for comparisons to be made to see whether misalignment effects really do change with gap size or not. Figure 5-35 shows the results for F^*_X divided up by the contributions from pressure, shear stress, and the total force. Shown are the values for the modified gap cases #9 and #10 as well as the original gap Cases #1 through #5 for comparison. Since there is a great deal of information to process from this simultaneous variation of two parameters, the moment M^*_Z is plotted separately in Fig. 5-36.

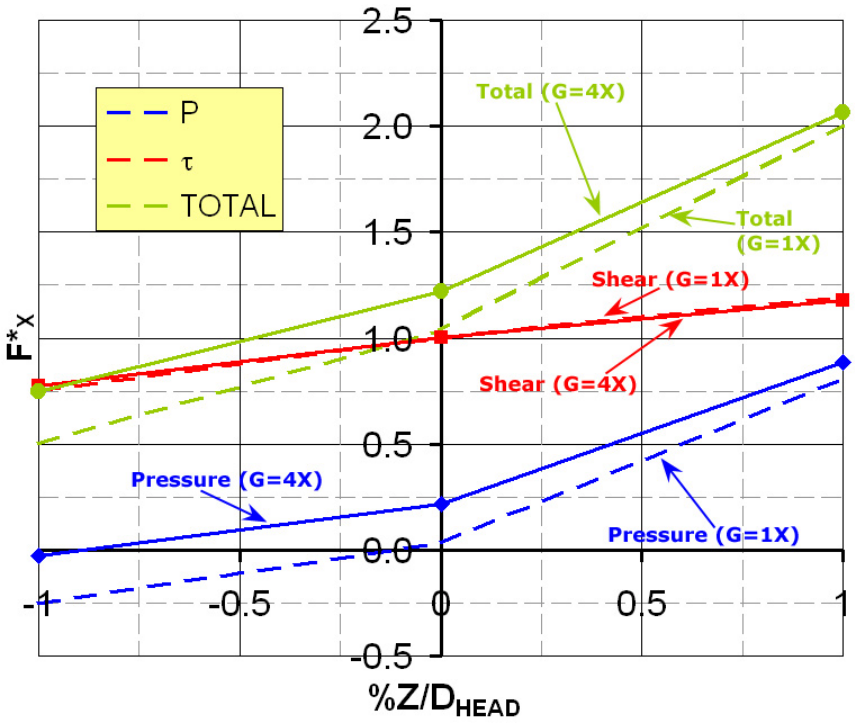

Figure 5-35. Variation of X-Direction Force Quantity F^*_X with Misalignment for Quadruple (4X) Gap Size, G/D_{HEAD}=6.67%, and Compared to Baseline Gap Size, G/D_{HEAD}=1.67%

Figure 5-35 shows many interesting features. As shown, the gap size change basically serves to shift the curves upward, without dramatically changing their slopes. Just as was shown in the simple gap variation study with an aligned gage head, the shear force shows little influence from gap size. This fact obviously remains true with misalignment. The pressure force, however, contributes additional force as gap size increases, which increases the total proportionally. However, gap change does seem to have a slightly larger effect on recession cases than protrusion cases. From this trend in *x*-direction force only, it seems that the influence of gap size grows with increasing recession due to the pressure force and decreases for greater protrusion.

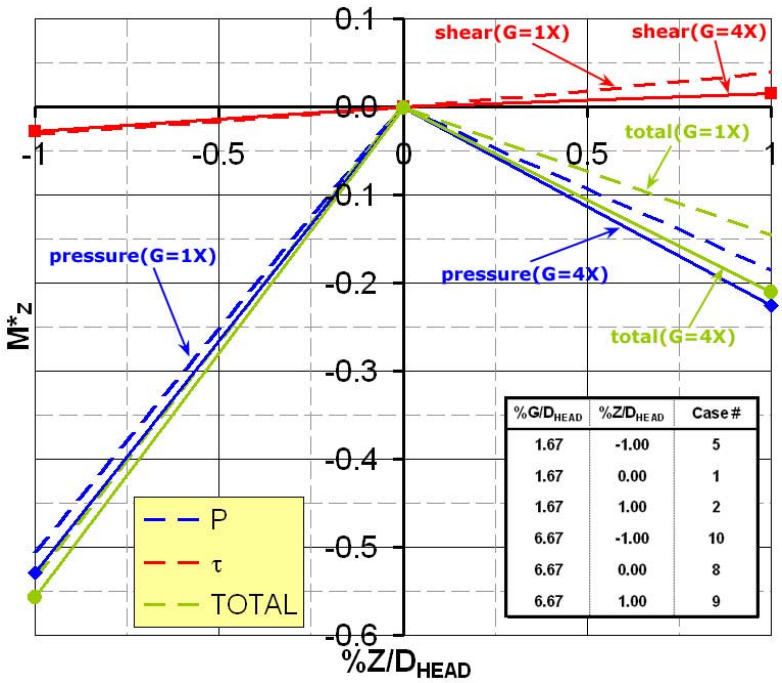

Figure 5-36. Variation of Z-Direction Moment Quantity M^*_Z with Misalignment for Quadruple (4X) Gap Size, G/D_{HEAD}=6.67%, and Compared to Baseline Gap Size, G/D_{HEAD}=1.67%

Fig. 5-36 shows that head recession effects have only a very slight dependence on gap size. Head Protrusion effects, however, do change somewhat. Both pressure and shear stress moment contributions become more negative with increased gap spacing. This has the effect of moving the shear component closer to the zero level, while pressure moves further negative. Figure 5-37 shows the resulting strain error for the two sets of cases. Again, the entire curve is shifted upward slightly due to the increased gap size. Looking at the respective difference between the misaligned and non-misaligned cases for each set, one sees that the quadruple gap does slightly decrease the changes. The difference between the 1% head protrusion and the aligned case, for example, reduces from about 101% to about 91% for the large gap. This decrease does support Allen's supposition on this point, but the effect is relatively minor considering that the overall deviance from the desired value of output is greater with the larger gap, and the head protrusion case is still off by over +/-100%. The recessed head, however, does exhibit a value closer to the desired value with a large gap size because of the cancellation of the force and moment effects on the head.

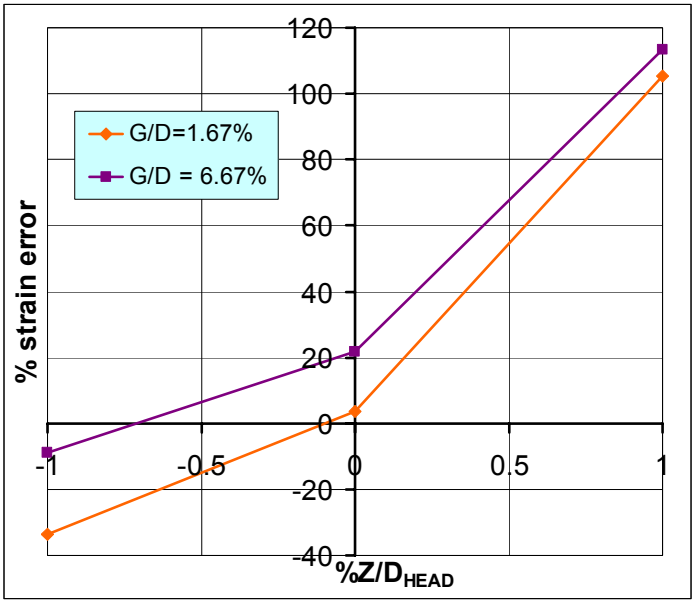

Figure 5-37. Strain Error with Misalignment Variation for Baseline Gap Size, G/D_{HEAD}=1.67%, and also with Quadruple Gap Size, G/D_{HEAD}=6.67%

Finally, the lip thickness effect variation from baseline Case #1 and Case #6 is considered briefly. In the channel flow cases involving a governing pressure gradient, the lip size made a significant impact on the outcome. Here, things are different. Without an imposed pressure gradient, the size of the lip has virtually no impact on the resulting forces or moments. Figure 5-38 (a) shows the results of dividing the lip thickness in half on all three global parameters: F^*_X, F^*_Y and M^*_Z. Next to it, Fig. 5-38 (b) shows the strain error from these two models resulting from F^*_X and M^*_Z, summed as usual. It is clear that, between these two cases, almost nothing happens. While the strain error does indeed increase slightly with lip size, the change is less than 0.25%, which is not a significant deviation after considering changes in excess of 100% caused by some of the other parameters. Because so little was seen from this parameter for these cases, no further c^* variation were tried. Although c^* has no real impact in a zero pressure gradient flow, it should not be overlooked. As soon as a pressure gradient is applied, lip thickness begins to get more important again. Since it is difficult in a real situation to guarantee that there will not be any pressure gradient, it is still wise to minimize lip thickness on the basis of the results of the last chapter.

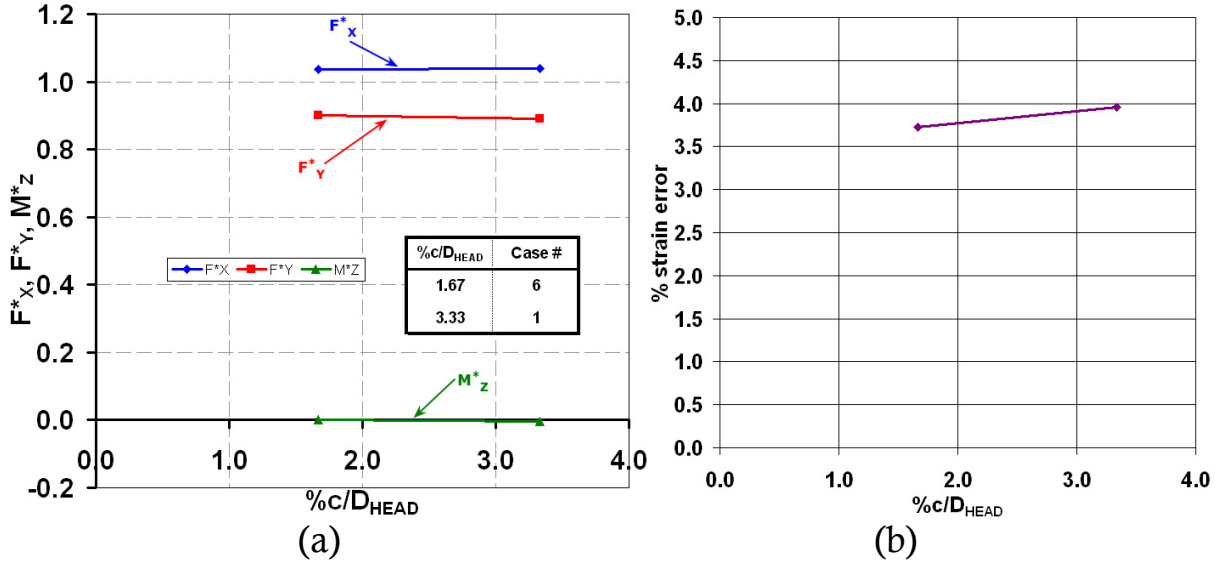

Figure 5-38. Total Lip Thickness Variation Effects on Global Parameters F^*_X, F^*_Y, and M^*_Z and Strain Error

This concludes this section concerning the results of the force effects on a direct measuring skin friction gage acting in a turbulent flow on a zero pressure gradient flat plate. Just like in Chapter 4, the numerical results are tabulated in Table 5-5 for use by others later. These values have been used in developing all of the graphs of this section.

Table 5-5. Numerical Summary of Relevant Dimensionless Force and Moment Results for Various External Flat Plate Flow Cases

Case #	F^*_X			F^*_Y			M^*_Z		
	total	pressure	shear	total	pressure	shear	total	pressure	shear
1	1.0371	0.0358	1.0013	0.9005	0.9009	-0.0004	-0.0060	-0.0097	0.0036
2	2.0052	0.8114	1.1938	7.1053	7.1176	-0.0123	-0.1451	-0.1848	0.0397
3	1.4155	0.2881	1.1274	3.2353	3.2527	-0.0174	0.0365	0.0099	0.0265
4	0.9053	-0.0076	0.9129	-8.0784	-8.0752	-0.0032	-0.6279	-0.6257	-0.0023
5	0.5048	-0.2484	0.7533	2.3194	2.3006	0.0188	-0.5343	-0.5041	-0.0301
6	1.0387	0.0373	1.0014	0.8906	0.8911	-0.0005	-0.0031	-0.0067	0.0036
7	1.0981	0.0972	1.0008	1.1198	1.1226	-0.0028	-0.0002	-0.0002	0.0000
8	1.2180	0.2172	1.0007	1.1335	1.1509	-0.0174	-0.0007	-0.0007	0.0000
9	2.0647	0.8884	1.1764	3.2333	3.2455	-0.0122	-0.2107	-0.2253	0.0146
10	0.7463	-0.0273	0.7736	1.2278	1.2257	0.0020	-0.5568	-0.5291	-0.0277

5.6 Validation and Verification

Almost all validation and verification for these complex models was carried out in two-dimensions rather than three. Although it would certainly be ideal to perform error analysis in 3D, it is unfortunately not realistic when considering the costs. The laminar channel cases of the last chapter were analyzed using a coarse and fine grid for each case, but the situation is somewhat different here. The number of elements used in each fine model is not all that much greater than the number for the channel cases, but the addition of the turbulence equations adds two more degrees of freedom per node (totaling six instead of four). In addition, the numerical complexity of the problem requires many more iterations to solve adequately. So, even with the current level of computing power available, it is still a considerable effort to solve a single problem in three dimensions.

In this light, it was necessary to reduce computational time, and solve only the minimum number of 3D cases required. Therefore, mesh refinement, boundary placement, and validation investigations were performed using two-dimensional projections of each case. The mesh density along the symmetry plane was preserved, so that each corresponding 2D case simply represents the 3D mesh without the extruded revolution about the gage axis. In two dimensions, the beam flexure was removed, so that flow rate through the gap was possible, leaving only the head. This can be justified from the results of the 3D models which show that the net pressure forces in the cavity really are nearly zero, as are the shear forces since the velocity in the cavity is basically zero.

Figure 5-39 shows the resulting mesh for the 2D version of the baseline Case #1, which looks identical to the images of Fig. 5-6. This is as it should be. Here, the region directly underneath the head in the cavity is meshed as well. This region was partially occupied by the flexible beam, which was removed for these 2D cases to allow flow to pass through the gaps. Although the 2D projection cannot hope to fully capture all of the effects of the full 3D problem, Fig. 5-38 is seen as a "worst case" scenario. In two dimensions, the head is a true obstacle, forcing the flow above and below it only (rather than the relief provided by flow moving around the sides of the head in three dimensions). Involving the third dimension allows the flow to move around the head in the *z*-direction, reducing the influence of the obstacle. Therefore, any

disruptions caused by the obstacle in 2D should be magnified, and the error study is performed based on this conclusion.

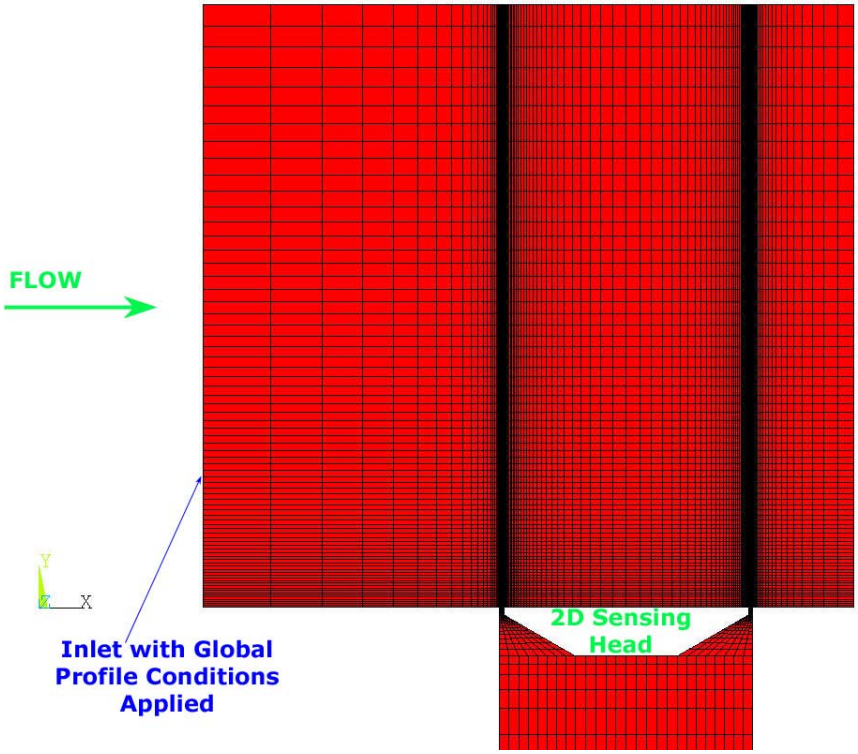

Figure 5-39. Mesh of 2D Projection Model of Case #1 for Mesh Studies

This section begins with a bit of validation, which is much more important in this instance than for the flow scenario of Chapter 4. The global problem is one of a flat plate, which is relatively straight forward when compared to typical problems often seen in the engineering world. The boundary layer growth itself is actually a parabolic problem and requires much less sophisticated equations to describe it than the Navier-Stokes formulation. The detail of the gage geometry, however, is a fully viscous problem, and the Navier-Stokes equations are sufficient and necessary for this application.

The validation issue is in using the RANS, or Reynolds Averaged Navier-Stokes equations, which add extra terms due to turbulence to the standard formulation covered in Chapter 3. The RANS equations themselves are of no concern on this topic, but the turbulence terms must therefore be modeled using additional information. This is a general concern in CFD calculations, as turbulence modeling errors are usually a significant source of uncertainty. There

are a variety of models ranging from very simple to highly complex in terms of intricacy and extra effort required. Schetz [1993] gives a good overview of most of the common options for those who are interested in the details of the current state of turbulence modeling.

The standard κ–ε model [Launder and Spalding, 1974] as given in Chapter 3 is the one employed here for the calculations. This formulation is probably the most well-known, and the most common model used in CFD applications. This model uses two separate additional equations beyond those prescribed for the RANS – one differential equation for κ and one for ε, from eqns. (3-11a) and (3-12a), respectively. The various two-equation formulations seem to, in general, be the best balance between capability and computational requirements. Higher order models (Reynolds Stress models, Large Eddy Simulation, etc.) can, in some cases, offer additional accuracy, but at the cost of significant computational effort, making the time required for solution too high for many engineers.

Although the κ–ε model is quite common and well validated, there can be concerns over its use in certain situations. This model tends to produce excess turbulence levels in regions of large strain. These include stagnation regions and regions of strong acceleration or deceleration [*Ansys Online Help,* 2001]. The choices in Ansys/FLOTRAN are somewhat limited, but the code does offer some alternatives to the standard κ–ε model. All the models are two-equation models as well (except for a zero equation mixing length model which was not employed here) and all are variations on the κ–ε model, but all four alternatives utilize alterations which are specifically designed to overcome some of the limitation of standard κ–ε.

These four alternatives include a well-known variation commonly referred to as the Renormalization Group (RNG) model [Yakhot, *et al*., 1992]. The RNG model modifies the constants of the equations with more complex forms and adds a couple of new terms in an attempt to alleviate the tendency toward overproduction of turbulence in stagnation regions by accounting for the strain rate.

The κ–ε (NKE) model due to Shih, *et al.* [1995] features changes made with similar motivations – to reduce overproduction of turbulence in sensitive areas. Shih *et al*. accomplish this by making complex changes to some of the constants by making them variable. Examples in their paper include boundary layer flows with favorable and adverse pressure gradients and a backward facing step, all of which are similar in many respects to the cases studied here. In these examples, the NKE variation in general produced better results than the standard form,

notably predicting the boundary layer thicknesses better for all the pressure gradient cases. Ansys/FLOTRAN recommends the NKE model for rotating flows in particular.

The κ–ε model (GIR) by Girimaji [1995] again alters the constants of standard κ–ε by making them extensive, complex non-linear functions of the strain tensor terms. The model contains terms especially accounting for rotational speed. Because of this, the GIR model is recommended by Ansys/FLOTRAN both for rotating flows and for flow with secondary vortices in the main flow.

Although all of these models are two-equation models for κ and ε, the variations and additions of the terms in the equations provide more realistic solutions for the regions in which the standard model might be suspect. A small validation study was made using these different turbulence model choices to assess the model dependence. The study consisted of successive variations of the 2D projection of baseline Case #1 (just as shown in Fig. 5-38). Everything remains the same – identical mesh, boundary conditions, solver controls, convergence levels, etc. – except that the various turbulence models were activated to understand the differences. After looking at these results, the maximum head protrusion Case #2 was also analyzed in the same manner with one of the alternate turbulence models, since this case is the one which obviously should create the largest disruption in the boundary layer and, therefore, the most complex flow. These results are presented in Table 5-6, with resulting force and moment components and the percent difference from the control case using the standard model.

Table 5-6: Results of Turbulence Model Dependence Study Showing Percent Differences from Various Turbulence Options

	BASELINE CASE #1				Z/D_{HEAD} = +1% CASE #2				
	F*X	F*Y	M*Z			F*X	F*Y	M*Z	
standard κ–ε	1.0335	2.3240	-0.0751		standard κ–ε	2.1490	19.8160	-0.7470	
RNG	1.0252	1.9675	-0.0593		NKE	2.1000	19.3460	-0.7270	
	0.80	15.34	21.07	<- % diff.		2.28	2.37	2.68	<- % diff.
NKE	1.0091	2.0486	-0.0615						
	2.36	11.85	18.14	<- % diff.					
GIR	1.0555	1.5978	-0.0393						
	2.13	31.25	47.64	<- % diff.					

The result of this is that, for both Cases #1 and #2, the differences are reasonable given the uncertainty in employing turbulence models in general. The desired measurement, F^*_X, is the paramount variable, and the percent differences between the various cases are small at 2% or less, even for the protrusion case. The other two parameters are not so nearly important, but the M^*_Z moment does have some utility. For Case #2, where the moment is large due to the misalignment, the percent difference is again small, illustrating consistency. For the baseline case, the percent differences in the moment are large, but the moment is nearly zero for all the models. In cases such as this, percent difference is not a very reflective measure of accuracy. Comparing the moment to the value of F^*_X for example, puts a better perspective on the numbers. For baseline Case #1, the predicted values of M^*_Z are small enough that they will have little to no effect on gage performance regardless of the turbulence model used. For F^*_Y, the differences are more significant for baseline Case #1, but as already discussed this is to be expected anyway due to the nature for the 2D problem, which should present an effect much worse than in 3D. Also, since the value of F^*_Y itself is somewhat arbitrary anyway, little concern is needed over this value, and predicting the value to even 20-30% is sufficient for the studies here.

After review, the results are actually quite good considering the uncertainty in using turbulence models in the engineering world. Even for Case #2, little difference was seen between the standard model and the NKE model variation. As a result, the issue is considered validated for the 3D cases studied. The standard κ–ε model was used for all cases in Sections 5.4 and 5.5, and it seems that standard κ–ε is sufficient to predict results for this application in this type of flow condition.

Convergence is again the first issue of verification to be studied. As with the channel problems, the models were converged to tight tolerances, although not quite as much as in Chapter 4 due to time constraints. Still convergence will be shown to be minimal compared to the ordered discretization error caused by the computational mesh. The channel flow cases were ideal in terms of convergence behavior. For those, the convergence monitors decreased in a steady, linear fashion to the stopping criteria almost from the start. Here, the situation was not so tidy. Although the convergence monitors did decrease, the behavior was often not so steady. The monitors exhibited oscillations, decreasing and increasing randomly in a somewhat downward trend. Typically as well, the monitor for one degree of freedom would decrease while

another increased. After some number of iterations, the opposite would occur. This is certainly caused by the high Reynolds number of the flow, the complex boundary conditions, the extra degrees of freedom from the turbulence models, the large variation in element size, and the importance of the convective coupled terms in the solution, etc.

Table 5-7. Maximum Values of Normalized Nodal Residual for All Cases

case	Maximum Nodal Residual (absolute value)					
	VX	VY	VZ	PRES	ENKE	ENDS
1	4.4×10^{-5}	1.6×10^{-5}	5.7×10^{-7}	4.6×10^{-6}	2.6×10^{-5}	1.5×10^{-5}
2	1.4×10^{-4}	7.9×10^{-6}	8.0×10^{-7}	2.9×10^{-6}	3.3×10^{-4}	8.3×10^{-4}
3	1.2×10^{-4}	2.1×10^{-4}	1.2×10^{-6}	2.1×10^{-5}	2.6×10^{-3}	2.4×10^{-1}
4	1.1×10^{-4}	8.2×10^{-6}	4.0×10^{-7}	9.0×10^{-7}	6.2×10^{-5}	2.4×10^{-3}
5	8.1×10^{-5}	1.3×10^{-5}	1.1×10^{-6}	1.1×10^{-6}	1.5×10^{-4}	7.3×10^{-2}
6	5.0×10^{-3}	$8{,}6 \times 10^{-5}$	3.0×10^{-6}	1.2×10^{-5}	1.6×10^{-5}	1.1×10^{-5}
7	1.1×10^{-4}	8.2×10^{-5}	4.0×10^{-7}	9.0×10^{-7}	6.3×10^{-5}	1.0×10^{-2}
8	8.4×10^{-5}	1.3×10^{-5}	1.0×10^{-6}	1.1×10^{-6}	1.6×10^{-4}	8.8×10^{-3}
9	1.6×10^{-4}	1.0×10^{-5}	5.5×10^{-7}	1.0×10^{-6}	6.4×10^{-4}	2.0×10^{-2}
10	1.1×10^{-4}	6.1×10^{-5}	3.0×10^{-6}	2.4×10^{-6}	3.6×10^{-3}	3.5×10^{-2}

As a result, it typically took many more iterations to solve the external flow problems to a level even approaching what the channel flow problems were converged to. Table 5-7 shows the results of the maximum normalized residual values for each degree of freedom at a node in each case. Again, this is the maximum magnitude seen for that degree of freedom by any one node. The bulk of the nodes in each problem exhibited much lower values, with average values throughout the domain of 1000 times less than the maximum being typical. Even these maximum numbers, however, are quite satisfactory.

It seems apparent from experience with the channel flow problems and looking at the values of Table 5-7 that convergence is not a primary issue in this case either. Since the results files are somewhat larger for these problems than the channel flow cases, a complete iteration convergence history was not saved for any of the cases like what was shown back in Fig. 4-28. This would have required a large amount of space for enough points to plot a history. However,

for the baseline case, the final 1000 iterations produced a change in F^*_X of 0.00004%, which is similar to what was shown in Fig. 4-28. Since these values are on the same general level and in both cases are extremely small compared to the mesh dependency error, convergence is considered to be a non-issue in the computational error effects analysis.

Just as in the previous channel flow situation, mesh dependence or ordered discretization error becomes the primary contributor in the accuracy estimations for the case of external turbulent flat plate flow. As with the turbulence modeling validation, most of this mesh refinement analysis was performed in two dimensions to make the processing time required more feasible. The mesh refinement study consisted of direct two dimensional projections of the 3D volume elements of the computational model for each of the ten cases.

Analysis consisted of utilizing two grids for each case – a 2D projection of the fine mesh used in the presented results, and a coarser model of uniform refinement ratio 0.68. This number was chosen in particular for reducing the *y*-direction points (those covering the boundary layer from 75 to exactly 51. A grid halving (ratio of 0.50) was initially tried, but that proved too few to capture the boundary layer well, leading the author to suspect that the asymptotic range was not reached at this level. In addition, it is not possible to go sufficiently finer, since the mesh spacing is already close to the y^+ transition value of 11.5. Crossing this boundary would make any comparison of results a meaningless exercise in this case. Although not a grid doubling or halving, this seemed sufficiently distinct to produce reasonable error estimates.

The order of convergence was initially analyzed for the baseline case only, just as with the laminar channel flow problems. Carefully converged models ($1x10^{-10}$ or less residual values) on the varying grids were examined, using refinement ratios of 0.68 and 1.16 from the baseline model. The third grid is only a small (16%) increase from the base grid, but that was the maximum amount that could be used before crossing the transition boundary and comprising the wall formulation of the turbulence model. Roache recommends a minimum 10% change for any grid refinement to be valid, so this is just over the minimum level required. For this reason, it was not used to calculate the error estimator, but was considered sufficient for estimating *p*. It seems from the extra 2D grids solved for baseline Case #1 that the spatial convergence behavior is again somewhat non-monotonic. All of the categories (for each of pressure, shear stress, and combined total) for the F^*_X parameter produced non-physical values of *p* (strongly deviant from the expected range of 1.0 to 2.0). Values for F^*_Y, and M^*_Z were found to be about 1.6 and just

under 1.0 respectively, although these values should be somewhat suspect based on the experience with F^*_X. This is unfortunate but once again expected given the nature of the SUPG advection algorithm. The solution values for this case were sufficiently different for the different grids that significant digits is not as central of a problem as in determining order of convergence in the last chapter. The problems with calculating p are more a function of the non-monotonicity of the spatial solution for these cases.

These values were then evaluated using a more appropriate method as outlined by Roy [2001], valid for mixed order spatial convergence exhibiting non-monotonic behavior. Roy's mixed order analysis uses three grids (the same three that were just used to determine p), and it retains the first two error terms from eqn. (3-22). In this case, that is the first and second order terms, with the leading truncation term as $O(h^3)$. Roy gives some lengthy formulas resulting from the algebraic mathematics, giving E_1 and thus A_1 based on the non-constant refinement ratios between the grids and the differences in solution between each two successive grids. The mixed order error estimator A_1 for the total contribution to F^*_X was found to be -9%, as an example. These numerical results will be completed and compared later to provide some perspective on the mixed order result.

All remaining cases consisted only of two grids, so the standard Richardson extrapolation error estimator was employed, as given in eqn. (3-26). In calculating the A_1 estimator, an order of convergence, p, of 1.0 was again used to be as conservative as possible. This value for baseline Case #1 was also calculated to see how well this procedure models the true non-monotonic behavior captured via the Roy method.

Values for A_1 resulting from the nominal 2D projection grid and the uniform coarsening of 0.68 grid are given in Table 5-8 for all three global parameters, divided up into the contribution to said parameters by pressure alone, shear stress alone, and the sum total. As Table 5-8 shows, there is considerable variation in the numbers, ranging from virtually zero to excessively high numbers. Clearly, some appreciation for the circumstances of each individual error estimation is required. This will begin after presenting the resulting *GCI* values based on the factor of safety of 3.0, given by eqn. (3-28). These *GCI* values are presented in Table 5-9 as a percentage.

Table 5-8. Richardson Extrapolation Error Estimator Values Given by Case Number as a Percentage

Case #	$\%A_1 F^*_X$			$\%A_1 F^*_Y$			$\%A_1 M^*_X$		
	pressure	shear	total	pressure	shear	total	pressure	shear	total
1	-61.8	-1.7	-3.7	-47.9	-179.2	-47.8	-101.1	-85.2	-102.0
2	-54.4	4.0	-20.8	-27.6	-3383.8	-27.4	-40.9	-179.6	-37.5
3	-55.8	3.7	-8.5	-71.9	-643.4	-71.7	-119.8	-147.5	-117.6
4	30.3	-8.7	-18.0	7.4	-134.4	7.2	44.0	32.8	43.8
5	-35.9	-2.2	30.3	-49.3	-217.1	-49.5	-5.7	-52.4	-6.4
6	-117.2	4.3	1.9	-88.7	-409.5	-88.7	-199.6	-156.7	-202.2
7	-80.5	4.7	-0.3	-32.3	-603.4	-32.1	-101.5	-175.6	-98.6
8	-15.3	3.9	0.1	-14.9	-214.0	-14.7	-19.3	-84.6	-16.8
9	-17.1	4.1	-5.9	-16.2	-76.8	-16.1	-32.0	-261.9	-31.1
10	135.3	-0.4	6.8	-2.8	-29.4	-2.9	-8.9	25.9	-9.3

Table 5-9. Roache GCI Values Given by Case Number as a Percentage

Case #	$\%GCI_{FINE} F^*_X$			$\% GCI_{FINE} F^*_Y$			$\% GCI_{FINE} M^*_X$		
	pressure	shear	total	pressure	shear	total	pressure	shear	total
1	185	5.1	11.1	143	537	143	303	255	306
2	163	12	62.4	82.8	10,151	82.2	122	538	112
3	167	11.1	25.5	215	1,930	215	359	442	352
4	90.9	26.1	54	22.2	403	21.6	132	98.4	131
5	107	6.6	90.9	147	651	148	17.1	157	19.2
6	351	12.9	5.7	266	1,228	266	598	470	606
7	241	14.1	0.9	96.9	1,810	96.3	304	526	295
8	45.9	11.7	0.3	44.7	642	44.1	57.9	253	50.4
9	51.3	12.3	17.7	48.6	230	48.3	96	785	93.3
10	405	1.2	20.4	8.4	88	8.7	26.7	77.7	27.9

The non-monotonic analysis by Roy's method can now be fully appreciated. The -9% error estimation predicted for the Case #1 quantity F^*_X by that analysis is clearly much greater than the value predicted in Table 5-8. This is, of course, the exact case made for using *GCI*,

which predicts 11% for this variable. Thus, the A_1 estimator is strongly liberal, while only the *GCI* is conservative. The actual non-monotonic error falls somewhere in between. The rest of the nine components in Tables 5-8 and 5-9 exhibit the same behavior – the non-monotonic error falling outside the error estimator and equaling just less than the GCI.

The results of Table 5-8 and 5-9 are actually quite interesting. The parameter F^*_X is obviously the most important of the three parameters by far. Of the other two, M^*_Z has moderate importance in some cases, while F^*_Y is difficult to interpret because of its arbitrary reference point. F^*_X shows excellent overall accuracy characteristics from these tables. The *x*-direction contributions by shear stress offers exceptional accuracy, especially when considering the fact that the shear stress is a derived quantity from the turbulence model which is sensitive to wall placement and turbulence levels. The *x*-direction contribution by the pressure shows somewhat higher levels of uncertainty, at least for the misalignment cases. For the aligned cases, the pressure contribution is so small as to have little impact on the total.

For these cases where the pressure becomes significant, however, the result seems somewhat counterintuitive. In most CFD applications – an airfoil analysis for example –, pressure tends to be the most accurate quantity, while shear stress is harder to capture with any certainty. Here, the opposite is true, which seems odd until the nature of the contributions is brought into the picture. The general cases involve the contribution of inviscid pressure contributions, which are much easier to calculate accurately. Here, the contribution is made by pressure in a very intricate flow feature trapped totally within the boundary layer itself. As discussed extensively in the previous two sections, the pressure force comes from dynamic pressure which survives the boundary layer. This is, of course, very difficult to calculate and quite sensitive. As was shown, something on the order of 2% of the dynamic pressure survives into the gap region. For misalignment cases, the pressure deviations are even greater. Even this 2% though, is still about 7 times the shear stress level, and so even a relatively small change in the gap region dynamic pressure can make a large impact on the total *x*-direction force. Thus, even errors of the magnitudes shown in the table are quite good given the sensitivity of the pressure imbalances at the wall of the boundary layer.

A similar argument can be made for F^*_Y, which is totally dominated by pressure differences between the cavity and the free-stream. Shear force produces so little *y*-direction force that the nonsensical values of the GCI calculated in that column are meaningless anyway.

As with the *x*-direction force, the F^*_Y pressure contribution is governed by a highly sensitive boundary layer calculation, in which a small deviation causes a small change in pressure, which integrates over the head to produce seemingly dramatic force changes. Of course, the argument has already been made that for the *y*-direction force is an arbitrary calculation anyway, since the absolute pressure is not accounted for and thus the F^*_Y force is only useful to compare two cases in a restricted sense.

Also for many of the zero misalignment cases, the moment in the *z*-direction is so small that error estimation has little meaning here as well. For these instances, the discussion of round-off error in Section 3.6 applies. The error estimation calculation requires a subtraction operation followed by a division operation among the solution results of the grids. From the round-off discussion, these two operations can cause significant difficulties in cases where the values are either close in magnitude or close to zero. Both of these qualities apply to the moment results for these cases, and thus the error estimators for these values must be considered accordingly. Fortunately, these instances where the error estimator of the moment is high are also instances where the value is close to zero. Thus, the contribution of the moment to the total output of the flexure in these cases is unimportant. For all cases (even misaligned cases), the shear force contribution is again too small to contribute in any case, and the values are excellent for the pressure contribution given the complexity of the situation. The uncertainties in the moment are much higher than in F^*_X in general, but this is already expected since the very nature of moment effects makes them quite sensitive to both the converged nodal values and the nodal placement together.

Finally, just for a test of the two-dimensional refinement method, a two grid refinement was done for the baseline case only in three dimensions. This extra effort could not be made for all cases, but seemed necessary for at least one trial. The baseline Case #1 mesh was used with a 0.68 refinement mesh, and the error estimation was calculated for the three global parameters. The result of this is that the A_1 estimators are -0.80%, -105%, and -25% for F^*_X, F^*_Y, and M^*_Z respectively. This indicates that for F^*_X and M^*_Z, the 2D projection models are a significant overestimation of A_1. This is as intended and reflective of the fact that the 2D case offers a larger disruption than the 3D case which can relieve the flow as necessary. Only F^*_Y shows any increased sensitivity in the 3D case, and this seems due to the fact that pressure operates over a

larger three-dimensional area for this case, which makes it even more sensitive to a small pressure adjustment than the two-dimensional line cases.

So, after this rather intricate and confusing analysis of the adequacy of the CFD models, a short summary is useful to highlight and clarify the main points and results. The three dimensional refinement case shows that the two dimensional refinement cases overestimate the F^*_X and M^*_Z error estimators A_1. The non-monotonic analysis described by Roy show the A_1 estimators to be insufficient for the respective 2D refinement models, but they may be more applicable to the three dimensional problems. Since the *GCI* is significantly conservative for even the 2D problems, it is assumed that it will be very conservative for the corresponding 3D counterpart. In general, the F^*_X parameter is the most accurate parameter, followed by the moment M^*_Z and finally the *y*-direction force F^*_Y, which is only marginally useful anyway.

Finally, the boundary placement is given brief consideration, although it will quickly be shown to be a non-issue like the iterative convergence error. For this issue, the two-dimensional projection technique is again employed as a tool for error analysis. With the baseline Case #1 2D projection, the boundary length upstream, L_{UPSTR}, and the boundary length downstream, L_{DNSTR}, were doubled one at a time. These results were then compared to the nominal case. The important issue again is that the problem is a physically parabolic one. Thus, there should be almost no downstream dependence of the problem (as a parabolic problem is a "one-way" street, with information moving downstream only).

Doubling the downstream boundary indeed had the expected effect. Comparison with the nominal case revealed that all force and moment coefficients are exactly the same, to the double precision output that Ansys/FLOTRAN provides. Thus, there was no change for all global coefficients. Doubling the upstream length produced slightly higher results. This comparison produced differences of 0.0120% for the F^*_X variable, 0.135% for the F^*_Y variable, and 1.75% for the M^*_Z variable. Just like with the turbulence and grid convergence cases, the nominal moment for the baseline Case #1 projection is only -0.075, so a 1.75% difference is quite minor. Since the error is assumed to be first order in length and length doubling was used, these percent differences are also equal to the Richardson extrapolation error estimator.

Although these values are measurable, the results are much less significant than the errors from the ordered discretization error. The width boundary in the *z*-direction was not studied since it is not possible to do so in two dimensions. Fig. 5-40 shows the full plot of skin friction

for baseline Case #1, which is a quantity that is quite sensitive to velocity variations. This plot was shown in Fig. 5-22, but for only the head region without the full outer wall area. Fig. 5-40 clearly shows that the variations remain concentrated in an area around the head only and do not propagate anywhere near the outer boundary at all. Even if the error was on the order of the upstream boundary, this is still less than the mesh error anyway. Finally, the outer boundary is a free one, which is somewhat less restrictive than a Dirichlet boundary anyway. Because of this heuristic reasoning, no effort was made to analyze this boundary further.

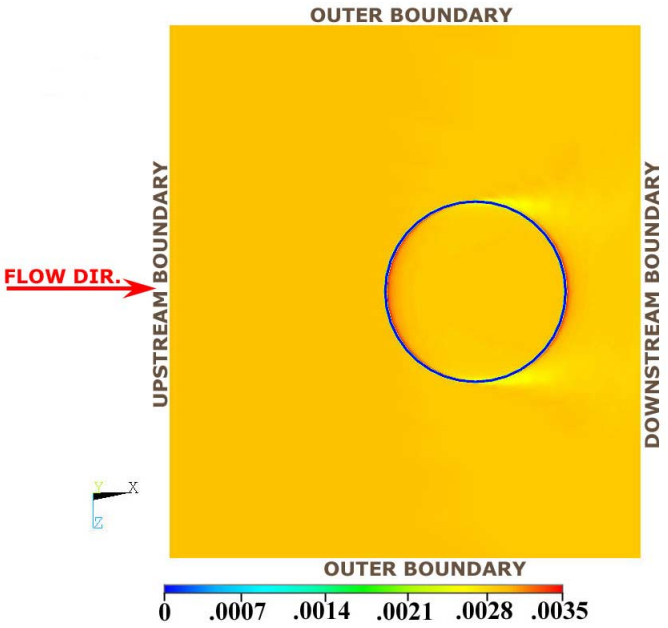

Figure 5-40. Skin Friction Contours on Sensing Head and Surrounding Wall for Entire Computational Region, Showing Boundary Placement

CHAPTER 6: Studies of Skin Friction Gages in Turbulent Pressure Gradient Flow

6.1 The Physical Models

Chapter 4 covered a laminar flow problem scenario with a large imposed pressure gradient, but no distinct convective presence. Chapter 5 covered a turbulent problem scenario with a high Reynolds number but with no pressure gradient. The similarities and differences in these two scenarios can be found by re-reading those sections. The results of the laminar flow channel analysis and of the turbulent external flat plate analysis stimulates a need to push a bit further into the examination of the detailed flow in and around a skin friction sensor. Thus, the next step taken in this chapter is to analyze a condition involving high Reynolds number AND significant pressure gradients.

The subject of this chapter is to extend the turbulent, external flat plate case to something similar, but with a pressure gradient imposed. By definition, a flat plate has no pressure gradient in normal external flow. A surface of this type must be curved to exhibit varying pressure. A curved surface, however, was not seen as a reasonable choice because of the complexity to model, as well as the uncertainty in calculating skin friction on a complex geometric surface. Also, the gage head is normally flat, so that at least a portion of the curved surface would need to be straight around the head itself. This type of problem seemed to have far too many extraneous issues to be of use in this matter. Channels generate pressure gradients as was seen in Chapter 4. The channel flow in Chapter 4, however, was at a very low Reynolds number, and a flow would need to be at very much higher Reynolds numbers to be comparable with the flat plate flow in Chapter 5. In this light, a compromise was made. The flow problems for this chapter are for high Reynolds number channels that involve diverging and converging geometry of slope, m, to generate negative and positive pressure gradients, respectively. The walls of the channels are

flat, solving the issue of placing the head on a curved surface. The Reynolds number of these models was chosen so that the boundary layer along the walls of the channel is quite thin compared to the channel cross-section. Thus, the channels are not fully-developed, and the bulk of the channel center remains fully inviscid. This is similar to the flat plate of the last chapter, but a pressure gradient is now imposed on the flow.

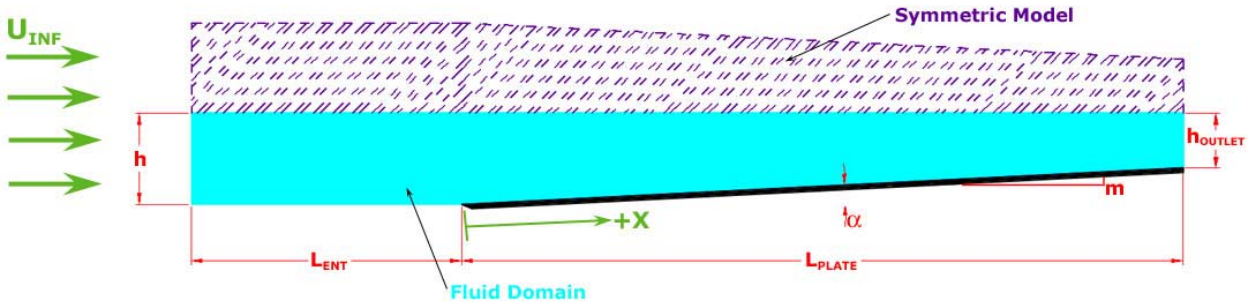

Figure 6-1. Scaled Drawing of 2D Global Converging Channel Model (Favorable Pressure Gradient)

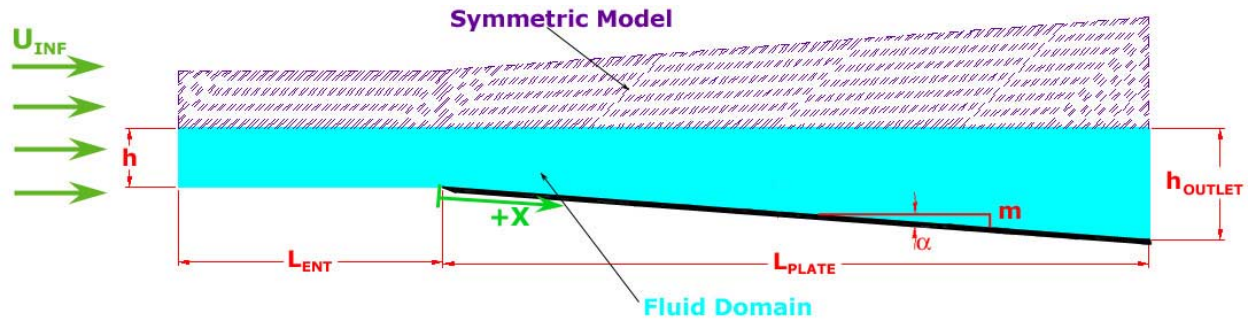

Figure 6-2. Scaled Drawing of 2D Global Diverging Channel Model (Adverse Pressure Gradient)

Fig. 6-1 shows a scaled drawing of the converging channel, and Fig. 6-2 shows the same scaled drawing for the diverging channel case. Since both global models are conceptually identical, the features of both are looked at together. In both cases, the channel is symmetric, thus avoiding the need to resolve two boundary layers in the computational model and saving a great deal of elements. Again, the wall is flat, mimicking the flat plate model, at least from the perspective of the skin friction gage buried within the boundary layer. For both models, the

positive *x*-axis runs parallel to the plate from the leading edge and the positive *y*-axis runs perpendicular to the plate out into the flow.

The two channel cases are dimensioned similarly to the straight flat plate, with the exception that the plate length is defined horizontally rather than along the plate. This was done simply to facilitate drawing the models. The heights h and h_{OUTLET} are the half-heights of the channels. Just like with the flat plate, an entrance length provides the flow with a chance to adjust to the presence of the wall leading edge. In these cases, the flow must not only adjust to the wall, but also make a turn into the channel at the same time.

The two cases presented in this chapter do not necessarily adhere to any physical situation. The entry length spans two streamlines, forming a streamtube. The global problems in Figs. 6-1 and 6-2 are simply numerical constructs designed to produce a localized effect in the boundary layer in the region of the gage. This pair of channel physical models was designed with a one-dimensional flow model governed by eqns. (6-1) and (6-2), which are just the incompressible momentum equation called Bernoulli's equation, and the supporting continuity equation for constant density flow.

$$u(x) = u_{INLET}\frac{A_{INLET}}{A(x)} \tag{6-1}$$

$$P(x) = P_{INLET} + \frac{1}{2}\rho\left[u_{INLET}^2 - u^2(x)\right] \tag{6-2}$$

For one dimensional incompressible flow, total pressure must remain constant, striking a balance between pressure and flow speed. This analysis does not take into account the viscous effects of the boundary layer of course, but serves as an excellent tool to design the basic geometry of the problems.

Design of the problem proceeded by balancing the various desirable criteria for each situation. The goal was to reproduce the conditions of the simple flat plate as much as possible. This consisted of matching the free-stream velocity above the gage location to the free-stream velocity of the flat plate case (103.4 m/s), matching the boundary layer thickness as closely as possible and, creating a large enough pressure gradient to create an interesting problem and to cause a large enough change in skin friction coefficient to be different from the zero gradient cases. Eqns. (6-1) and (6-2) were employed, followed by the useful Java boundary layer applets [Devenport, 2002] to get a rough estimate of the boundary layer properties of the channels. One

important design criterion imposed was to avoid boundary layer separation for the diverging channel. This limited the level of acceptable pressure gradients. The channel height values must also be sized correctly to be much higher than the maximum boundary thickness predicted by the Java applets for each channel. The dimensionless scaling was preserved from the flat plate problems to provide consistency. For this, length scaling L_∞ is 0.075 m, scaling velocity V_∞ is 103.4 m/s, and density ρ_∞ of 1.225 kg/m^3. The dimensionless free-stream velocity applied at the inlet is no longer equal to 1.0, as the goal was to create a boundary layer edge velocity of 1.0 directly above the gage location. This required the use of eqn. (6-1) to calculate the entrance velocity required to produce this condition. The final geometry for both cases is given in Table 6-1.

Table 6-1. Relevant Geometry and Variable Definitions for Global 2D Converging and Diverging High Reynolds Number Channels, Shown Dimensionally (left) and Non-dimensionally (right) for each Case

variable	Converging channel (Fig. 6-1)		Diverging channel (Fig. 6-2)		Flat Plate (Chapter 5)	
	(-)	(*)	(-)	(*)	(-)	(*)
u_{INLET}	70 m/s	0.677	180 m/s	1.740	103.4 m/s	1.0
v_{INLET}	0 m/s	0	0 m/s	0	0 m/s	0
P_{OUTLET}	0 Pa	0	0 Pa	0	0 Pa	0
m	0.05		0.075		0	
α	2.862^O	0.05 rad	4.289^O	0.075 rad	0	0
L_{ENT}	112.5 mm	1.5	112.5 mm	1.5	112.5 mm	1.5
L_{PLATE}	300 mm	4.0	300 mm	4.0	300 mm	4.0
h	37.5 mm	0.50	24.8 mm	0.33	18.75 mm	0.25
h_{OUTLET}	22.5 mm	0.30	47.3 mm	0.63	18.75 mm	0.25
μ	1.9×10^{-5} Pa-s	2.0×10^{-6}	1.9×10^{-5} Pa-s	2.0×10^{-6}	1.9×10^{-5} Pa-s	2.0×10^{-6}
ρ	1.225 kg/m^3	1	1.225 kg/m^3	1	1.225 kg/m^3	1

Also, in an effort to quantify the strength of the pressure gradient, the correlation parameter which originally was proposed by Clauser [1954] to govern equilibrium pressure gradients in analyzing turbulent boundary layers was used. This correlation is given in eqn. (6-3).

$$\beta = \frac{\delta_1}{\tau_W} dP/dx \tag{6-3}$$

In this equation, the displacement thickness is given as δ_1 to avoid confusion with the non-dimensionalization scheme. Clauser originally performed some experiments with this parameter between 0 (a flat plate flow) and 7.0. The value β is useful, because it gives a pressure gradient strength in terms of the pressure gradient, shear stress, and a boundary layer parameter, all of which are important in the skin friction gage performance.

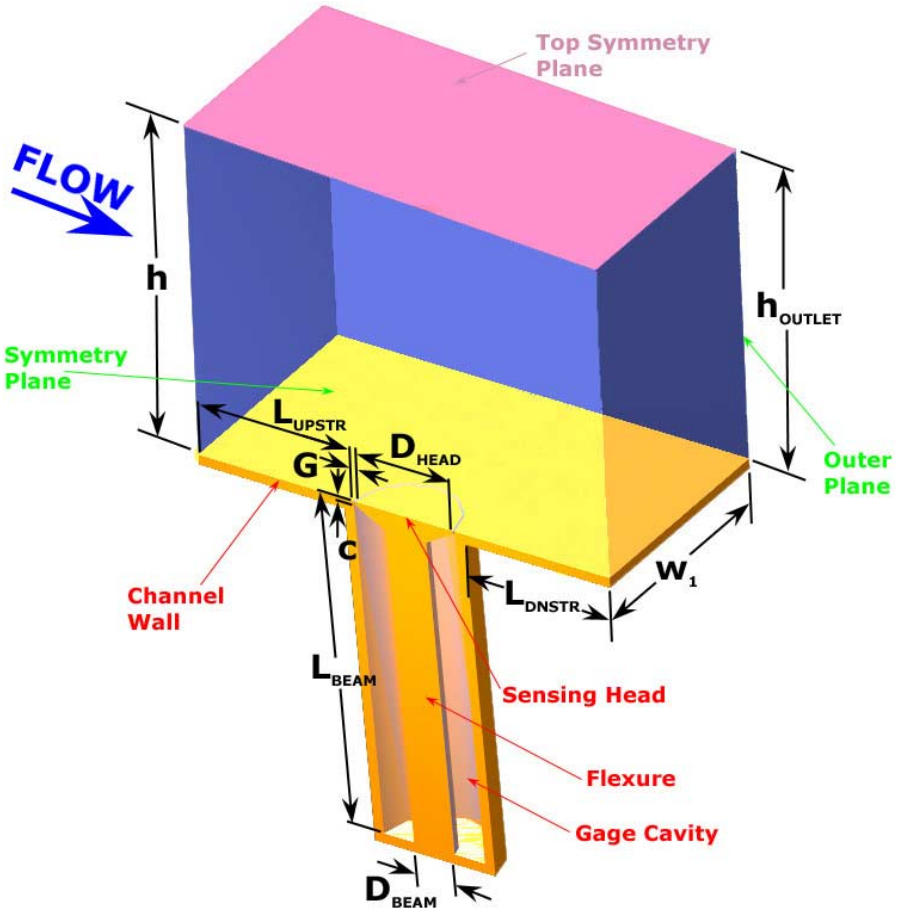

Figure 6-3. Scaled Drawing of 3D Embedded Region with Skin Friction Showing Relevant Dimensions for Converging Channel Case (Favorable Pressure Gradient)

From these global problems, the embedded region around the skin friction gage is again employed, just as in Chapter 5. Figures 6-3 and 6-4 show scaled images of the two embedded problems which correspond to the global problems of Figures 6-1 and 6-2.

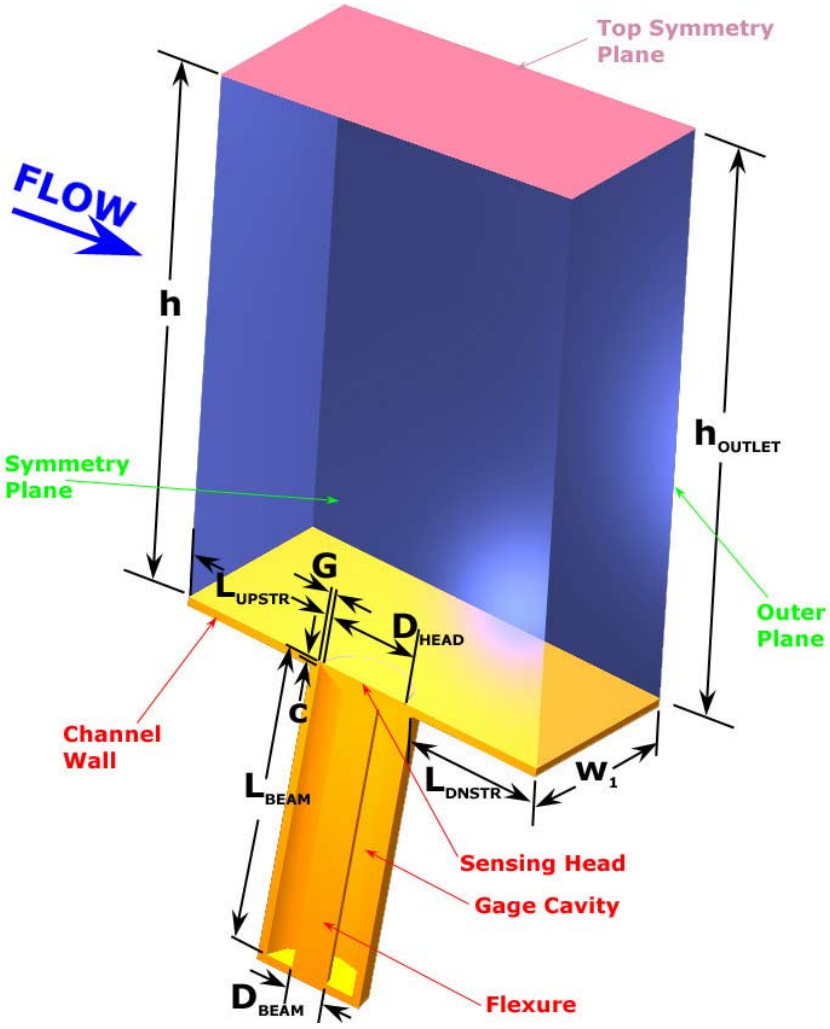

Figure 6-4. Scaled Drawing of 3D Embedded Region with Skin Friction Showing Relevant Dimensions for Diverging Channel Case (Adverse Pressure Gradient)

Table 6-2 gives the associated geometry for these two cases. Additional fluid properties and information was reused from Table 6-1. Just like in Chapter 5, the inlet and outlet conditions of the embedded problems come from the corresponding solutions from the global 2D problems. The distance along the plate to the center of the head corresponds to a Reynolds number that is comparable to the gage position along the turbulent flat plate studied in the

previous chapter. The *x*-direction distance along the wall that governs the Reynolds number is recorded in Table 6-2 with the other relevant gage geometries. Here, only the baseline configurations are considered with gage geometry corresponding to the baseline Case #1 of the turbulent, flat plate problem in Chapter 5 and the head aligned with the wall. No additional parameter variation or misalignment conditions are considered in conjunction with the pressure gradient.

Table 6-2. Relevant Geometry and Variable Definitions for 3D Embedded Problems for Converging and Diverging Channels, Shown Dimensionally (left) and Non-dimensionally (right) for each Case

variable	Converging channel (favorable pressure gradient) (Fig. 6-3)		Diverging channel (adverse pressure gradient) (Fig. 6-4)	
	(-)	(*)	(-)	(*)
x_{GAGE}	255.2 mm	3.402	260.9 mm	3.479
h	25.6 mm	0.3408	43.1 mm	0.5740
h_{EXIT}	24.0 mm	0.3194	45.5 mm	0.6065
L_{HORIZ}	32.0 mm	0.4267	32.5 mm	0.4337
L_{UPSTR}	12.1 mm	0.1611	12.4 mm	0.1650
L_{DNSTR}	12.1 mm	0.1611	12.4 mm	0.1650
w_1	16.0 mm	0.2136	16.3 mm	0.2175
G	0.127 mm	0.001693	0.127 mm	0.001693
c	0.254 mm	0.003386	0.254 mm	0.003386
D_{HEAD}	7.62 mm	0.1016	7.62 mm	0.1016
D_{BEAM}	3.175 mm	0.0423	3.175 mm	0.0423
L_{BEAM}	25.4 mm	0.3386	25.4 mm	0.3386
Λ	30^O	0.524 rad.	30^O	0.524 rad.

As in the previous chapter, it is advantageous to look at the dimensions of the gage in terms of wall units. This again has the utility of relating the results of the flow conditions studied here to other flow conditions that share similar wall unit dimensions. Table 6-3 gives the

gage parameters of the baseline configuration in terms of wall units for the favorable pressure gradient, converging channel and the adverse pressure gradient, diverging channel.

Table 6-3. Relevant Variations and Case Nomenclature for Three-Dimensional Embedded Region Pressure Gradient Models

parameter	Converging channel (dP/dx<0)	Diverging channel (dP/dx>0)
G^+	37.1	28.3
c^+	74.2	56.7
D^+_{HEAD}	2226.0	1700.0
D^+_{BEAM}	927.0	708.0
L^+_{BEAM}	7421.0	5668.0
Z^+	0	0

6.2 The Computational Models

The computational model of each channel case is a straightforward extension of the physical model. With one exception, the meshing and boundary conditions are the same as Chapter 5. The global problem models are shown in Figs. 6-5 and 6-6 for the converging and diverging cases, respectively. The mesh is similar to the flat plate mesh of Chapter 5, marked by highly concentrated elements near the wall, with fewer elements near the top centerline of the model. To enhance the viewing potential of the images, the view is zoomed in to show the region at the start of the plate for both figures. The structured mesh covers the plate length in this way.

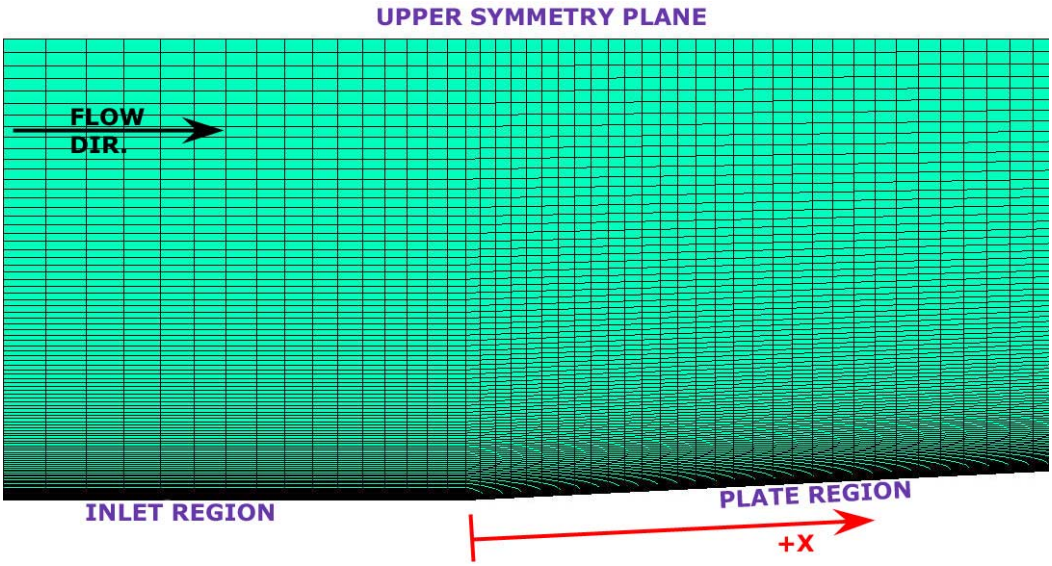

Figure 6-5. Mesh of 2D Global Converging Channel Problem in the Leading Edge Region

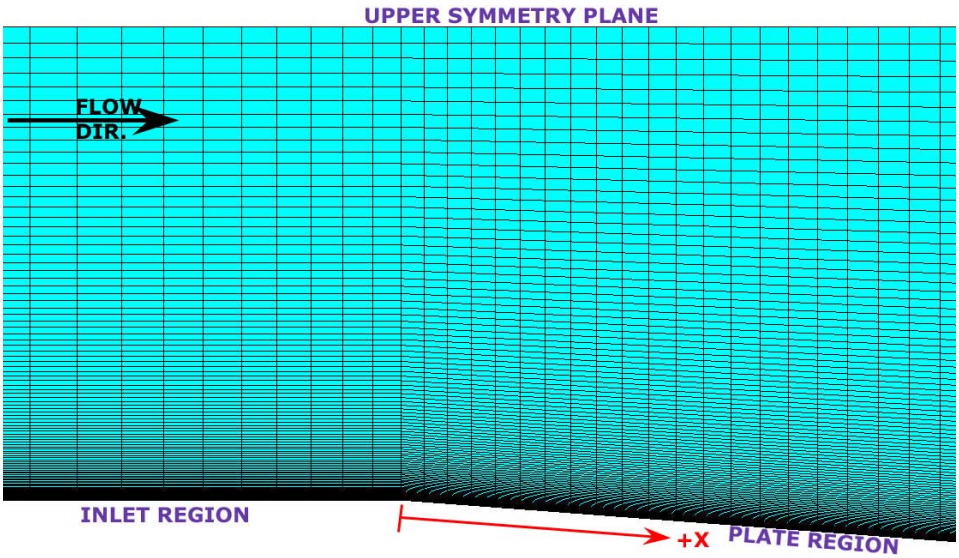

Figure 6-6. Mesh of 2D Global Diverging Channel Problem in the Leading Edge Region

Here again, the design of the mesh required keeping the near wall node of the first element close to a y^+ of 11.5 without being lower. This constraint was more difficult to satisfy in these cases since the boundary layer characteristics are somewhat more complex than the simple flat plate, but (after some trial and error) the result is quite satisfactory as shown in the next section. A total of 100 points was used in the vertical direction in both cases. In the flat plate problem, there was little happening above the boundary layer, so the computational domain

required almost no points in that region. Although the mesh is still highly staggered in favor of the wall area, there are some stream-wise effects happening here in the inviscid region of the problem, so more points were used to account for this.

For the embedded region computational models, identical structured grids were built consisting of approximately 118,000 elements each. These grids reflect a somewhat larger number of elements than the flat plate cases of Chapter 5 (compared to Table 5-3). With more points in the vertical (*y*) direction, and a more complex situation, the increase was deemed necessary.

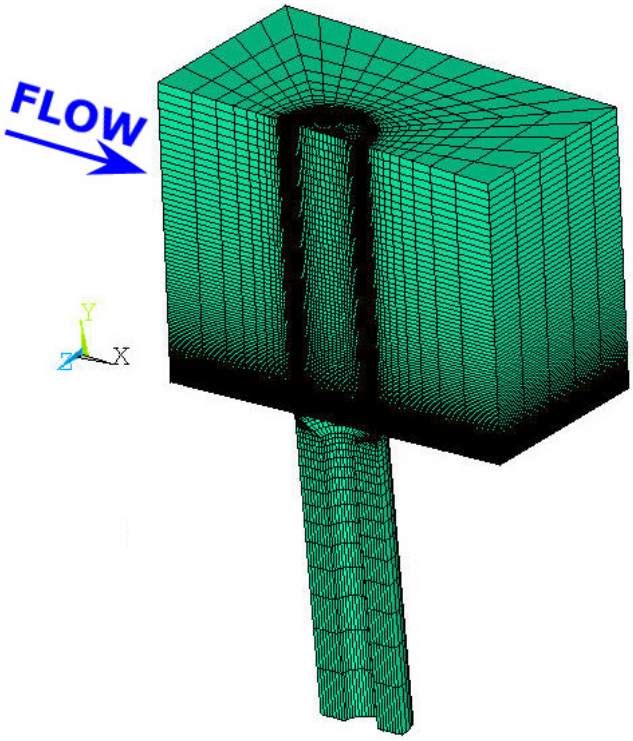

Figure 6-7. Mesh of 3D Embedded Region for Converging Channel Case (dP/dx < 0)

Figures 6-7 and 6-8 show the resulting finite element meshes for the converging and diverging embedded regions, respectively. Just like previous work, elements are concentrated heavily near the wall and in the gap region, with coarser regions near the outside of the boundary layer and deep into the cavity where there is little happening. The vertical distance and point spacing at the inlet and outlet was kept the same as the corresponding global problem meshes to make the boundary condition application accurate without requiring interpolation.

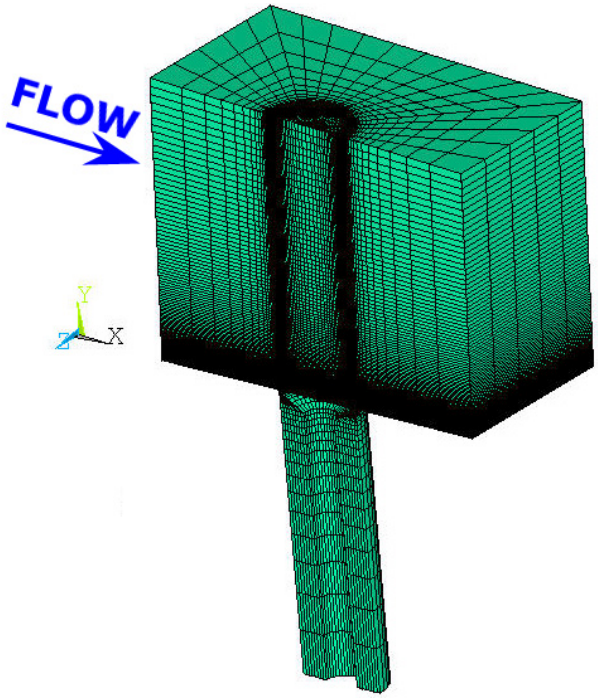

Figure 6-8. Mesh of 3D Embedded Region for Diverging Channel Case (dP/dx > 0)

Finally, Fig. 6-9 shows a close-up view of the upstream gap region of the converging channel case, Fig. 6-9 (a), and the diverging channel case, Fig. 6-9 (b), for comparison. The meshes are slightly more dense than, but generally consistent with, those used in the flat plate problem computational models in Chapter 5.

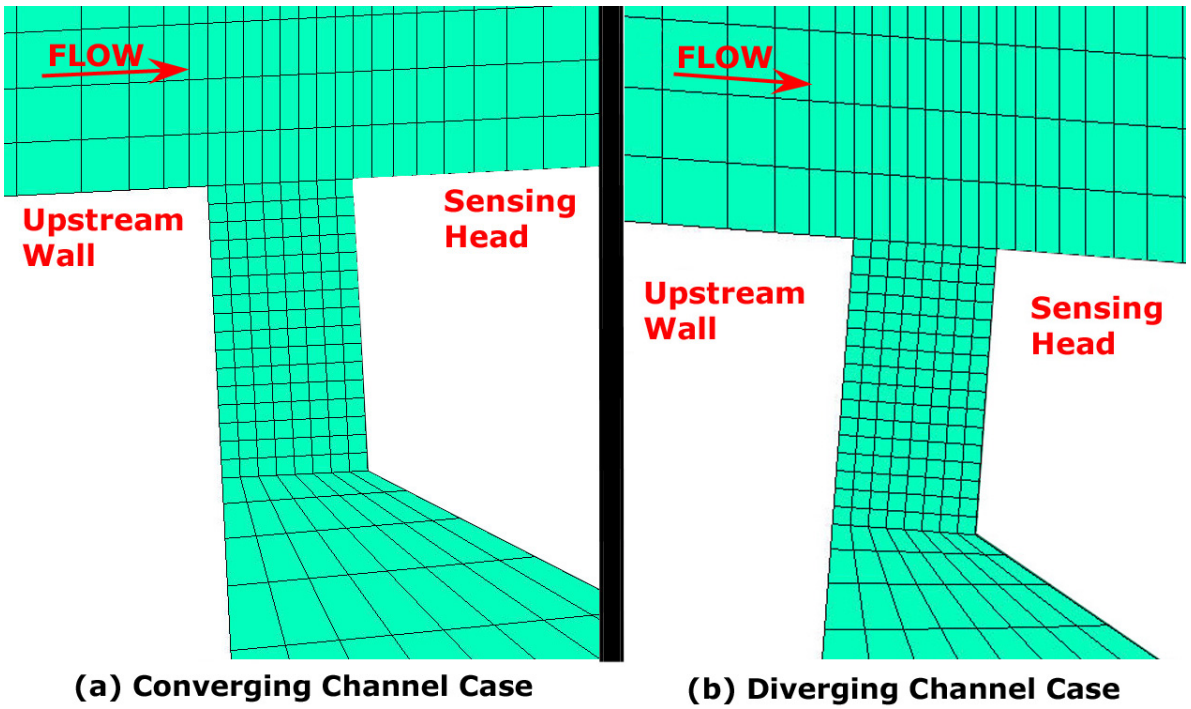

Figure 6-9. Mesh of Upstream Gap Region along Gage Symmetry Plane for Converging and Diverging Channel Cases

The boundary conditions for the global and embedded problems are the same as they were for Chapter 5, with one notable exception. The walls all received the no-slip condition and the inlet length of the two global problems before the plate received the symmetry condition of no vertical velocity with other conditions left free. The inlet of each global problem received the usual turbulence conditions of 0.0 for turbulent kinetic energy, and 1.0 for turbulent dissipation, as well as a vertical velocity component of 0.0, and the dimensionless stream-wise value, u_{INLET}, as given in Table 6-1. The outlet of both global problems was given a pressure condition of 0.0.

The significant difference from the flat plate problem of Chapter 5 to these problems here is that here the top surface of both global problems and both embedded problems represents a symmetry plane. Thus, a normal velocity of zero was imposed on all those surfaces. This is unlike Chapter 5 in which the correct condition on the top surface was a free boundary. Here, the upper surface forms the streamtube, forcing all flow to enter the inlet and exit the single outlet of the computational region. Because of this, pressure is solved relative to the outlet condition, balanced by the changing velocity imposed by the continuity equation.

One note about the pressure is that it is important to remember that the pressure solution over the computational domain is calculated relative to the outlet. Thus, the diverging channel case will predict negative pressure values as dictated generally by eqn. (6-2). Obviously, a negative absolute pressure is non-physical, but the solution is only relative to the reference point of the outlet, so the solution is valid. Also, note again that the conditions of these problems show that only the gradients of pressure are important anyway, so the pressure level itself is irrelevant.

With these conditions applied to the global problems, the embedded problems use the same scheme where applicable. In addition, the centerline of the gage represents a symmetry plane, while the outer z-boundary was left as free, just like in Chapter 5. The lateral distance in the z-direction of the embedded models, w_1, was increased some from that for the flat plate case in Chapter 5 just to make allowances for unexpected features of a more complex flow.

As for the flat plate case in Chapter 5, inlet conditions for the embedded region problems consisted of direct transfer of u, v, κ, and ε from the global solutions. In addition, P was directly transferred from the appropriate station of the global solution to the embedded region outlet. Although analytically it is known that pressure is approximately constant normal to a boundary layer flow, it was thought best to transfer the exact numerical solution to the outlet for consistency. The numerical condition does confirm that the pressure changes very little along this boundary.

6.3 Solution of the Global Channel Problems without a Gage

The global problems provide the basis for the embedded problems to come, so the results from these two problems are given before moving into the embedded region cases with the gage involved. The analysis begins with the resulting shear stress coefficient plot from these two solutions as shown in Fig. 6-10, compared to the nominal flat plate case for reference. Remember that one of the desired features of these problems was to produce a shear stress significantly different from the flat plate flow. In all cases, the coefficient is normalized by the reference free-stream dynamic pressure, the same as used on the flat plate. There is no correction made for the changing edge velocity at various stations in the boundary layer of the channel problems. The diverging channel case obviously avoids separation along its length, as desired.

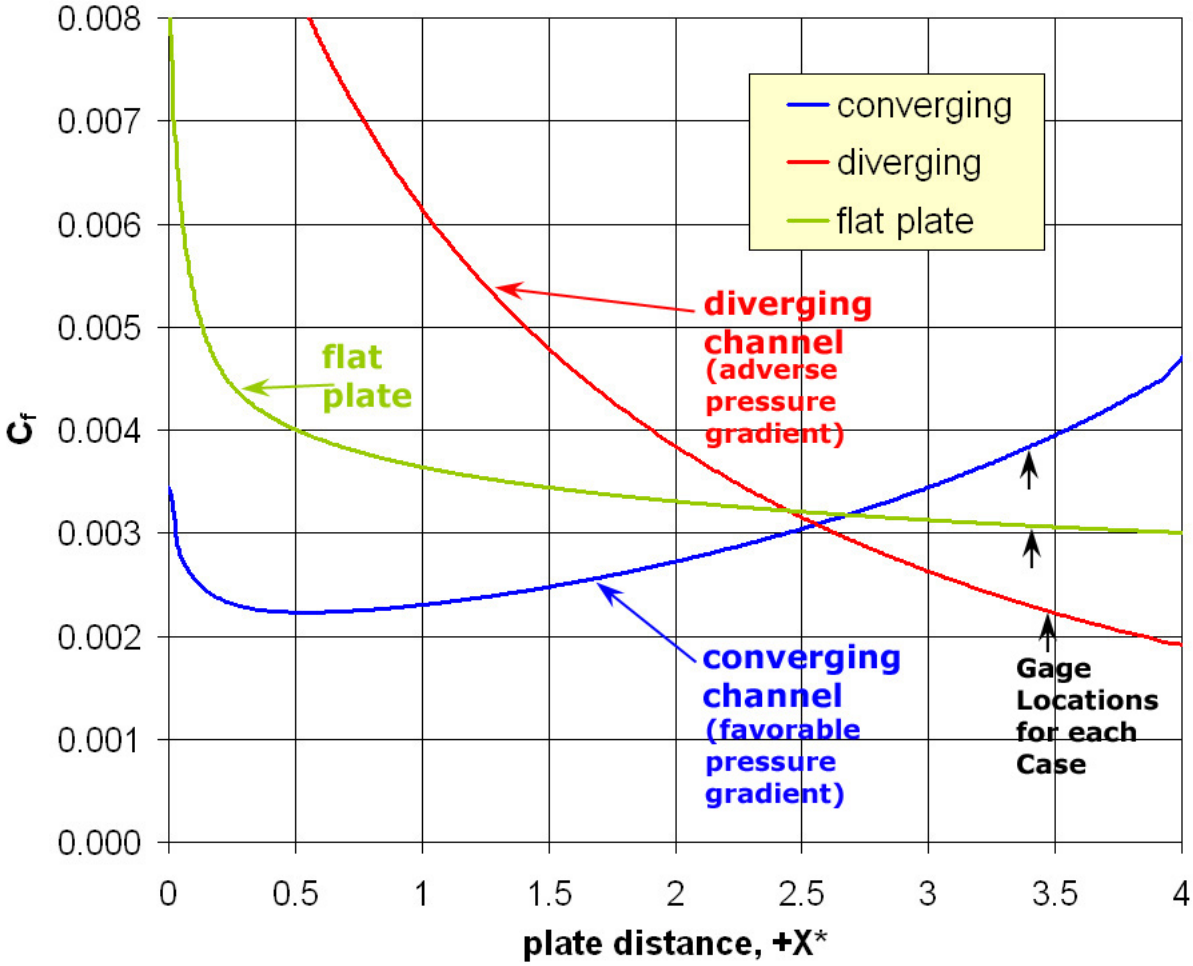

Figure 6-10. Comparison of Global Problem C_f Results for Converging, Diverging, and Flat Cases, Coefficient Based on Reference Dynamic Pressure

The position chosen for the center of the gage head in all three problems is illustrated by a black arrow head on all three curves, located just before an x^* station of 3.50. For all three cases, the edge velocity at the top of the boundary layer is approximately 1.0. This was a desired feature, as was keeping the channel gage cases at a similar Reynolds number based on plate length as for the flat plate flow. This obviously was accomplished too, since the arrow heads are approximately lined up vertically. Because the dynamic pressure is the same in all three cases at this point, comparing the C_f values between cases is more straightforward.

From the information in Fig. 6-10, the target C_f value for each problem was calculated, numerically integrating over the head length at the appropriate station for each case just as before. This number works out to be 0.00384 for the converging channel, and 0.00224 for the

diverging case. Both numbers are sufficiently different from the flat plate case ($C_f = 0.00307$) as to be useful. The issue of separation was also avoided in the adverse pressure gradient case, since the skin friction coefficient value remains significantly above zero even at the end of the plate.

The x-direction velocity contour distributions are given by Figs. 6-11 and 6-12. Looking at these contours provides some indication of the boundary layer thickness for each case. The boundary layer appears very thin for the favorable pressure gradient flow in Fig. 6-11, almost too small to see. This was a major limiting factor in the design of that problem. Although increasing the plate slope could have increased the pressure gradient further, the boundary layer continues to get thinner as this occurs. The thickness of the boundary layer for the adverse pressure gradient case in Fig. 6-12 is much larger.

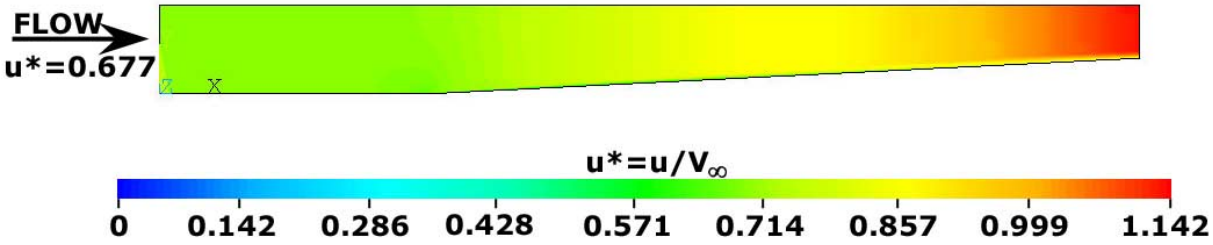

Figure 6-11. Contour Plot of Dimensionless X-Direction Velocity Solution for Converging Channel Case (dP/dx < 0)

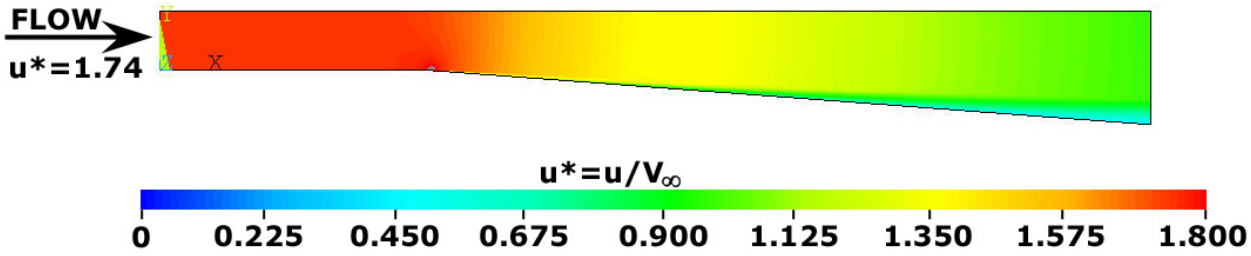

Figure 6-12. Contour Plot of Dimensionless X-Direction Velocity Solution for Diverging Channel Case (dP/dx > 0)

The resulting pressure distributions for the two cases are presented in Figs. 6-13 and 6-14. These solutions match up quite well with the simple 1D predictions of eqn. (6-2). Both plots are given relative to the pressure of zero set on the outlet face. Of course, the gradient of

pressure is more directly important here. Therefore, the flow is further validated by showing a plot of the pressure gradients compared to the simple 1D predictions of eqns. (6-1) and (6-2) in Figs. 6-15 and 6-16 for the two relevant cases. A simple, centered operator finite difference was used for the discrete solution of pressure along the centerline of each case, so this explains some of the waviness seen in the numerical solution. The trend and approximate values, however, line up extremely well with the predictions. The small variation in each case can be explained by considering that the effective cross-sectional area is changed slightly by the presence of the boundary layer.

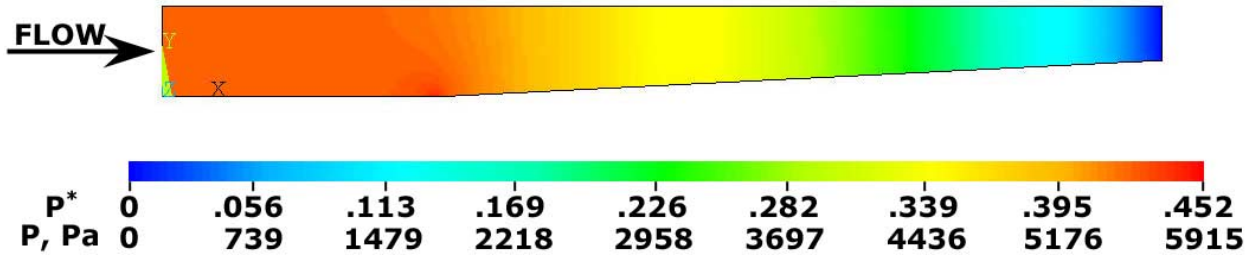

Figure 6-13. Contour Plot of Pressure Solution for Converging Channel Case (dP/dx < 0), Scaled Non-dimensionally and Dimensionally

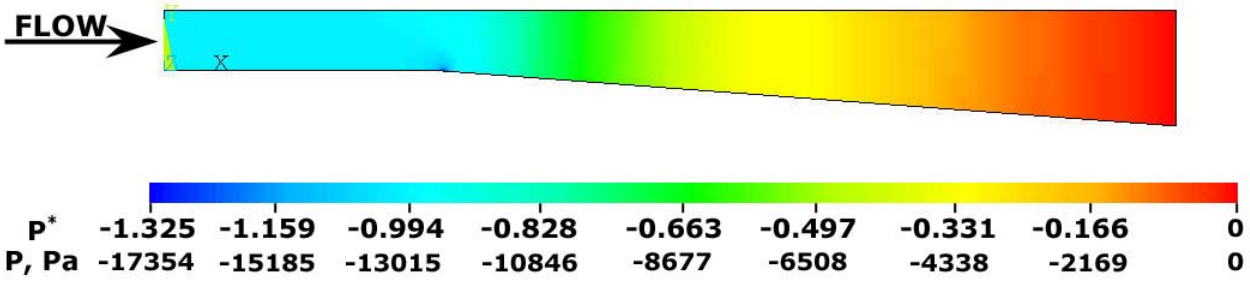

Figure 6-14. Contour Plot of Pressure Solution for Diverging Channel Case (dP/dx > 0), Scaled Non-dimensionally and Dimensionally

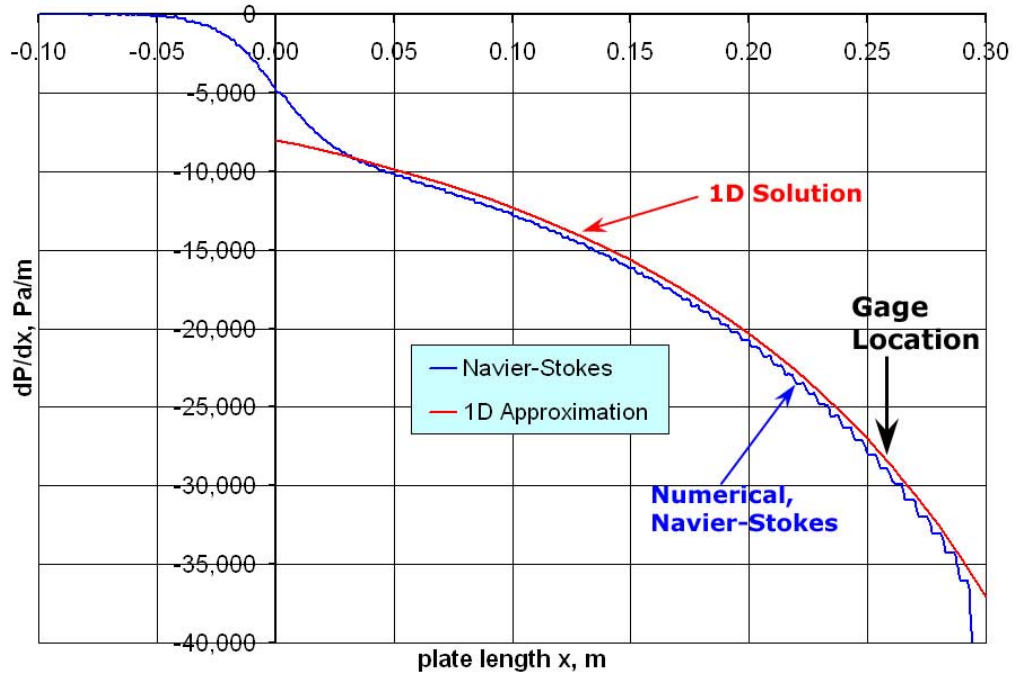

Figure 6-15. Pressure Gradient as a Function of Plate Station for Converging Case, Compared to 1D Analytical Solution from Equation (6-2)

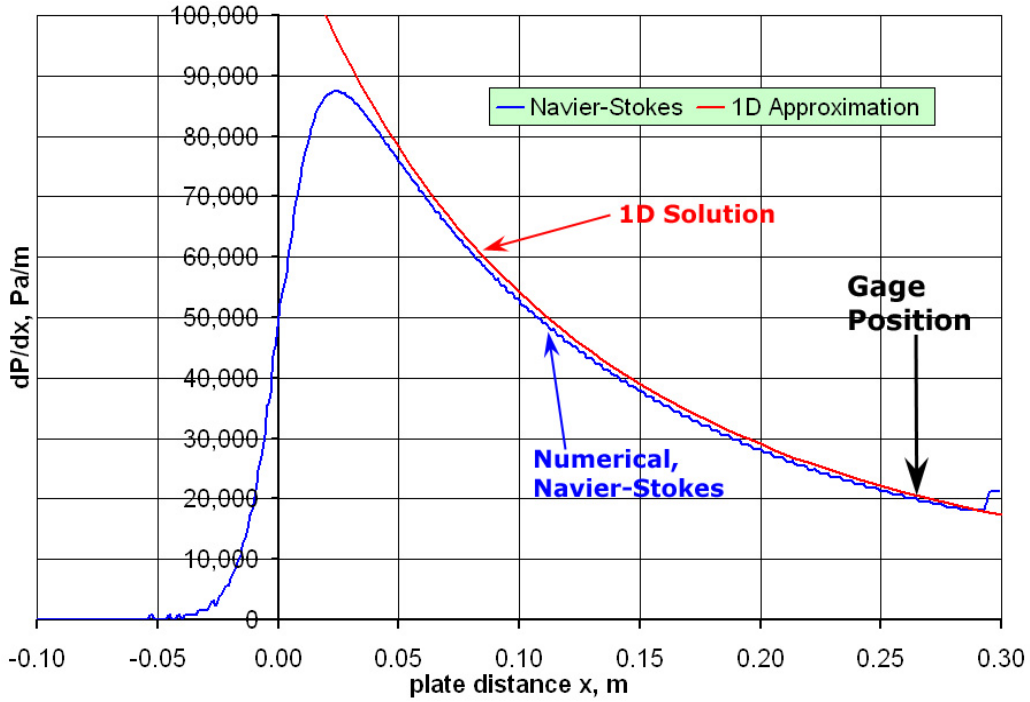

Figure 6-16. Pressure Gradient as a Function of Plate Station for Diverging Case, Compared to 1D Analytical Solution from Equation (6-2)

The work of Clauser [1954] using his pressure gradient parameter given in eqn. (6-3) showed that positive values around 3.0 or so showed significant departure in characteristics from the flat plate case. The idea then, was to target symmetric values of +/- 3.0 for these two cases. The diverging channel case produced an average pressure gradient in the region of the embedded problem 19,933 Pa/m or 0.1141 in dimensionless terms. The displacement thickness was estimated by numerical integrating the boundary layer profile value $(1 - u^*/U^*_{EDGE})$ at the station corresponding to the head center. These results generated an estimated β of 2.61. The converging channel case showed an average pressure gradient of -28,391 Pa/m or -0.1626 in dimensionless terms. This is somewhat higher in magnitude than the diverging case, but produced an estimated β of only -0.44. Raising the pressure gradient higher by tilting the wall more only made the boundary layer thinner, and β remained basically unchanged. Thus, symmetry in the β parameter is not really a valid expectation, and these values were considered acceptable given the magnitude of the actual pressure gradients for both cases.

Finally, Fig. 6-17 shows a plot of y^+ along the wall for both cases to show that this important criterion was well satisfied for both cases. Further, the value is consistent enough for both cases to justify the validity of making comparisons between the two.

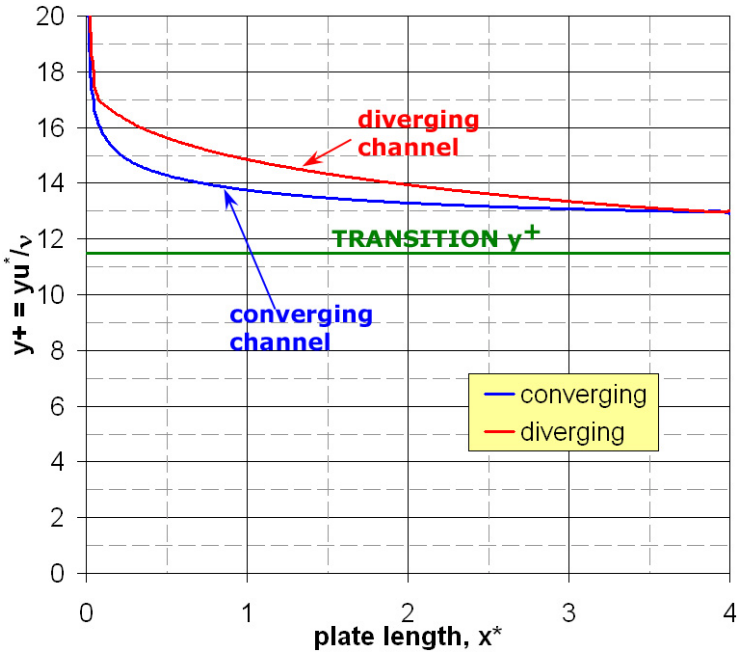

Figure 6-17. Plot of Global 2D Channel Solution y^+ Values, Including Transition y^+ Limit

6.4 Flowfield Results

6.4.1 Velocity Field Results

As before, a look at the flow field through the gap can be insightful in understanding the relationships and roles of the resulting forces in the gage performance. The flow results of the two cases are presented in Figs. 6-18 and 6-19, showing the flow patterns at the gage symmetry plane. Figures 6-18 (a) and 6-19 (a) are for the upstream gap region, and Fig. 6-18 (b) and 6-19 (b) show the downstream gap region, with the center of the head of each figure removed so that the gap area can be enlarged for clarity.

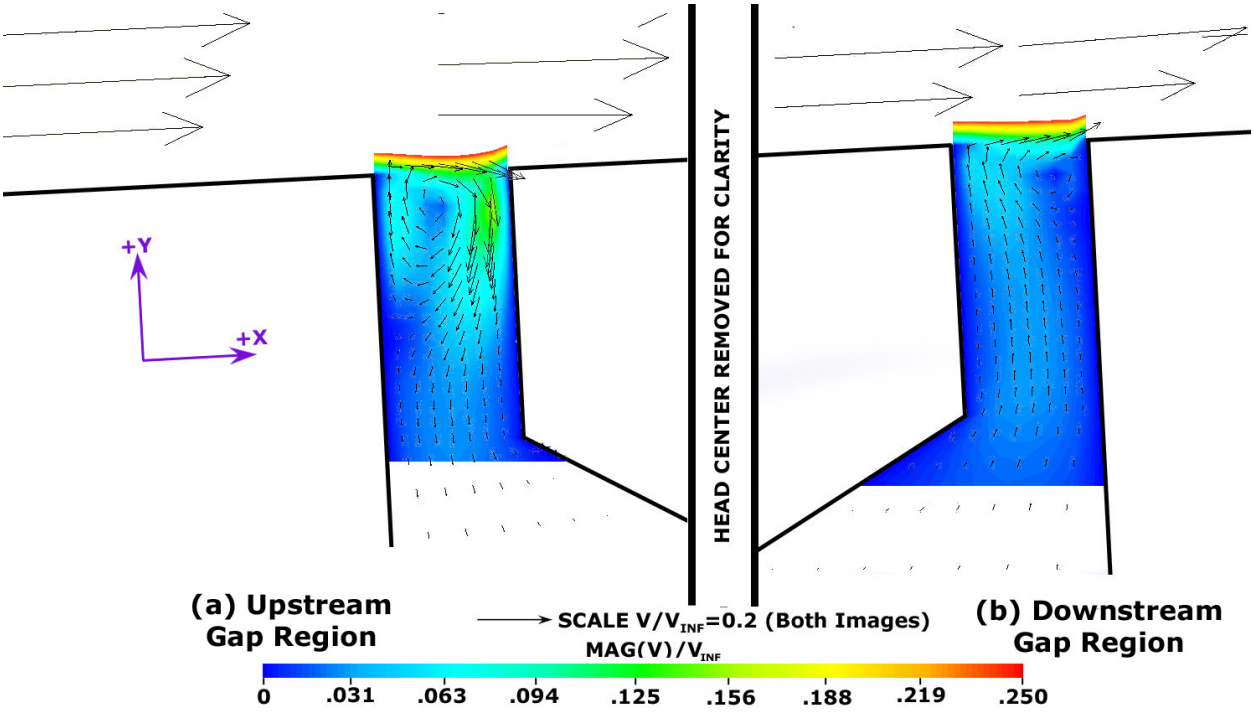

Figure 6-18. Scaled Vector Field Overlaid with Velocity Magnitude Contours for the Converging Channel (dP/dx<0) Case in the Gap Regions (Vector Points Arbitrarily Selected for Clarity)

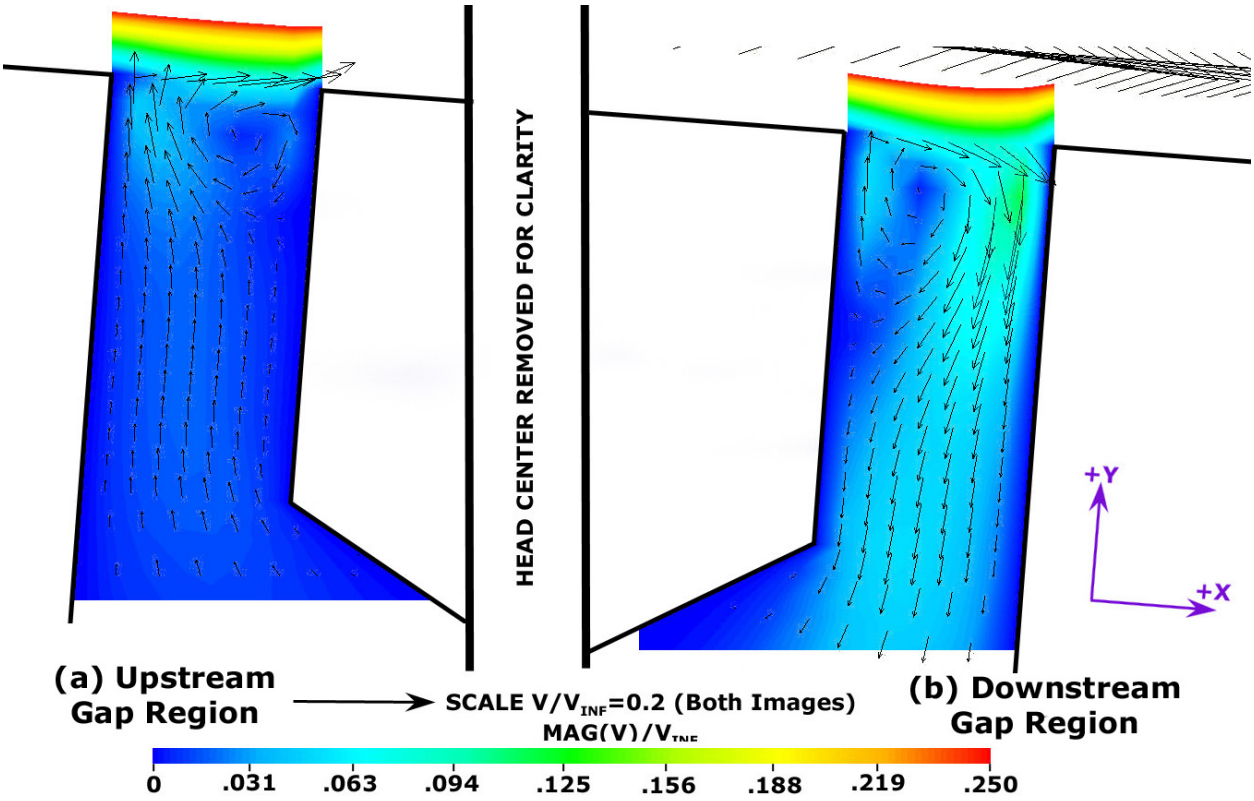

Figure 6-19. Scaled Vector Field Overlaid with Velocity Magnitude Contours for the Diverging Channel (dP/dx>0) Case in the Gap Regions (Vector Points Arbitrarily Selected for Clarity)

The converging channel case, Fig. 6-18, shows some recirculation in the upstream gap, but a significant flow rate passes into the cavity from this gap. Flow moves out of the downstream gap area. Some blockage is again created here by recirculation, but a significant flow rate moves back out into the flow. The flow rate is somewhat higher in magnitude compared to what was seen in the baseline flat plate case of Chapter 5. In that case, most of the gap showed circulating motion, and only a small flow actually entered the cavity. Here, the velocity is around 2-3% of the free-stream velocity.

The diverging channel case, Fig. 6-19, shows similar but opposite behavior. Flow enters from the downstream gap, moves in the negative *x*-direction through the cavity, and exits back out from the upstream gap. Again, some recirculation can be seen, but the fraction of the total flow exhibiting this behavior is much smaller than in the flat plate cases of Chapter 5 and the overall flow is significant and follows a distinct path.

In both cases, the important result is that the flow follows the path from high pressure to low pressure, as caused by the pressure gradient applied in each case. The magnitudes of the velocity present in the gap (approximately 10% of the free-stream velocity) is generally consistent with the magnitudes seen in the baseline flat plate case of Chapter 5, but the fraction of this flow entering the cavity region is much greater than in the flat plate cases. This change in behavior is certainly caused by the fact that there is now a pressure difference between the upstream and downstream gap regions in both cases, providing a driving force for the flow in the gap and cavity regions. The complex patterns seen in the gaps themselves for both cases will reflect the transmission of pressure forces seen in the next sub-section.

6.4.2 Stress Field Results

In Chapter 4, the issue of the validity of an assumed linear pressure gradient in the gap was addressed. The general conclusion from that chapter correlated with the conclusions of Everett [1958], which was that the assumption was not generally valid, but that increasing the lip to gap ratio (*c/G*) of the gage made the actual variation most linear. Thus, a very high *c/G* value could be approximated with a linear pressure drop in the channel. The flow conditions in which Everett investigated this assumption were quite similar to the laminar channel flow in Chapter 4, and this investigation continues here with these high Reynolds number cases. As with the results in Chapter 4, traces of pressure are presented along the lip surface from the top of the head exposed to the flow downward into the cavity to the end of the lip. These traces are given at various angle stations around the circular head, starting at the upstream edge of the gage.

Figure 6-20 shows the pressure traces from the converging channel case. Just as for the flat plate cases in Chapter 5, this figure shows that the same stagnation region appears on the upstream face of the lip as a result of the rapid flow deceleration moving into the gap. In fact, this effect is quite strong, particularly on the upstream symmetry plane. The downstream part of the face (from 90 to 180 degrees) shows some pressure change in a pattern similar to the baseline channel case from Chapter 4, but the pattern is no longer symmetric about the cavity region.

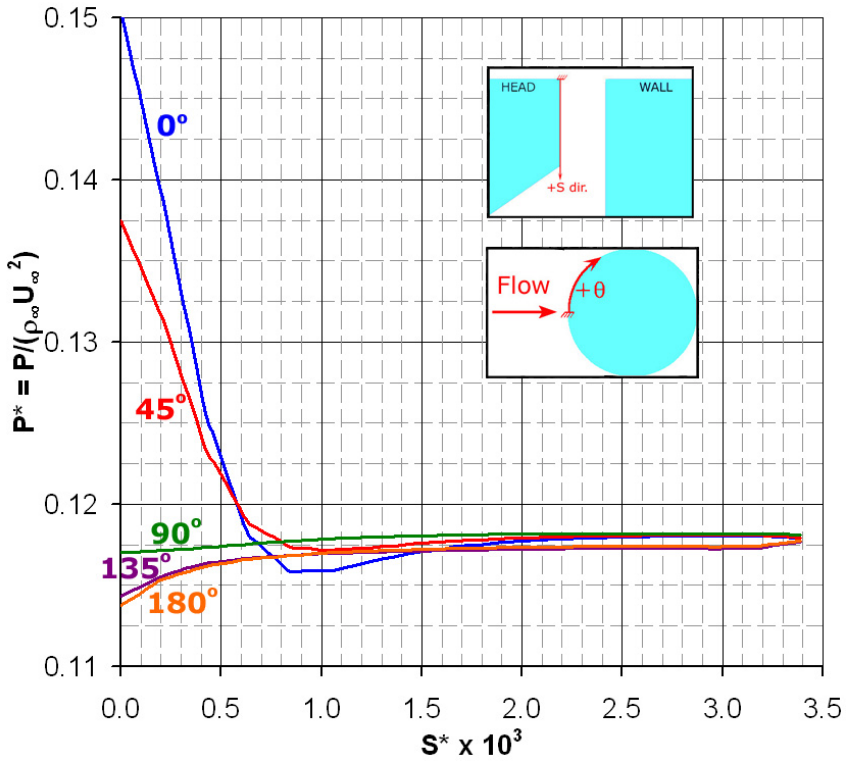

Figure 6-20. Dimensionless Pressure Traces at Various Angle Stations in the Gap Area along the Lip Surface of the Converging Channel Case

In similar fashion, the pressure traces along the lip surface for the adverse pressure gradient diverging channel case are shown in Fig. 6-21. This figure shows a more intricate pattern than the converging channel case above. With the knowledge from the last section that the flow is actually reversed in this case, an interesting set of features emerges. On the upstream side, the same stagnation pressure region exists that was highlighted earlier. Comparing with Fig. 6-20, the increase above the 90 degree line is about the same amount as in the converging channel case. Since the dynamic pressure is similar in both cases, this is logical. On the downstream side, one would expect that the pressure in the gap would be high since the pressure gradient is positive overall for this case. Figure 6-21 shows that this is not the case, however. The pressure on the downstream gap actually decreases considerably, apparently caused by the presence of the gap, and the pressure driven flow enters through this gap rather than exiting as in the first case. Farther down into the gap, the pressure on the downstream side does rise back up to the expected levels, but the behavior near the surface significantly deviates from the expected

outcome. It is clear that for both cases there is no semblance of a linear pressure pattern in the gap region.

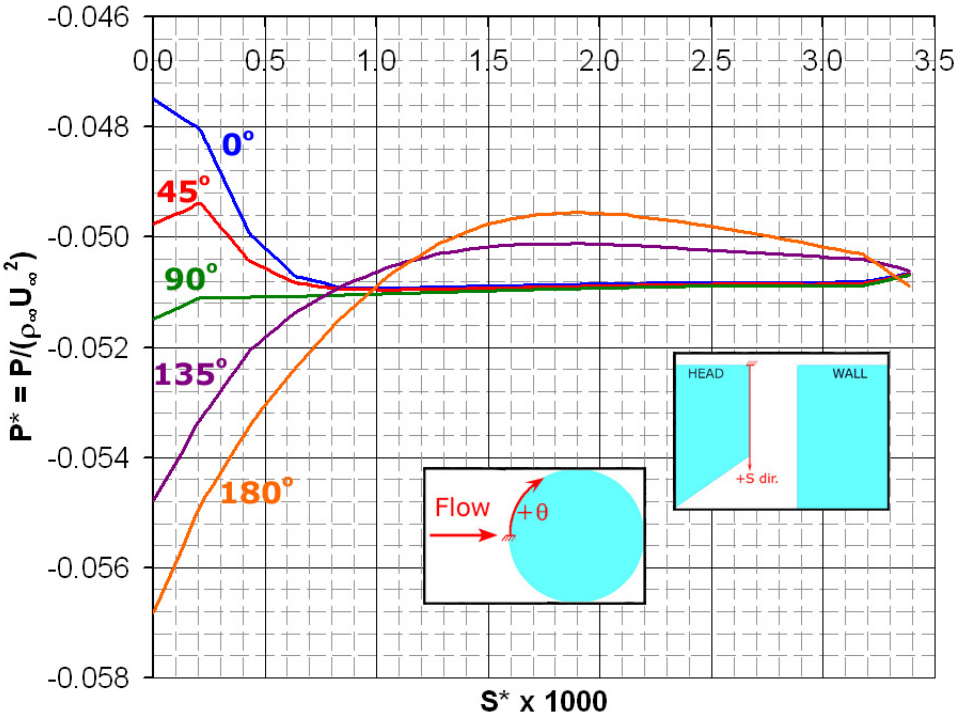

Figure 6-21. Dimensionless Pressure Traces at Various Angle Stations in the Gap Area along the Lip Surface of the Diverging Channel Case

The pressure contours over the head will obviously reflect the data shown in the previous two figures. Those two figures give an indication of the lip force defined by Allen [1976]. In addition, there is the issue of the imposed pressure gradient over the top of the head, and the complex interactions around the gap. Figure 6-22 shows the pressure contours over the head surface for the converging channel case, as seen from upstream and above the head. Just like in Fig. 6-20, a stagnation region clearly appears along the front surface. In addition, the negative pressure gradient is clearly visible on the top of the head. This pressure variation will lead to a strong positive *z*-direction moment. This is opposite to the additional positive force caused by the lip force or the stagnation region on the front of the head.

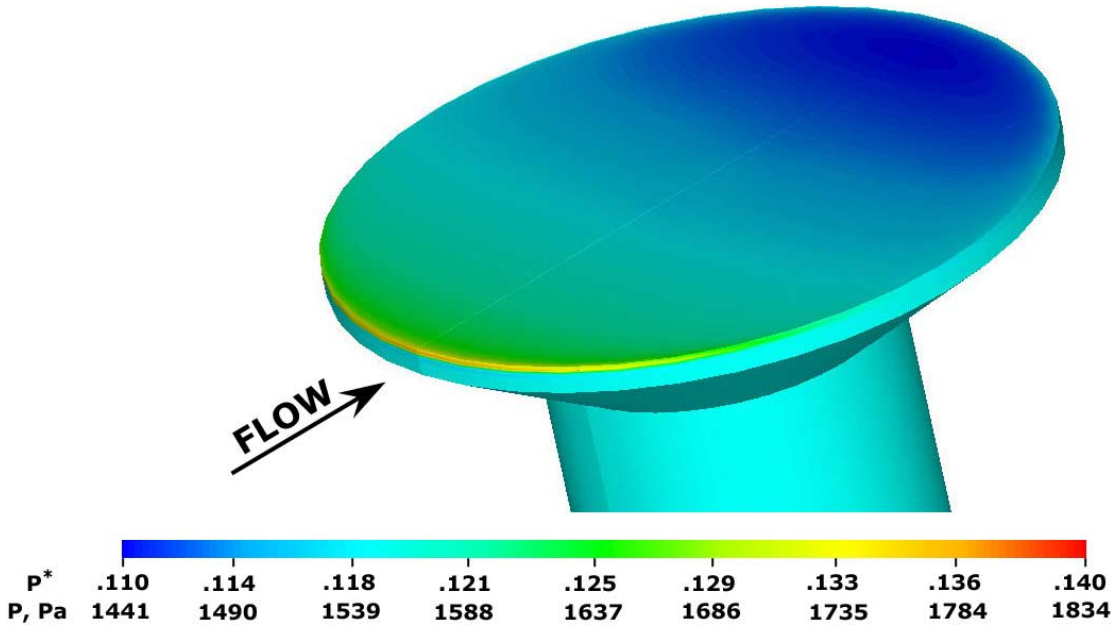

Figure 6-22. Pressure Contours over 3D Head Surface of Converging Channel Case, Scaled Dimensionally and Non-dimensionally

Figure 6-23 shows a side view of the pressure field on the symmetry plane of this same converging channel case. The side view more clearly shows the pressure along the lip surface into the gap that Fig. 6-20 illustrated. In addition, it is perhaps easier to see the pressure variation resulting from the pressure gradient, as well as the pressure changes occurring right at the edge of the gap entrances in Fig. 6-23.

Figure 6-24 shows a split view of the head surface of the diverging channel case. Figure 6-24 (a) shows the head viewed from generally upstream and above the head, while Fig. 6-24 (b) shows the head viewed from downstream and above. The stagnation region at the front can be seen, as can the low pressure region along the back of the lip surface. This combination still yields a positive net lip force, despite the pressure gradient. In this case as well, the pressure gradient along the top of the head produces a negative z-direction moment contribution. Thus, this diverging case is expected to be the worst of the two cases in terms of accuracy since the contributions sum rather than cancel.

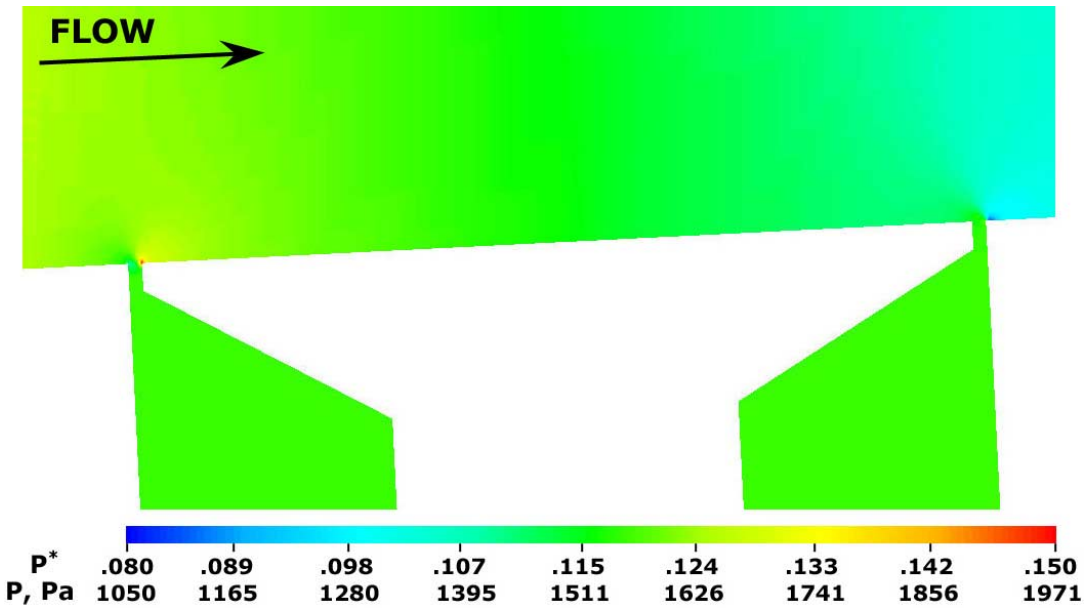

Figure 6-23. Pressure Contours along Symmetry Plane of Converging Channel (Favorable Pressure Gradient) Case, Scaled Dimensionally and Non-dimensionally

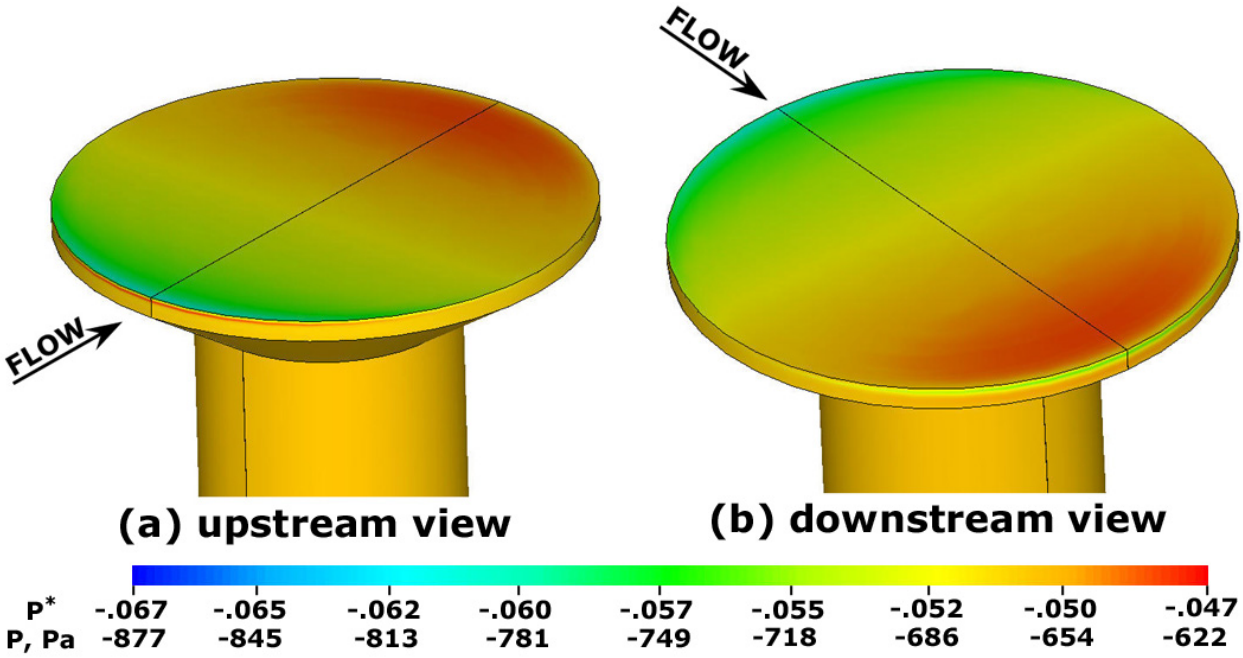

Figure 6-24. Pressure Contours over 3D Head Surface of Diverging Channel (Adverse Pressure Gradient) Case, Scaled Dimensionally and Non-dimensionally

Finally, a shear stress plot is given for the converging channel case in Fig. 6-25. Except for some small increase near the leading edge of the head, the skin friction coefficient remains

relatively undisturbed despite the large pressure effects happening on the gage. The target C_f value is again 0.00384 for this case. The figure shows that the head sees this value over most of its surface. This leads to the conclusion that the shear stress (friction) force contribution will be close to what it is supposed to be.

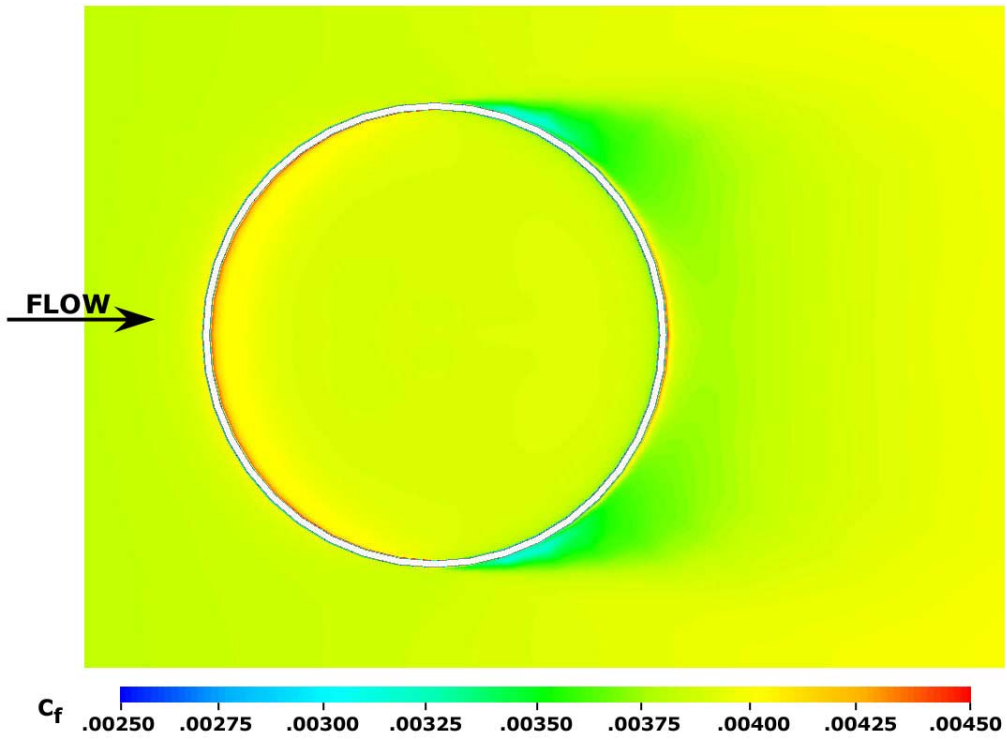

Figure 6-25. Skin Friction Coefficient Contours over Head Surface and Surrounding Wall Area for Converging Channel (Favorable Pressure Gradient) Case

Figure 6-26 shows a plot of skin friction coefficient for the diverging case. Similarly here, the nominal level is close to the target value of 0.00224, and the flow is mostly undisturbed, except near the leading edge and near the extreme outer edge. Both Fig. 6-25 and Fig. 6-26 exhibit the same characteristics that were seen in Chapter 5: a local skin friction increase near the leading edge of the gage and the edge of the downstream wall, and a localized decrease at the outer gage edge, trailing downstream over the wall for some distance. This is an effect of the flow through the gap, and it has only a small effect on a well-aligned sensing head.

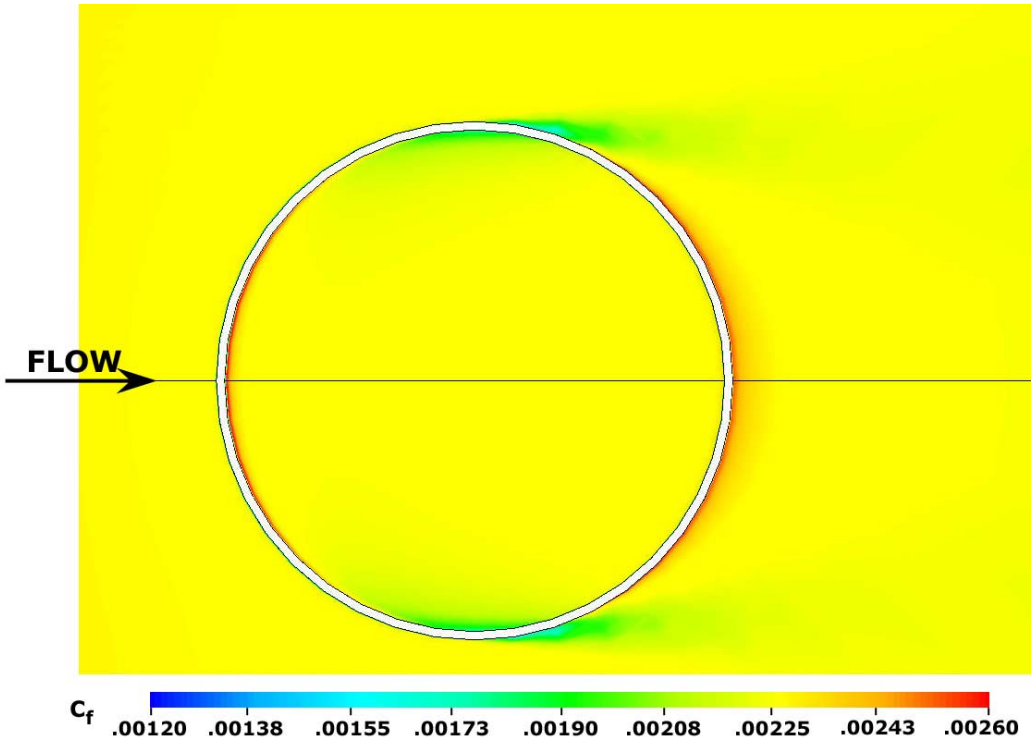

Figure 6-26. Skin Friction Coefficient Contours over Head Surface and Surrounding Wall Area for Diverging Channel (Adverse Pressure Gradient) Case

6.5 Force and Moment Results

Now, the force and moment results of the two pressure gradient cases are presented. Here, they are given only in tabular format, since there are not a sufficient number of similar cases to justify plots. The dimensionless force results are given in Table 6-4. The results indicated by the stress field plots do indeed have their implied effects on the total force values.

In both cases, shear stress contribution is well-predicted. Contribution by the lip (pressure) force is a concern in the converging channel case (which raises the error level in F^*_X up to 9%), but this same value works out to be small in the diverging channel case. This is supported by Fig. 6-21, where the upstream and downstream values of pressure cross midway into the cavity. Thus, the pressure variation has only a small net effect on the force. In both cases, moment is a strong contributor to the total strain in the flexure as a result from the normal force term caused by the pressure gradient.

Table 6-4. Results of Global Force and Moment Parameters for Favorable and Adverse Pressure Gradient Varying Area Channel Cases

component	Converging channel ($dP/dx < 0$)			Diverging Channel ($dP/dx > 0$)		
	pressure	shear	total	pressure	shear	total
F^*_X	0.0624	1.0275	1.0899	0.0079	0.9941	1.0020
F^*_Y	-9.7316	-0.0063	-9.7379	9.2651	0.0056	9.2707
M^*_Z	0.4929	0.0082	0.5011	-0.5570	-0.0021	-0.5591
% strain error	-6.0 %			17.0 %		

The overall outcome of these two cases is actually quite encouraging. These two models represent high Reynolds number flow conditions with significant pressure gradient levels. Under these conditions, the indicated stream-wise force error was only 9% and the highest strain error level found was only 17%, which are no more significant than the errors induced by a large gap in the preceding chapter for a comparable case without a pressure gradient. This speaks well about the ability of this basic design to minimize the potential problems caused by pressure gradients in general. The pressure field plots indicate that making the head diameter smaller would further reduce the effects of the pressure gradient via the normal force term. Although only one head size was studied here, this conclusion is supported both by logical supposition and by the data available here.

It is also known from earlier that minimizing the lip size can have an effect on this result. Minimizing lip size will also minimize the contribution by pressure to F^*_X. However, from the data in Table 6-3, this could actually make the situation slightly worse since the positive pressure force somewhat offsets the negative strain error contribution from the moment. In the diverging channel case, minimizing the pressure is desirable, but the force is small. It only adds about 1% to the strain error total, so a lip size change there would have very little effect. This suggests that there might be some optimal non-zero lip thickness that would correctly balance the two pressure effects (force and moment) for the converging channel case while still remaining small enough that the force contribution by pressure will be minor in the diverging case. A similar result was seen for the negative pressure gradient case in Chapter 4, with the exception that the moment effect was small enough that offsetting the moment with the extra force seemed too risky for

what amounted to less than 1% of possible benefit. Thus, it was recommended there that the lip be simply made as small as possible. Here, the data suggests that there possibly could be some benefit in high convection applications to optimizing the lip thickness to a non-zero value.

Without further detailed study of this lip thickness effect, it is impossible to say whether the optimum lip size would hold for a wide range of pressure gradient levels and flow conditions. Designing an individual gage for each specific pressure gradient level is not practical unless the lip size could be fixed for at least a reasonably large range of pressure gradient levels. Although increasing the lip size further could possibly have some benefit in these cases, the danger in doing this is high without understanding the full ramifications of doing so and any such action would have to be studied very carefully. In the absence of such data, the only course of action is to minimize the lip thickness and live with the moment generated by the pressure gradient on the head. This value could be estimated with pressure sensors in the same region or analyzed with CFD solutions and subtracted from the resulting skin friction measurement as a reasonable alternative.

Finally, it is very important to note here that acceptable gage accuracy can be achieved without a viscous liquid fill in the gage cavity for cases with rather strong favorable and adverse pressure gradients. This has a great practical advantage because of the many problematic and challenging issues surrounding the liquid-filled gages.

6.6 Validation and Verification

The usual issues in verification and validation are discussed here as appropriate to these two pressure gradient cases. Since these two models are similar in most ways to the flat plate cases of Chapter 5, many aspects of these issues have been covered there already. Validation, in fact, is such an example. The last chapter covered a study of the adequacy of the turbulence model performance in and around the complex gap region for a flat plate case. Based on the results of that study and supporting evidence of the effective viscosity determination of the baseline case given in that chapter, the turbulence model is assumed valid (or at least adequate) for these cases here as well. It can be said that similar effective viscosity plots were seen for these two cases also – a damping of turbulence in the gap and cavity regions similar to Fig. 5-15. Since there are no differences in these two cases which would be considered an issue in the

standard κ–ε performance, the default turbulence model was used again here without additional specific assessment.

Convergence has been a non-issue so far when considered against the other sources of computational model error. This is true again here. Normalized residual values for each individual degree of freedom are given in Table 6-5 for both pressure gradient cases. The levels are consistently low for all degrees of freedom for both problems. As before, these numbers are the maximum absolute values for any node in the model, so most nodal values are much lower.

Table 6-5. Normalized Maximum Magnitude Nodal Residual Values Given by Degree of Freedom for Each Case

Degree of freedom	Converging case	Diverging case
VX	3.1×10^{-5}	4.7×10^{-5}
VY	1.1×10^{-4}	1.5×10^{-5}
VZ	1.3×10^{-5}	1.0×10^{-5}
PRES	1.5×10^{-4}	2.2×10^{-5}
ENKE (κ)	1.0×10^{-5}	1.5×10^{-5}
ENDS (ε)	2.7×10^{-5}	2.0×10^{-5}

As a confirmation that the residual values are indeed sufficiently low, an iterative history for each case is given if Fig. 6-27, with Fig. 6-27 (a) for the converging channel case and Fig. 6-27 (b) for the diverging channel case. In both graphs, a percent difference from the final value is tabulated for the global force components as well as the strain error. The diverging channel case in particular has a significant iterative convergence error at the start of the history, but most of the error damps out by the stopping point. The converging channel case shows low levels throughout, although the convergence is highly non-monotonic. Looking near the stopping point, it is apparent for both cases that the percent differences for all the monitors have reduced to something on the order of 0.1%. This is more than reasonable and insignificant relative to the mesh dependence error contributions.

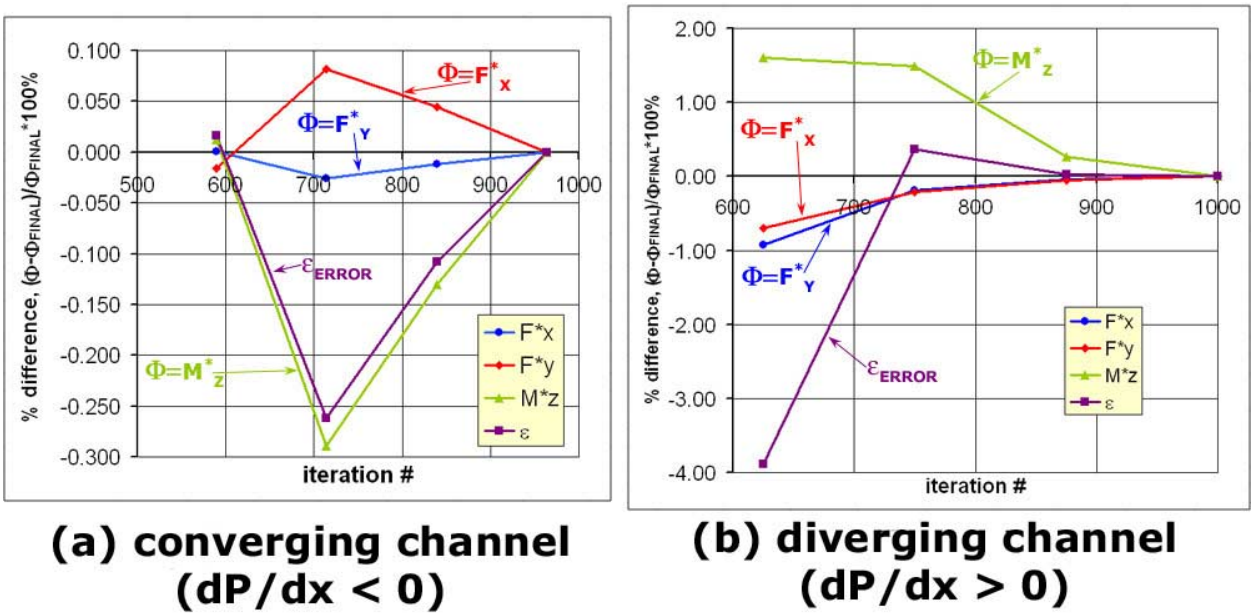

Figure 6-27. Iteration History Illustrating Convergence Level for each Global Force Component

The ordered mesh dependence study proceeds just as it did earlier. For each of the two pressure gradient cases, a representative two-dimensional model was created, using the identical structured mesh for the 2D projection. This projection was solved using the same boundary conditions (exempting the *z*-direction boundaries of course) and the solution calculated as a "worst-case" scenario, based on the fact that the sensing head in this 2D case is a stronger obstruction to the flow. For generating Richardson extrapolation error estimators, a second coarser 2D grid was created, this time with a refinement ratio of 1.333. This results in 75 points across the boundary layer, compared with 100 in the main grid.

Table 6-6 gives the resulting error estimation values, A_1, for each global parameter in the two pressure gradient cases, broken up by the pressure contribution, the shear stress contribution, and the weighted sum of the two for each variable. The results appear quite similar to what was seen for the flat plate case in Chapter 5, although the overall estimations here are actually somewhat improved over those cases when considering the practical implications of the table.

As before, there is a large variation in the error estimations for the different contributions made to force and moment. F^*_X is the primary variable to study, and, for both of these cases, the contribution to this parameter by pressure is small compared to the shear stress contribution. This is particularly true for the diverging channel case, where pressure contributes only 0.79% of

the total x-direction force on the head. Even though the error estimation predicts a seemingly excessive level of uncertainty (200%) for this value, the small fraction of the total that the pressure term contributes cannot meaningfully impact the total force even with the indicated uncertainty level in the results. In other words, the uncertainty in this term results in an uncertainty of only +/-1.6% in the total. With smaller error levels predicted by the shear stress, Table 6-6 shows that the accuracy of the total is estimated to within approximately 5.3% (or 16% GCI) or less for both cases. The exact opposite scenario occurs for the moment, M^*_Z. There, the pressure error levels are small, while the shear stress levels are excessive. Since the shear contributes almost nothing to the moment though, the total levels are just slightly higher than for the *x*-direction force. The F^*_Y variable is the only parameter of the three that shows significant uncertainty values, being approximately one order of magnitude higher than the other two. The case for the accuracy and subjectivity of this parameter was already made in detail in Chapter 5, however, so the reader is referred back to Section 5.6 for that discussion. It will not be repeated here, except to say that these levels are more than acceptable for the purposes of that parameter as used here.

Table 6-6. Richardson Extrapolation Error Estimator and GCI Values for Pressure Gradient Cases, Given by Individual Global Parameter and Divided by Shear and Pressure Contributions

Parameter & case		pressure		shear stress		total	
		A_1	GCI_{FINE}	A_1	GCI_{FINE}	A_1	GCI_{FINE}
Converging channel (dP/dx<0) case	F^*_X	-30.5	91.6	-0.8	2.4	-2.7	8.2
	F^*_Y	-87.2	261.7	-144.2	432.7	-87.0	261.1
	M^*_Z	8.2	24.6	-61.6	184.8	7.5	22.4
Diverging channel (dP/dx>0) case	F^*_X	198.9	596.8	-2.9	8.7	-5.3	16.0
	F^*_Y	-46.1	138.4	-80.1	240.4	-46.2	138.6
	M^*_Z	-9.7	29.0	98.9	296.7	-9.4	28.1

Finally, the boundary placement dependence was looked at briefly for the baseline flat plate case in Chapter 5, and was shown to be small compared to the error just discussed. Since these two cases are under similar conditions (similar Reynolds number, identical gage geometry, similar flow patterns, etc.), the study done in that chapter is considered to be valid for these two pressure gradient cases as well. Just to be sure, all three boundaries – L_{UPSTR}, L_{DNSTR}, and w_1 – have been increased from that case, so the boundary error should be even more of a non-issue here.

CHAPTER 7: Concluding Remarks

7.1 Overview of Significant Results

The results presented here have been the outcome of a broad effort to fulfill the goals set out in the beginning of this document. These goals are reproduced again here as a reminder of the major conclusions of this work.

(1.) understand the detail of the flow physics in and around a typical direct measuring skin friction gage as well as the causes and contributions to error in measurement caused by the complex and subtle flow and stress fields involved

(2.) develop general guidelines for minimizing inherent errors in direct measuring, non-nulling skin friction sensor design

(3.) quantify and provide typical performance benchmark data and also develop a procedure for estimating error in an actual experiment using a skin friction gage

These objectives have been met directly and indirectly in a number of ways. Skin friction gage behavior was studied here in a range of flow situations including: (a) laminar and turbulent flows, (b) internal and external flows, (c) liquid and gaseous flows, and (d) flows with and without pressure gradients. The flowfield results presented give fundamental information of some of the qualitative and quantitative features of the respective flow situations that are caused by the presence of the skin friction gage floating head and flexure in the wall. These features, in turn, drive the performance of the skin friction gage and provide understanding about the sources of any error in the force and moment components for the gage. Also, in a simultaneous fulfillment of goals (1) and (3), the force results presented for the flow cases studied were divided up into the contribution by pressure and the contribution by shear stress to the total forces and moments. This tabulation indicates situations where induced errors are caused exclusively by either pressure forces or shear stress forces, as well as situations where the sources contribute by either summing together or partially canceling each other out.

First, the laminar channel flow problems showed the importance of proper alignment of the sensor, even in a flow of very small Reynolds number. In this case, the misalignment variable *Z* was the dominant effect. The effects of misalignment were found to be significant, changing the output by up to 15% for head protrusion and 10% for head recession in the range studied. The governing presence of the negative pressure gradient causes some positive strain error in the flexure even at perfect alignment, so recession of the sensing head first causes the strain error to reduce to zero before moving into the negative region. This study thus shows that head recession tends to be less costly than an equal amount of protrusion given a choice between the two.

The lip played an important role in the flow caused by the pressure gradient, because the lip of the gage controls the effective area over which the pressure differences are allowed to act. This lip force can be approximated by the contribution by pressure to F^*_X. Results show that minimizing the lip size can reduce the effect of the lip force to very low levels. Although pressure can still have a small effect even at zero lip thickness, this is negligible and provides accurate measures to within 1%. Thus, minimizing lip size in the presence of a pressure gradient under low Reynolds number conditions is a direct realization of the second objective. In addition, the detailed results can provide some estimates for the third objective under low Reynolds number, fully viscous conditions like these. The results confirmed the conclusions of Everett [1958], who suggested that the pressure variation into the gap along the lip surface cannot be simply treated as a linear function. Data here shows that pressure is indeed a non-linear function of distance into the gap, but larger lip to gap (*c/G*) ratios produce increasingly linear characteristics. Thus, for a very deep gap, a linear correction may be useful for a viscous (low Reynolds number) flow situation at the discretion of the researcher.

The low Reynolds number of this flow reduces significantly the importance of convection. Under these conditions, the gap size had only a minor influence on the accuracy of the measurement. Although research indicated that reducing the gap size as small as possible has some benefit, this effect is much smaller than the other variables in the study.

Second, the external, turbulent flat plate flows paint a different picture of gage behavior. Here, the importance of convection was increased dramatically, while the removal of the governing pressure gradient in the flow shuffled the importance of the design parameters. In this case, gap size took on an increased role, providing significant strain errors in the flexure up to

20% in the range studied. A suggested design rule provides both an estimate of error caused by the flow through the gap and a design tool to size the gap for a specific application.

For these cases, lip thickness had no effect on the outcome. For zero pressure gradient flow at perfect alignment, the lip force is small, causing only a relatively minor level of strain error. Reducing the lip size had little effect on the resulting strain error, since the lip force application point is very close to the surface edge. It is still wise to minimize the lip size in general, however, to make a more versatile design and to prepare for experiments where unexpected pressure gradients may occur.

Once again, misalignment took precedence as the major contributor to error in the turbulent, external flow problems, producing errors of over 100%. A comparison of Allen's experimental work with the present numerical misalignment results shows good correlation in terms of the general qualitative trends. Allen divides the forces into the lip component $(1-c/2a)C_L$, which can be compared to the F^*_X contribution by pressure, the friction component, C_f, and the moment component, (b/aC_N), which can be compared to the total moment M^*_Z (most of which comes from pressure). Note that negative M^*_Z has the effect of adding to the total resultant error. Allen shows a trend of strongly increasing moment effect, or large negative M^*_Z for head recession, while head protrusion shows a shallow decrease (positive M^*_Z) at a point of inflection, followed by a weaker negative M^*_Z effect for larger head protrusions. This is the behavior predicted here. Additionally, the lip force is positive for protrusion and negative for recession, a feature which is also generally predicted here. Further numerical comparison is difficult due to the large discrepancy in flow conditions.

Third, the results for the high Reynolds number pressure gradient flow cases indicate that the baseline geometry of the skin friction gage as studied here can significantly reduce the effects of either a sizable favorable or adverse pressure gradient. The data indicated that this gage suffered only a 6% deviation from the nominal target output for the favorable pressure gradient case, and 17% deviation for the adverse pressure gradient case. This error level is manageable. Previous results from the laminar channel flow study indicate that this error level could possibly be reduced even further with intelligent design of the lip and gap surfaces. The resulting pressure traces along the lip surface indicate that the assumed linear pressure variation through the gap as suggested by Coles [1953] and studied by Everett [1958] has no validity for these flow conditions. Finally, the adverse pressure gradient case indicated that the pressure force was

reduced to a small level, and that the 17% error associated with this case was caused almost exclusively by the *z*-rotation moment caused by the pressure gradient. This indicates that a smaller lip thickness will not necessarily improve the accuracy of a skin friction gage under this type of pressure gradient.

The estimates of computational error given for all cases provide reasonable assurances that the results are adequate for the purposes intended. For comparative purposes, the work of Levy, *et al*. [2002] is cited. These authors summarized data resulting from a CFD drag prediction study by several different numerical codes on an external wing-body configuration. The results of that work included that fact that the total drag predictions, C_D, ranged from 0.0226 to 0.0500, which is more than a factor of 2. This information serves two purposes – first to assert that the results given here, including the A_1 estimators and the *GCI*, are quality estimates with reasonable error bounds given the current capabilities of CFD technology. In a broader sense, the fact that drag could only be predicted accurately to within a factor of 2 underscores the need for experimental skin friction measurements using devices like those studied here. One can see that even the worst cases studied here showed output errors of about 100%, which is still as good as the best estimate from the Levy, *et al*. [2002] CFD wing-body cases. Careful control over the skin friction gage design and installation as guided by the results given here can significantly reduce the error in measurement to much lower levels.

The oil fill issue is indirectly addressed throughout this document. Ansys/FLOTRAN does not have the capability to analyze a free surface boundary of the complexity between viscous oil and air in a small gap like in a skin friction gage, since the surface tension of the fill oil is such an essential part of that analysis as discussed by Frei and Thomann [1980]. This is an extremely difficult problem to solve. But, all of the air flow cases studied here assumed no oil filling, and this gave the external air the freedom to maneuver through the cavity as required by the numerical solution. This issue was, therefore, addressed based on a "worst case" scenario. The results highlight the worst error levels that the gage could see. Although the analysis of Frei and Thomann [1980] does not model the reality of using oil fill, it does predict that filling the cavity with oil could only make the situation better than that predicted here for as long as the oil remained in the cavity.

Finally, the derivation of a friction Reynolds number was presented, and this seemed to make much more sense than using free-stream representation for the purpose of talking about the

conditions under which the gage operates (free-stream Reynolds number values are still necessary for talking about things like turbulence levels, skin friction levels, etc.). This friction Reynolds number is defined in an identical way as the dimensionless wall units of the various gage parameters and variations based on the definition of y^+. The use of the turbulent boundary layer inner wall units can be reflected on by looking at them as a friction Reynolds number. The gap friction Reynolds number, G^+, in particular seems to be a good candidate for characterizing the conditions of the skin friction gage.

The conditions of the laminar channel flow here result in a G^+ of 0.033. Although u_τ is a quantity that is really only employed with respect to turbulent analyses, the mathematical definition is used for the laminar channel flow problem to calculate G^+ of the channel. For the turbulent external flat plate flow, the value of G^+ works out to be 33.2. It is hoped that these numbers are more significant in addressing the gage conditions than a free-stream representation which does not adequately reflect the operation of the gage. Using a friction Reynolds number (a "+" quantity) should provide broader applicability of the results from this study.

Finally, in terms of broader applicability of the results, the performance of a direct measuring skin friction gage as studied here looked at a gage that had a head diameter much larger than the gap that surrounded it (G/D_{HEAD}=1.67% for the baseline case). This fact is useful based on the empirical observation that some of the results are a function of the gap size directly and not a function of the ratio between the gap and the head diameter. Thus, many of the results presented here can be extended to devices with different G/D_{HEAD} ratios as long as the head diameter is still much larger than the gap. In particular, a formula was presented for estimating the lip force error caused by stagnating pressure on the lip surface. This was assumed to be a function of gap size alone, and it could be extrapolated to other device geometries under similar flow conditions. The head diameter itself also seemed to play a role in the normal force. Although only one head diameter size was studied, the results suggest that minimizing the head diameter will have a direct result on the magnitude of the normal force term (which contributes to the output through the *z*-direction moment).

In this way, it is possible to analyze the effects of pressure gradients in the flow by simply integrating the pressure gradient over the head to get an estimate of the normal force and resulting *z*-direction moment for a given head size. Also the effects of the convective stagnation on the head can be estimated for any gap size in the range studied. The effects of the lip force

caused by pressure gradients in the flow were shown to be very complex, but the magnitude of the effect was shown to be small, particularly in the diverging channel, adverse pressure gradient case. Much of this information could be useful is addressing quality of measurement in a wide range of gage geometries.

Although it seems possible to extrapolate much of the perfectly aligned effects of the lip and normal force terms to other geometries, flow conditions, etc., misalignment seems particularly complex and difficult to model in any simple analytical way. The comparison of the numerical results with the results of Allen shows that these incompressible flow results the main physics involved in the misalignment problem. Estimating the exact magnitude of the influence of misalignment for any general flow condition, however, is a much more difficult prospect. O'Donnell [1964] came to the same conclusion, explicitly stating that an analytical description of misalignment was probably not feasible.

In general, this study illustrates and validates the use of CFD for analyzing and designing skin friction gages. The success of calculating the flow rates and flow patterns in the tiny gap regions speaks to the utility of the technique. This study has used CFD to provide the first detailed look at some of the effects that were unreachable by Dhawan [1952], Acharya *et al.* [1984] and others who tried to experimentally measure these effects and were unable to do so. The correlation and comparison with experimental literature has been relatively successful and shows good agreement while providing a fundamental understanding of the flows and effects for direct measuring, non-nulling skin friction gages.

7.2 Future Study

This study has attempted only to analyze a generic situation involving skin friction gage performance. The idea here has been that a user of this information can pick any set of scaling parameters and values that result in the dimensionless values from these problems and make use of the valid solution. Thus, an infinite family of scaled, similar problems is provided in one tabulated solution. Although a great effort has been made to select the problems treated here so as to be as useful and general as possible, there will certainly be a need for study of specific performance effects on specific gages under specific flow conditions. Also, further work in using a specific application to validate the solutions provided here is necessary, since the

comparison with experimental results in this document is limited by a lack of appropriate experimental data.

Beyond the issue of validation with applied experiment, the next logical step is to further increase the flow complexity to compressible, subsonic conditions and then supersonic cases. These will represent many more situations for which engineers are interested in the use of skin friction gages. It is certainly argued here that even the relatively low speed, incompressible cases presented capture much of the physical aspects of a broader level of situations based on the similarities with the results of Allen. However, compressible problems will involve more complex effects including the issues of temperature and heat transfer which were not dealt with here, but which will certainly produce results as interesting as any of the issues presented in this work.

Even in the flow regime studied here, there are additional issues that need more understanding. A treatment of the oil fill problem including the effects of both convection and surface tension of the oil is needed to fully understand the usefulness of the oil fill in cases where it is used and to quantitatively assess any benefits that the oil might have in decreasing the effects of a pressure gradient. This analysis would require a code capable of gas-liquid interface boundary conditions, as well as a surface tension effect for the liquid coupled into the force term of the Navier-Stokes equations of motion.

The issue of an optimum lip thickness is another point which requires additional study to resolve. The work presented here indicates that there may possibly be a non-zero lip thickness which may be optimum for a sufficient range of flow conditions in a pressure gradient. Finding this optimum value for a set of conditions would be a useful result for superior skin friction gage design.

The issue of tilt was also discussed briefly. Tilting caused by deflection under loading of an otherwise untilted gage head was shown to be inconsequential for the sizes and styles of skin friction gages studied here. However, if a gage is tilted due to poor fabrication or installation, errors due to head tilt could become an issue. This is loosely related to misalignment, but only misalignments normal to the wall surface were studied here. Work in understanding tilting would complement the head protrusion and head recession results given here.

Finally, there are other styles of direct measuring skin friction gages exist which would benefit from study. This work picked a generic version of the most typical style of gage used at

this time, but the field of tiny MEMS gages is emerging. Many of these gages are much smaller than what was studied here, and their tiny size results in different constraints and flexure designs. Even without the geometry alterations, the size of the gages alone may have some impact on the performance analysis of the skin friction gage. The skin friction gages studied here were much larger than the fluid particles in the flow so the common continuum approach is justified, but it is not clear what impact there may be on the flow in a MEMS-type situation where this assumption may no longer be true in the very tiny gap regions.

References:

[1] Acharya, M., Bornstein, J., Escudier, M. P., and Vokurka, V. "Development of a Floating Element for the Measurement of Surface Shear Stress". *AIAA Journal*. Vol. 23. No 3. Pgs. 410–415. 1984.

[2] Allen, Jerry M. "Systematic Study of Error Sources in Supersonic Skin-Friction Balance Measurements." NASA-TN-8291. Washington: Oct, 1976.

[3] Allen, Jerry M. "Improved Sensing Element for Skin-Friction Balance Measurements." *AIAA Journal*. Vol. 18, no 11. Pgs. 1342–1345. Nov, 1980.

[4] Anderson, John David Jr. *Fundamentals of Aerodynamics*. 2nd Ed. New York: McGraw-Hill, 1991.

[5] *Ansys Online Help*. Release 6.0. Canonsburg, PA: ANSYS, Inc., September 19, 2001.

[6] Bathe, Klaus-Jordan. *Finite Element Procedures*. Prentice Hall, 1995.

[7] Bertin, John J. and Smith, Michael L. *Aerodynamics for Engineers*. 3RD Ed. Upper Saddle River, NJ: Prentice Hall, 1998.

[8] Blottner, Frederick G. "Accurate Navier-Stokes Results for the Hypersonic Flow over a Spherical Nosetip." AIAA Journal of Spacecraft and Rockets. Vol 27, no 2. Pgs 113 – 122. March/April 1990.

[9] Brandt, Achi. "Multi-Level Adaptive Solutions to Boundary-Value Problems." *Mathematics of Computation*. Vol 31, no 138. Pgs. 333–390. April, 1977.

[10] Brooks, A.N. and Hughes, T.J.R. "Streamline Upwind/Petrov-Galerkin Formulations for Convection Dominated Flows with Particular Emphasis on the Incompressible Navier-Stokes Equations." *Computer Methods in Applied Mechanics and Engineering*. Vol 32, Pgs.199–259. 1982.

[11] Brown, K.C. and Joubert, P.N. "The Measurement of Skin Friction in Turbulent Boundary Layers with Adverse Pressure Gradients". *Journal of Fluid Mechanics*. Vol 35. No 4. Pgs. 737–757. 1969.

[12] Budynas, Richard G. *Advanced Strength and Applied Stress Analysis*. Boston: McGraw-Hill, 1977.

[13] Clauser, F.H. "Turbulent Boundary Layers in Adverse Pressure Gradients". Journal of Aerospace Sciences. Vol 21. Pgs. 91–108. 1954.

[14] Coles, Donald. “Measurements in the Boundary Layer on a Smooth Flat Plate in Supersonic Flow.” Ph.D. Dissertation, California Institute of Technology, Pasadena, CA, 1953.

[15] Dershin, Harvey and Gallaher, William H. “Direct Measurement of Compressible, Turbulent Boundary Layer Skin Friction on a Porous Flat Plate with Mass Injection”. AIAA Paper 67-194. Pages 10. New York: AIAA Publishing, 1967.

[16] Devenport, W.; Kapania, R.; Rojiani, K.; and Singh, K. “Java Applets for Engineering Education”. Virginia Tech Aerospace and Ocean Engineering 21 Feb. 2002. <http://www.engapplets.vt.edu>.

[17] Dhawan, Satish. "Direct Measurements of Skin Friction." NACA-Report-1121. Washington: 1952.

[18] Dow Chemical Company. “Synthetic Glycerine Products”. Form no. 115-00645-497 SMG. April 1997.

[19] Eimer, Manfred. “Direct Measurement of Laminar Skin Friction at Hypersonic Speeds.” Ph.D. Dissertation, California Institute of Technology, Pasadena, CA, 1953.

[20] Everett, Harold Ulrich, Jr. “Calibration of Skin Friction Balance Discs for Pressure Gradient.” M.S. Thesis, University of Texas, August, 1958.

[21] “FIDAP 8 Theory Manual.” Fluent, Inc. 2 Dec. 2001. <http://sp81.msi.umn.edu:999/fluent/fidap/help/ theory/thtoc.htm>.

[22] Fowke, James G. "Development of a Skin-Friction Balance to Investigate Sources of Error in Direct Skin-Friction Measurements." M.S. Thesis, Mechanical Department, University of Virginia, Charlottesville, VA, 1969.

[23] Frei, D. and Thomann, H. “Direct Measurements of Skin Friction in a Turbulent Boundary Layer with a Strong Adverse Pressure Gradient”. *Journal of Fluid Mechanics*. Vol 101, No 1. Pgs. 79–95. 1980.

[24] Froude, W. “Experiments on the Surface-Friction Experienced by a Plane Moving Through Water”. 42ND British Association Report, Pgs 118 – 124. 1872.

[25] Girimaji, S.S. “Fully Explicit and Self-consistent Algebraic Reynolds Stress Model.” Technical Report 95-82, ICASE, 1995.

[26] Godunov, S. K. “Finite Difference Method for Numerical Computation of Discontinuous Solutions of the Equations of Fluid Dynamics.” *Siberian Mathematical Journal*. Vol 47 Pgs. 271 – 306. 1959.

[27] Griffiths, David F. “The ‘No Boundary Condition’ Outflow Boundary Condition”. *International Journal for Numerical Methods in Fluids*. Vol 24. Pgs 393 – 411. 1997.

[28] Hakkinen, Raimo J. “Measurements of Turbulent Skin Friction on a Flat Plate at Transonic Speeds.” NACA-TN-3486. Washington: September, 1955.

[29] Haridonidis, J. “The Measurement of Wall Shear Stress”. *Advances in Fluid Mechanics Measurements*. Pgs 229 – 261. Springer-Verlas, 1989.

[30] Hirt, F., Zurflah, U., and Thomann, H. “Skin Friction Balances for Large Pressure Gradients”. *Experiments in Fluids*. Vol 4. Pgs 296 – 300. Springer-Verlag, 1986.

[31] Hosder, Serhat. Personal Conversation. 2002.

[32] Karamcheti, Krishnamurty. *Principles of Ideal-Fluid Aerodynamics*. Malabar, FL: Krieger Publishing Co., 1966.

[33] Kays, W.M. and Crawford, M.E. *Convective Heat and Mass Transfer*. 3RD Ed. New York: McGraw-Hill, 1993.

[34] Kong, F. and Schetz, Joseph A. “Turbulent Boundary Layer over Porous Surfaces with Different Geometries”. AIAA 82-0030, 20TH Aerospace Sciences Meeting, Orlando, FL, January 11-14, 1982.

[35] Kohnke, Peter, Ed. *ANSYS Theory Reference*. Release 5.7. Canonsburg, PA: ANSYS, Inc., March 2001.

[36] Kronsjö, Lydia, and Dahlquist, Germund. “On the Design of Nested Iterations for Elliptic Difference Equations”. *BIT*. Vol 12. Pgs 63 – 71. 1972.

[37] Launder, B.E., and Spalding, D.B. “The Numerical Computation of Turbulent Flows.” *Computer Methods in Applied Mechanics and Engineering*. Vol. 3, Pgs. 269–289. 1974.

[38] Levy, David W.; Zickuhr, Tom; Vassberg, John; Agrawal, Shreekant; Wahls, Richard A.; Pirzadeh, Shahyar; and Hemsch, Michael J. “Summary of Data from the First AIAA CFD Drag Prediction Workshop.” AIAA 2002-0841. 40TH Aerospace Sciences Meeting, Reno, NV, January 14-17, 2002.

[39] Matthews, John H., and Fink, Kurtis D. *Numerical Methods Using MATLAB*. 3RD Ed. Upper Saddle River, NJ: Prentice Hall, 1999.

[40] Magill, Samantha A. “Study of a Direct Measuring Skin Friction Gage with Rubber Compounds for Damping.” M.S. Thesis, Aerospace and Ocean Engineering Department, Virginia Polytechnic Institute and State University, Blacksburg, VA, 1999.

[41] Nitsche, W., Haberland, C., and Thunker, R. “Comparative Investigations of the Friction Drag Measuring Techniques in Experimental Aerodynamics”. ICAS-84-2.4.1, 14TH ICAS Congress, 1984.

[42] Oberkampf, William L. and Blottner, Frederick G. “Issues in Computational Fluid Dynamics Code Verification and Validation.” *AIAA Journal*. Vol 36, no 5. Pgs 687 – 695. May 1998.

[43] O’Donnell, Francis B. “A Study of the Effect of Floating-Element Misalignment on Skin-Friction-Balance Accuracy.” Technical Report: Defense Research Laboratory DRL-515, CR-10. OCLC#6360963, University of Texas (Austin). March 3, 1964.

[44] O’Donnell, F.B., and Westkaemper, J.C. “Measurements of Errors Caused by Misalignment of Floating-Element Skin Friction Balances.” *AIAA Journal*. Vol. 3, no. 1. Pgs. 163–165. January 1965.

[45] Paik, Seungwoock and Schetz, Joseph A. “Simultaneous Direct Measurement of Skin Friction and Heat Flux in a Supersonic Flow.” *The Sixth Asian Congress of Fluid Mechanics: Proceedings*. V.T Chew and C.P. Tso Ed. Volume 2. Singapore. May 22 – 26, 1995.

[46] Panton, Ronald L. *Incompressible Flow*. New York: John Wiley & Sons, 1984.

[47] Patankar, S.V. and Spalding, D. B. “A Calculation Procedure for Heat, Mass and Momentum Transfer in Three-dimensional Parabolic Flows”. *International Journal of Heat and Mass Transfer*. Vol 15. Pgs 1787 – 1806. Pergamon Press, 1972.

[48] Pelletier, Dominique H. Personal Correspondence. 2000.

[49] Pelletier, D.H. “Finite Element Solution of the Navier-Stokes Equations for 3-D Turbulent Free Shear Flows.” Ph.D. Dissertation, Aerospace and Ocean Engineering Department, Virginia Polytechnic Institute and State University, Blacksburg, VA, 1984.

[50] Reddy, J.N. *An Introduction to the Finite Element Method*. 2ND Ed. Boston, MA: McGraw-Hill, 1994.

[51] Renardy, Michael. “Imposing ‘No’ Boundary Condition at Outflow: Why Does It Work?” *International Journal for Numerical Methods in Fluids*. Vol 24. Pgs 413 – 417. 1997.

[52] Rice, J.G. and Schnipke, R.J. "A Montotone Streamline Upwind Finite Element Method for Convention-Dominated Flows." *Computer Methods in Applied Mechanics and Engineering*. Vol. 48, Pgs. 313 – 327. 1985.

[53] Roache, Patrick J. *Verification and Validation in Computational Science and Engineering*. ISBN 0-913478-08-3. Albuquerque, NM: Hermosa Publishers, 1998.

[54] Roache, Patrick J. "Quantification of Uncertainty in Computational Fluid Dynamics." *Annual Review of Fluid Mechanics*. Vol 29, Pgs 123 – 160. 1997.

[55] Roache, Patrick J. "Perspective: A Method for Uniform Reporting of Grid Refinement Studies." ASME Journal of Fluids Engineering. Vol 116, no 3. Pgs 405 – 413. September 1994.

[56] Roy, Christopher J. "Grid Convergence Error Analysis for Mixed-Order Numerical Schemes." AIAA Paper 2001-2606, 15TH AIAA Computational Fluid Dynamics Conference, Anaheim, CA, June 11-14, 2001.

[57] Roy, Christopher J.; McWherter-Payne, Mary A.; and Oberkampf, William L. "Verification and Validation for Laminar Hypersonic Flowfields". AIAA Paper 2000-2550. Fluids 2000, Denver, CO., June 19-22, 2000.

[58] Sang, Alexander. "Study of Rubber Damped Skin Friction Gages for Transonic Flight ". M.S. Thesis, Aerospace and Ocean Engineering Department, Virginia Polytechnic Institute and State University, Blacksburg, VA, 2001.

[59] Schetz, Joseph A. "Direct Measurement of Skin Friction in Complex Fluid Flows". *Applied Mechanics Review*. Vol 50, no 11, part 2. Pgs S198 – S203. November 1997.

[60] Schetz, Joseph A. *Boundary Layer Analysis*. Englewood Cliffs, NJ: Prentice Hall, 1993.

[61] Schetz, Joseph A. and Kong, F. "Turbulent Boundary Layer over Solid and Porous Surfaces with Small Roughness". AIAA 81-0418, 19TH Aerospace Sciences Meeting, St. Louis, MO, January 12-15, 1981.

[62] Schetz, Joseph A. and Nerney, Brian. "Turbulent Boundary Layer with Injection and Surface Roughness". *AIAA Journal*. Vol 15, no 9. Pgs 1288 – 1294. September 1977.

[63] Schnipke, Rita J., and Rice, James G. "Application of a New Finite Element Method to Convection Heat Transfer". 4TH International Conference on Numerical Methods in Thermal Problems, Swansea, U.K. Pgs 424 – 435. July, 1985.

[64] Seto, Jeffrey and Hornung, Hans. “Internally Mounted Thin-Liquid-Film Skin-Friction Meter – Comparison with Floating Element Method With and Without Pressure Gradient.” AIAA 91-0060, 29TH Aerospace Sciences Meeting, Reno, NV, January 7-10, 1991.

[65] Shames, Irving H. and Dym, Clive L. *Energy and Finite Element Methods in Structural Mechanics*. Philadelphia: Taylor and Francis, 1985.

[66] Shevell, Richard S. *Fundamentals of Flight*. 2ND Ed. Englewood Cliffs, NJ: Prentice Hall, 1989.

[67] Shih, Tsa-Hsing; Liou, William W.; Shabbir, Aamir; Yang, Zhigang; and Zhu, Jiang. “A New κ–ε Eddy Viscosity Model for High Reynolds Number Turbulent Flows.” *Computers in Fluids*. Vol 24, no 3. Pgs 227 – 238. 1995.

[68] Shutts, W. E.; Hartwig, W. H.; and Weiler, J. E. “Turbulent Boundary Layer and Skin Friction Measurements on a Smooth, Thermally Insulated Flat Plate at Supersonic Speeds.” Defense Research Laboratory DRL-364, CM-823. University of Texas (Austin), 1952.

[69] Smith, D. W. and Walker, J. H. “Skin Friction Measurements in Incompressible Flow.” NASA TR R-26, 1959.

[70] Smith, Theodore. "Development and Ground Testing of Direct Measuring Skin Friction Gages for High Enthalpy Supersonic Flight Tests". Ph.D. Dissertation, Aerospace and Ocean Engineering Department, Virginia Polytechnic Institute and State University, Blacksburg, VA, 2001.

[71] Stewart, James. *Calculus*. 2ND Ed. Pacific Grove, CA: Brooks/Cole Publishing Co., 1991.

[72] Tannehill, John C., Anderson, Dale A., and Pletcher, Richard H. *Computational Fluid Mechanics and Heat Transfer*. 2ND Ed. Philadelphia: Taylor and Francis, 1997.

[73] Trottenberg, Ulrich; Oosterlee, Cornelis; and Schuller, Anton. *Multigrid*. San Diego: Academic Press, 2001.

[74] Turgeon, É.; Pelletier, D.; Étienne, S. and Borggaard, J. “Sensitivity and Uncertainty Analysis for Turbulent Flows.” AIAA Paper 2002-0985, 40TH Aerospace Sciences Meeting, Reno, NV, January 14-17, 2002.

[75] Voisinet, Robert L. P. “Temperature Step Effects on Direct Measurement of Skin-friction Drag”. AIAA Paper 78-779, 1978.

[76] Walters, Robert. “AOE6145 Computational Fluid Dynamics”. *Lecture Notes*. Department of Aerospace Engineering, Virginia Tech, Blacksburg, VA. Fall 2000.

[77] Westkaemper, John C. "Step-Temperature Effects on Direct Measurements of Drag." *AIAA Journal*. Vol 1, no 7. Pgs. 1708–1710. July, 1963.

[78] Winter, K.G. "An Outline of the Techniques Available for the Measurement of Skin Friction in Turbulent Boundary Layers." *Progress in Aerospace Sciences*. Vol 18, Pgs. 1–57. Oxford, England: Pergamon Press, 1977.

[79] Yakhot, V.; Orszag, S. A.; Thangam, S.; Gatski, T. B.; and Speziale, C. G. “Development of Turbulence Models for Shear Flows by a Double Expansion Technique.” Physics of Fluids A. Vol 7, no 7. Pgs. 1510 – 1520. July, 1992.

Appendix A: Commercial Code Contact Information

ANSYS/FLOTRAN

version 6.0, September 19, 2001

Created by:

Ansys, Inc.

address:	Southpointe 275 Technology Drive Canonsburg, PA 15317
website:	http://www.ansys.com
email:	ansysinfo@ansys.com
phone:	724.514.3304
fax:	724.514.9494

Local support and distribution by:

Mallett Technology, Inc.

address:	121 Hillpointe Drive, Suite 300 Canonsburg, PA 15317-9502
website:	http://www.mallett.com
phone:	724-746-7000
fax:	724-746-7001

Appendix B: Derivation of Non-dimensionalization Scheme

Although non-dimensionalization is a common technique in computational methods, schemes often vary between individual implementations. The Navier-Stokes equation set as solved by Ansys/FLOTRAN was given in Section 3.2, along with a dimensionless scheme appropriate to that particular formulation. The dimensionless forms of those equations are derived here as proof that the scheme chosen is consistent with the Ansys/FLOTRAN equation set.

Continuity:

Starting from an expanded form of eqn. (3-5b):

$$\frac{\partial \rho}{\partial t} + \frac{\partial (\rho u_i)}{\partial x_i} = 0 \qquad \text{(B-1a)}$$

substituting from Table 3-2:

$$\frac{\partial (\rho_\infty \rho^*)}{\partial \left(\frac{L_\infty t^*}{V_\infty} \right)} + \frac{\partial (\rho_\infty \rho^* V_\infty u_i^*)}{\partial (L_\infty x_i^*)} = 0$$

canceling and simplifying,

$$\frac{\rho_\infty V_\infty}{L_\infty} \frac{\partial (\rho^*)}{\partial (t^*)} + \frac{\rho_\infty V_\infty}{L_\infty} \frac{\partial (\rho^* u_i^*)}{\partial (x_i^*)} = 0$$

gives the resulting dimensionless continuity equation:

$$\frac{\partial \rho^*}{\partial t^*} + \frac{\partial (\rho^* u_i^*)}{\partial x_i^*} = 0 \qquad \text{(B-1b)}$$

Momentum:

Starting from an expanded form of eqn. (3-6b) – (3-8b)

$$\frac{\partial(\rho u_j)}{\partial t}+\frac{\partial(\rho u_i u_j)}{\partial x_i}=\rho g_j-\frac{\partial P}{\partial x_j}+R_j+\frac{\partial}{\partial x_i}\left[\mu\left(\frac{\partial u_i}{\partial x_j}+\frac{\partial u_j}{\partial x_i}\right)\right] \tag{B-2a}$$

and substituting from Table 3-2:

$$\frac{\partial\left(\rho_\infty \rho^* V_\infty u_j^*\right)}{\partial\left(\frac{L_\infty t^*}{V_\infty}\right)}+\frac{\partial\left(\rho_\infty \rho^* V_\infty^{\,2} u_i^* u_j^*\right)}{\partial\left(L_\infty x_i^*\right)}=\left(\rho_\infty \rho^*\right)\left(\frac{V_\infty^{\,2} g_j^*}{L_\infty}\right)-\frac{\partial\left(P^* \rho_\infty V_\infty^{\,2}\right)}{\partial\left(L_\infty x_j^*\right)}$$

$$+\left(\frac{\rho_\infty V_\infty^{\,2}}{L_\infty}\right)R_j^*+\frac{\partial\left(\left(\mu^* \rho_\infty V_\infty L_\infty\right)\left[\frac{\partial\left(V_\infty u_i^*\right)}{\partial\left(L_\infty x_j^*\right)}+\frac{\partial\left(V_\infty u_j^*\right)}{\partial\left(L_\infty x_i^*\right)}\right]\right)}{\partial\left(L_\infty x_i^*\right)}$$

collecting and simplifying,

$$\frac{\rho_\infty V_\infty^{\,2}}{L_\infty}\frac{\partial\left(\rho^* u^*\right)}{\partial t^*}+\frac{\rho_\infty V_\infty^{\,2}}{L_\infty}\frac{\partial\left(\rho^* u_i^* u_j^*\right)}{\partial x_i^*}=\frac{\rho_\infty V_\infty^{\,2}}{L_\infty}\left(\rho^* g_j^*\right)-\frac{\rho_\infty V_\infty^{\,2}}{L_\infty}\frac{\partial P^*}{\partial x_j^*}$$

$$+\frac{\rho_\infty V_\infty^{\,2}}{L_\infty}R_j^*+\frac{\rho_\infty V_\infty^{\,2}}{L_\infty}\frac{\partial\left(\mu^*\left[\frac{\partial u_i^*}{\partial x_j^*}+\frac{\partial u_j^*}{\partial x_i^*}\right]\right)}{\partial x_i^*}$$

gives the dimensionless momentum equation set:

$$\frac{\partial\left(\rho^* u^*\right)}{\partial t^*}+\frac{\partial\left(\rho^* u_i^* u_j^*\right)}{\partial x_i^*}=\rho^* g_j^*-\frac{\partial P^*}{\partial x_j^*}+R_j^*+\frac{\partial}{\partial x_i^*}\left(\mu^*\left[\frac{\partial u_i^*}{\partial x_j^*}+\frac{\partial u_j^*}{\partial x_i^*}\right]\right) \tag{B-2b}$$

Energy:

First, analyzing the stagnation temperature alone:

$$T_0 = T + \frac{V^2}{2c_P} \tag{B-3a}$$

$$T_0 = \left(T^* T_\infty\right) + \frac{\left(V_\infty{}^2 u^{*2}\right) + \left(V_\infty{}^2 v^{*2}\right) + \left(V_\infty{}^2 w^{*2}\right)}{2\left(c_P{}^* \frac{V_\infty{}^2}{T_\infty}\right)}$$

$$T_0 = \left(T^* T_\infty\right) + \frac{T_\infty V_\infty{}^2 \left(u^{*2} + v^{*2} + w^{*2}\right)}{2 V_\infty{}^2 c_P{}^*}$$

$$T_0 = T_\infty \left(T^* + \frac{\left(u^{*2} + v^{*2} + w^{*2}\right)}{2c_P{}^*} \right)$$

showing that the stagnation temperature is consistent with the temperature non-dimensionalization scheme:

$$T_0 = T_\infty T_0{}^* \tag{B-3b}$$

Starting from an expanded form of eqn. (3-9b):

$$\frac{\partial\left(\rho c_P T_0\right)}{\partial t} + \frac{\partial\left(\rho u_j c_P T_0\right)}{\partial x_j} = \frac{\partial}{\partial x_j}\left(k \frac{\partial T_0}{\partial x_j} \right) + u_j \mu \left(\frac{\partial}{\partial x_j}\frac{\partial u_j}{\partial x_i} + \frac{\partial}{\partial x_j}\frac{\partial u_k}{\partial x_k} \right)$$
$$- \frac{\partial}{\partial x_i}\left[\frac{k}{c_P}\frac{\partial}{\partial x_i}\left(\tfrac{1}{2} \left| u_k u_k \right| \right) \right] + Q_V + \mu \left(\frac{\partial u_i}{\partial x_k} + \frac{\partial u_k}{\partial x_i} \right) \frac{\partial u_i}{\partial x_k} + \frac{\partial P}{\partial t} \tag{B-4a}$$

substituting from Table 3-2 and eqn. (B-3b):

$$\frac{\partial\left(\rho_\infty\rho^*\frac{V_\infty^{\,2}}{T_\infty}c_P^{\,*}T_\infty T_0^{\,*}\right)}{\partial\left(\frac{L_\infty t^*}{V_\infty}\right)}+\frac{\partial\left(\rho_\infty\rho^* V_\infty u_j^{\,*}\frac{V_\infty^{\,2}}{T_\infty}c_P^{\,*}T_\infty T_0^{\,*}\right)}{\partial\left(L_\infty x_j^{\,*}\right)}=\frac{\partial\left(\left(\frac{L_\infty\rho_\infty V_\infty^{\,3}k^*}{T_\infty}\right)\frac{\partial\left(T_\infty T_0^{\,*}\right)}{\partial\left(L_\infty x_j^{\,*}\right)}\right)}{\partial\left(L_\infty x_j^{\,*}\right)}$$

$$+\left(V_\infty u_j^{\,*}\right)\left(\rho_\infty V_\infty L_\infty\mu^*\right)\left(\frac{\partial}{\partial\left(L_\infty x_j^{\,*}\right)}\frac{\partial\left(V_\infty u_j^{\,*}\right)}{\partial\left(L_\infty x_i^{\,*}\right)}+\frac{\partial}{\partial\left(L_\infty x_j^{\,*}\right)}\frac{\partial\left(V_\infty u_k^{\,*}\right)}{\partial\left(L_\infty x_k^{\,*}\right)}\right)+\left(\frac{\rho_\infty V_\infty^{\,3}}{L_\infty}Q_V^{\,*}\right)$$

$$-\frac{\partial}{\partial\left(L_\infty x_i^{\,*}\right)}\left(\frac{\left(\frac{L_\infty\rho_\infty V_\infty^{\,3}}{T_\infty}k^*\right)}{\frac{V_\infty^{\,2}}{T_\infty}c_P^{\,*}}\frac{\partial}{\partial\left(L_\infty x_i^{\,*}\right)}\left(\tfrac{1}{2}\left|\left(V_\infty u_k^{\,*}\right)\left(V_\infty u_k^{\,*}\right)\right|\right)\right)$$

$$+\left(\rho_\infty V_\infty L_\infty\mu^*\right)\left(\frac{\partial\left(V_\infty u_i^{\,*}\right)}{\partial\left(L_\infty x_k^{\,*}\right)}+\frac{\partial\left(V_\infty u_k^{\,*}\right)}{\partial\left(L_\infty x_i^{\,*}\right)}\right)\frac{\partial\left(V_\infty u_i^{\,*}\right)}{\partial\left(L_\infty x_k^{\,*}\right)}+\frac{\partial\left(\rho_\infty V_\infty^{\,2}P^*\right)}{\partial\left(\frac{L_\infty t^*}{V_\infty}\right)}$$

simplifying:

$$\frac{\rho_\infty V_\infty^{\,3}T_\infty}{T_\infty L_\infty}\frac{\partial\left(\rho^* c_P^{\,*}T_0^{\,*}\right)}{\partial t^*}+\frac{\rho_\infty V_\infty^{\,3}T_\infty}{T_\infty L_\infty}\frac{\partial\left(\rho^* u_j^{\,*}c_P^{\,*}T_0^{\,*}\right)}{\partial x_j^{\,*}}=\frac{\rho_\infty L_\infty V_\infty^{\,3}T_\infty}{L_\infty^{\,2}T_\infty}\frac{\partial}{\partial x_j^{\,*}}\left(k^*\frac{\partial T_0^{\,*}}{\partial x_j^{\,*}}\right)$$

$$+\frac{\rho_\infty V_\infty^{\,3}L_\infty}{L_\infty^{\,2}}u_j^{\,*}\mu^*\left(\frac{\partial}{\partial x_j^{\,*}}\frac{\partial u_j^{\,*}}{\partial x_i^{\,*}}+\frac{\partial}{\partial x_j^{\,*}}\frac{\partial u_k^{\,*}}{\partial x_k^{\,*}}\right)-\frac{\rho_\infty V_\infty^{\,3}L_\infty T_\infty\left|V_\infty^{\,2}\right|}{V_\infty^{\,2}L_\infty^{\,2}T_\infty}\frac{\partial}{\partial x_i^{\,*}}\left(\frac{k^*}{c_P^{\,*}}\frac{\partial}{\partial x_i^{\,*}}\left(\tfrac{1}{2}\left|u_k^{\,*}u_k^{\,*}\right|\right)\right)$$

$$+\frac{\rho_\infty V_\infty^{\,3}}{L_\infty}Q_V^{\,*}+\frac{\rho_\infty V_\infty^{\,3}L_\infty}{L_\infty^{\,2}}\mu^*\left(\frac{\partial u_i^{\,*}}{\partial x_k^{\,*}}+\frac{\partial u_k^{\,*}}{\partial x_i^{\,*}}\right)\frac{\partial u_i^{\,*}}{\partial x_k^{\,*}}+\frac{\rho_\infty V_\infty^{\,3}}{L_\infty}\frac{\partial P^*}{\partial t^*}$$

yielding the dimensionless energy equation:

$$\frac{\partial\left(\rho^* c_P^{\,*}T_0^{\,*}\right)}{\partial t^*}+\frac{\partial\left(\rho^* u_j^{\,*}c_P^{\,*}T_0^{\,*}\right)}{\partial x_j^{\,*}}=\frac{\partial}{\partial x_j^{\,*}}\left(k^*\frac{\partial T_0^{\,*}}{\partial x_j^{\,*}}\right)+u_j^{\,*}\mu^*\left(\frac{\partial}{\partial x_j^{\,*}}\frac{\partial u_j^{\,*}}{\partial x_i^{\,*}}+\frac{\partial}{\partial x_j^{\,*}}\frac{\partial u_k^{\,*}}{\partial x_k^{\,*}}\right)$$

$$-\frac{\partial}{\partial x_i^{\,*}}\left(\frac{k^*}{c_P^{\,*}}\frac{\partial}{\partial x_i^{\,*}}\left(\tfrac{1}{2}\left|u_k^{\,*}u_k^{\,*}\right|\right)\right)+Q_V^{\,*}+\mu^*\left(\frac{\partial u_i^{\,*}}{\partial x_k^{\,*}}+\frac{\partial u_k^{\,*}}{\partial x_i^{\,*}}\right)\frac{\partial u_i^{\,*}}{\partial x_k^{\,*}}+\frac{\partial P^*}{\partial t^*}\qquad\text{(B-4b)}$$

Species Transport:

Starting from an expanded form of eqn. (3-10b)

$$\frac{\partial(\rho C_i)}{\partial t} + \frac{\partial(\rho u_j C_i)}{\partial x_j} = \frac{\partial}{\partial x_j}\left(\rho D_{mi}\frac{\partial C_i}{\partial x_j}\right) \tag{B-5a}$$

and substituting from Table 3-2:

$$\frac{\partial(\rho_\infty \rho^* C_i^*)}{\partial\left(\frac{L_\infty t^*}{V_\infty}\right)} + \frac{\partial(\rho_\infty \rho^* V_\infty u_j C_i^*)}{\partial(L_\infty x_j^*)} = \frac{\partial}{\partial(L_\infty x_j^*)}\left((\rho_\infty \rho^* V_\infty L_\infty D_{mi}^*)\frac{\partial C_i^*}{\partial(L_\infty x_j^*)}\right)$$

simplifying:

$$\frac{\rho_\infty V_\infty}{L_\infty}\frac{\partial(\rho^* C_i^*)}{\partial t^*} + \frac{\rho_\infty V_\infty}{L_\infty}\frac{\partial(\rho^* u_j C_i^*)}{\partial x_j^*} = \frac{\rho_\infty V_\infty}{L_\infty}\frac{\partial}{\partial x_j^*}\left(\rho^* D_{mi}^*\frac{\partial C_i^*}{\partial x_j^*}\right)$$

yielding the dimensionless species equation:

$$\frac{\partial(\rho^* C_i^*)}{\partial t^*} + \frac{\partial(\rho^* u_j C_i^*)}{\partial x_j^*} = \frac{\partial}{\partial x_j^*}\left(\rho^* D_{mi}^*\frac{\partial C_i^*}{\partial x_j^*}\right) \tag{B-5b}$$

Turbulent Kinetic Energy:

Starting from an expanded form of equation (3-11b)

$$\frac{\partial(\rho\kappa)}{\partial t} + \frac{\partial(\rho u_i \kappa)}{\partial x_i} = \frac{\partial}{\partial x_i}\left(\frac{\mu_T}{\sigma_K}\frac{\partial \kappa}{\partial x_i}\right) + \mu_T\left(\frac{\partial u_i}{\partial x_k} + \frac{\partial u_k}{\partial x_i}\right)\frac{\partial u_i}{\partial x_k} - \rho\varepsilon \tag{B-6a}$$

and substituting from Table 3-2:

$$\frac{\partial\left(\rho_\infty \rho^* V_\infty{}^2 \kappa^*\right)}{\partial\left(\frac{L_\infty t^*}{V_\infty}\right)} + \frac{\partial\left(\rho_\infty \rho^* V_\infty u_i{}^* V_\infty{}^2 \kappa^*\right)}{\partial\left(L_\infty x_i{}^*\right)} = \frac{\partial}{\partial\left(L_\infty x_i{}^*\right)}\left(\frac{\left(\rho_\infty V_\infty L_\infty \mu_T{}^*\right)}{\sigma_K}\frac{\partial\left(V_\infty{}^2 \kappa^*\right)}{\partial\left(L_\infty x_i{}^*\right)}\right)$$
$$+\left(\rho_\infty V_\infty L_\infty \mu_T{}^*\right)\left(\frac{\partial\left(V_\infty u_i{}^*\right)}{\partial\left(L_\infty x_k{}^*\right)} + \frac{\partial\left(V_\infty u_k{}^*\right)}{\partial\left(L_\infty x_i{}^*\right)}\right)\frac{\partial\left(V_\infty u_i{}^*\right)}{\partial\left(L_\infty x_k{}^*\right)} - \left(\rho_\infty \rho^* \frac{V_\infty{}^3 \varepsilon^*}{L_\infty}\right)$$

simplifying:

$$\frac{\rho_\infty V_\infty{}^3}{L_\infty}\frac{\partial\left(\rho^* \kappa^*\right)}{\partial t^*} + \frac{\rho_\infty V_\infty{}^3}{L_\infty}\frac{\partial\left(\rho^* u_i{}^* \kappa^*\right)}{\partial x_i{}^*} = \frac{\rho_\infty V_\infty{}^3 L_\infty}{L_\infty{}^2}\frac{\partial}{\partial x_i{}^*}\left(\frac{\mu_T{}^*}{\sigma_K}\frac{\partial \kappa^*}{\partial x_i{}^*}\right)$$
$$+\frac{\rho_\infty V_\infty{}^3 L_\infty}{L_\infty{}^2}\mu_T{}^*\left(\frac{\partial u_i{}^*}{\partial x_k{}^*} + \frac{\partial u_k{}^*}{\partial x_i{}^*}\right)\frac{\partial u_i{}^*}{\partial x_k{}^*} - \frac{\rho_\infty V_\infty{}^3}{L_\infty}\rho^* \varepsilon^*$$

and yielding the dimensionless κ equation:

$$\frac{\partial\left(\rho^* \kappa^*\right)}{\partial t^*} + \frac{\partial\left(\rho^* u_i{}^* \kappa^*\right)}{\partial x_i{}^*} = \frac{\partial}{\partial x_i{}^*}\left(\frac{\mu_T{}^*}{\sigma_K}\frac{\partial \kappa^*}{\partial x_i{}^*}\right) + \mu_T{}^*\left(\frac{\partial u_i{}^*}{\partial x_k{}^*} + \frac{\partial u_k{}^*}{\partial x_i{}^*}\right)\frac{\partial u_i{}^*}{\partial x_k{}^*} - \rho^* \varepsilon^* \qquad \text{(B-6b)}$$

Turbulent Dissipation:

Starting from eqn. (3-12b):

$$\frac{\partial(\rho\varepsilon)}{\partial t} + \frac{\partial(\rho u_i \varepsilon)}{\partial x_i} = \frac{\partial}{\partial x_i}\left(\frac{\mu_T}{\sigma_\varepsilon}\frac{\partial \varepsilon}{\partial x_i}\right) + C_{1\varepsilon}\mu_T \frac{\varepsilon}{\kappa}\left(\frac{\partial u_i}{\partial x_k} + \frac{\partial u_k}{\partial x_i}\right)\frac{\partial u_i}{\partial x_k} - C_2 \rho \frac{\varepsilon^2}{\kappa} \qquad \text{(B-7a)}$$

and substituting from Table 3-2:

$$\frac{\partial\left(\left(\rho_\infty \rho^*\right)\frac{V_\infty{}^3 \varepsilon^*}{L_\infty}\right)}{\partial\left(\frac{L_\infty t^*}{V_\infty}\right)} + \frac{\partial\left(\left(\rho_\infty \rho^*\right)\left(V_\infty u_i{}^*\right)\left(\frac{V_\infty{}^3 \varepsilon^*}{L_\infty}\right)\right)}{\partial\left(L_\infty x_i{}^*\right)} = \frac{\partial}{\partial\left(L_\infty x_i{}^*\right)}\left(\frac{\left(\rho_\infty V_\infty L_\infty \mu_T{}^*\right)}{\sigma_\varepsilon}\frac{\partial\left(\frac{V_\infty{}^3 \varepsilon^*}{L_\infty}\right)}{\partial\left(L_\infty x_i{}^*\right)}\right)$$

$$+C_{1\varepsilon}\left(\rho_\infty V_\infty L_\infty \mu_T^*\right)\frac{\left(\frac{V_\infty^3\varepsilon^*}{L_\infty}\right)}{\left(V_\infty^2\kappa^*\right)}\left(\frac{\partial\left(V_\infty u_i^*\right)}{\partial\left(L_\infty x_k^*\right)}+\frac{\partial\left(V_\infty u_k^*\right)}{\partial\left(L_\infty x_i^*\right)}\right)\frac{\partial\left(V_\infty u_i^*\right)}{\partial\left(L_\infty x_k^*\right)}-C_2\left(\rho_\infty\rho^*\right)\frac{\left(\frac{V_\infty^3\varepsilon^*}{L_\infty}\right)^2}{\left(V_\infty^2\kappa^*\right)}$$

simplifying:

$$\frac{\rho_\infty V_\infty^4}{L_\infty^2}\frac{\partial\left(\rho^*\varepsilon^*\right)}{\partial t^*}+\frac{\rho_\infty V_\infty^4}{L_\infty^2}\frac{\partial\left(\rho^* u_i^*\varepsilon^*\right)}{\partial x_i^*}=\frac{\rho_\infty V_\infty^4 L_\infty}{L_\infty^3}\frac{\partial}{\partial x_i^*}\left(\frac{\mu_T^*}{\sigma_\varepsilon}\frac{\partial\varepsilon^*}{\partial x_i^*}\right)$$
$$+\frac{\rho_\infty V_\infty^6 L_\infty}{V_\infty^2 L_\infty^3}C_{1\varepsilon}\mu_T^*\frac{\varepsilon^*}{\kappa^*}\left(\frac{\partial u_i^*}{\partial x_k^*}+\frac{\partial u_k^*}{\partial x_i^*}\right)\frac{\partial u_i^*}{\partial x_k^*}-\frac{\rho_\infty V_\infty^6}{V_\infty^2 L_\infty^2}C_2\rho^*\frac{\left(\varepsilon^*\right)^2}{\kappa^*}$$

to obtain the dissipation equation:

$$\frac{\partial\left(\rho^*\varepsilon^*\right)}{\partial t^*}+\frac{\partial\left(\rho^* u_i^*\varepsilon^*\right)}{\partial x_i^*}=\frac{\partial}{\partial x_i^*}\left(\frac{\mu_T^*}{\sigma_\varepsilon}\frac{\partial\varepsilon^*}{\partial x_i^*}\right)\qquad\text{(B-7b)}$$
$$+C_{1\varepsilon}\mu_T^*\frac{\varepsilon^*}{\kappa^*}\left(\frac{\partial u_i^*}{\partial x_k^*}+\frac{\partial u_k^*}{\partial x_i^*}\right)\frac{\partial u_i^*}{\partial x_k^*}-C_2\rho^*\frac{\left(\varepsilon^*\right)^2}{\kappa^*}$$

In all equations, the dimensionless form of the respective equation is identical to the dimensional form.

Appendix C: Procedure for Using Nested Iteration in Ansys

The procedure of nested iteration was discussed extensively in Section 3.3 of this document. This simple precursor to multigrid consists of using an interpolated solution generated on a coarse grid as a starting guess on a fine grid. The idea is that, even with the interpolation, the coarse solution is a much better initial guess for iterative solution than a random starting point. Ansys/FLOTRAN does not implement either multigrid or nested iteration directly as a feature. However, it is possible to create a nested iteration procedure using some other commands built into Ansys.

The Ansys/FLOTRAN program offers a technique they term "submodeling," which is a feature designed with structural analysis in mind. In submodeling, small, intricate features like fillets can be neglected in a large global model, but solved for by creating a model of only that region around the fillet to resolve the sensitive stresses in that area. Doing this requires the solution from the global problem, which is used for boundary conditions for the region around the fillet. This technique is very similar to what was done in Chapters 4 and 5 with respect to the global versus local fluids problems.

Submodeling requires that the global model and the local feature model be located in the same spatial coordinates. Then, all boundary nodes from the local problem are imported into the previously solved global problem, the values interpolated based on the spatial coordinates of the boundary nodes, and then brought back to the local problem, and applied as boundary conditions. This technique assumes that the boundaries are sufficiently far away from the fillet or whatever so that they are not disturbed.

From this, nested iteration can be created using the following steps. Assuming two problems are created with the jobnames "coarse" and "fine":

1. Solve coarse.db model to satisfaction.
2. Build and mesh fine.db model, insuring that the model lies in the same spatial coordinates as the coarse model.
3. In the fine model (after meshing), go to Main Menu>Preprocessor>Create>Nodes>Write Node File, and save the node list file as (fine jobname).node. This is a complete list of the spatial coordinates of all nodes in fine.db.
4. Close fine.db, and open coarse.db. Load the converged results file for this model.

5. In Main Menu>General Postprocess>Submodeling>Interp DOF, and select (fine jobname).node as the node list file and (fine jobname).cbdo as the submodeling file to save to. Ansys/FLOTRAN will interpolate the solution onto the fine grid. This step may take some time.
6. Close the coarse.db model, and open the (fine jobname).cbdo file in a word processing editor, like Microsoft Word on a PC, or NEDIT in UNIX that has the "find and replace" feature. Find all instances of "D," and replace with "IC,". This changes the command list from applying as boundary conditions (which are fixed) to initial conditions. This operation can take considerable time on a PC, and seems to go much faster on a UNIX machine (less than 10 seconds on an SGI O2 workstation). Save the modified file, and exit the editor.
7. Open up fine.db again in Ansys. Switch to either the PREP7 or SOLU menus (not the Begin level).
8. Select Utility Menu>File>Read Input From, and select the (fine jobname).cbdo file. This operation will apply all degrees of freedom on all nodes as initial conditions from the coarse model.
9. Save the fine.db model, and proceed.

Appendix D: Derivation of Richardson Extrapolation Error Estimator with Truncated Terms

Using a Taylor series expansion for a grid of element size, *h,* about the "exact" infinite density grid solution:

$$f = f_{\mathrm{EXACT}} + \frac{\mathrm{d}f_{\mathrm{EXACT}}}{\mathrm{dS}}\mathrm{h} + \frac{1}{2}\frac{\mathrm{d}^2 f_{\mathrm{EXACT}}}{\mathrm{dS}^2}\mathrm{h}^2 + \frac{1}{6}\frac{\mathrm{d}^3 f_{\mathrm{EXACT}}}{\mathrm{dS}^3}\mathrm{h}^3 + \mathrm{O}(\mathrm{h}^4) \tag{D-1}$$

Since the derivatives of f_{EXACT} are, by definition, independent of the grid size h, they are given a more compact notation.

$$f = f_{\mathrm{EXACT}} + g_1\mathrm{h} + g_2\mathrm{h}^2 + g_3\mathrm{h}^3 + \mathrm{O}(\mathrm{h}^4)$$

or…

$$f = f_{\mathrm{EXACT}} + \sum_{\mathrm{K}=1}^{\infty} g_{\mathrm{K}}\mathrm{h}^{\mathrm{K}} \tag{D-2}$$

where g_P is a function of flow conditions and independent of the grid size.

For any solution on a grid, i, with a method of arbitrary order of convergence, p, the terms g_1 to g_{P-1} will be exactly zero, so eqn. (D-2) can be expanded as:

$$f_{\mathrm{i}} = f_{\mathrm{EXACT}} + g_{\mathrm{P}}\mathrm{h}_{\mathrm{i}}^{\mathrm{P}} + g_{\mathrm{P+1}}\mathrm{h}_{\mathrm{i}}^{\mathrm{P+1}} + g_{\mathrm{P+2}}\mathrm{h}_{\mathrm{i}}^{\mathrm{P+2}} + \ldots \tag{D-3}$$

This expansion in eqn. (D-3) can be used for two successive grids of different element size h, labeled 1 for the finer grid and 2 for the coarser grid. Multiplying the fine grid equation by $(h_2/h_1)^P$ produces the eqn. set (D-4):

$$\frac{\mathrm{h}_2^{\mathrm{P}}}{\mathrm{h}_1^{\mathrm{P}}} f_1 = \frac{\mathrm{h}_2^{\mathrm{P}}}{\mathrm{h}_1^{\mathrm{P}}} f_{\mathrm{EXACT}} + \frac{\mathrm{h}_2^{\mathrm{P}}}{\mathrm{h}_1^{\mathrm{P}}} g_{\mathrm{P}}\mathrm{h}_1^{\mathrm{P}} + \frac{\mathrm{h}_2^{\mathrm{P}}}{\mathrm{h}_1^{\mathrm{P}}} g_{\mathrm{P+1}}\mathrm{h}_1^{\mathrm{P+1}} + \frac{\mathrm{h}_2^{\mathrm{P}}}{\mathrm{h}_1^{\mathrm{P}}} g_{\mathrm{P+2}}\mathrm{h}_1^{\mathrm{P+2}} + \ldots \tag{D-4a}$$

$$f_2 = f_{\mathrm{EXACT}} + g_{\mathrm{P}}\mathrm{h}_2^{\mathrm{P}} + g_{\mathrm{P+1}}\mathrm{h}_2^{\mathrm{P+1}} + g_{\mathrm{P+2}}\mathrm{h}_2^{\mathrm{P+2}} + \ldots \tag{D-4b}$$

Subtracting (D-4b) from (D-4a) produces the following:

$$\left(\frac{h_2}{h_1}\right)^P f_1 - f_2 = \left(\frac{h_2}{h_1}\right)^P f_{\mathrm{EXACT}} - f_{\mathrm{EXACT}} + g_{\mathrm{P}}\left(\mathrm{h}_2^{\mathrm{P}} - \mathrm{h}_2^{\mathrm{P}}\right) + g_{\mathrm{P+1}}\left(\mathrm{h}_2^{\mathrm{P}}\mathrm{h}_1 - \mathrm{h}_2^{\mathrm{P+1}}\right) + g_{\mathrm{P+2}}\left(\mathrm{h}_2^{\mathrm{P}}\mathrm{h}_1^2 - \mathrm{h}_2^{\mathrm{P+2}}\right) + \ldots$$

which can be re-arranged using the definition of r_{12} as h_2/h_1, a term that, by definition is always greater than one. This re-arrangement produces eqn. (D-5).

$$r_{12}^{P} f_1 - f_2 = \left(r_{12}^{P} - 1\right) f_{\text{EXACT}} + g_P(0) + g_{P+1} h_2^{P+1} \left(\frac{1}{r_{12}} - 1 \right) + g_{P+2} h_2^{P+2} \left(\frac{1}{r_{12}^2} - 1 \right) + \ldots \tag{D-5}$$

Assuming that $O(h_1) = O(h_2)$, or alternately that $O(r_{12}) = 1$, eqn. (D-5) can be re-arranged and simplified as follows:

$$f_{\text{EXACT}} = f_1 + \frac{f_1 - f_2}{r_{12}^{P} - 1} + O(h^{P+1}) \tag{D-6}$$

Eqn. (D-6) of course, shows the exact solution to be the fine grid solution plus some other terms which represents an error between the two solutions.

The fractional difference between the fine grid and the exact solutions can be defined as:

$$A_1 \equiv \frac{f_1 - f_{\text{EXACT}}}{f_{\text{EXACT}}} = \frac{f_1}{f_{\text{EXACT}}} - 1$$

or…

$$A_1 = f_1 \left[f_1 + \frac{f_1 - f_2}{r_{12}^{P} - 1} + O(h^{P+1}) \right]^{-1} - 1$$

or…

$$A_1 = f_1^{-1} f_1 \left[1 + \frac{\frac{f_1 - f_2}{r_{12}^{P} - 1} + O(h^{P+1})}{f_1} \right]^{-1} - 1 \tag{D-7}$$

From Stewart [1991], the mathematical definition of a binomial expansion is given in eqn. (D-8), valid for any condition for which k is real and the absolute value of x is less than one ($|x|<1$).

$$(1 + x)^k = 1 + kx + \frac{k(k-1)}{2!} x^2 + \frac{k(k-1)(k-2)}{3!} x^3 + \ldots \tag{D-8}$$

For $k = -1$, this binomial expansion reduces to eqn. (D-9).

$$(1 + x)^{-1} = 1 - x + x^2 - x^3 + \ldots \tag{D-9}$$

With the term in brackets standing for $(1+x)$ and k being equal to -1, the binomial expansion from (D-9) can be substituted into eqn. (D-7) to yield:

$$A_1 = 1 - \left[\frac{f_1 - f_2}{\left(r_{12}^{P} - 1\right) f_1} + O(h^{P+1}) \right] + \left[\frac{f_1 - f_2}{\left(r_{12}^{P} - 1\right) f_1} + O(h^{P+1}) \right]^2 - \left[\frac{f_1 - f_2}{\left(r_{12}^{P} - 1\right) f_1} + O(h^{P+1}) \right]^3 + \ldots - 1$$

or…

$$A_1 = -\frac{f_1 - f_2}{\left(r_{12}^P - 1\right) f_1} + O(h^{P+1}) + \left[\frac{f_1 - f_2}{\left(r_{12}^P - 1\right) f_1}\right]^2 + \ldots \tag{D-10}$$

Using the definition of the normalized error term, E_1, from Roache [1998], A_1 can be represented by eqn. (D-11):

$$A_1 = E_1 + O(E_1^2, h^{P+1}) \tag{D-11}$$

with E_1 given by eqn. (D-12):

$$E_1 = \frac{f_2 - f_1}{\left(r_{12}^P - 1\right) f_1} \tag{D-12}$$

This approximation shows the normalized error estimator is equal to the fractional error estimator, accurate to an order of truncation of h^{P+1}, and the normalized error squared. This analysis is valid for E_1 less than one, so E_1^2 must be small as well.

Appendix E: Derivation of Global Force Parameters with Respect to Non-dimensionalization Procedures

Although not directly a part of the Navier-Stokes formulation itself or a factor in the input selection, the integration of total force is the primary result of interest from the CFD solution output. If non-dimensionalization is used (as it has been in this document), most secondary quantities – like velocities, pressures, effective viscosity, etc. can be recompiled into dimensional form via the use of Table 3-2. The global or integrated force parameters, however, require a bit more thought to transform the output of Ansys/FLOTRAN into the variables defined in eqns. (4-4), (4-5), and (4-6).

The global forces as output by Ansys/FLOTRAN are a mixture of integration of pressure and shear stress, which are both surface forces, or force per unit area. The non-dimensional pressure and shear stress can be seen from Table 3-2 or worked out dimensionally, and will be of the form given by eqns. (D-1a) and (D-1b).

$$\tau_W^* = \frac{\tau_W}{\rho_\infty V_\infty^2} \tag{E-1a}$$

$$P^* = \frac{P}{\rho_\infty V_\infty^2} \tag{E-1b}$$

From the Ansys/FLOTRAN manual, the *INTSRF* command performs the integration of these forces over a selected surface area, which basically does a numerical integration of eqns. (E-2) and (E-3) to get the respective force and moment components of the vectors.

$$\vec{F} = \int_A \vec{P}\, dA + \int_A \vec{\tau}_W\, dA \tag{E-2}$$

$$\vec{M} = \int_A \vec{r} \times \vec{P}\, dA + \int_A \vec{r} \times \vec{\tau}_W\, dA \tag{E-3}$$

In three dimensions, surface area is simply normalized by L_∞^2 to make it dimensionless. Thus, the following substitutions can be made into eqns. (E-2) and (E-3):

$$\vec{F} = \int_A \left(\rho_\infty V_\infty^2 \vec{P}^*\right) d\left(A^* L_\infty^2\right) + \int_A \left(\rho_\infty V_\infty^2 \vec{\tau}_W^*\right) d\left(A^* L_\infty^2\right)$$

$$\vec{M} = \int_A \left(L_\infty \vec{r}^*\right) \times \left(\rho_\infty V_\infty^2 \vec{P}^*\right) d\left(A^* L_\infty^2\right) + \int_A \left(L_\infty \vec{r}^*\right) \times \left(\rho_\infty V_\infty^2 \vec{\tau}_W^*\right) d\left(A^* L_\infty^2\right)$$

From Stewart [1991], the constants can be brought out of the cross-product in the moment equation to produce eqn. (E-4) for the force vector and eqn. (E-5) for the moment vector.

$$\vec{F} = \left(\rho_\infty V_\infty^2 L_\infty^2\right)\int_A \vec{P}^* \, dA^* + \left(\rho_\infty V_\infty^2 L_\infty^2\right)\int_A \vec{\tau}_W^* dA^* \tag{E-4}$$

$$\vec{M} = \left(\rho_\infty V_\infty^2 L_\infty^3\right)\int_A \vec{r}^* \times \vec{P}^* \, dA^* + \left(\rho_\infty V_\infty^2 L_\infty^3\right)\int_A \vec{r}^* \times \vec{\tau}_W^* \, dA^* \tag{E-5}$$

Since the actual code output is in terms of the dimensionless asterisk quantities, these equations show the relationship between the dimensional and dimensionless force and moment results. Re-arranging produces eqns. (E-6) and (E-7),

$$\vec{F} = \left(\rho_\infty V_\infty^2 L_\infty^2\right)\vec{F}^* \tag{E-6}$$

$$\vec{M} = \left(\rho_\infty V_\infty^2 L_\infty^3\right)\vec{M}^* \tag{E-7}$$

which show that the dimensionless output of the forces of Ansys/FLOTRAN can be multiplied by $\rho_\infty V_\infty^2 L_\infty^2$ to get the original dimensional values for each component. Likewise, multiplying the output moment components by $\rho_\infty V_\infty^2 L_\infty^3$ will get the dimensional moment contributions. This transformation can be used to move from dimensionless to dimensional results as necessary. If the problem is two-dimensional instead of three dimensional, the integration area will be a line rather than a surface. In this case, one of the dimensional scaling terms is removed, and the transformation is $\rho_\infty V_\infty^2 L_\infty$ for the force terms and $\rho_\infty V_\infty^2 L_\infty^2$ for the moment terms.

A translation of the force and moment system is also required, whether dimensional or not. Ansys/FLOTRAN tabulates the resulting vector system about the global origin of the model, which is probably not where the head center of the sensor is located. Thus, the system needs to be moved to the equivalent system applied on the head, located at the coordinates (x_H, y_H, z_H) in Cartesian space. Fig. 4-16 shows the required system conventions for this gage head.

The translation will not affect the components of the force vector, but the moment vector is indeed affected. Fig. D-1 shows the move, which will produce an additional moment about the new point calculated by the vector cross product **r** *x* **F**. The resulting system about the head center is termed the prime, ', system in this appendix only. The general relationship between it and the original system about the origin is given in relations (E-8) and (E-9).

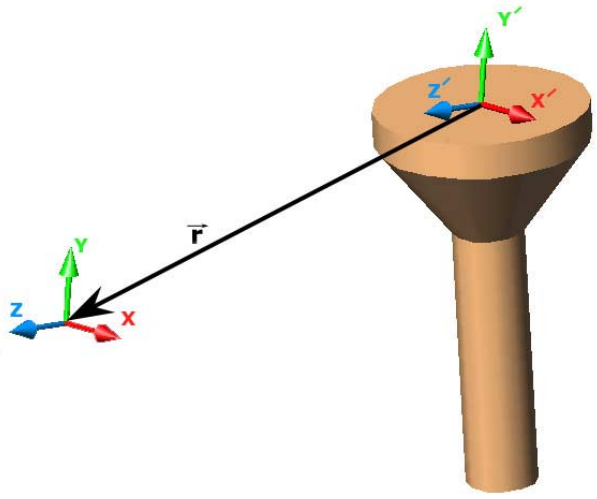

Figure E-1. Translation of Force/Moment System from Global Origin to Head Center

$$\vec{F}' = \begin{Bmatrix} F_X \\ F_Y \\ F_Z \end{Bmatrix} \tag{E-8}$$

$$\vec{M}' = \begin{Bmatrix} M_X + r_Y F_Z - r_Z F_Y \\ M_Y + r_Z F_X - r_X F_Z \\ M_Z + r_X F_Y - r_Y F_X \end{Bmatrix} \tag{E-9}$$

All results presented throughout this document are in terms of the head center system, which employed this translation. For the cases of the skin friction gages, the *z* component of force and the *x* and *y* components of moment are zero by symmetry. For a gage with head center located at an arbitrary point (x_H, y_H), thus making $\boldsymbol{r} = \{-x_H, -y_H, 0\}$, relations (E-8) and (E-9) simplify to the eqns. of (E-10) and (E-11). These two equations were used on every model to insure correct calculation of the total forces and moments about the head center of the gage.

$$\vec{F}' = \begin{Bmatrix} F_X \\ F_Y \\ 0 \end{Bmatrix} \tag{E-10}$$

$$\vec{M}' = \begin{Bmatrix} 0 \\ 0 \\ M_Z - x_H F_Y + y_H F_X \end{Bmatrix} \tag{E-11}$$

Vita

The author was born on September 13, 1976 to Andrew and Deborah MacLean. He lived his entire childhood life in Georgetown, NY in central New York State, attending Otselic Valley Central School in that area. Following high school, he attended the Rochester Institute of Technology in Rochester, NY where he pursued a combined set of degrees in the mechanical engineering department. This endeavor resulted in a Bachelor of Science in mechanical engineering with an aerospace concentration and a Master of Science in mechanical engineering, advised by Dr. P. N. Venkataraman in that department in a thesis involving developing code for airfoil optimization algorithms. He then came to Virginia Tech in Blacksburg, VA to pursue a PhD in aerospace engineering with Dr. Joseph Schetz. Upon submission of this document, he is seeking employment in a field related to CFD.

CONTACT EMAIL: matt@chimeracfd.com